Winter 2022

Concurrent Measurements of Inflow, Power Performance and Loads for a Grid-Synchronized Cross-Flow Turbine Operating in a Tidal Estuary

Patrick W. O'Byrne
University of New Hampshire, Durham

Comments

DOI: https://dx.doi.org/10.34051/p/2023.13

Concurrent Measurements of Inflow, Power Performance and Loads for a Grid-Synchronized Cross-Flow Turbine Operating in a Tidal Estuary

By

Patrick W. O'Byrne

BS Mechanical Engineering, University at Buffalo, 2014

THESIS

Submitted to the University of New Hampshire

in Partial Fulfillment of

the Requirements for the Degree of

Master of Science

in

Ocean Engineering

December 2022

This thesis has been examined and approved in partial fulfillment of the requirements for the degree of Master of Science in Ocean Engineering by:

Thesis Director, Martin Wosnik, Associate Professor of Mechanical Engineering and Director of the Center for Ocean Engineering

Erin Bell, Department Chair and Professor, Civil and Environmental Engineering

Thomas Lippmann, Professor of Earth Sciences and Ocean Engineering

On December 7, 2022

Approval signatures are on file with the University of New Hampshire Graduate School.

ACKNOWLEDGEMENTS

Thank you to my parents Tim and Colleen O'Byrne for raising me an environment where I could grow up to feel capable to be the change I want to see in the world. Thank you to my brother Kevin for your friendship. Thank you to our grandfather Ray Lyons who taught us to live fearlessly and that we can do anything we set our minds too. Thank you to my partner, Elizabeth who encouraged and supported my choice to pursue a graduate education. We have allowed each other to pursue our dreams unopposed and I know we have our best years ahead of us, I love you dearly and am forever grateful.

The success of this project is representative of the cumulative efforts of everyone who has contributed to the design, development and operation of the UNH Living Bridge Turbine Deployment Platform. Thank you to Ian Gagnon who's platform design continues to provided a safe and stable structure. Thank you to Kaelin Chancey for the extensive development of the instrumentation deployment systems and tidal current resource characterization at this site. Thank you to Martin Wosnik who works tirelessly to keep this work well funded and to grow the knowledgebase surrounding tidal energy converter devices. Thank you to John Hunt who has been our boat captain and led nearly every trip to the platform. John provides a continuous record of knowledge and skills required to operate and troubleshoot the platform. Thank you to Mason Bichanich and Michael Monahan who contributed a significant amount of time and energy in preparation and execution of the Fall 2021 measurement campaign.
This thesis was partially funded by the Alliance for Sustainable Energy, LLC, Managing and Operating Contractor for the National Renewable Energy Laboratory for the U.S. Department of Energy. I would specifically like to extent my appreciation to Casey Nichols, Robert

Raye and Aidan Bharath for their efforts in integrating our platform instrumentation into the MODAQ environment, this effort would not have been possible without them.

Thank you to Northeast Integrations Dylan Kimmel, Chris Fuller and Jeff Stevens for their continued support in the maintenance and operation of the platform.

Thank you to Joshua Ulliac, formerly of New Energy Corporation, for his support troubleshooting and repairing the control system.

Thank you to Laura Gustafson, formerly of SMSOE, for all her purchasing help which was an integral part of completing the UNH MODAQ build on time.

Thank to Corina Gudinas for her help replacing the power supplies within the MacArtney multiplexer, this was a critical task that required her specialized skill and patience.

I would like to thank my former colleagues at AGTServices who taught me everything I know about generators and power systems "Its just steel, Copper and insulation". Specifically Mike Bresney, Vinny Rigosu, Bill Dollard, Chuck Marino, Nick Rebich, Paul Jensen, Kurt Carlone, Terry Benson, Tracey Stephenson, Rick Buechner and Allan Concepcion, along with all the winders and craftsman that taught me so much over the years.

TABLE OF CONTENTS

LIST OF TABLES

LIST OF FIGURES

LIST OF ACRONYMS

ADCP - Acoustic Doppler Current Profiler

ADV - Acoustic Doppler Velocimeters

BA - Biological Assessment

BDI - Bridge Diagnostics Inc

CACTUS - Code for Axial and Cross-flow Turbine Simulation

CB - Control Breaker

CORE - UNH Center for Ocean Renewable Energy

CTD - Conductivity, Temperature, Depth

DAQ - Data Acquisition

dia - diameter

DOE - Department of Energy

EMEC - European Marine Energy Centre Ltd

GND - Ground

GPS - Global Positioning System

HDPE - High Density Poly Ethylene

HV - High Voltage

IEA - International Energy Agency

IEC - International Electrotechnical Commission

IMU - Inertial Measurement Unit

IR - Insulation Resistance

K1 - Generator Connection Contactor

K2 - Turbine Brake Contactor

LB - Living Bridge

LB-DAS - Living Bridge Data Acquisition System

LB-Server - Living Bridge Server

LV - Low Voltage

MCC - Motor Control Center

MHK - Marine Hydrokinetic

MHKDR - Marine Hydrokinetic Data Repository

MOIS - Modular Ocean Instrumentation System

MODAQ - Modular Ocean Data Acquisition System (by NREL)

MUX - Multiplexer

NACA - National Advisory Committee for Aeronautics

NAN - Not a Number

NECI - New Energy Corporation Inc

NEI - Northeast Integration

NEPA - National Environmental Policy Act

NI - National Instruments

NSF - National Science Foundation

NMFS - National Marine Fisheries Services

NOAA - National Oceanic and Atmospheric Administration

NREL - National Renewable Energy Laboratory

NTP - Network Time Protocol

ORPC - Ocean Renewable Power Company

PF - Power Factor

PGP - Programmatic General Permit

PRIMRE - The Portal and Repository for Information on Marine Renewable Energy

QC - Quality Control

ReDAPT - Reliable Data Acquisition Platform for Tidal

RMS - Remote Monitoring System

RMS - Root Mean Square

RPM - Rotations per minute

R1 - Startup Relay

R2 - Grid OK signal

R3 - Rectifier OK signal

R4 - Brake Resistor OK signal

R5 - Generator Isolator signal

SCADA - Supervisory Control and Data Acquisition

TEAMER - Testing Expertise and Access to Marine Energy

TEC - Tidal Energy Converter

TIG - Tungsten Inert Gas

TIP - Turbine Interface Panel

TRL - Technical Readiness Level

TDP - Turbine Deployment Platform

TPM - Turbine Pitching Mechanism

UNH MODAQ - UNH iteration of the NREL Modular Ocean Data Aquisition System

USACE - United States Army Corps of Engineers

UNH - University of New Hampshire

VGP - Vertical Guide Post

VPI - Vacuum Pressure Impregnation

WEC - Wave Energy Converter

WMDS - Wildlife Mitigation Device System

LIST OF SYMBOLS

Fundamentals of Cross Flow Turbines Equations Symbols

$\rho =$ density of water [kg/m^3]

$\beta =$ Preset Blade Pitch Angle [°] (positive angle = the toe in direction)

$\omega =$ Angular Velocity

$T =$ Torque

$A_{rotor} =$ Projected area of rotor perpendicular to flow direction

$V =$ Flow Velocity (U_∞ & U_{in})

$P_{device} =$ Power extracted by a device

$P_{available} =$ Maximum power available in the flow

$C_p =$ Power Coefficient

$C_t =$ Thrust Coefficient

$\lambda =$ Tip Speed Ratio (TSR)

$\alpha =$ Angle of Attack (AoA)

$\theta =$ Blade Angular Position

$r =$ Rotor radius

$F_l =$ Lift force acting on rotating blade

$F_d =$ Drag force acting on rotating blade

Turbine Pitching Mechanism Dimensions

$x_1 =$ Horizontal distance between load cells and spanning beam axis

$x_2 =$ Horizontal distance between bow anchor point and spanning beam axis

$x_3 =$ Horizontal distance between stern anchor point and spanning beam axis

$x_4 =$ Horizontal distance between bow side of strong-back and spanning beam axis

$x_5 =$ Horizontal distance between centerline of turbine shaft and spanning beam axis

$z_1 =$ Vertical distance between turbine centerline and spanning beam axis

$z_2 =$ Vertical distance between strong-back anchor point and spanning beam axis

$z_3 =$ Vertical distance between surface of TDP deck and spanning beam axis

$\theta_B =$ Angle of tension link load cell w.r.t. horizontal (ebb tide thrust calibration)

$\theta_S =$ Angle of tension link load cell w.r.t. horizontal (flood tide thrust calibration)

Turbine Pitching Mechanism Forces

$M_{SB} =$ Summation of moments about the spanning beam axis

$F_{Thrust} =$ Thrust force on turbine from tidal current

$F_{Port} =$ Reaction force measured by port side thrust load cell

$F_{Starboard} =$ Reaction force measured by starboard side thrust load cell

$F_{TL-Ebb} =$ Tension link load cell force in ebb direction

$Fx_{TL-Ebb} =$ Horizontal component of F_{TL-Ebb}

$Fz_{TL-Ebb} =$ Vertical component of F_{TL-Ebb}

$F_{Sim-Thrust}Ebb =$ Simulated thrust force from ebb tide direction

$F_{Thrust-Ebb} =$ Thrust force on turbine from ebb tides

$F_{LC-sum} =$ Port and starboard load cell summation (what is measured)

$static_{weight} =$ F_{LC-sum} when no external loads are applied

$m_{Ebb} =$ average slope between initial and final calibrations

$F_{TL-Flood} =$ Tension link load cell force in flood direction

$Fx_{TL-Flood} =$ Horizontal component of $F_{TL-Flood}$

$F_{Sim-Thrust}Flood =$ Simulated thrust force from flood tide direction

$F_{Thrust-Flood} =$ Thrust force on turbine from flood tides

$m_{Flood} =$ average slope between initial and final calibrations

ADCP Section

$V_{ADCP-Beam} =$ ADCP along beam water velocity [m/s]

$f_{Source} =$ Source Frequency [Hz]

$f_{Doppler} =$ Doppler shift Frequency [Hz]

$C =$ Speed of sound in water [m/s]

$\alpha =$ Acoustic Beam Angle [°]

V_{X-ADCP} = ADCP velocity estimate in along platform direction (+ in ebb direction)

V_{Y-ADCP} = ADCP velocity estimate in cross platform direction (+ in Portsmouth shore line direction)

$Heading_{pier}$ = 105.05°

θ_P = $Heading_{pier}$ - 90° [converted to radians]

V_{North} = Converted velocity estimate to true North heading

V_{East} = Converted velocity estimate to East heading relative to true North

ADV Section

$V_{ADV-Beam}$ = ADV along beam water velocity [m/s]

$\Delta\varphi$ = Phase difference between successive sound pulses measured by each receiver [unitless]

V_{X-ADV} = ADV velocity estimate in along platform direction (+ in flood direction)

V_{Y-ADV} = ADV velocity estimate in cross platform direction (+ in Portsmouth shore line direction)

Power Measurements

RPM_{shaft} = Rotational rate of the drive shaft (ie the cross flow turbine) [revolutions per minute]

f_{RPM} = Turbine rotation rate [Hz]

f_G = Generation frequency [Hz]

$\#ofpoles$ = The # of individual permanent magnetic poles on the generator field (summation of North and South poles)

Results Section

f_N = Nyquist frequency [Hz]

f_s = Sample frequency [Hz]

N = Time series record Length

ABSTRACT

Concurrent Measurements of Inflow, Power Performance and Loads for a Grid-Synchronized Cross-Flow Turbine Operating in a Tidal Estuary

by

Patrick O'Byrne

University of New Hampshire, December 7, 2022

The adaptation of sustainable fluid energy conversion technologies, such as wind or tidal energy, requires numerical modeling tools that are able to accurately predict device performance and loading in an effort to reduce the costs of turbines, deployment platforms and mooring structures. To validate models, data sets from turbines operating in real flow environments are required. Particularly for tidal energy, data sets of inflow (tidal current resource), power performance (electrical power and shaft speed), and thrust loading for any scale device are rare because the work to date has largely been funded by private developers and the data is not made publicly available. This "silos" the development of knowledge around operating devices to individual developers, which slows the pace of commercialization for the technology sector as a whole.

The research project presented here utilized an existing tidal turbine, a modified New Energy Corp EVG-025 vertical axis cross flow turbine (3.2m dia. X 1.7m tall), deployed at the UNH Tidal Energy Test Site at the Memorial Bridge in Portsmouth, NH. Significant improvements were made to the existing system, including the first grid synchronous operation, the development of a new data acquisition system (DAQ) and adding time synchronization across new and existing DAQ's to allow for accurate performance and load characterization of the device.

A significant data acquisition campaign was conducted during the fall of 2021, with over 750 kWh hours of renewable tidal energy delivered to the NH grid during 29 days of turbine operation. Turbine power performance and thrust loading was characterized over a range of inflow operating conditions. Spectral analysis indicates the effects of turbulent structures on thrust loading and power output. The results further highlight the need for accurate instrument location and temporal resolution for accurate tidal resource characterization when siting new projects. This data set with all the concurrent measurements is sufficiently detailed for numerical model validation in real tidal flows. After significant quality control (QC) processing, the data set has been published in a public database, MHKR/PRIMRE. (Link: MHKDR-394)

CHAPTER 1

Introduction

1.1 Transition to Marine Renewable Energy

1.1.1 Need for Renewable Energy

Humanity is in desperate need to decarbonize the energy industry to reduce greenhouse gas emissions which are causing global temperature rise [9]. Atmospheric temperatures are significantly affected by greenhouse gas levels (primarily carbon dioxide, CO2 and methane, CH4) that maintain solar energy within the atmosphere that otherwise would have been reflected back into space. Variation in CO2 and CH4 gas concentrations have been found to be common over Earth's history with direct evidence during the past 800,000 years of the Quaternary period [10]. During this time ice was formed and preserved on the Antarctic and Greenland Ice sheets. The ice traps gas bubbles as it was formed which contain a snapshot of the surface level atmospheric gas concentration. Ongoing ice core sampling projects have been conducted, on both ice sheets, to develop a time series of gas concentration by analyzing the gas content at different depth levels of ice, which correspond to different points in time [10]. For more information on how the ice layers are dated refer to [11].

Changes in atmospheric CO2 concentration in the ice core record have been linked to periods of glaciation and interglaciation which typically vary from 200 ppm during glacial expansion to 280 ppm during glacial retreat on a roughly 100,000 year cycle. The Holocene Epoch is defined as the interglaciation period starting 11,000 years ago which has been characterized by stable moderate temperatures and enabled the expansion and progression

of humanity. Continuous sampling of atmospheric gas concentration at the Mauna Loa site in Hawaii began in 1958 and has shown a consistent year over year rise in atmospheric CO2 levels now exceeding 415 ppm in September 2022, well above any levels detected in the ice core data [12]. This rise in atmospheric CO2 concentration has occurred much more rapidly than typical cycles over the Quaternary period. These gas levels have not likely been present in the atmosphere since the Mid-Piacenzian Warm Period 3 to 3.3 million years ago [13]. During that period the average earth temperature was approximately 3C higher and ocean levels were approximately 20m higher than today.

It is the shifting climate that will result from global temperature rise that provides the incentive to decarbonize every sector of our global economy to limit the extent the climate may shift. Ultimately, removal of the excess CO2 in our atmosphere to reverse climate effects will be required to preserve the earth climate that has supported the global expansion and proliferation of humanity and protect us from an unpredictable climate future.

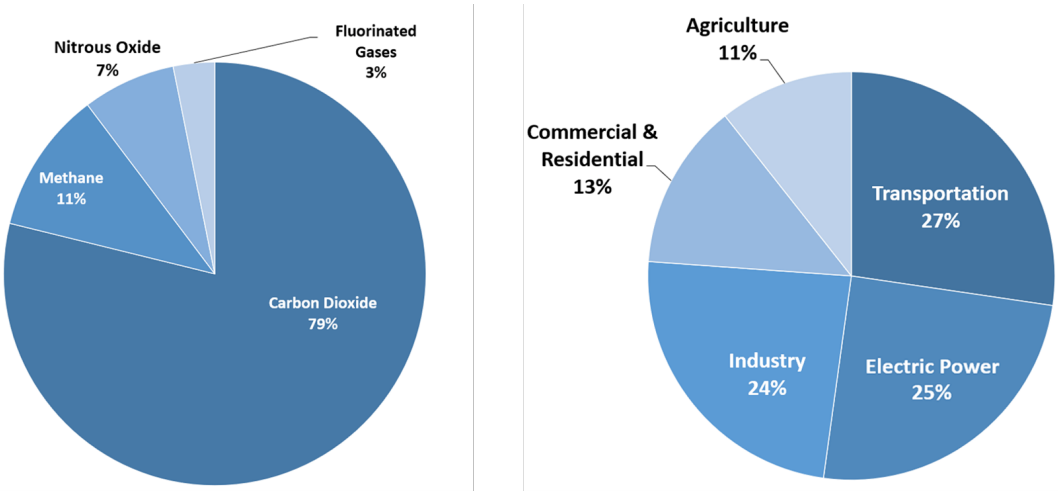

Figure 1.1: [Left] Overview of U.S. Greenhouse Gas Emissions in 2020. [Right] Sources of U.S. Greenhouse Gas Emissions in 2020. [1]

Carbon dioxide is a primary exhaust gas from the combustion of fossil fuels and is the largest source of green house gas emissions, accounting for nearly 80% of the emissions in the U.S.(Figure 1.1[Left]). To reduce CO2 emissions across the economy it is useful to understand which sectors are most directly linked to fossil fuel consumption, to focus technology

development specifically in those areas. Transportation, electrical power generation and general industrial combine for over 75% of the total CO2 emissions annually in the US making them key sectors to decarbonize first (Figure 1.1 [Right]).

1.1.2 History of Water Power and Scale of Energy Demand

There are many sustainable/non-carbon energy sources available for electrical power generation on this planet including, wind, solar, geothermal, nuclear and water power. Waterpower has been used as a sustainable energy resource that has played a key role in industrialization, from water wheels that drove mills alongside rivers to modern hydroelectric generating facilities [14]. Conventional hydropower, which relies on an impoundment or dam to store a reservoir of water, accounted for over 6% of the nearly 4 trillion kilowatt hours (kWh) of electricity produced in the US in 2021. Figure 1.2 presents the complete breakdown of electrical generation share by fuel source in the U.S. in 2021.

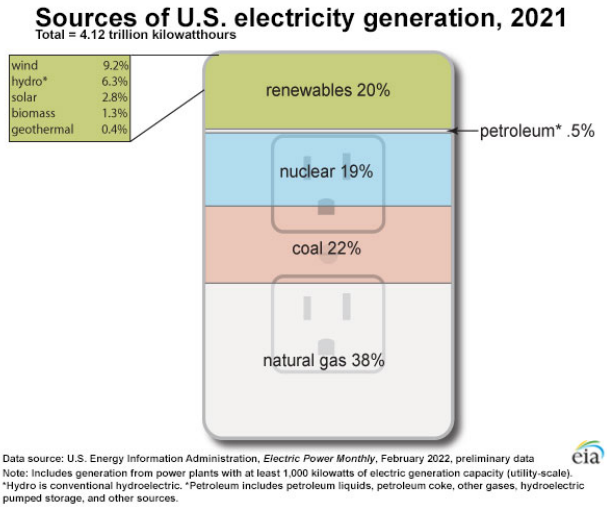

Figure 1.2: Sources of Electrical Generation in the United States in 2021. [2]

1.1.3 Marine Renewable Energy Resource

Recent marine renewable energy resource characterization studies in the U.S. have shown a technical resource available in wave, tidal currents, ocean current, ocean thermal and run

of the river environments, greater than 57% of U.S. 2019 electricity demand ([3] & [15]). Of this overall technical resource roughly 10% is from tidal currents and 4% is from river currents which (combined) have the potential to provide electrical power to over 30 million homes in the U.S. (based on an average annual consumption of 10,649 kWh per household in 2019 [3]). More than 95% of the total U.S. tidal energy resource is located in Alaska equating to more than 20x the current electricity demand of the state [16]. This large potential means that by capturing just 5% of the resource a significant achievement could be made toward decarbonizing Alaska's economy.

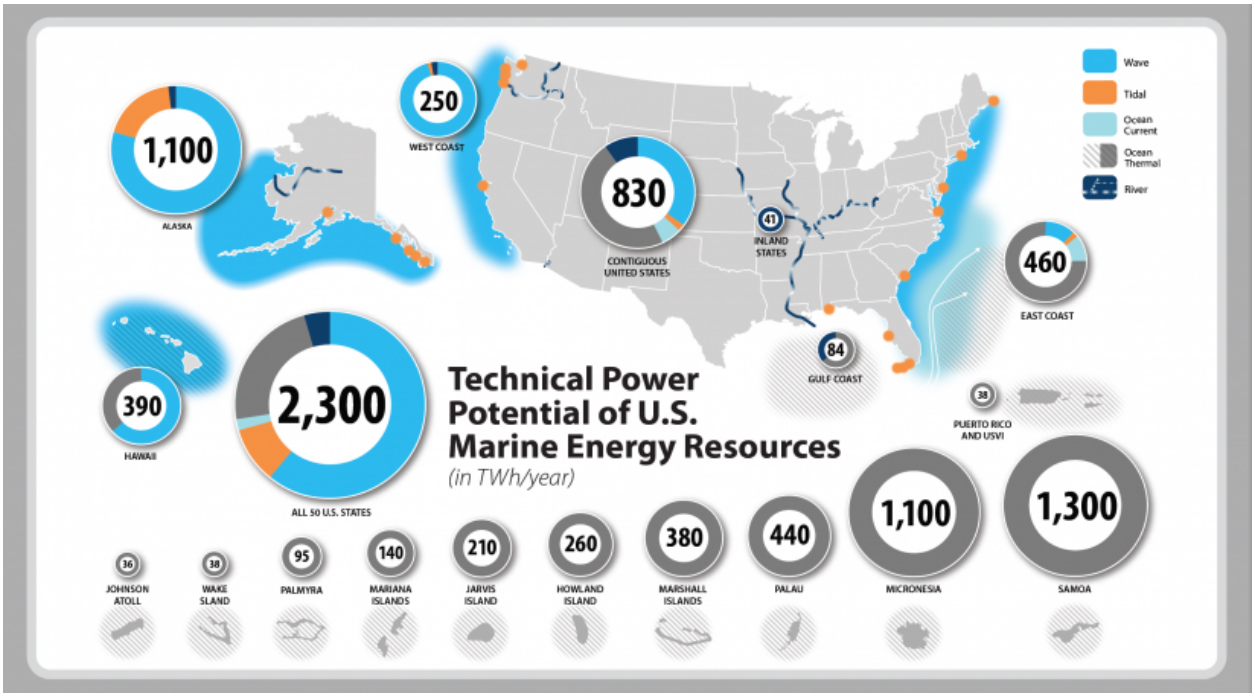

Figure 1.3: Technical Power Potential of US Marine Energy Resources [3]

Tidal energy converters (TEC) transform the kinetic energy from moving water that is driven by tidal forces into another useful form that can be readily used or stored. Tidal forcing on the Earth's oceans are driven by the gravitation force of attraction that the moon and sun exert on the water, combined with the centrifugal forces generated as earth rotates about the barycenter of the earth-moon-sun system ([17] & [18]). The variation in orbit and tilt of each celestial body drive the long term variations in the primary tidal signal and make

up the remaining tidal constituents, first presented by Doodson in 1922 [19]. This precise understanding allows tidal levels and corresponding tidal currents to be forecasted well into the future with just a short amount of data collected from a specific site of interest. The ability to forecast the tides makes this renewable energy source particularly attractive when compared to wind and solar which are affected by local climate and are difficult to forecast longterm.

Run of the river energy converters differ from conventional hydro power plants as there is no dam associated with the project and they utilize the same technology as TEC's. Wave energy converters (WEC) convert the energy available in a wave field, either the vertical motion associated with variation in sea level as the wave propagates past a point or by converting the energy available in the waves orbital velocities below a wave or a combination of both. Although wave energy accounts for the majority of the marine renewable energy resource (1,400 TWh/yr), TEC devices are the closest technology to commercialization due to the development parallels with wind energy conversion devices.

1.2 Tidal Energy History and Environmental Impacts

1.2.1 Tidal Barrages

Tidal energy has been recognized as a useful energy source for over 1000 years, traditionally through the use of tidal barrages [20]. Tidal barrages capture incoming tidal flows and then control the release of the water to drive a mill or turbine to do useful work. This technology requires specific geography suitable for project development with modern projects including a 240MW plant in La Rance, France constructed in 1966, and a 254MW plant located in South Korea constructed in 2011 [20].

Tidal barrages introduce significant environmental impact to the coastal marine ecosystems where they are located and limit commercial/recreational boating access to the impounded areas. The environmental impacts of tidal barrage sites are outlined in Hooper & Austen 2013 [21] which include:

1. Benthic ecosystem due to changes in local sediment morphology
2. Limit of fish passage for anadromous fish species to access essential spawning habitat
3. Changes in local water level and flow rates affect shoreline plant and animal communities along with pollution dispersion or release

Due to these geographic, economic and environmental challenges a limited number of tidal barrage sites have been developed.

1.2.2 Instream Tidal Energy Devices

Recently, researchers and technology developers have turned to point source or instream devices that utilize the kinetic energy available in naturally occurring energetic flow environments to generate electricity. The tidal energy converter (TEC) that is the subject of this thesis falls into this category. This technology can significantly decrease the environmental impact of a project and increase the number of locations where tidal energy projects can be located. These projects impose new potential environmental impacts, when compared to tidal barrage sites, and are studied closely in conjunction with turbine technology development. The Ocean Energy System 2020 State of the Science Report [22] outlines potential environmental impacts of tidal current, river current and wave energy devices on marine ecosystems. Environmental monitoring techniques and lessons learned are also presented from data collected around TEC systems installed around the world [22]. The primary environmental impacts of concern include:

1. Collision Risk of marine animals with static and dynamic components of an installation
2. Underwater noise generated from devices
3. Electromagnetic fields surrounding undersea cables
4. Habitat effects from mooring structures throughout water column

5. Changes to oceanographic system due to installation (water current, direction, wave height) and their associated effects on sediment transport and water quality

The advancement of TEC devices is intimately tied to the understanding and mitigation of potential environmental impacts because of the requirements imposed by law and implemented by regulating bodies surrounding marine mammal, endangered species and essential fish habitat protection. The combination of studying environmental impacts along with TEC technology development will help to improves device design, reduce costs, and streamline environmental permitting for future projects.

1.3 Tidal Energy Opportunities/Markets

1.3.1 Remote microgrids

Remote and island communities have been identified as early opportunities where TEC projects are economically suitable solution to meet existing energy needs [23]. Historically, these locations have relied heavily on diesel powered generators to meet energy demands and limited land availability make solar installations a challenge. Tidal energy has a unique opportunity to help provide a predictable and sustainable renewable energy resource in some coastal communities.

Ocean Renewable Power Company (ORPC) is a US based turbine developer that has partnered with the village of Igiugig, AK and the Department of Energy (DOE) to develop the Igiugig Hydrokinetic Project in the Kvichak River. The village of Igiugig is a Sovereign Native American village that is home to 68 residents and is located at the confluence of the Kvichak River and Iliamna Lake in remote south west Alaska [24]. The ORPC RivGen System, capable of producing 40kW at 2.25m/s, has been deployed in the Kvichak River since 2019 with a second system installed in 2021 [25]. With both systems installed, along with a battery storage system, the community will be able to transition from diesel generators to a renewable electricity generation source. This project represents the successful application

of TEC technology in a remote micro-grid setting.

1.3.2 Commercial Scale Opportunities

The predictability of tidal power also makes it an attractive commercial scale renewable power source for grid operators. A 2008 study by Jack Hardisty analyzed the phase lag of the tidal signal around the island of the United Kingdom [26]. The study determined a continuous baseload of about 45MW could be achieved by deploying TEC devices at 6 strategic locations around the island. The tidal energy resource in Alaska's also lends itself to commercial scale electrical power generation due to the size of the resource compared to the existing demand. This excess energy beyond the electrical power demand could be used to generate green hydrogen which is an effective means of storing energy for use in other sectors. Heavy machinery manufacturers already produce hydrogen models and the shipping industry is showing signs of transitioning to hydrogen for their fuel source [27].

1.4 Path to Commercialization

The path to commercialization TEC technology requires continued efforts to develop and refine modeling tools, long term operational experience to improve reliability, and quantifying & mitigating environmental risks to stream line permitting.

1.4.1 Fundamentals of Cross-Flow Turbine Operating Theory

The amount of power available to extract from a moving fluid has been extensively studied and theoretical limits determined. The basic physical model consists of a one dimensional streamtube with an actuator disk to simulate the rotor drag on the free steam. The pressure drop across this disk, combined with the velocity reduction between locations upstream and downstream, and the rotor or disk area are representative of the power extracted by a device. For a complete derivation the reader is directed to [6] section 4.4, [5] section 2.1 or [28]. The theory results in the following basic working equations for turbine power and thrust force.

The power available in the flow over an area perpendicular to the flow, A_{rotor}, is

$$P_{available} = \frac{1}{2}\rho A_{rotor} V^3 \tag{1.1}$$

The power converted by the device is

$$P_{device} = T\ \omega = \frac{1}{2} C_p \rho A_{rotor} V^3 \tag{1.2}$$

where the power coefficient C_p is defined as the fraction of the available power that is converted to usable power.

$$C_p \equiv \frac{P_{device}}{P_{available}} = \frac{T\ \omega}{\frac{1}{2}\rho A_{rotor} V^3} \tag{1.3}$$

Note that in the one-dimensional streamtube derivation C_p is defined as the fluid-dynamic efficiency of the rotor, i.e., as the fraction of the available power in the flow that is converted to rate of shaft work. Sometimes C_p can also be defined as the overall efficiency of the tidal energy conversion system, including rotor efficiency, gearbox efficiency (if used), generator and power conversion efficiency, i.e., as the fraction of the available power in the flow that is converted to electrical power.

The resulting force on the device in the flow direction, or thrust force, can be written as

$$F_{Thrust} = \frac{1}{2} C_t \rho A_{rotor} V^2 \tag{1.4}$$

where the thrust coefficient C_t is defined by this equation.

The discussion and equations above apply to axial-flow or cross-flow turbines, and the symbols used in the equations are defined as

$P_{available}$ = Maximum power available in the flow

ρ = Fluid density

A_{rotor} =Device swept area perpendicular to the flow direction

V = Fluid velocity

P_{device} = Power extracted by a device

C_p = Power Coefficient

F_{Thrust} = Thrust force on device

C_t = Thrust Coefficient

T = Torque (of turbine rotor)

ω = angular velocity (of turbine rotor)

Cross-flow turbines have a rotor axis that is oriented perpendicular to the principal flow direction and blades that rotate around this axis, thereby changing their angle of attack with blade position throughout the rotation. Figure 1.4 by *Bachant 2016* [4] illustrates the principle forces, F_l (lift) and F_d (drag), acting on a cross-flow turbine blade at radius, r, at angular position, θ, with angular velocity, ω, with inflow velocity vector, U_{in}. The relative velocity U_{rel} that the turbine blade experiences is the vector summation of the of the inflow velocity U_{in} and blade relative velocity $\omega * r$, neglecting effects of induction. The blade angle of attack (AoA), α, is the angle between U_{rel} and the blade chord (chord line of a hydrofoil profile is the line connecting leading and trailing edges).

Rotor shaft speed is parameterized by the non-dimensional variable tip speed ratio (λ), a non-dimensional rate of rotation, defined in Equation 1.5.

$$\lambda \equiv \frac{\omega * r}{U_\infty} \tag{1.5}$$

Where:

λ = Tip Speed Ratio (TSR)

ω = Shaft angular velocity

r = Rotor radius

U_∞ = Free stream fluid velocity (U_{in})

The actuator disk model is a good representation for axial flow turbines where the rotor axis of rotation is aligned with the principle flow direction and the blades spin in a plane perpendicular to that axis. The blade angle of attack, α, remains constant for an axial flow turbine blade at a given radial position for a uniform inflow.

The nature of cross flow turbine operation results in a changing angle of attack, α, on the blade over each blade rotation about the rotor shaft, even in a uniform inflow. Cross-flow turbines operating in the marine environment are subject to relatively low fluid velocities (2-5m/s) when compared to wind (13-25m/s) but operate in a fluid with much higher density. This requires more robust designs, which have higher solidity and lead to lower tip speed ratios. High tip speed ratios for cross flow turbines reduce the envelop that the angle of attack

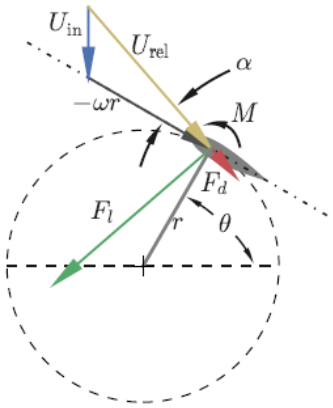

Figure 1.3: Vector diagram of velocity and forcing on a cross-flow turbine blade element. Note that the free stream velocity U_∞ is oriented from top to bottom (identical to U_{in} for purely geometric calculations), the blade chord (dash-dotted line) is coincident with the tangential velocity (i.e., zero preset pitch, which would offset the geometric angle of attack α), and the drag vector is magnified by a factor of two (approximately, relative to the lift vector) to enhance visibility.

Figure 1.4: Cross Flow Turbine Blade Forcing Diagram from *Bachant 2016* [4]

can vary during operation Figure 1.5 [5]. In cases where the tip speed ratio is sufficiently low, the angle of attack, α can reach critically high levels where dynamic stall can occur. Dynamic stall is the separation of flow from the air foil surface which causes a vortex to be shed affecting the loading on the blade. This phenomenon must be accounted for to accurately model the performance of a device operating within this range.

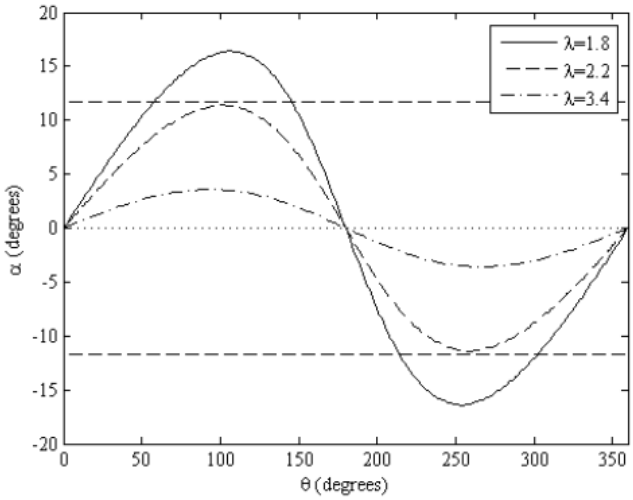

Figure 2.4 Theoretical turbine blade angle of attack at various tip speed ratios, including estimated induction. Dashed horizontal lines show typical static stall angle.

Figure 1.5: Cross flow turbine blade angle of attack, α, vs blade angular position, θ, at various tip speed ratios λ *Bachant 2011* [5]

1.4.2 Cross Flow Turbine Model Development History

In the 1970's Sandia National Labs (SNL) extensively tested airfoils for axial flow and cross flow wind energy conversion devices. This led to the multiple stream tube model (MST), first introduced by *Strickland 1975*, for cross flow turbines [29]. This model attempted to characterize the variation in loading that a cross flow device experiences.

This model provided the basis for (CACTUS) Code for Axial and Cross-flow developed by *Murray and Barone in 2011* at SNL for use with cross flow marine hydro kinetic (MHK) devices [30]. *Wosnik and Bachant in 2016* evaluated the performance of CACTUS and other existing performance models when applied to the cross flow MHK turbines and concluded

that CACTUS under performed for low tip speed ratio devices where dynamic stall was likely to occur [31].

Currently over 25 turbine developers are listed in the Portal and Repository for Information on Marine Renewable Energy (PRIMRE) database, funded by the US DOE Water Power Technologies Office, highlighting the impact continued model development will have on the industry [32]. The National Renewable Energy Lab (NREL) is leading efforts to expand the existing models for MHK cross flow devices with their open source OpenFast software [33]. Additionally, commercial software *Tidal Bladed* was developed by DNV which was validated in conjunction with the ReDAPT project (EU) [34]. It is not clear on the fidelity of this model and it is rumored *Tidal Bladed* is longer being supported by DNV.

To support model development and validation data on operating devices in real flow environments is critical. Collecting concurrent tidal resource (U_{in}), Power (P_{Device}), thrust load,(F_{Thrust}), and shaft speed,(ω) will provide inputs to allow models to be tested. Successful model development and validation will help to improve turbine design and reduce costs to construct and maintain TEC systems.

1.4.3 Existing Global Test Facilities

Commercial scale TEC devices (100's of kW to >1MW) have been tested over the past decade primarily at the European Marine Energy Centre (EMEC) Fall of Warness test site located in the Orkney Islands in north Scotland, UK. This location is ideal for completing accredited testing of commercial scale devices. Accredited testing is the systematic quantification of device performance by a third party adhering to an accepted set of criteria. EMEC is an accredited test agency and completes device testing for turbine developers in accordance with the IEC TC-114 technical committee and corresponding TS-62600 standards package for marine energy conversion systems. Accredited testing is a critical step in advancing TEC technology because it provides power generation developers, who secure funding for projects, and insurance agencies, who underwrite projects, confidence in the technology performance

and in operating costs [35]. Aside from EMEC, four more locations where full scale devices can be tested were identified around the world and are summarized in the Tidal Energy Test Site Spreadsheet in Appendix A. The International Energy Agency (IEA), Ocean Energy Systems (OES) 2021 report also provides an overview on the current state of the marine renewable energy industry globally [36].

Testing devices at commercial scale however is extremely costly and is only feasible after extensive testing and qualification of scale devices. Thirteen test sites were identified around the world where scale devices can be tested which are summarized in Appendix A. IEC accredited testing of scale devices is available at the EMEC Shapinsay Sound test site located Scotland, UK.

The vast majority of these test sites both scale and commercial are located in Europe which poses a challenge for US based turbine developers. EMEC does offer accreditation services of device performance testing outside of their test sites but a suitable test site is still required. An example where this was completed is the Verdant Power, East River Project, completed in 2021. For this project, EMEC provided third party verification that Verdant Power adhered to the IEC standards during the operating tests of their Tri Frame System. This test site, however, was only permitted and maintained by the private development company, Verdant, which does not readily allow for continued testing at this site past Verdant.

Under the new Atlantic Marine Energy Center, funded by the US Department of Energy, UNH is working towards developing the Tidal Energy Test Site at Memorial Bridge in Portsmouth, NH as an accredited test site for scaled tidal turbines up to 3m in size.

1.4.4 Existing Data Sets

Nearly all of the power performance data sets collected on operating TEC devices are sponsored by the technology developers themselves. This means that the data is held privately and only disseminated through white papers where the data has been normalized in means

to prevent replication or further use. This pattern has hindered the development of the industry as a whole because researchers and developers cannot learn from the successes and mistakes of other projects in a cohesive fashion. Multiple parties wind up facing challenges that someone else may have already solved, wasting time and slowing the commercialization of the technology. Historically developers of these larger projects have built and tested devices and then lost funding and with it, the knowledge gained.

18 publicly available data sets related to axial and cross flow turbines (modeling and field data) were identified and the variables recorded are summarized in the Tidal Energy Data Sets Spreadsheet in Appendix A. These data sets are either currently available or under a limited non-disclosure timeline to provide sufficient time for the creators to make use of the data first before it becomes public. The relevant parameters identified include, grid connectivity, inflow current, wake data (downstream from operating and stalled turbine), thrust force (operating and stalled turbine), electrical power, shaft speed, shaft torque, system model. Even though some of these data sets have operated under government funding the extent of the data disseminated is limited to the project scope of that funding. For example, you may only have access to ADCP data collected around an operating turbine at the EMEC site but there is no access to the turbine power performance parameters collected and held by the developer [37]. This presents a challenge to make use of the publicly available data and without a complete picture of device performance and inflow characterization physical models cannot be validated. Correspondingly, there is need for publicly funded data acquisition campaigns on operating TEC systems where a complete characterization of tidal resource, turbine thrust and power performance can be collected.

1.5 Thesis Goals

This thesis seeks to collect concurrent tidal resource, turbine thrust and power performance data on the existing turbine installed on the UNH Turbine Deployment Platform (TDP) at the Memorial Bridge while operating in grid synchronous mode. This project will utilize

existing power conversion components and adding time synchronization across the instrumentation package. By collecting concurrent flow, power performance and thrust load data on the installed New Energy cross-flow turbine we seek to provide data to support the development of predictive design and analysis tools. Improving the data acquisition capability on the platform will aid in moving the site toward an accredited test platform for MHK devices under IEC standard 62600-202.

Three data sets were established as goals for the project which seek to provide insight on long term system performance and location specific fine scale variability.

1. Continuous data set of electrical power vs tidal current resource over a lunar month.

2. Turbine thrust loading vs large scale turbulent fluctuations.

3. Electrical power vs large scale turbulent fluctuations.

These data sets will be used to generate power performance curves used to characterize device performance including non-dimensional power vs flow speed C_P vs λ and non-dimensional thrust vs flow speed C_T vs λ. Time series frequency analysis will be used to determine the tidal current eddy scales that have a measurable effect on thrust loading and power production.

1.6 Thesis Outline

This thesis provides a background on the operation and data collection systems on the Living Bridge Turbine Deployment Platform (LB-TDP) in chapter 2 along with the repairs/upgrades made to operate the system and collect data to meet the goals of this project in chapter 3. Each instruments deployment specifications and data quality control processing techniques are given in chapter 4 and results are presented in chapter 5. Conclusions and future work are discussed in chapter 6. Appendices follow the list of references and provide supporting information to the work presented herin.

CHAPTER 2

Background on Living Bridge Tidal Energy Conversion System

2.1 Intro to Living Bridge Project

The University of New Hampshire Living Bridge Project (NSF Award #1432060) began in August 2014, and coincided with the 2013 replacement of the Memorial Bridge connecting Portsmouth, NH and Kittery, ME (Figure 2.1). The new bridge utilized a novel gusset-less truss connection design which provided the motivation to instrument the bridge with structural health monitoring sensors [38].

Additionally, it was proposed the new sensor suite could be powered with a locally available renewable energy source, tidal current energy. Bridges are constructed at natural constriction in rivers, to reduce span distances. These natural constrictions are well suited for instream tidal energy turbine installations because they typically coincide with a reduction in the cross-sectional area which causes an increase in water velocity since mass flow rates must be conserved. The bridge support structure offers attachment points for tidal energy conversion installations, and the proximity to the bridge infrastructure readily allows access for electrical grid integration and internet connectivity.

To access the tidal energy resource, a floating turbine deployment platform (TDP) was designed and constructed with high density poly ethylene (HDPE) pontoons for buoyancy and a galvanized steel frame for structural strength. Vertical guide posts (VGP's) were installed as mooring points for the platform on the Portsmouth-facing side of Pier #2, outside the shipping channel (Figure 2.1). The VGP's are 6.7 m tall, made of 16-inch diameter galvanized steel pipe, provide stand-off distance from the bridge pier and allow the platform

Figure 2.1: Memorial Bridge between Portsmouth, NH and Kittery, ME [Looking NNW]. Tidal energy test site location is adjacent to Portsmouth-facing side of pier #2.

to travel vertically with changing water levels. The platform has nominal dimensions of 15m x 6m and is capable of deploying axial and cross-flow tidal energy converters (TEC's) up to $\approx 3m$ in diameter. Turbines are connected to the TDP via a 16-inch diameter horizontal pipe, or spanning beam, and a turbine specific interface bracket. Turbines are deployed through a moon pool (3.3 m x 5.7 m) via a winch actuated turbine pitching mechanism (Figure 2.2). A "droop cable" provides a flexible connection for power and data betweeen the TDP and the Memorial Bridge systems. The "droop cable" is a cable bundle containing three separate cables, 480VAC 3-phase connection, 120VAC 10A circuit, and a network cable. Detailed design specifications for the TDP and VGP are given in Gagnon, 2018 [6].

2.2 Unique Tidal Energy Test Site Opportunity

This installation provides a unique opportunity for researchers and developers to further TEC technology design and assess the environmental impacts in a relevant flow environment. The Department of Energy (DOE) uses a scale known as a Technical Readiness Level (TRL) to define the maturity of emergent technologies. TRL's range from the youngest, level 1 coinciding with basic principle observations, to the oldest, level 9 coinciding with the

Figure 2.2: An overview of the primary TDP structural and turbine pitching mechanism components. [A] Vertical guide post assembly, [B] HDPE pontoons, [C] TDP steel frame, [D] Adapter bracket, [E] Spanning beam, [F] Strongback, [G] Electric winch.

successful completion of a full scale project [39]. TRL level 6 categorizes scale model testing in relevant environments which aligns with the ability of this test site to operate scale TEC's in grid connected mode. The TDP provides unique open access data, through the Marine Hydrokinetic Data Repository (MHKDR), and testing capabilities for researchers to monitor how TEC devices perform in a real flow environment over meaningful deployment time scales (months to years). Access to this facility will be available under the DOE initiative TEAMER (Testing Expertise and Access to Marine Energy).

Tidal energy conversion project permitting has posed as a significant challenge for regulating bodies due to the variety of new/unstudied potential environmental impacts introduced by these devices (subsection 1.2.2 for a description of these impacts). Preliminary research has been conducted in laboratory and field settings on environmental impacts of TEC's in

an effort to retire risk associated with these potential impacts. Significant knowledge gaps remain due to a lack of available devices in the water to monitor/study which has limited the progression of this technology toward commercialization. Environmental monitoring remains an active area of research in this field, to continue collecting data to inform regulating bodies and streamline project permitting [22]. The LB-TDP is a unique test facility that has obtained regulatory approval despite these existing challenges. Leveraging the existing United States Army Corp of Engineer (USACE) permit associated with the reconstruction of the Memorial Bridge itself helped to fast tract the environmental permitting of this project. Notable factors contributing to the approval of the project include:

1. The preparation of a comprehensive biological assessment (BA), conducted by UNH and Barrett Energy Resources Group LLC of Concord Massachusetts, under the instruction of the DOE. The report addresses potential environmental impacts including noise pollution and blade strike. The findings suggested the project would not likely adversely affect threatened or endangered species (Atlantic Sturgeon and Shortnose Sturgeon) or their critical habitats and would not affect essential fish habitat for other non-endangered species.

    (a) Existing noise studies in the literature (referenced in BA):

        i. Field trials without operating turbines: Busy ports like Portsmouth harbor (McKenna et al. 2012)

        ii. Field trials with operating turbines: Ocean Renewable Power Companies (ORPC) TidGen Power System in Cobscook Bay, Maine (Deveau et al, 2011)

        iii. Field trials with operating turbines: European Marine Energy Center's (EMEC) Open Hydro's Open Centre Turbine in Orkney, Scotland (Subacoustech, 2008)

        These studies indicated that noise produced by the TEC at the Memorial Bridge site may be heard by endangered species (sturgeon). However, the

existing noise levels, from ship traffic, already exceed the external noise behavioral impact thresholds for sturgeon. Correspondingly, the existing sturgeon will already have adapted to these existing and longstanding impacts associated with the commercial port setting.

(b) Existing blade strike studies in the literature (referenced in BA):

i. Laboratory setting: (Jacobson et al 2012; Castro-Santos and Haro 2013)

ii. Field trials at the ORPC site: (Zydlewski et al. 2016; Shen et al. 2016; Viehman 2015)

These studies indicate the fish can identify moving turbines and make evasive maneuvers to avoid them. The UNH TDP is a floating platform with the rotating turbine located near the water surface, creating spatial separation between the endangered Sturgeon, which typically occupy the lower portion of the water column, and the device. The DOE submitted the BA to the National Marine Fisheries (NMFS) who found that project would comply with Section 7 of the Endangered Species Act and the Magnuson-Stevens Act.

2. Based upon the review of the BA by the NMFS the project was categorically excluded from further NEPA review under 10 C.F.R § 1021.410 and Appendix B5.25 to Subpart D of § 1021.

3. The UNH USACE permit application was categorized as a category 1 exclusion under the USACE State of New Hampshire's Programmatic General Permit (PGP) corresponding with a minimal individual or cumulative impact on waters of the United States including wetlands.

2.3 History of the Tidal Energy Conversion System at Memorial Bridge

During the summer of 2018 New Energy Corporation Inc (NECI) delivered the TEC system consisting of an underwater turbine, permanent magnet generator, and necessary electrical components required for grid/off-grid connected operation and control of the device. The turbine is a H-Darrius type 4 blade-cross flow turbine measuring 3.2m diameter and 1.7m tall. The hydro-foil profile is a NACA 0021 with a 10 inch chord length. The struts that connect the blades to the drive shaft impose a preset blade pitch angle $\beta = +4^{\circ}$ with a positive angle corresponding with the toe in direction. The turbine supplied is a modified NECI EnviroGen-025H model turbine which typically has a blade diameter of 3.4m, with a design rating of 25kW at 3m/s flow velocity. The modification of the UNH turbine was required to accommodate the dimensions of the existing moon pool. The modification from the original 025H model is a reduction in strut length which reduced the overall diameter to 3.2m. When the TDP was constructed the moon pool was designed for an Instream Energy cross-flow turbine measuring 3m in diameter and 1.5m tall. Instream Energy was not able to deliver the turbine to the project and NECI was selected as an alternate supplier. NECI built and delivered turbine in approximately a 6-month time frame. The TEC was assembled on the TDP by NECI and UNH personnel prior to being towed to the Memorial Bridge on June 8th, 2018 by Pepperrell Cove Marine Services (Newington, NH) (Figure 2.3).

2.3.1 Background on the commissioning of the TEC system at the TDP

NECI provided an electrical commissioning procedure to direct the installation and operation of the TEC entitled *17D04 – UNH Living Bridge Electrical Commissioning Procedure Rev. 1a* [40]. The power conversion system is controlled by the Voltsys VS80A rectifier with user interface software entitled *PWRCRVDL800D17*, which is installed on the UNH field laptop. The power conversion system is designed to operate in two distinct modes either grid-connected or off-grid. In grid-connected mode, DC power is delivered from the rectifier

Figure 2.3: Initial turbine assembly and installation (Gagnon 2018, Figure 7.9 [6])

to the Ginlong, model Solis-36K-US 480VAC, UL1741 grid-tie inverter which synchronizes to the Memorial Bridge 480 three-phase grid (Figure 2.4). In off grid mode, DC power is delivered from the rectifier to an 11 Ohm resistor bank capable of dissipating up to 25kW of power continuously.

The 17D04 procedure outlines the initial commissioning steps for validating system wiring against the projects electrical drawings - Living Bridge 25 KW Envirogen Installation Drawings [8]. Next, the procedure outlines the rectifier settings that the user must verify prior to operation in either grid connected or off grid modes. Finally, the procedure outlines the electrical qualification tests that verify the systems control logic response during potential situations the system could experience while operating in grid connected mode.

During the initial commissioning, the system was not able to operate in grid connected mode due to errors recorded in the inverter and therefore the final electrical qualification tests could not be completed as outlined in 17D04 section 4.5 & 4.6. From the initial installation in June of 2018 to September of 2019 the system was operated in off grid mode and only under direct operator supervision (no power performance tests were completed

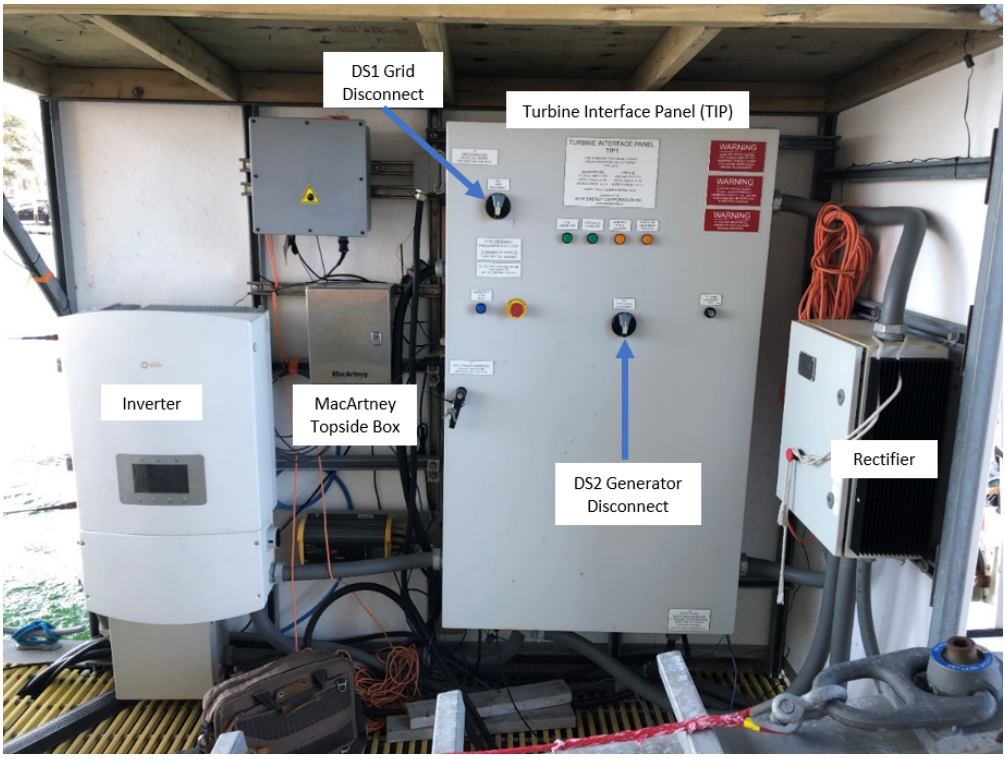

Figure 2.4: The components located within the power electronics shelter on the TDP

while the system was left unattended). This limitation was self-imposed by the UNH team as they continued to troubleshoot the grid connection issue and build confidence operating the system. Continued electrical troubleshooting efforts to address the grid connection issues were collaborative between UNH team members, NECI and Northeast Integration (NEI). NEI serves as the electrical contractor supporting the entire Memorial Bridge system. NEI also designed, installed, and services the electrical connections between the TDP and the motor control center (MCC) that manages the bridge's 480VAC power distribution.

The primary error associated with the inability to operate in grid-connected mode was an inverter error that displayed 'ILeak-PRO04 error' on the Solis LCD screen. According to the troubleshooting resources provided by the inverter manufacturer the 'ILeak-PRO04 error' indicates the system has a continuous leakage current >300ma, the highest threshold [41]. Ginlong was consulted in November 2018, and they suggested the error could be associated with a faulty inverter unit entirely and recommended the inverter be replaced. On February

27, 2019, the original inverter was replaced with a new unit of the same specifications, provided complementary by Ginlong. When the team tried to operate in grid connected mode with the new inverter installed the same 'ILeak-PRO04 error' appeared and the unit was not able to synchronize.

2.3.2 Background on the TDP Structure

In addition to the grid connectivity issues, the initial deployment of the TDP and TEC system was subject to some mechanical issues. The first being on the initial deployment day of the TDP, without the TEC system, on March 31, 2017 when the originally specified chain pile guides did not perform as intended (Gagnon, 2018 Figure 7.3 [6]). The pile guides became bound in the fast currents of the ebb tide and restricted the platform from traversing vertically beside the VGP's and the starboard pontoon began to submerge. This was identified quickly and arrangements were made to free the bound pile guides and remove the platform from the VGP's the same day without further incident. The pile guides were then redesigned to the existing configuration and has operated successfully since it was installed June 22, 2017 (Gagnon, 2018 Figure 7.4 [6]).

After the TEC system was deployed on the platform in June 2018 the adapter bracket, connecting the turbine to the spanning beam, experienced larger than expected deformation. The original adapter bracket was made of 5/8" steel plate and weighed approximately 300lbs. A new adapter bracket was designed and fabricated out of 3/4" and 1" steel plate and weighed approximately 700lbs. The redesigned adapter bracket has successfully performed since its installation in October, 2018.

On August 6, 2018 while operating in off-grid mode a bolt pattern connecting the generator frame to the bearing shaft failed (Figure 2.5 [Left]). This event occurred when the electric brake was engaged which separates the generator from the load and then short circuits the three generator phases together (Figure 2.5 [Right]). The electric brake causes an increase in stator winding current which increases the back electro-magnetic field (emf) imposed on

the rotating permanent magnet field poles. The interaction of these magnetic fields impose a large torque on the shaft, counter to the direction of shaft rotation, which causes the turbine to come to a stop and prevents further rotation. In this case the forces on the stator were strong enough to break the bolts between the bearing housing and the stator frame. When this occurred, the turbine was rotated out of the water and repairs were coordinated with NECI to occur during the week of 10/1/2018. The platform was removed from the VGP's and towed back to the UNH pier where the turbine was removed from the turbine pitching mechanism (TPM) to analyze the extent of the damage. Fortunately, no significant damaged occurred and the lower housing was modified to accommodate new, stronger bolts. This repair was successful and has been operational since 10/4/2018.

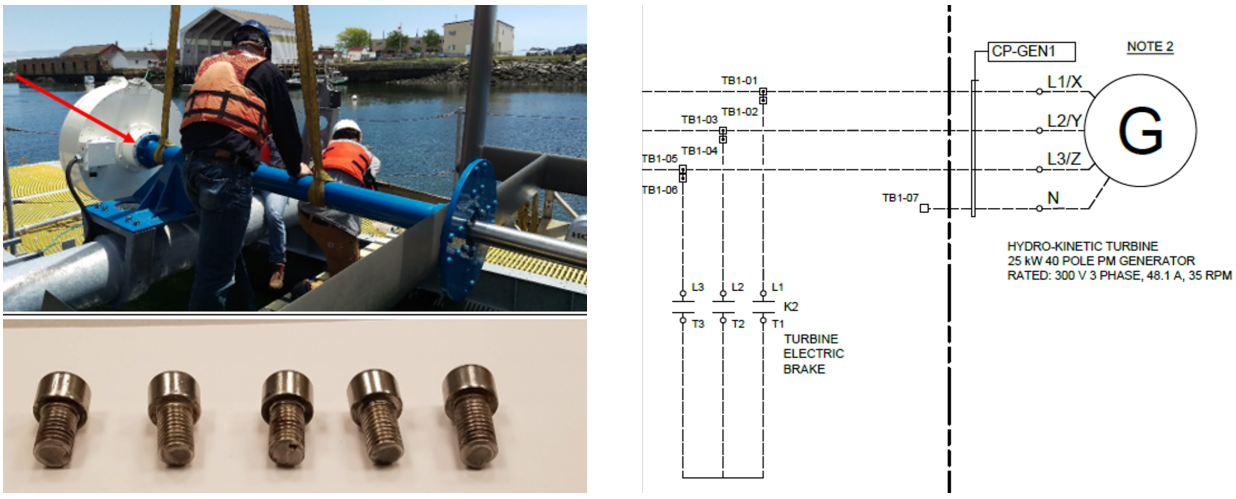

Figure 2.5: [Left] Photo indicating location of sheared bolt ring connecting the bearing housing to the generator stator frame (Chancey, 2019 Figure 5.2 [7]). [Right] 3-Line electrical drawing indicating the electric brake on the generator circuit (Adapted from NECI, 2019 drw# E05-003 [8]).

As a part of the original system design a limited pressurized generator housing was included to prevent corrosion. Pressurized nitrogen bottles and a regulator were used to introduce a nitrogen "blanket" and limit the available oxygen around the stator and field components. The system was not intended to be a complete self-contained pressure vessel so there was a natural release of the gas around the shaft seals. After the stator housing to generator frame bolts were replaced this nitrogen blanket system was no longer functional.

It is speculated that when the generator was aligned to the shaft after the repairs , the shaft seal tolerances were left larger than originally specified which allowed the gas to escape at in increased rate. The nitrogen bottles would empty very quickly and it fell out of practice to operate this nitrogen gas blanket system. No additional efforts have been made to address this deviation from the original system design to date. No inspection of the internal generator components to assess the state of potential corrosion due to the lack of the nitrogen blanket has been completed.

2.4 History of Data Acquisition Systems at UNH TDP

The Living Bridge Project began with the installation of the Bridge Diagnostic Inc. (BDI) structural monitoring sensors on the Memorial Bridge span in February 2016. This installation was completed on March 8, 2017 prior to the installation of the TDP on March 31, 2017. The variation in project timelines and contractors led to independent data acquisition (DAQ) system development.

2.4.1 Bridge Diagnostic Inc. Data Acquisition System (BDI-DAQ)

Bridge Diagnostics Inc (BDI) designed and installed the DAQ system that acquires data from the structural health monitoring instrumentation installed on the Memorial Bridge. The BDI DAQ system includes 16 strain rosettes (3 readings each, principal stresses), 2 uniaxial strain gauges, 2 biaxial tilt meters and 12 biaxial accelerometers [42] (Figure 2.6 [Left]). In addition, 8 half bridge strain gauges were installed on the vertical guidepost support members, to which the TDP is moored (Figure 2.6 [Right]). The BDI DAQ cabinet is located in the same room as the LB-Server on the Memorial Bridge deck.

2.4.2 Living Bridge Data Acquisition System (LB-DAS)

The DAQ for the TDP "baseline instrumentation" package was developed by NEI using a General Electric (GE) supervisory control and data acquisition (SCADA) software known

as Cimplicity. Cimplicity is a tool that is used to create custom user interfaces known as "projects" for specific data acquisition and handling applications. The Cimplicity project created by NEI for this application, will be referred to as the Living Bridge data acquisition system (LB-DAS) [43]. The LB-DAS runs on a dedicated Windows server, referred to as the Living Bridge Server (LB-Server), which is located in a small room on the street level of the Memorial Bridge beside the stairs that lead to the control room. NEI provides troubleshooting and maintenance that support the continued use of this system. The baseline instruments integrated the LB-DAS summarized in Table 2.1.

Manufacturer	**Model**	**Description**	**Parameters Measured**
LinkQuest Inc.	FlowQuest 1000 kHz ADCP (Q. 2)	4-Beam Acoustic Doppler Current Profiler (ADCP)	Current Speed and Direction
Valeport	CTD+	Conductivity, Temperature, Depth (CTD), '+' indicates additional sensors can be integrated	Water Temperature, Salinity, Depth (Pressure), Chlorophyll, and Turbidity
MacArtney	LUXUS Compact Camera (Q. 2)	Underwater Camera	Visual Information
AirMar	WeatherStation 200WX (Q.2)	Multiple Sensor Weather Instrument	Wind Speed and Direction, Air Temperature, Humidity, and Barometric Pressure

Table 2.1: LB-DAS Baseline Instrumentation

The LB-DAS utilizes a custom multiplexer (MUX), developed by MacArtney Underwater Technologies on their NEXUS MK-C platform, to transmit data between the baseline instruments, located on the platform to the LB-Server. The weather stations bypass the multiplexer, the platform weather station data is connected to a serial to network converter and the tower weather station uses a NMEA to serial converter housed in the BDI cabinet.

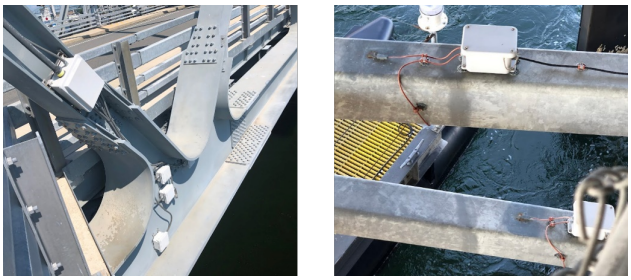

Figure 2.6: [Left] Memorial Bridge structural health monitoring sensors. [Right] VGP support member strain gauge termination.

The MUX contains three spare MOXA 5250A serial device ports, one for an weather station, a second for a turbine RPM sensor and a third allocated as a spare [44]. The RPM port was specified in the design from the original project turbine vendor (Instream Energy) but was not utilized in the NECI design. UNH does not possess the RPM sensor originally specified by Instream Energy, or otherwise at this time. Additional resources including the electrical drawings for the MUX are available in *UNH -NEXUS MK-C - OT Manual - REV A* [44].

The MacArtney LUXUS compact underwater cameras were originally deployed as a part of a Wildlife Mitigation Device System (WMDS) – Fish Deterrent System deployed by Lite Enterprises Inc. This WMDS system had limited success and is no longer used on the TDP. The cameras, however, can be utilized for underwater monitoring and configured to take snapshots at discrete time intervals or record continuous video footage. Refer to page 93 of Chancey, 2019 [7] for an overview of the WMDS system design and page 56 of NEI, 2017 [43] for camera configuration procedures. The WMDS cabinet was removed from the TDP on 7/20/2021.

2.4.3 Existing DAQ summary

The benefit of the existing LB-DAS is the ability to remotely (1) monitor data acquisition in real time, (2) start and stop deployments of individual instruments, and (3) configure instrument deployment parameters. This allows for individual instruments to be deployed or removed without disrupting the entire LB-DAS. The data collected from the LB-DAS is stored in a Microsoft SQL database which can be queried locally using SQL Management Studio or remotely by access the LB-Server via OpenVPN [43]. Instruments can be remotely configured by terminating the connection with the Cimplicity Project then establishing a connection through the manufacturer provided configuration software, which are loaded on the LB-Server. This enables full access to alter and verify deployment settings remotely.

2.4.4 UNH modular ocean data acquisition system (UNH MODAQ)

A secondary data acquisition system to the LB-DAS, was conceived with the intent of supporting short-term deployments of additional instruments from the TDP Figure 2.7. The design was initially based on the National Renewable Energy Laboratory's (NREL) modular ocean instrumentation system (MOIS) which utilizes the National Instruments (NI) cRIO platform [45]. At NREL, the MOIS design evolved and is now referred to as the modular ocean data acquisition system (MODAQ). The MODAQ concept is a flexible data acquisition system designed by NREL to support marine renewable energy field research. MODAQ itself is a baseline LabVIEW project that enables rapid integration of deployment specific instrument packages paired with a watertight enclosure housing power distribution, remote relays and cRIO controller [46] The custom development of the NREL MODAQ concept at UNH will be referred to as UNH MODAQ.

The UNH MODAQ system was intended to allow for rapid integration of new instrumentation as measurement campaigns change over time. Existing instrumentation that needed to be integrated into a DAQ included two Nortek Vector Acoustic Doppler Velocimeters (ADV's), two thrust load cells, an inertial measurement unit (IMU), turbine performance (Voltsys rectifier), wave staff, and two Nortek Signature ADCP's. Additionally, this DAQ would allow for data collection during platform deployments in remote locations without access to a bridge power grid and server, like the General Sullivan Bridge tidal energy test site where UNH had previously tested tidal energy converters [47].

2.5 Limitations of existing DAQ's

The three existing DAQ systems – LB-DAS, BDI DAQ and UNH MODAQ – have four main issues.

First there was no predictable way to ensure accurate time correlation of measurements between the separate DAQ systems. Both the BDI DAQ and LB-DAS used their respective

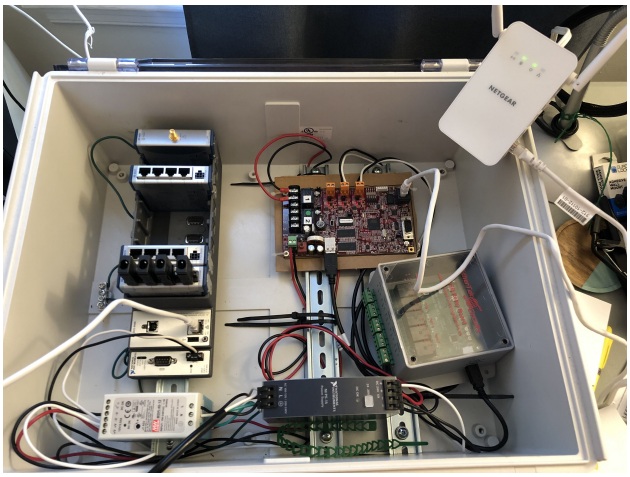

Figure 2.7: UNH-MODAQ components during early development (early 2019)

servers' internal clock to time stamp the acquired data. This time source is susceptible to drift and irregularities. The UNH MODAQ system, is designed to use pulse per second (PPS) Coordinated Universal Time (UTC) acquired from a GPS antenna through the NI-9467 GPS C-Series Module. This is a reliable time synchronization method but does not address the known time errors present in the LB-DAS and BDI DAQ data sets.

Second, the LB-DAS, is not flexible for on-platform instrumentation expansion via the MacArtney MUX beyond the two currently available serial ports. Any expansion beyond this would require extensive modification to the MacArtney MUX or bypassing it. Additionally programming new instruments in Cimplicity would require additional contracts with NEI or extensive development time from students would be needed. The LB-DAS has proven to be a reliable system for long term data acquisition with the longest continuous record obtained by the system from 6/22/17 to 11/7/17. This measurement campaign was completed before the TEC was installed on the platform and serves as a tidal current resource characterization at the site following the IEC TS 62600-201 standard (Chancey, 2019 section 2.1.3 [7]).

Third, during previous measurement campaigns, turbine power output data had not yet been integrated into the LB-DAS. Power measurements were recorded with a field laptop connected directly to the rectifier which allows for data logging over a USB connection. To enable this, the user needs to open the rectifier software, *PWRCRVDL800D17*, and select

File ≫ Logging Enabled. This will automatically cause a csv file to open and log data at a frequency up to 10Hz. This data is time stamped via the internal battery powered clock in the rectifier which can be manually synchronized to the field laptop's internal clock at the beginning of each measurement campaign. During previous measurement campaigns, where power was recorded in this manner, tidal current resource was characterized with Nortek ADV's. These ADV's were also manually synchronized to the field laptops internal clock immediately prior to their deployments. Details of the experimental design and results can be found in Chancey, 2019 section 2.2.3 [7]. Additional specifications regarding the rectifier can be found in the *Voltsys Rectifier Installation Manual* [48].

Lastly, there simply had not been sufficient resources available to complete the UNH MODAQ system as intended. Most of the required system components and instruments had been purchased previously on a separate marine renewable energy infrastructure grant, which did not include personnel time to design and implement the system [49].

CHAPTER 3

Measurement Preparations

3.1 UNH MODAQ

The development of the UNH MODAQ system was motivated by a need to acquire time synchronized data from instruments not already integrated into the LB-DAS system. This was made possible through the collaboration between NREL and UNH as a part of the NREL Performance and Loads Measurement Campaign. The instrumentation integrated into UNH MODAQ are summarized in Table 3.1 along with additional instrumentation available for future integration.

Manufacturer	Model	Description	Parameters Measured
Yost Labs	Watertight 3-Space Sensor	Inertial Measurement Unit (IMU)	Platform motion
LCM Systems	PTC-1 (Q. 2)	100kN low profile universal load cell (tension and compression)	Turbine thrust loads on platform supports
Sensing System Corporation	Submersible Tension Link Load Cell	20,000lb tension link load cell (tension only)	Simulate thrust loads on the PTC-1 load cells
Antenna Plus	APCCWGM S2222RP3WH	MIMO LTE cellular PCS GPS WiFi combo antenna	GPS signal input for NI-9467 c-series module
Voltsys	VS80A/DL800	Wind turbine controller and data logger	Power and RPM data
Nortek	Vector (Q. 2)	Acoustic Doppler Velocimeter (ADV)	Current speed and direction
Additional Instruments Available for Integration			
Nortek	Signature 1000 (Q. 2)	5-Beam Acoustic Doppler Current Profiler (ADCP)	Current speed and direction, tidal elevation
Akamina	AWP-24-3	Wave height gauge	Wave height and length

Table 3.1: UNH MODAQ Integrated Instrumentation

3.1.1 Time Synchronization

The UNH MODAQ system provides accurate time stamps with a NI-9467 GPS c-series synchronization module. A GPS receiver provides the input time source to the module which then generates a PPS UTC time signal available to the cRIO-9066 controller with +/- 100ns accuracy. This time signal is applied to sampled and streamed data as it is received by the cRIO which allows accurate correlation of data collected between different instruments.

To allow for accurate correlation/comparison between, UNH MODAQ, LB-DAS and BDI DAQ connected instruments, a network time protocol (NTP) server was installed on the LB-Server subnet on 7/6/2021. This device uses a GPS time source to provide a NMEA 0183 signal over Ethernet which any device on the subnet can use as a reference point to synchronize its own internal clock too. The NTP server selected was a Masterclock NTP-100-GPS model with a GPS timing accuracy of +/- 2ms [50]. This model includes an internal oscillator with a stability range of +/- 250ms/year, which takes over if the GPS signal is lost. This NTP server was installed in the server room at the Memorial Bridge and the GPS receiver mounted on the stairwell leading to the bridge control room (Figure 3.1). Using the MasterSyncPC software the LB-Server internal clock was set to synchronize to the NTP server time signal every minute with an average correction value of 0.0067 seconds during the Fall 2021 measurement campaign.

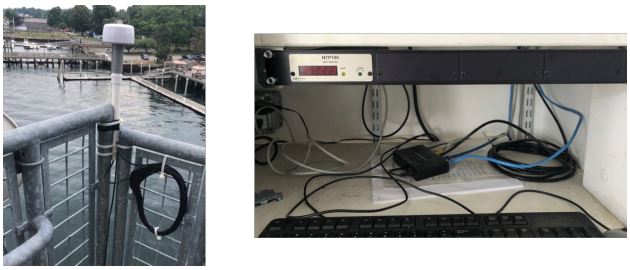

Figure 3.1: [Left] NTP GPS receiver installed on stairwell leading up to Memorial Bridge Control Room [Right] NTP Server installed in the server room located on the Memorial Bridge deck level

3.1.2 UNH MODAQ Development

The development of the UNH-MODAQ system combined existing hardware and instrumentation into a new enclosure. A steel enclosure, with interior dimensions measuring 22inW x 28inL x 10inD, was selected to allow sufficient room for expansion as the instrumentation package grew over time. The enclosure was factory treated with an ANSI 61 polyester powder coating on all surfaces to protect the steel from corrosion. An insulating board was installed over the steel mounting plate to provide isolation between electrical components and ground potential. The CompactRIO chassis and DC power supplies are mounted to standard 35mm DIN rail for modular assembly while the Mini-PC, RMS-100 boards and RMS add on relay board are mounted directory to the insulation board plate. Instrument data and power cables interface with the enclosure through a waterproof Roxtec EzEntry cable gland providing 32 ports for cables which are routed in wire ducts once inside the enclosure. The primary hardware components that make up UNH MODAQ are summarized in Table 3.2. A complete component list for the UNH MODAQ system is in Appendix E.

Component ID	**Specifications**	**IP Address**	**Description**
Mini PC	Beelink Mini PC 4 Core 8th Intel Core i5-8259U 3.8Ghz 16 GB RAM 512 GB Hard Drive	192.168.3.105	Provides a unique location for Labview development and code storage. Allows the enclosure to operate independently without the need of another pc to interact with network devices within the enclosure.
NI 9066 cRIO FPGA controller	667 MHz Dual-Core CPU, 256 MB DRAM, 512 MB Storage, Zynq-7020 FPGA, 8-Slot CompactRIO Controller	192.168.3.110	Data acquisition system that streams serial instrument data strings, samples analog instrument signals and provides accurate time stamping via a satellite GPS connection.
Ethertek Remote Monitoring System	RMS -100 (Q. 2)	192.168.3.120 & 192.168.3.121	Network connected remote monitoring boards with web user interface that have power relays switching up to 240v - 5 amps AC/DC current, voltage meters +/- 100VDC, temperature sensors and alarm/notification/shutdown capabilities for monitoring and reporting system health.
Ethertek USB Relay Board	5 additional power relays for RMS-100 (Q. 2)	Accessed through the RMS-100	One USB relay board is connected to each RMS-100 board.
Network Switch	Stride Unmanaged - SE2-SW5U, 5 Ethernet ports, 10/100Base-T (RJ45) ports	NA	Used to interface internal network devices (with static ip addresses) to one another and with connect to an external network
DC Power Supplies	5, 9, 12, & 24 VDC	NA	Separate AC to DC power supplies for various voltage levels requirements of the instruments.

Table 3.2: UNH MODAQ Primary Components

3.1.3 Network Integration

Network connectivity to the enclosure is routed from an external RJ-45 network jack to a five port Ethernet switch. The network enabled devices within the DAQ have static IP address assigned and are summarized in Table 3.2. Each RMS-100 board has two integrated power relays and is limited to one external 5 port relay add on board. A third relay add on board has been purchased and the mounting positions integrated into the base plate but an additional RMS-100 board would be required to operate it. An additional RMS-100 board could be stacked on top of the existing two boards and an expanded network switch would be required.

3.1.4 Power Distribution

UNH MODAQ is powered by 120VAC through a male IEC 320-C14 extension cable. This was chosen because the standard male wall plug, NEMA 5-15P, to female, IEC 320-C13, cable are quite common and are used to power most pc and monitors. When UNH MODAQ is deployed on the platform it should be powered by the 120VAC 10A CB4 breaker in the TIP panel fed from the 480VAC to 120VAC transformer. If UNH MODAQ is being bench tested in the lab it can be powered by a standard 120VAC wall outlet. AC power is routed into the enclosure and connected to 10A control breakers followed by a surge suppressor before entering the AC power distribution terminal block, TB-1 (Appendix C drw.# POB.2021.1). From TB-1 individual terminal blocks direct AC power to the 24VDC, 9VDC, 5VDC and 12VDC power supplies along with a standard outlet that powers the mini PC standard power adapter. The DC power supply output voltages are connected to TB-2, TB-3, TB-4 and TB-5 respectively for further routing to individual instruments. Each of the DC power supply output voltages are also connected to a RMS-100 volt meter to monitor power supply voltage and log voltage data during a deployment. TB-6 is not connected to a power supply and is available for future expansion. Power distribution and relay connections are primarily routed on the mounting plate level of UNH MODAQ as shown in Figure 3.2.

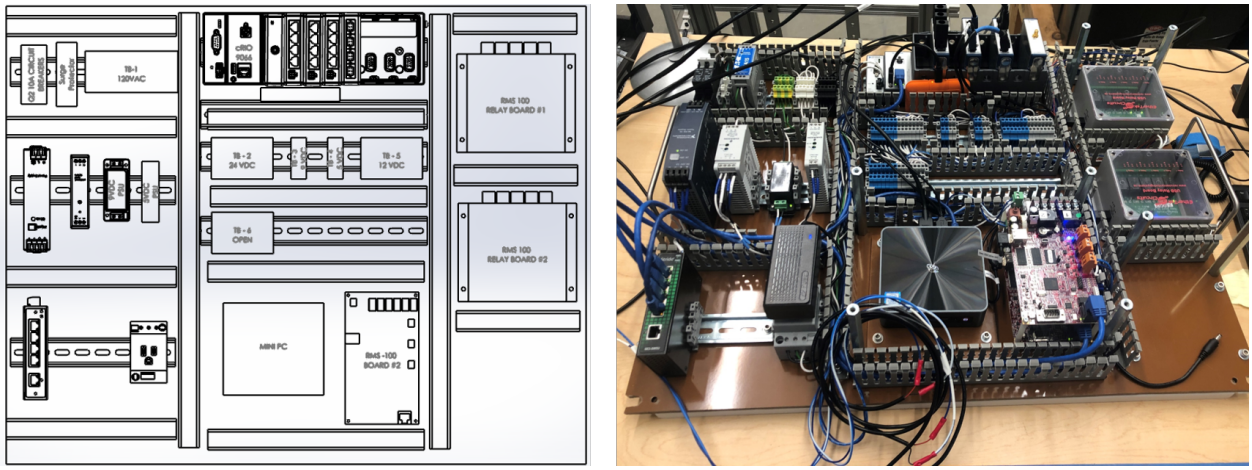

Figure 3.2: [Left] Solid work model of UNH MODAQ mounting plate used to determine enclosure size & component layout [Right] Photo of components assembled and completed wiring on the mounting plate

Programmable instruments, including the Nortek Vector ADV's and YOST IMU, have independent data and power cables routed through the cable gland. Each power cable is connected to relays on the RMS-100 platform to enable remote power cycling to help reset instruments while deployed. DB9 cables were selected for data cables on serial instruments to simplify connection to the field laptop for deployment configuration using the standard instrument manufacturer's software. Twist lock barrel style power cables were selected for programmable instruments to ensure a secure connection. Analog instruments, like the thrust and tension link load cells, have power and data routed in the same cable which are M16, series 425, miniature connectors. Two 24VDC radial cooling fans were integrated into the design to help distribute heat within the enclosure and promote heat transfer through the enclosure walls. These fans are connected to a single relay on the RMS-100 platform. Each instrument has the data and power connections detailed in a separate drawing (Appendix C).

Data recorded from each instrument connected to UNH MODAQ is saved in one hour increments as a TDMS file and stored on the external solid state hard drive connected to a USB port on the CompactRIO chassis. WinSCP software is used to download files from this hard drive to the mini-pc from its directory on the CompactRIO's Linux platform. TDMS files can be quickly viewed using the free TDMS Viewer software Scout.

The current iteration of UNH MODAQ can readily expand the number of connected instruments. Three additional modules are open on the CompactRIO chassis, allowing up to 12 additional instruments, with four channels per module. There are 13 available ports in the existing Roxtec gland with current gland allocations detailed in Appendix D. There are four remaining relay positions and two remaining volt meters available on the existing RMS-100 platforms. If an additional RMS-100 board is acquired it can be used with an existing third relay board to add seven more relays and three more volt meters.

3.1.5 Existing DAQ Maintenance

A timeline of maintenance tasks performed on the existing LB-DAS and BDI DAQ systems are summarizes in Appendix F.

3.2 Grid Synchronization

To prepare for the intended measurement campaign, grid-synchronous operation needed to be available. The primary error associated with the inability to synchronize to the grid was an inverter error ILeak-PRO04. On September 23, 2019 UNH met with NEI to discuss the troubleshooting efforts that had taken place to date and reviewed the original electrical drawings provided by NECI [8]. The conversation centered on identifying potential ground loops within the electrical drawings that may be causing the ILeak-PRO04 error. Several potential candidates for ground loops were identified in the wiring and an outing to the platform was scheduled for the following day.

The error was resolved when the neutral connection of the wye connected generator, TB1-07, was separated from its connection to PDB4-N. PDB4-N is a terminal block in the 480VAC power distribution bank that the neutral from the synchronous 480 VAC bus is terminated. It should be noted that the generator neutral should have been terminated in an open terminal block to coincide with the *NECI University of New Hampshire Portsmouth Memorial Bridge - Living Bridge 25 Kw Envirogen Installation Drawings drawing E05-003* [8] (Figure 3.3). It

is likely that this connection was terminated during the initial commissioning as there was no reference to a modification during subsequent troubleshooting over the following year. TB1-07 is currently left open circuit and insulated to allow access to the generator neutral for future generator testing.

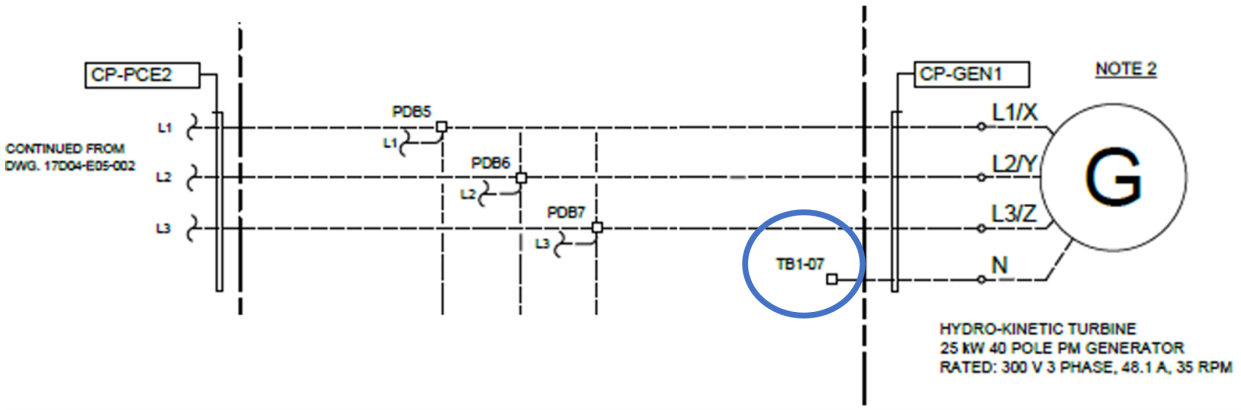

Figure 3.3: Generator wiring diagram indicating neutral should be left open circuit (TB1-07). Adapted from [8] drw# 17D04-E05-003

On large synchronous machines a generator neutral is typically connected to a neutral grounding transformer which helps to limit the current associated with a ground fault on one of the high voltage circuits. When these faults occur the resulting arc is similar to a Tungsten Inert Gas (TIG) welder which can result in extensive damage to the generator core, winding or bus work. A neutral grounding transformer is not economically feasible for the 25kW generator on this TECS installation for two reasons. One, the initial cost of this protection system is on the order of generator itself. Second, a generator/motor of this size is not designed to be serviced in the field, rather it is designed for longevity with a trade off on serviceability. This is accomplished through a process known as Vacuum Pressure Impregnation (VPI) which seals the winding to the frame and provides extreme durability and resistance to ground faults within the stator winding [51]. In summary, the risk of ground faults within a winding of this design is low and little time or money would be saved if a ground fault were to occur with or without a neutral grounding protection system.

3.2.1 Completing Initial Commissioning Procedure

After the generator neutral connection was opened, the system was able to operate in grid-connected mode and the inverter began to display a status message "LmtByPlmt". This is short for "limit by power limit" and is believed to be the result of the discrepancy between the nameplate power ratings between the generator/rectifier, both rated at 25kW, and the inverter, rated at 36kW. The rectifier outputs a maximum of 25kW at 35rpm, and it is likely that this threshold has momentarily been reached during operations which would triggered the "LmtByPlmt" status on the inverter. This status does not impede the system from functioning and operating in grid-connected mode.

After successful grid-synchronization the original commissioning tests, outlined in *NECI 17D04 – UNH Living Bridge Electrical Commissioning Procedure* section 4.5 & 4.6, could be completed [40]. The goal of these tests was to ensure that the control system responds to potential operating conditions while synchronized to the grid as designed. Two such scenarios were specified by NECI including a full load rejection test and a phase in-balance test. A full load rejection simulates a local outage on the power grid which should cause the inverter to trip offline and trigger an error that engaged the electric brake thereby stopping the turbine from rotating. The phase in-balance test simulates irregularity of voltage between each phase A-B, B-C, and A-C which should be relatively stable during operation. This situation could occur if one phase has a low resistance path to ground resulting in a reduction in voltage or a high resistance joint in the electrical circuit causing an increase in voltage. In this scenario, like the first, the inverter should trip offline and trigger an error that engaged the electric brake thereby stopping the turbine from rotating. Lastly, each of the four emergency stops capable of stopping the system and engaging the brake were tested for functionality while the turbine was operating.

These tests we completed on December 15, 2020 in coordination with NEI and UNH personnel. The full load rejection test was simulated by opening the generator breaker in the MCC room on the bridge deck. The phase in-balance was simulated by isolating the

generator breaker in the MCC room then lifting and insulating the C-phase connection. In each test the breaker was then energized and the team on the platform attempted the typical synchronization procedure [52]. During the grid outage test the inverter broke synchronization, as expected, and was not able to synchronize at all during the phase in-balance test. Both tests were followed by the inverter shutting down and the turbine entering a "free spinning mode". "Free spinning mode" is when the turbine can rotate with the flow without any means of regulating shaft speed. The electric brake should have engaged during this two fault conditions rather than the turbine be allowed to spin freely.

There are four E-stops wired into the system that cause inverter to break synchronization and mechanically brake the turbine. These E-stops are located in the following locations:

1. MCC Room: In the generator breaker cabinet in the MCC room
2. Pier Cap: In a dedicated terminal box where the "droop cable" is terminated.
3. TDP: On the starboard side of the bow side of the moonpool on the TDP, across from the power electronics enclosure
4. TIP Panel: On the exterior of the turbine interface panel

The E-stop located on the pier cap was found to be defective and was replaced by NEI at a later date. The remaining three were tested and found to be functional. At this point, although the control system was not engaging the electric brake as designed, both UNH and NEI personnel were satisfied with the performance of the inverter from a grid protection perspective, and it was concluded that the system could operate safely in unmanned operating conditions. In hindsight this control logic error should have been addressed at this time and was eventually resolved during the summer of 2021 (Details on these repairs in subsection 3.2.3).

3.2.2 Subsequent Power Electronics Troubleshooting

During the Spring of 2021 a new error was encountered when running the system in synchronous grid connected mode. First on April 14, 2021, during an attempt to synchronize the system to the grid the inverter prevented synchronization and displayed the error PV-ISO-PRO-02. This error is associated with a low insulation resistance between the inverter input positive DC conductor and ground [53]. At that time the system was reset and was able to successfully synchronize and no additional troubleshooting was pursued at that time.

This error was recorded on five additional occasions and was typically correlated with the ramp up of the overnight ebb tide: 5/13, 6/21, 6/24, 6/25 and 7/19/21 (Figure 3.4). This became a problem as the system would be found the following day in "free spinning mode", where the rectifier was electrically disconnected from the generator. In this condition the dump load was also disconnected from the generator meaning shaft speed could not be regulated.

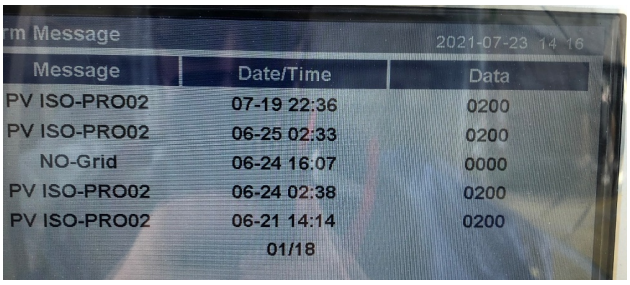

Figure 3.4: Inverter alarm message display indicating inverter faults recorded between 6/21/21 and 7/19/21

To determine which component was causing this error to occur, all the DC current carrying conductor insulation was tested using a handheld battery operated megaohm meter known as a "megger". The DC bus leading from the rectifier to the inverter and rectifier to dump load were isolated from there terminals and tested at 1kVDC between each conductor (that share a conduit run) and each conductor to ground (Figure 3.5 [Left]). All cable test results were excellent with insulation resistance (IR) readings greater than 11Gohms conductor to ground. These results indicated the problem was not likely within one of these

conduits.

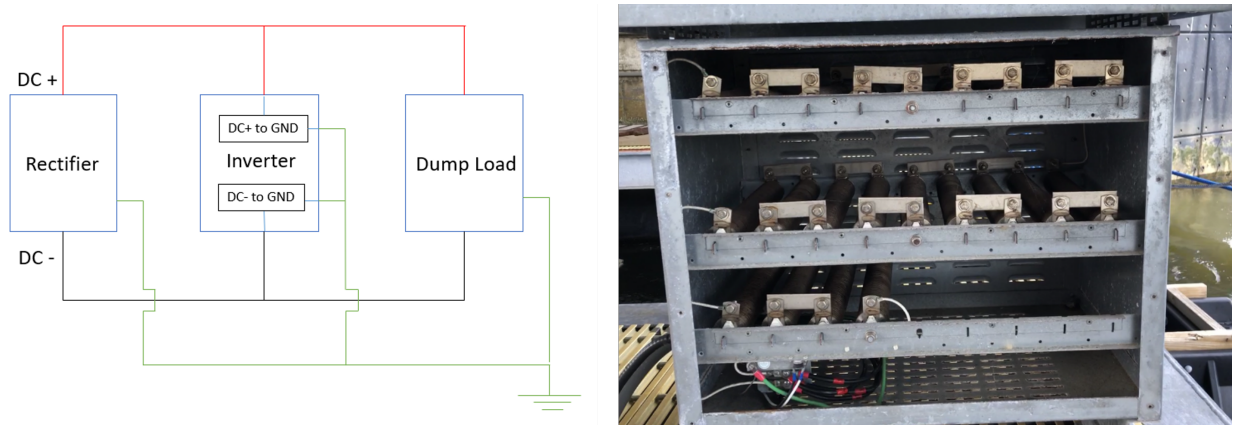

Figure 3.5: [Left] Simplified DC circuit illustrating how the inverter is monitoring the voltage potential on both the positive and negative side of the DC voltage output from the rectifier to ground, known as insulation resistance. By the nature of the design of the rectifier the inverter monitors the rectifier to inverter connection and the rectifier to dump load connection. [Right] Photo of the 22 internal resistors connected in series that make up the 11 Ohm resistor bank. This figure illustrates there are many possible paths for voltage to track to ground within the resistor bank circuit.

The dump load is designed to provide an electrical load for the generator and is rated at 25kW. This component is comprised of 22 resistors connected in series for a total electrical resistance of 11 Ohms that are mounted within a steel enclosure. The power is dissipated through the resistors as heat and the entire circuit is isolated from ground potential, i.e. the steel enclosure itself and the steel bar each resistor is mounted too (Figure 3.5 [Right]). The design of the dump load inherently has many potential paths for voltage to track to ground because of the exposed coiled conductors, the 22 mounting points between the resistor and steel frame and the steel bars that the insulators are mounted too.

To test if the dump load circuit could be the cause of the PV-ISO-PRO-02 error, the circuit was isolated from the rectifier to perform an insulation resistance test with the megger. The IR tests performed on the dump load had poor results and clearly indicated this component was to blame for the inverter error. During the IR tests the megger could not build 500VDC to ground. This is indicative of high levels of current leaking to ground such that the unit cannot maintain 500VDC output which is based upon the maximum available

power output from the handheld battery powered unit.

Once the dump load was identified as the flawed component the failure sequence of events was identified which illustrated why the unit could synchronize during the day and then not synchronize at night.

1. A strong ebb tide begins to ramp up (usually on the overnight tide).
2. The DC voltage output of the rectifier is high enough to turn on the inverter.
3. Once the inverter turns on it begins monitoring the IR of DC+ to GND and DC- to GND (Figure 3.5 Left).
4. The inverter has a grid compliance standard that requires a minimum of five minutes to pass between initialization and synchronization. During this period if voltages levels exceed 480 VDC than the rectifier will connect the dump load circuit to the generator load to regulate shaft speed.
5. When the load was connected to the dump load, the dump load circuit insulation resistance would fail causing current to leak from the dump load circuit to ground.
6. The inverter, which monitors this quality of circuit insulation, would see a drop in voltage occurred somewhere in the circuitry and trigger the PV-ISO-PRO-02 error.
7. The error is then transmitted to the rectifier which causes the rectifier auxiliary relay Q3+ and Q3-, connected to R3 in the TIP panel, to switch state to open circuit during a fault.
8. This in turn causes the K1 generator disconnect to open, separating the generator from the rectifier (Figure 3.6).

3.2.3 Breaking Circuit Troubleshooting

In parallel to troubleshooting the hardware that caused the inverter error, UNH worked with NECI to troubleshoot the control logic deficiency that allowed the unit to "free-spin" after

an inverter error. This is the same issue that was first identified during the commissioning tests performed on 12/15/2021 resulting in the turbine "free-spinning" after the full load rejection and phase in-balance tests but was not pursued at that time.

In the design of this TEC the rectifier is the primary means of controlling shaft speed by either directing power to the grid, the dump load or both. For this to take place, the generator must remain connected to the rectifier through the K1 generator connection contactor. However, in the event of rectifier error the K1 connection must be opened, and the electric brake engaged by closing the K2 turbine break contactor. The control logic that allows the generator to remain connected to the rectifier is hardwired using 24VDC relays routed through a central safety relay SR1. When the inverter registered the PV-ISO-PRO-02 error, the signal is transmitted to the rectifier causing a rectifier error, which resulted in the 24VDC rectifier ok signal R3 opening. This should have engaged the break, per the original design, but was not deemed functional through multiple testing iterations between NECI and UNH personnel. An additional logic statement was proposed by NECI that would engage the electric brake in the event R3 opened indicating a rectifier error, denoted in red in Figure 3.6. This was connected by UNH on August 20, 2021 and successfully engaged the electric break during a simulated rectifier error test by manually opening the R3 circuit.

3.2.4 Rectifier Rebuild

On July 28, 2021, the dump load was removed from the platform and transported to Chase Ocean Engineering Laboratory for further testing and repair (Figure 3.7 [Left]). The initial testing consisted of testing the entire circuit than splitting the circuit in half to identify if there was a specific point of insulation failure or if the issues were systemic (Figure 3.7 [Right]). The poor IR test results indicated the majority of the insulation in the circuit was contaminated and or had failed (Appendix G Table G.1). The next step was to disassemble all the resistors, series connections and jumpers from the steel frame.

A trial test was performed on resistor 10 to assess a possible refurbishment technique for

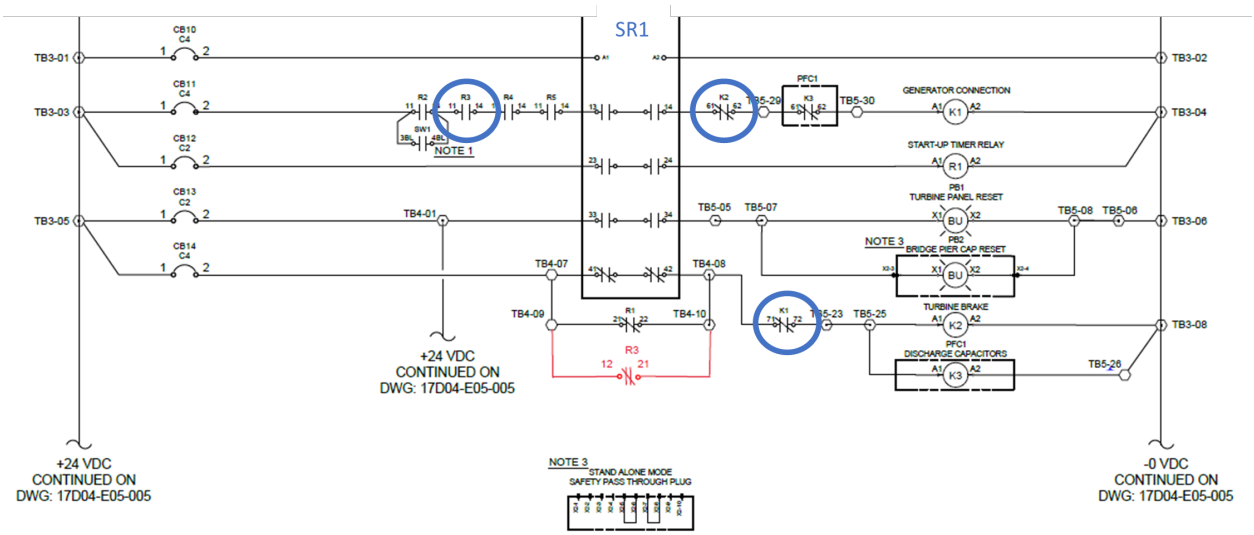

Figure 3.6: This drawing shows the inputs to the safety relay SR1 in the de-energized states, coming from the left side of the drawing. Those inputs are Startup Relay - R1, Grid OK signal - R2, Rectifier OK signal - R3, Brake Resistor OK signal - R4, and Generator Isolator signal - R5 along with various control breakers (CB) being closed. If all the input conditions to the safety relay are satisfied than the relay changes state causing the Turbine Brake Contactor - K2 to be opened and the Generator Connection Contactor - K1 to be closed. The control system is designed such that the K2 and K1 can never be connected at the same time and if one changes state than the other should follow. The additional circuit used to force the electric brake to engage during the PV-ISO-PRO-02 error is shown in red. This drawing is adapted from [8] drw: 17D04-E05-004.

the remaining resistors, as opposed to purchasing a complete new set of resistors. Resistor 10 was cleaned with a nylon brushes and denatured alcohol to removed rust, contamination etc. on the insulator surface and resistor element. The resistor was allowed to dry overnight under a plastic tent with a halogen work light to provide heat. This technique is typical for electrical components as a dry warm environment helps to stabilize and improve IR test results. The results of this tests were positive, and it was decided to clean the remaining resistors in the same fashion (Appendix G Table G.3).

The design of these resistors made them susceptible to contamination over time and the resulting failure of the insulation system. The resistors are comprised of a steel coil, carrying the current, a ceramic insulator, the coils are wrapped around, and a steel beam the insulator is mounted on which is at electrical ground potential. The ceramic insulator

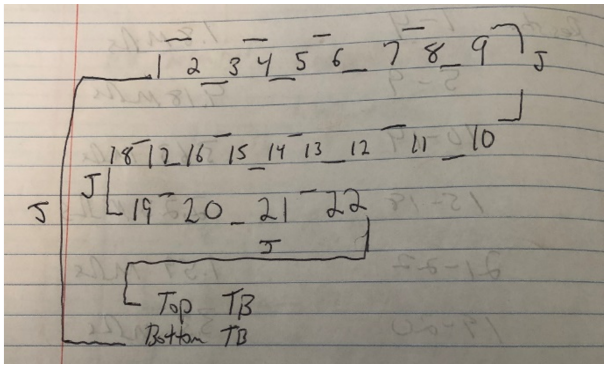

Figure 3.7: [Left] Dump Load lifted off UNH Galen J at the UNH Pier in New Castle, NH on 7/28/2021. [Right] Dump load resistor bank wiring diagram used to identify individual component electrical test results.

is made up of several sections that allow for expansion of the steel coil that surrounds it but introduce multiple failure points in the insulation system at the joints between each insulator. To improve the design of the insulation system, the steel beams were sanded smooth and insulated with 1 half-lapped layer of Kapton tape, with a dielectric strength of 6000V. This addition provides a layer of insulation between the ceramic insulators and the ground potential of the steel beam (Figure 3.8 [Left]). This insulation was tested by wrapping the insulated layer with aluminum foil to provide a means of applying voltage between the insulator to the steel beam. The test was performed at 1000VDC and a value of greater than 11G-Ohms was recorded indicating excellent results exceeding the limits of the meter (Figure 3.8 [Right]).

Additionally, a 120VAC 350W strip heater was integrated into the resistor bank design (Figure 3.9 [Left]). This would help to maintain a higher air temperature inside the resistor bank relative to atmospheric temperature. By keeping the internal temperature higher than the surrounding air, it will prevent condensation from occurring on the internal surfaces of the resistor bank and thereby limit corrosion. The resistor bank enclosure was cleaned and coated with cold-galvanizing spray before the rebuilt resistors were installed. Resistors were installed and an IR test series was performed before the series connections were completed between each resistor (Appendix G Table G.4 & Table G.5). The series connections were

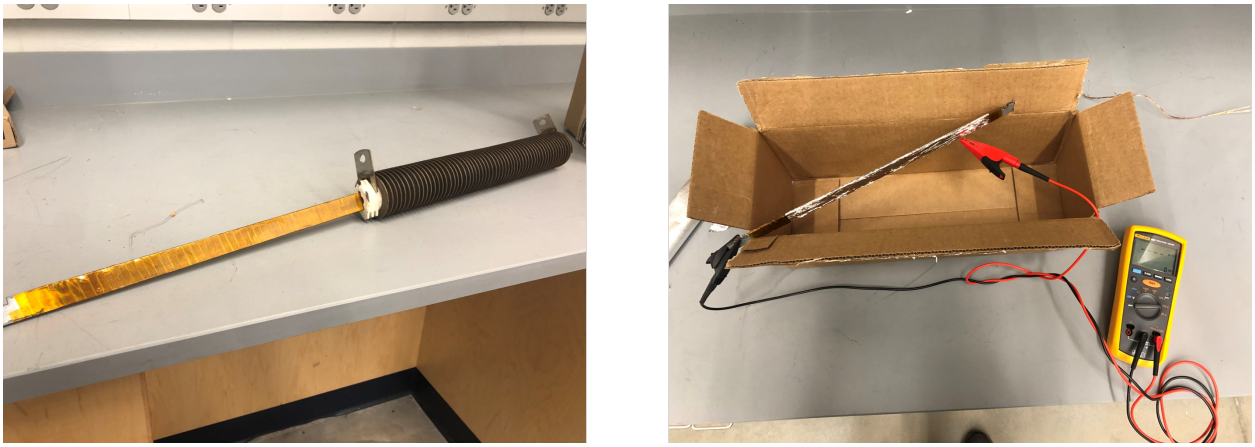

Figure 3.8: [Left] Rebuilt resistor with insulated steel beam. [Right] Bench testing Kapton insulation.

installed, along with the jumpers, on 9/22/2021 and the insulation testing was completed again (Appendix G Table G.6). All the series connections were checked for adequate electrical contact using a feeler gauge and then No-Ox grease was applied to help prevent oxidation (Appendix G Table G.7). Contact was deemed sufficient for operation, but an additional series connection, between each resistor, would improve the contact area and reduce current density across each series connection.

Finally, insulators were fabricated to isolate the resistor bank enclosure from the steel platform to give operators control of the ground plane of the enclosure itself. With this in place, operators could isolate the enclosure and prevent the same PV-ISO-PRO-02 error quickly in the future by lifting the ground wire coming from the rectifier and terminated to a grounding lug on the inside of the enclosure frame. On October 1, 2021 the resistor bank was reinstalled on the platform and leads 1 & 2 (incoming HV) from the rectifier were connected to resistor 1 and leads 4 & 5 (outgoing LV) were connected to resistor 22 (Figure 3.9 [Right]). The strip heater was wired into CB-7 in the TIP and the current draw was verified as 2.93A with a handheld meter. CB-7 is a 4A breaker fed from the output of the two-phase 480VAC to single-phase 120 transformer in the TIP.

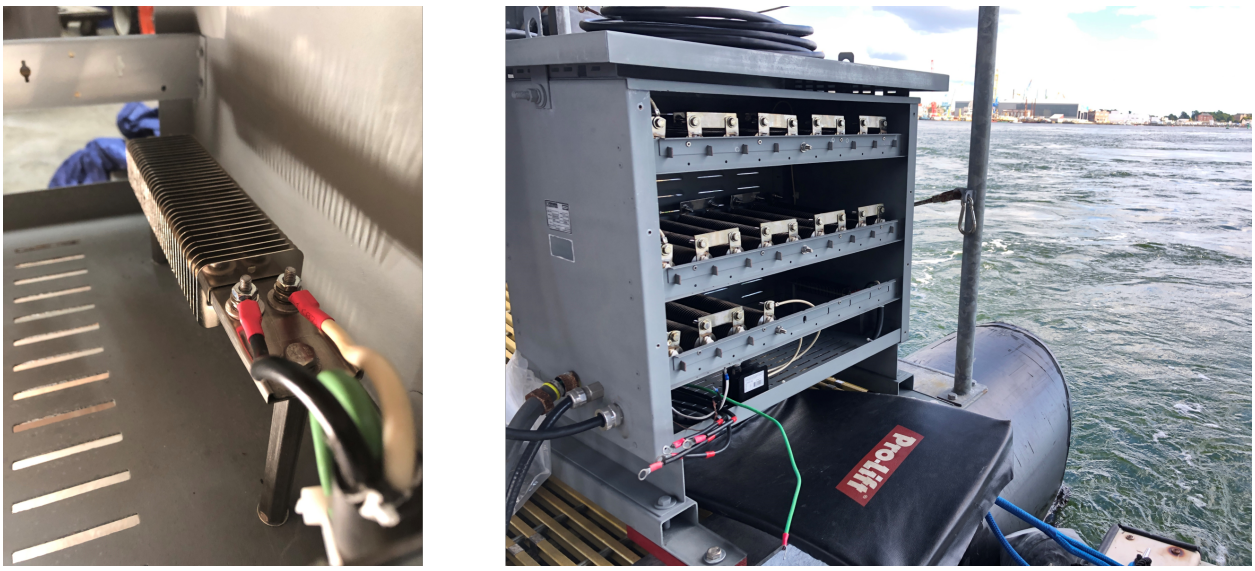

Figure 3.9: [Left] Strip heater installed in resistor bank enclosure. [Right] Dump load resistor bank installed on platform.

CHAPTER 4

Instrumentation Deployment Methods and Data Quality Control

4.1 Thrust Load Deployment Methods and Data Quality Control

4.1.1 Thrust Load Measurement Methods

Turbines are attached to the TDP via the interface bracket that is mounted to the spanning beam. The spanning beam is a 16in diameter galvanized pipe that spans the platform moon pool and allows turbines to be rotated in and out of the water utilizing the custom designed roller bearing assembly, strongback I-beam and winch. This system is known as the turbine pitching mechanism (TPM). The roller bearing assembly locates the spanning beam on the platform but allows it to rotate when moments are applied. When the turbine is deploy two locking arms, attached to the spanning beam, interface with the clevis/load cell assembly that is bolted to the TDP structure, via a pinned connection(Figure 4.1 [Left]). The turbine thrust force is assumed as resultant force applied at the center of the turbine, and can be calculated from the load cell measurements with a moment balance about the spanning beam axis of rotation (Figure 4.1 [Right]).

To estimate the thrust force that causes the measured reaction, it is assumed that the structure is rigid with no relative motion (Equation 4.1). It is also assumed that the thrust force is uniformly distributed across the swept area allowing a resultant force to be estimated at the turbine center. From these assumptions, the sum of the moments about the spanning beam must be equal to zero resulting in a balance between the load cell reaction force and the applied thrust force (Equation 4.2).

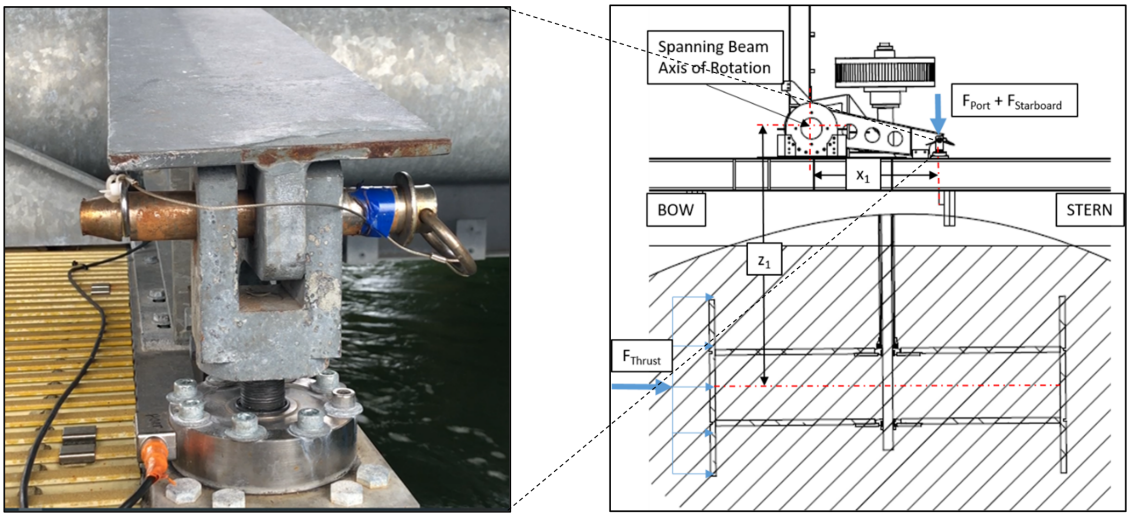

Figure 4.1: [Left] Photo of clevis and load cell assembly (1 of 2), bolted to the TDP on edge of the moon pool. [Right] Diagram of the TDP illustrating moment arms for thrust measurements, side view in top half, cut through turbine center plane in bottom half: x_1 is the moment arm for vertical forces measured with the two load cells, z_1 is the moment arm for horizontal thrust force applied to turbine center, both with respect to the axis of the spanning beam.

$$\sum M_{SB} = 0 \tag{4.1}$$

$$F_{Thrust} = \frac{x_1}{z_1}(F_{Port} + F_{Starboard}) \tag{4.2}$$

Where:

M_{SB} = Summation of moments about the spanning beam axis

F_{Thrust} = Thrust force on turbine from tidal current

F_{Port} = Reaction force measured by port side thrust load cell

$F_{Starboard}$ = Reaction force measured by starboard side thrust load cell

x_1 = Horizontal distance between load cells and spanning beam axis

z_1 = Vertical distance between turbine centerline and spanning beam axis

4.1.2 In-Situ Load Cell Calibration

In-situ calibrations of the load cells were performed both before and after the measurement campaign in the fall of 2021. This in-situ calibration process utilized the strong back I-Beam and existing anchor points on the TDP combined with an inline load cell and a chain fall to impose known loads on the turbine pitching mechanism, for the ebb and flood directions. The applied loads could then be converted to equivalent thrust loads through a moment balance around the axis of the spanning beam. The load cell instruments used in this calibration are summarized in Table 4.1.

TDP Location	Port Load Cell	Starboard Load Cell	In-Situ Calibration Setup
Manufacturer	LCM Systems	LCM Systems	Sensing Systems Corp.
Model	PTC-1	PTC-1	11767
Serial Number	539482	539483	18013101
Load Rating	100 [kN]	100 [kN]	20 [klb]
Load Directionality	Tension and Compression	Tension and Compression	Tension Only
Calibration Date	5/25/2021	5/26/2021	5/18/2021
Calibration Provider	GEOKON	GEOKON	Sensing System Corp.

Table 4.1: Load Cell Sensor Information

Prior to completing the initial calibrations in the ebb tide direction, the tension link load cell was installed between the winch and strong back anchor point. The locking arm pins were removed and the turbine was pitched out of the water while recording the tension link load cell data. The maximum force measured was just below 1400lbs which occurred as the winch began to rotate the turbine out of the water and gradually decreases to approx. 950lbs when the turbine is rotated completed out of the water. When the turbine is rotated back into the water the maximum force measured was $\approx 1250 lbs$ which occurs when the strongback was near vertical, just before the locking arm pins were installed. This test provided a safe working limit for applying loads to the system via the strongback, based on loading conditions the structure frequently experiences. A maximum allowable in line load of 1250lbs on the tension link load cell was used during the calibration process.

The in-situ calibrations were completed at slack tide while the turbine was braked to limit any fluid dynamic drag on the structure. Without fluid dynamic drag and with no load applied to the tension link load cell, the thrust load cells are in compression due to the moment caused by the weight of the turbine, the adapter plate, etc. When flow is in the ebb direction the turbine thrust will act to reduce this compressive force on the load cells. When flow is in the flood direction the turbine thrust will act to increase this compressive force. This can be simulated with the calibration setup shown in Figure 4.2. The photo insert in Figure 4.2 shows the tension link load cell and chain fall set up towards the bow for ebb direction calibration, for flood direction calibration they would be set up towards the stern.

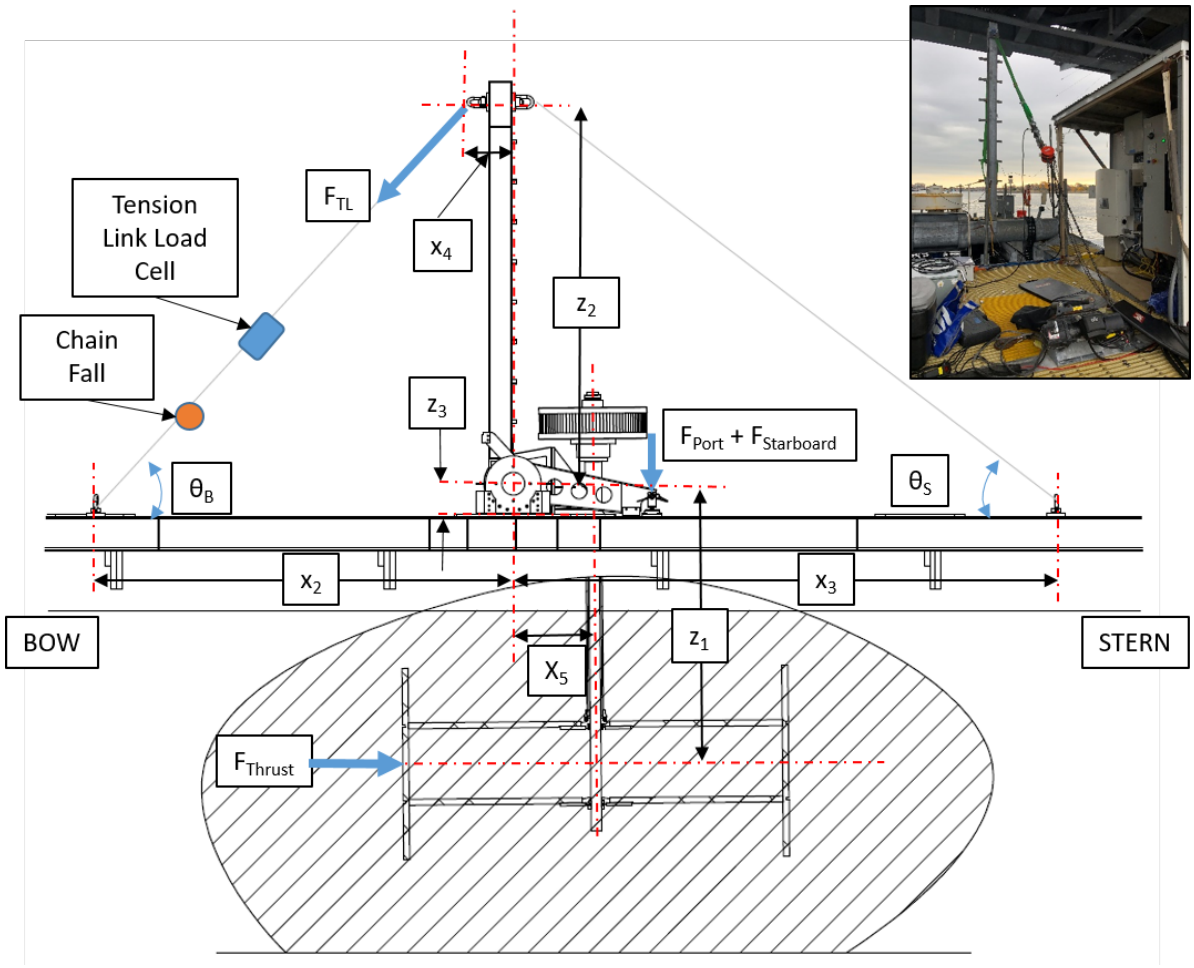

Figure 4.2: Setup for thrust load cell calibration, here the tension link load cell and chain fall are set up for ebb direction calibration. The photo insert shows the ebb calibration being performed on the platform on 11/10/2021. The variables are defined in Table 4.2.

The calibration process for both the ebb and flood directions was completed in about 30 minutes. Loading was applied to the system in approx. 100lb increments allowing around 10 seconds for data collection at each successive loading level. Once the maximum load limit was reached the system was incrementally unloaded in the same fashion. The initial calibration was completed on 11/10/21 and the final calibration was completed on 12/08/21.

Distance from spanning beam centerline to:	Symbol	Horizontal/Vertical	Value
Center of turbine swept area	z_1	V	97.06 [in]
Strong-back anchor point	z_2	V	134.31 [in]
Surface of TDP deck	z_3	V	11.37 [in]
Thrust load cell	x_1	H	48.5 [in]
Bow anchor point	x_2	H	145.43 [in]
Stern anchor point	x_3	H	189.35 [in]
Bow side of strong-back	x_4	H	8.57 [in]
Centerline of turbine shaft	x_5	H	28 [in]
In-situ load angle for ebb tide thrust calibration	θ_B	Angle of tension link load cell w.r.t. Horizontal	45.05 [°]
In-situ load angle for flood tide thrust calibration	θ_S	Angle of tension link load cell w.r.t. Horizontal	37.57 [°]

Table 4.2: Summary of Thrust Load Dimensions

To convert the applied load from the tension link load cell to an equivalent thrust force on the turbine, their moments about the centerline of the spanning beam have to be equal (Equation 4.3). For this calculation, the tension link force was resolved into its horizontal and vertical components (Equation 4.4 & Equation 4.5).

$$\sum M_{SB} = 0 \qquad \text{(Equation 4.1)}$$

$$F_{Sim-Thrust}Ebb = \frac{z_2}{z_1}Fx_{TL-Ebb} + \frac{x_4}{x_1}Fz_{TL-Ebb} \tag{4.3}$$

$$Fx_{TL-Ebb} = F_{TL-Ebb}\cos\theta_B \tag{4.4}$$

$$Fz_{TL-Ebb} = F_{TL-Ebb} \sin \theta_B \tag{4.5}$$

Where:

F_{TL-Ebb} = Tension link load cell force

Fx_{TL-Ebb} = Horizontal component of F_{TL-Ebb}

Fz_{TL-Ebb} = Vertical component of F_{TL-Ebb}

$F_{Sim-Thrust}Ebb$ = Simulated thrust force from ebb tide direction

The initial and final calibrations for the ebb direction calibration are shown in Figure 4.3. A linear regression was used to determine a relationship between the reaction force recorded by the load cells and the thrust force applied to the turbine (Equation 4.6).

$$F_{Thrust-Ebb} = \frac{F_{LC-sum} - static_{weight}}{m_{Ebb}} \tag{4.6}$$

Where:

$F_{Thrust-Ebb}$ = Thrust force on turbine from ebb tides

F_{LC-sum} = Port and starboard load cell summation (what is measured)

$static_{weight}$ = F_{LC-sum} when no external loads are applied

m_{Ebb} = average slope between initial and final calibrations (-1.8954)

The in-situ calibration set up was then moved to the stern side of the platform corresponding with flood tide thrust load on the turbine. To convert the applied load from the tension link load cell to an equivalent thrust force on the turbine, their moments about the centerline of the spanning beam have to be equal, similar to Equation 4.3 above. In this configuration the line of action of the vertical component of $F_{TL-Flood}$ passes through centerline of the spanning beam and therefore does not produce a moment. A moment balance yields the following relationship between the applied load from the tension link load cell and the simulated thrust force in the flood direction (Equation 4.7).

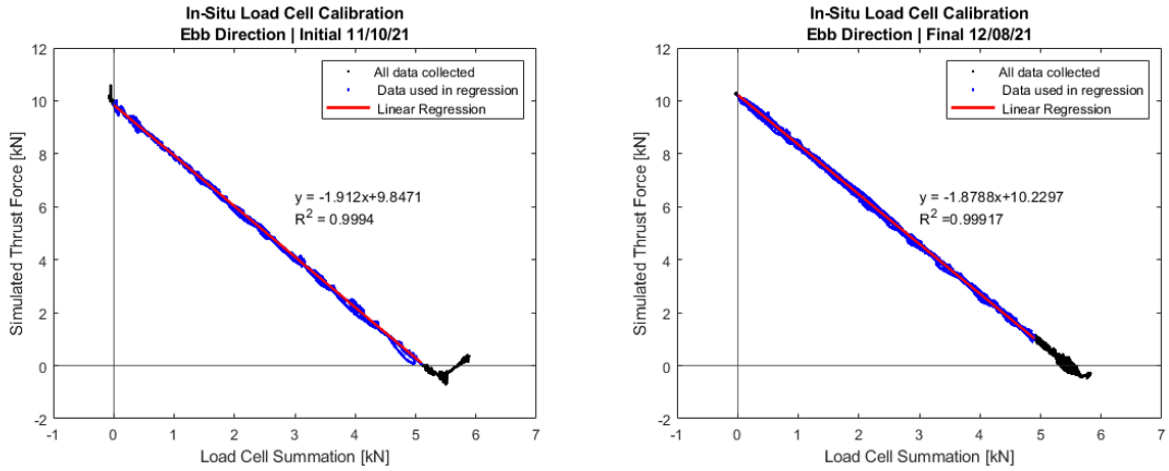

Figure 4.3: Simulated thrust force vs sum of port and starboard thrust load cells (Ebb Direction). [Left] Initial calibration on 11/10/2021. [Right] Final calibration on 12/8/2021.

$$\sum M_{SB} = 0 \qquad \text{(Equation 4.1)}$$

$$F_{Sim-Thrust}Flood = \frac{z_2}{z_1} Fx_{TL-Flood} \tag{4.7}$$

$$Fx_{TL-Flood} = F_{TL-Flood} \cos\theta_S \tag{4.8}$$

Where:

$F_{TL-Flood}$ = Tension link load cell force

$Fx_{TL-Flood}$ = Horizontal component of $F_{TL-Flood}$

$F_{Sim-Thrust}Flood$ = Simulated thrust force from flood tide direction

The initial and final calibrations for the flood direction calibration are shown in Figure 4.4. A linear regression was used to determine a relationship between the reaction force recorded by the load cells and the thrust force applied to the turbine (Equation 4.9).

$$F_{Thrust-Flood} = \frac{F_{LC-sum} - static_{weight}}{m_{Flood}} \tag{4.9}$$

Where:

$F_{Thrust-Flood}$ = Thrust force on turbine from flood tides

m_{Flood} = average slope between initial and final calibrations (1.9938)

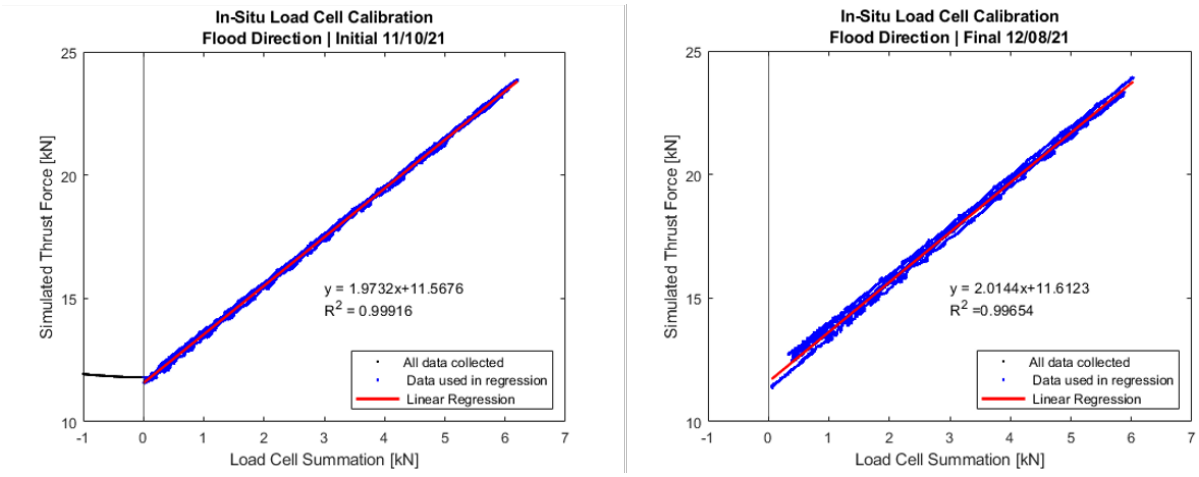

Figure 4.4: Simulated thrust force vs sum of port and starboard thrust load cells (Flood Direction). [Left] Initial calibration on 11/10/2021, [Right] Final calibration on 12/8/2021.

4.1.3 Static Weight Discrepancy Review

The y-intercept of the calibration plots (Figure 4.3 & Figure 4.4) represent the combined load cell force when no external forces are applied to the system, i.e. the self-weight of the deployed turbine and mounting components. The calibration results from the initial and final tests theoretically should have produced the same y-intercept ($self_{weight}$) for all four results (Table 4.3). This discrepancy is likely due to the moment imposed on the structure due to the self weight of the calibration set up. The calibration set up consisted of a chain fall, tension-link load cell, lifting strap and various shackles with an estimated combined weight of 100lbs. This weight on the turbine pitching mechanism was not included in the calibration curves.

The static weight of the turbine was estimated using a real data set during the deployment(Figure 4.5). Slack tide was identified by selecting a time window were the along

platform velocity component of the bow ADV was close to $0m/s$, in this case around a low tide. A standard deviation filter that retained values within one standard deviation from the mean was applied to the data set three times. From this filtered data set the mean was computed to estimate the static combined force on the load cells as $static_{weight} = 10.7045kN$. This value will be used in the conversion equations, Equation 4.6 & Equation 4.9, to estimate turbine thrust force from the measured combined load cell data collected.

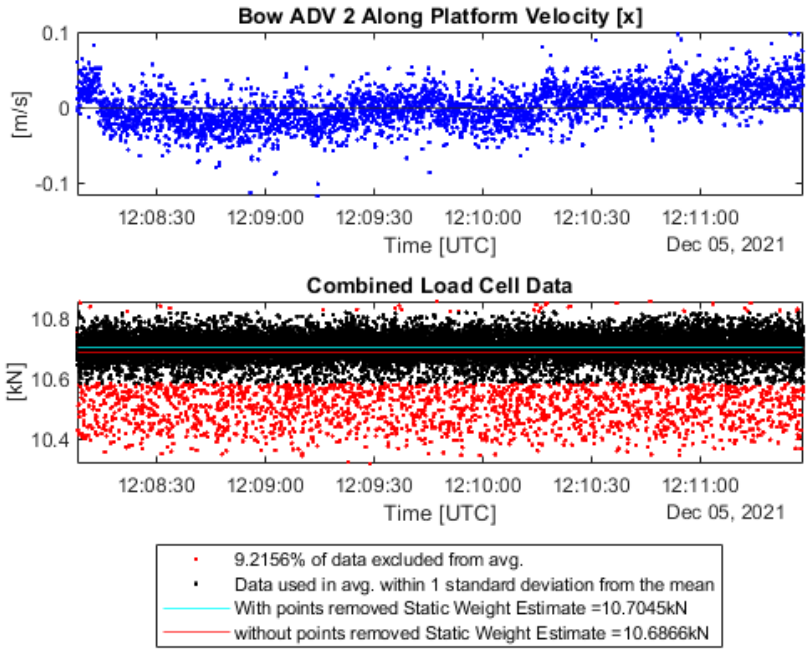

Figure 4.5: [Top] Bow ADV 2 along platform velocity indicating slack tide. [Bottom] Combined port and starboard load cell data collected over same time interval and used to estimate $static_{weight}$.

	Ebb Tide		Flood Tide		Estimate from Data
	Initial	Final	Initial	Final	(Figure 4.5)
$self_{weight}$	9.8471 [kN]	10.2297 [kN]	11.5676 [kN]	11.6123 [kN]	**10.7056 [kN]**
slope (m)	-1.912	-1.879	1.9732	2.0144	-

Table 4.3: In-Situ Thrust Load Cell Calibration Results

4.1.4 Data Guide - Thrust Load Cells

Load Cell Data was collected nearly continuously from 11/10/21 to 12/08/21 except in instances when MODAQ was powered down for troubleshooting etc. There are two primary data sets obtained during this time:

1. Nov. 10-24, 2021: Thrust force data collected while the turbine was operating in grid synchronous mode (including some days of partial turbine operation).

2. Nov. 25 - Dec 8, 2021: Thrust load data collected while the turbine was braked (not rotating) in the water due to issues with grid synchronization caused by the inverter.

The first data set serves the primary focus of this thesis, providing turbine thrust force estimates for a grid synchronized tidal turbine. The second data set presents a unique opportunity to characterize the form drag on a turbine at rest in a real turbulent flow. Night owl security camera footage could be used to view the position of the braked rotor blades with respect to the oncoming flow to aid in this analysis.

4.1.5 Thrust Load Cell Sign Flip Algorithm

There was an error within the data acquisition system, which sampled and recorded the raw load cell signal. When the load cells experienced a tensile load, the output should be a negative number but, all data recorded was positive. This error was introduced to true tensile data points only, and after the manufacturer calibration coefficients were applied, preserving the correct magnitude of the value. The directionality of the signal "positive" compression, "negative" tension) was lost at this point prior to saving each data point.

This presented a unique challenge to design an algorithm to determine if/when a data point needed to have a negative sign applied to it to retrieve the intended load direction.

The sign-flip algorithm developed utilized baseline knowledge of the deployment to identify simple criteria that accurately indicates if a data point should be in tension. Primarily

the port and starboard load cell signals should nearly always be trending together which can be characterized by the sign of the derivative of each signal. Insights on the system that are utilized in the filter are listed here. The final design of the filter included 23 different logical outcomes that each data point could fall into resulting in accurate sign flip decision making in most cases.

1. The starboard side load cell has a static offset of $\approx 5.5kN$ of greater compressive force than the port side load cell due to limitations in vertical alignment of the clevis to locking arm pin connection.
    (a) A difference time series was created to aid in the analysis by subtracting the original port side signal from the starboard signal.
        i. The difference between the starboard and port side load cells is positive when the both the starboard and port load cell are in compression. The value also remains positive for a small interval when the port load cell is lightly loaded in tension.
        ii. The difference between the starboard and port side load cells is negative for all times when the port load cell is in tension because of the initial offset in load between each sensor. The port side load cell switches to tension first and correspondingly will have a higher magnitude in tension than the starboard load cell.
2. The above criteria worked well for identifying many points where the sign should be flipped but, the turbine pitching mechanism is well balanced during operation causing the signals to frequently oscillate around zero. This introduced some challenges to improve the accuracy of the filter during important times (ie. while the turbine was operating and producing power).
    (a) Utilizing the derivative of the original port and starboard load cell signals proved to be an effective means to identify if the sign needed to be flipped.

i. If the derivative of the original signals were trending together this would indicate the sign of both signals should be the same.

ii. If the derivative of the original signals were trending apart this would indicate the sign of the signals should be different.

4.1.6 Sign Flip Algorithm - Results

In Figure 4.6 a short 5 second time series is presented to show how frequently loads change between tension and compression and the results of the sign-flip algorithm.

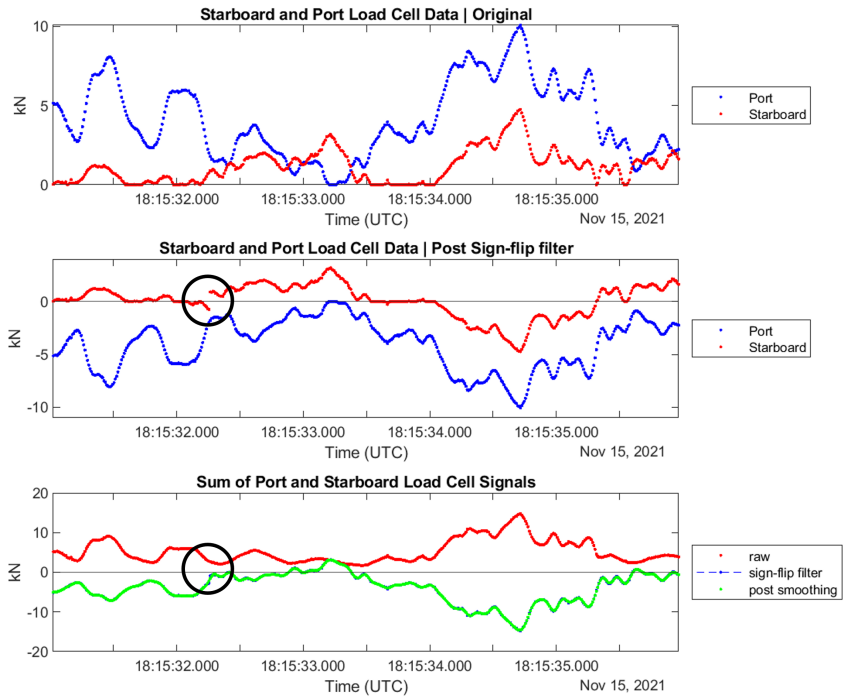

Figure 4.6: [Top] Raw recorded port (blue) and starboard (red) thrust load cell data; [Middle] Individual load cell results after the sign flip algorithm was applied; [Bottom] Summation of the load cell data for: raw data (red), post sign-flip algorithm (blue – hidden under green line), post smoothing filter (green).

It was determined that a perfect sign flip algorithm, accounting for all possible scenarios, could not be defined. In the middle plot of Figure 4.6 there is evidence where the filter did not act as intended (circled in black). These errors manifest as sharp discontinuities in the

combined load cell summation time series used to estimate turbine thrust forces. To account for these discontinuities, the matlab smoothing function "smoothdata" was applied to the summation of the sign-flipped port and starboard load cell time series to smooth the signal in areas where the sign-flip algorithm did not operate as intended. The smoothdata function selected utilized a Savitzky-Golay filter with a window size of 10 data points. This style filter fits a second-degree polynomial over each successive window of data points. A window size of 10 data points was selected for the 100Hz load cell data in order to preserve variability less than 10Hz. A sample of the results of the smoothing function is plotted in green on the bottom plot of Figure 4.6. The smoothing function results in some loss in variability over short time scales, but increases the reliability of the combined load cell data in accurately representing the instantaneous thrusts load on the turbine by removing the discontinuities introduced by the sign-flip algorithm.

The parameters of the smoothing function were defined such that the filter would smooth the data over small enough scales so that the dominant frequencies experienced by the structure would not be removed from the signal. Figure 4.7 illustrates that the load cell data processed, through the sign flip algorithm and smoothing function, contain the dominant frequencies present in the raw unprocessed signal. The turbine average shaft speed was computed over this time interval and found to be 2.85sec/rev (21 RPM) corresponding with a frequency of $f_{RPM} = 0.35075Hz$ (Figure 4.7 red). The fundamental blade passage frequency (Figure 4.7 blue) is the number of blade $N = 4$ multiplied by the shaft speed f_{RPM}, $(4 * f_{RPM} = 1.403Hz)$. The AC voltage waveform produced by the generator (or any motor) will cause a mechanical vibration at that frequency. The average generation frequency over this time period was computed as $7.015Hz$ (Figure 4.7 black).

An artifact of the smoothing function, circled in red, is introduced at high frequencies in the processed data.

4.1.7 Load Cell Missing Time Points

The load cell time series are nearly continuous over the deployment length, with only missing time points when the entire MODAQ platform was shut down for troubleshooting. It is important to perform a check of the record length, N, over each discrete time series prior to any frequency analysis. This is completed by determining the expected number of points by multiplying the number of seconds in the discrete time interval by the sample rate and comparing it to the number of data points in the real data set over the same discrete time interval. Additional information regarding load cell data processing can be found in [54].

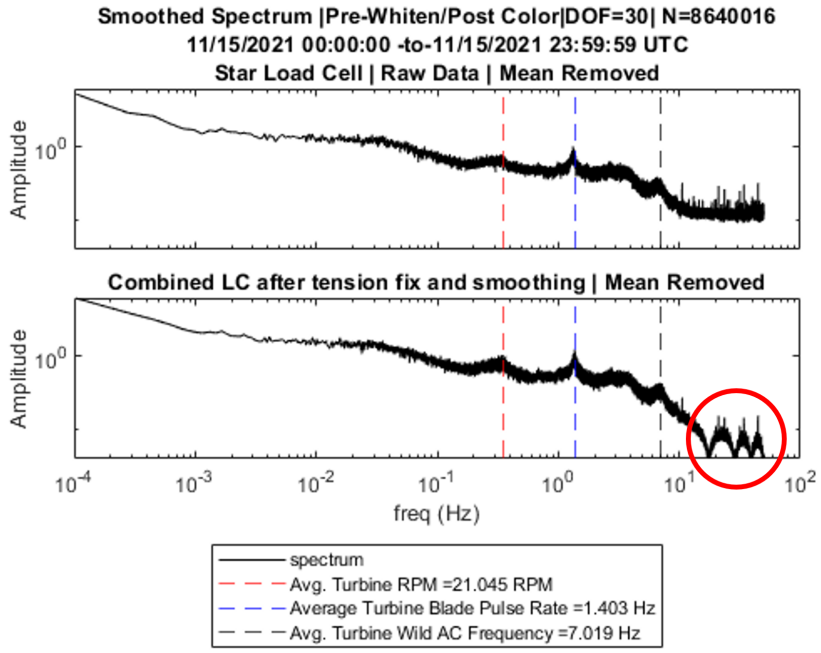

Figure 4.7: [Top] Spectrum of the raw starboard load cell signal and indicates the dominant frequencies present; [Bottom] Spectrum of combined port and starboard load cell after sign flip algorithm and smoothing function were applied. The high frequencies, circled in red, are an artifact of the smoothing function but the dominant frequencies less than 10Hz still remain viable for future analysis.

4.2 ADCP Deployment Methods and Data Quality Control

4.2.1 ADCP Operating Principle

Acoustic Doppler Current Profilers (ADCP) are underwater instruments that estimate velocity utilizing the Doppler effect. Multiple active acoustic transmitters (usually 4) are positioned, at different angles, around the instrument that transmit/receive sound pulses. After an initial sound pulse (source) is generated the transducer "listens" for the reflected signal (echo) off of particles (receivers) in the water. This principle assumes that the particles (receivers) in the water are moving with the water they are entrained in and not moving relative to it. If the particles are moving relative to the instruments transducers than a Doppler shift will occur between the source sound frequency, f_{Source}, and the received sound frequency, $f_{Doppler}$. Only reflected sound in the along beam direction can be measured by the receiver and therefore the ADCP measures along beam particle velocities, $V_{ADCP-Beam}$ Equation 4.10.

$$V_{ADCP-Beam} = \frac{C f_{Doppler}}{2 f_{Source} \cos \alpha} \tag{4.10}$$

Where:

$V_{ADCP-Beam}$	= Along beam water velocity [m/s]
f_{Source}	= Transducer source sound frequency [Hz]
$f_{Doppler}$	= Doppler shift frequency [Hz]
C	= Speed of sound in water [m/s]
α	= Acoustic beam angle [°]

ADCP's range gate velocity estimates into depth bins (minimum size of 0.25m for FlowQuest 1000) with knowledge of the speed of sound in water, which is strongly dependent on temperature along with density and pressure. Correspondingly, ADCP's typically have integrated temperature and pressure sensors to monitor changes in sound speed throughout a deploy-

ment (as does the FlowQuest 1000). The combination of along beam velocity measurements, oriented in different directions, on an ADCP allows for 3-dimensional velocity to be computed and transposed into a known coordinate system. Typical coordinate systems are instrument coordinates, relative to the instrument body, and compass coordinates which utilize an onboard compass and further transpose measurement into North, East and up directions.

There are two distinct operating principles for ADCP's narrow band and broad band. Narrow band instruments transmit sound pulses at a particular operating frequency, 1000kHz for example, and then measure the Doppler shift directly between the source and received sound pulses. The along beam water velocity can then be estimated by Equation 4.10. If there is relative motion of the receiver away from the source than $f_{Doppler} < f_{Source}$. If there is relative motion of the receiver is moving toward the source than $f_{Doppler} > f_{Source}$.

Broad band instruments transmit sound at various frequencies within a defined frequency "band", around a specific operating frequency, and use time dilation to estimate water velocity. This method is equivalent to the frequency shift method used in narrow band instruments. Time dilation utilizes the operating principle that if two subsequent sound pulses, separated closely in time Δt, will have the same Δt if they are reflected by a stationary particle. If there is relative motion between the particle and the instrument than there will be a phase shift in the received signal of the second sound pulse compared to the echo from the first sound pulse. This phase shift can be a more accurate means of measuring the Doppler shift but can introduce phase ambiguities. The phase shift can only be resolved between 0° and 360° which causes values greater than 360° to "wrap" around 0° and become ambiguous. This could be avoided by keeping Δt sufficiently small but there is a trade off with the accuracy of the velocity estimates. To improve velocity estimate accuracy, broadband instruments implement ambiguity resolution techniques to "unwrap" the phase which is why anticipated water velocity ranges must be imported during instrument configuration before deployment. For more on broadband acoustic devices refer to *Principles of Operation A*

Practical Primer [55].

4.2.2 ADCP Deployment Specifications

Two LinkQuest FlowQuest 1000kHz ADCP's were deployed at the bow (ADCP2) and stern (ADCP1) of the floating TDP. The instruments were connected to the platform multiplexer as a part of the LB-DAS with deployment parameters configured in the manufacturer software, *FlowQuest-1000* (Appendix H - Table H.1). Data is stored by the LB-DAS in an SQL database where users can query data for analysis. The ADCP's were deployed with the top of the units approximately at the water level which can expose the integrated pressure sensor above the water level due to passing waves and platform motion. The temperature sensor location within the ADCP is not specified. Integrated pitch and roll sensors combined with bottom tracking mode allow for accurate range gating of data from the floating platform.

4.2.3 ADCP Deployment Orientation & Location

The ADCP's were deployed utilizing the instrument coordinate axis, XYZ, which reports velocity estimates in each direction relative to the deployment orientation. The positive x-direction corresponds with the vector from beam 3 to beam 1 which is shown in Figure 4.8. Both bow and stern instruments were deployed in the same orientation with the positive x-axis aligned parallel to the platform frame in the ebb tidal flow direction (Figure 4.8). The positive y-axis is shown below and combined with the x direction creates a two-dimensional plane parallel to the platform deck surface. The positive z-axis follows a right-handed Cartesian coordinate system and is positive downward. During previous studies, it was shown that an accurate compass calibration could not be completed, likely due to the large steel structure to which the instrument is deployed. The directional accuracy of the ADCP was estimated to be 2.0035° based upon the constraints of platform motion within the vertical guide posts (Chancey, 2019 p.21 [7]). The distance from the center of the bow ADCP to the turbine axis was 7.23 m, or the ratio of distance to turbine diameter $x/D \approx 2.3$. The

distance from the center of the stern ADCP to the turbine axis was 5.72 m, or $x/D \approx 1.8$. All velocity data presented herein are converted to the NOAA standard of positive velocities corresponding with flood tides. Final data tables contain velocity estimates in the instrument deployment orientation.

To convert both ADCP data sets from the instrument coordinate system x and y velocity estimates to a North and East coordinate system it is assumed the platform is parallel to the bridge pier it is moored too which has a 105.05° heading relative to true north.

$$V_{North} = -V_{X-ADCP} \sin\theta_P - V_{Y-ADCP} \cos\theta_P \tag{4.11}$$

$$V_{East} = V_{X-ADCP} \cos\theta_P - V_{Y-ADCP} \sin\theta_P \tag{4.12}$$

$$\theta_{NE} = 90° - \left(\arctan \frac{V_{North}}{V_{East}}\right)^{\circ} \tag{4.13}$$

Where:

V_{X-ADCP}	= ADCP velocity estimate in along platform direction (+ in Ebb direction)
V_{Y-ADCP}	= ADCP velocity estimate in cross platform direction (+ in Portsmouth shore line direction)
$Heading_{pier}$	= 105.05°
θ_P	= $Heading_{pier}$ - 90° [converted to radians]
V_{North}	= Converted ADCP velocity estimate to true North heading
V_{East}	= Converted ADCP velocity estimate to East heading relative to true North
θ_{NE}	= Resolved velocity direction with North = 0 °

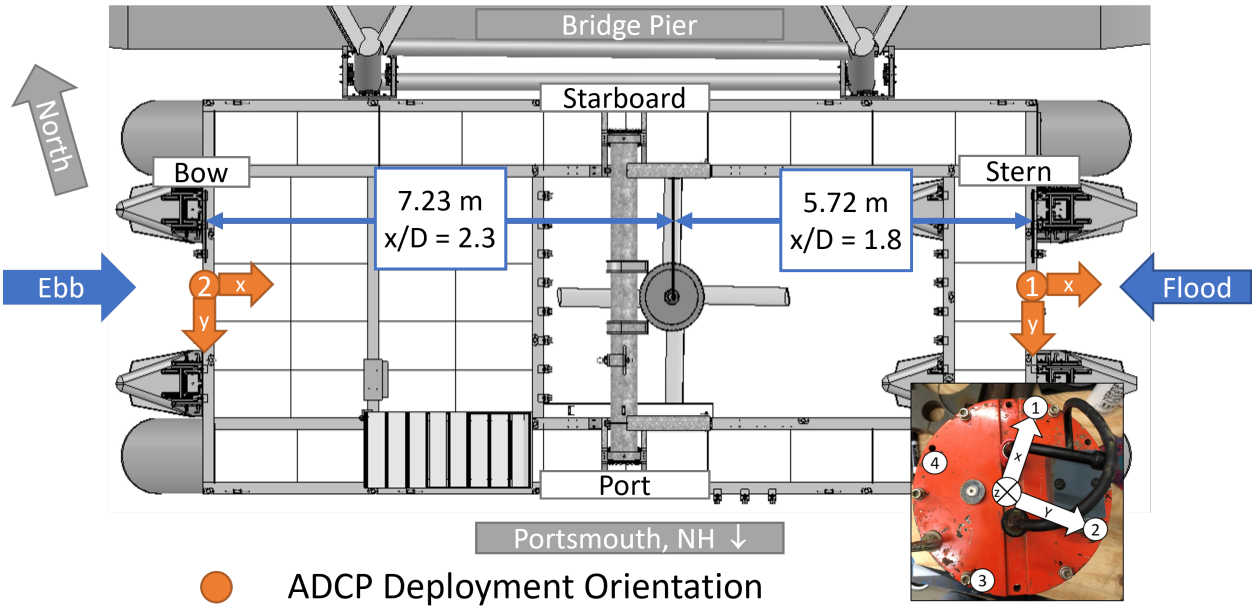

Figure 4.8: Top view of platform indicating deployed orientation of ADCP's and location with respect to the turbine centerline. Photo insert: ADCP instrument coordinate axis and beam labels.

4.2.4 ADCP UNH TDP Water Column Data Introduction

In the deployed orientation during this study, ADCP beam 4 (channel #3) on both the bow and stern instruments intersects the bridge pier approximately 8m below the water level. This is apparent in the top plot of Figure 4.9, for the 60 minute average selected here, where there is significant velocity reduction around 8m.

This interference affects the velocity estimates reported in a few depth bins above and below this point. The instrument appears to recover its ability to accurately estimate velocity by rejecting beam 4 and only utilizing three beams at greater depths to the bottom boundary layer where velocity goes to zero. In the ebb flow direction, the directional data below 8 m suggests there is a significant difference in direction (veer) in the inflow profile between the upper and lower parts of the flow. The full water column data estimated by the instruments is not the focus of this study, rather the velocity bins over the turbine swept area but this is important information for users of the data set in different applications.

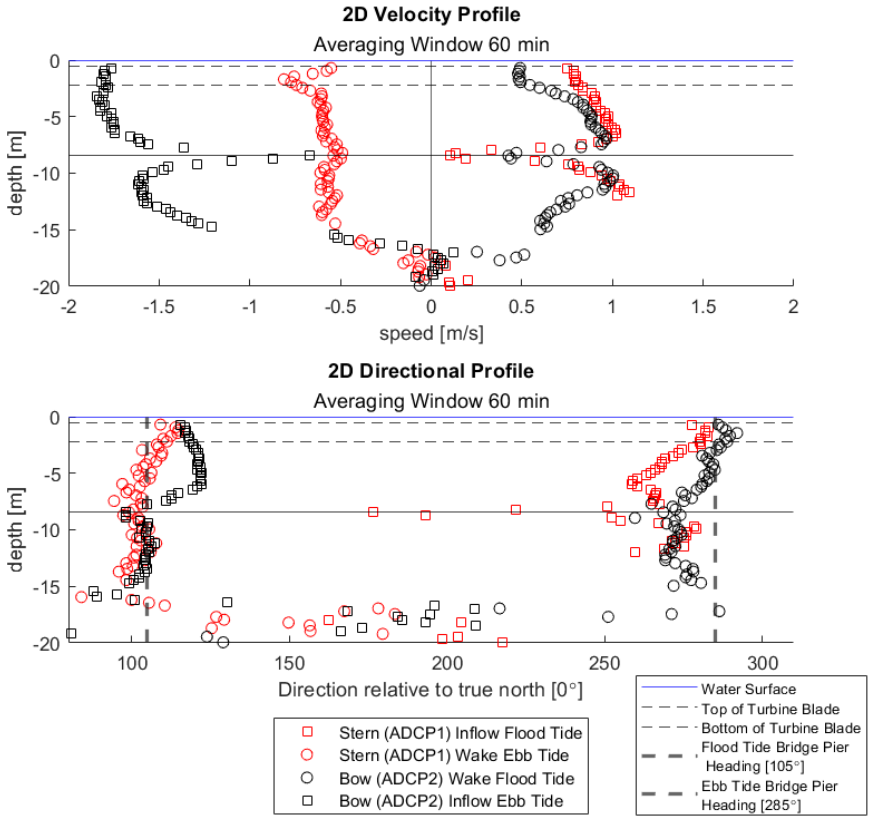

Figure 4.9: ADCP tidal current measurements on bow and stern of TDP. Velocity magnitude [Top] and direction [Bottom]. Plotted is the 60 min average of horizontal velocity magnitude, from the 2 minute ensemble averages for each depth bin during a peak flood tidal flow (10/14/21 21:57 to 22:57 UTC) and subsequent peak ebb tidal flow (10/15/21 02:57 to 03:57 UTC). The turbine was operating as expected, synchronized during the ebb tide and free spinning on the flood. The velocity values plotted are the combined x and y horizontal velocity magnitude. Only depth bins with more than 25% of acceptable values (ones that passed the QC process) during the hour long averaging window are included.

4.2.5 ADCP Data Guide

The ADCP's were deployed from the bow and stern of the TDP beginning on October 12, 2021 and ending on December 13th, 2021. Table 4.4 presents a summary of ADCP deployment specifications during the fall 2021 measurement campaign. Additional information is summarized in (Appendix H Table H.1).

The ADCP instrument deployment included some variability in the continuity of the data collection. The outline of these deviations is listed below with details on how these issues

Manufacturer	LinkQuest	
Model	FlowQuest 1000	
Location	Stern	Bow
S/N	014595	014594
Reference #	1	2
Distance to turbine centerline [m]	5.72	7.23
Deployment Dates	10/12/21 to 12/13/21	
Operating Frequency [kHz]	1000	
Transducer Depth[m]	0.37	
Bin Size[m]	0.25	
Max Working Distance [m]	25	
Ensemble [s]	120	
Ping Interval [s]	2	

Table 4.4: ADCP Deployment Summary

were dealt with in subsection 4.2.6.

1. From 10/15/21 to 10/21/21 the multiplexer, which powers the instruments, was not properly network-connected resulting in the internal power relays being inoperable. This resulted in no data collection from either ADCP during this time frame. On 10/21 the network connection was reset and the data collection resumed. Unfortunately, the turbine was operating well during this time frame and no other velocity data was collected at the site (acoustic Doppler velocimeters were deployed in November).

2. The Bow ADCP2 LB-DAS record included gaps in data collection that were determined to be from a deteriorating/intermittent connection of the power supplied to the instrument at the instrument bulkhead. This resulted in some data being recorded to the instruments' internal data logger and some being recorded by the LB-DAS. Missing data points in the internal data logger and LB-DAS records did not always coincide with one another upon inspection. Network connection issues between the instrument and the LB-DAS were suspected to be the cause of the errors during the deployment. The corrosion on the power cable was not discovered until after the instruments were recovered (Figure 4.10). After 11/30/2021 there was little Bow ADCP data recorded to either the instrument internal logger or LB-DAS record available for analysis.

3. The Stern ADCP LB-DAS data record contained some data gaps where the instrument recorded data was available to fill in these missing points. The cause of these missing points is likely attributed to times when the LB-DAS was undergoing troubleshooting to try and resolve the connectivity issues with the Bow ADCP. In these situations, the Cimplicity Project could have been rebooted which would have stopped data collection to the LB-DAS but power could still be present allowing the instrument to continue data collection to its internal recorder.

Figure 4.10: Photos indicating the extent of the corrosion present on the bow ADCP data/power cable after the instrument was removed on 12/13/21. [Left] Corrosion evident on SubConn connector. [Right] Corrosion present on bow ADCP bulkhead pin.

4.2.6 ADCP Missing Time Points and Data Gap Fill

Ideally, a data set collected by an instrument consists of equally spaced (discrete) time points, and measured values corresponding to each time point. Experimental data must contain a discrete and continuous time series (over a defined record length) to allow for frequency analysis. If many successive data points in a continuous time vector are missing/erroneous the signal variability can be altered or lost. However, a bigger problem occurs if a time point is missing altogether in the record and the time vector is no longer discrete and continuous. In the measurements reported here, missing time points occurred due to an intermittent power connection to the bow ADCP (introduced in subsection 4.2.5) and due

to user-imposed thresholds for logging data on the Shark 100 Meter (discussed in section 4.4). In both cases, the occurrence and duration of missing time point events in each time series was unpredictable (i.e., how often and how many successive time points would be missing). This required a custom algorithm to rebuild each time vector that approximated a discrete and continuous time vector over the record length.

For the ADCP's, the goal of this effort was to identify missing time points in each ADCP LB-DAS record and insert new time points to create a more continuous time vector. Missing time points were first compared to each ADCP's respective internal data logger record and if not available, an artificial time point was created. In the combined time series produced by this method, the last column of the data array indicates the source that the time point was derived from. The labels are: (1) for LB-DAS, (2) for FQ (FlowQuest ADCP instrument internal data logger) or (3) for an artificially generated time point (based on the sample rate and containing no data values). This preserves the option of future data set users to work with the original LB-DAS data or use a different approach in filling data gaps by filtering for rows that contain a 1 in the final column.

It is then up to the discretion of the data analyzer on how the missing data values at these time points should be populated. Missing data values associate with artificially generated time points can be generated based upon the data around them (interpolation or otherwise), replaced with a mean value, or large sections of data which have many successive missing data values can be ignored during analysis.

All data (including the ADCP's) recorded to the LB-DAS were assigned a time point from the LB-Server CPU clock, as each data signal was received from each instrument. The LB-Server CPU clock was synchronized to a GPS time source was a Masterclock NTP 100-GPS server and the connection is detailed in subsection 3.1.1. It is important to note the LB-DAS streams the ADCP data and does not trigger the instrument to sample directly. Data recorded to the internal ADCP data logger (FQ record) was subject to time drift from the ADCP's internal battery powered clock. This time drift was quantified over the

deployment period and then the time vector was corrected by the following process:

- At the beginning of the data record, real identical data values in the LB-DAS and FQ records were identified, that should be aligned in time, and the initial offset between the two time vectors was determined.
- This process was repeated at the end of the record to determine how much the clocks deviated over time. By removing the initial offset in time a linear drift rate was approximated.
- The initial offset and drift rate were applied to the FQ record time vector to align the data points more closely to the real time values.
- This process was completed for the Bow and Stern ADCP FQ record time vectors independently because they had different initial offsets and were subject to independent internal clock drift rates.

Once the FQ record time vector was corrected to be more closely aligned with GPS time the process of filling in missing data points could begin.

1. An artificial time series was created starting at the initial time in the ADCP LB-DAS (and time corrected FQ records) and ending at the same time point the records end. A $\Delta t = 120s$ was selected for the artificial time series, since the ADCP's were set to record an ensemble average every two minutes. This provided a complete artificial time vector where each time point could be used as a reference to search around to identify if a ADCP LB-DAS time point or FQ time point existed. ADCP LB-DAS time points were tested against the artificial time vector with a search range of $+60s$ from each artificial time point. This accounted for deviations in the real data collection associated with starts and stops from power cycling the instruments during troubleshooting events. If an ADCP LB-DAS time point was identified within this range it was selected for the final output data array and the corresponding data values were populated in the

variable columns. If no LB-DAS time point existed within this range then the artificial time point was selected for the output data array and not-a-number values (NANs) were assigned in the variable columns.

2. The output data array was then tested against the corrected FQ record time vector, only looking at time points when an artificial time point was selected during the previous step. Again a search window of $+60s$ was selected to account for starting and stopping of the data acquisition due to loss of power to the instrument.

A sample of these results is presented in Figure 4.11 which shows there were significant amounts of time when data was only recorded to the internal logger (FQ record) and not the LB-DAS (Cimplicity). The FQ record and LB-DAS records were "combined" into a final data record with the method described above.

From this method, the resulting data set, containing LB-DAS, FQ and artificial time points, was subject to possible "time jitte" between successive points. To determine how prevalent time jitter may be in the time series a test was performed to determine the number of time points less than 00:01:45 apart. Points that were in this range were thought to be unacceptable and possibly repeats of one another. The results are quantified in Table 4.5 and indicate a relatively few number of points flagged compared to a significant number of points being added to each record from the FQ data set. These flagged data points were left in the resultant data set from this step and were addressed in subsection 4.2.7.

	Stern ADCP 1	Bow ADCP 2
Total # of data points expected over each record:	44,449	42,948
# of points available in LB-DAS record:	38,069	27,715
# of points added from FQ records:	1,717	4,620
% increase in points available for analysis:	3.86%	10.75%
# of flagged points (successive points less than 105sec apart):	239	169

Table 4.5: ADCP Data Gap Fill Results

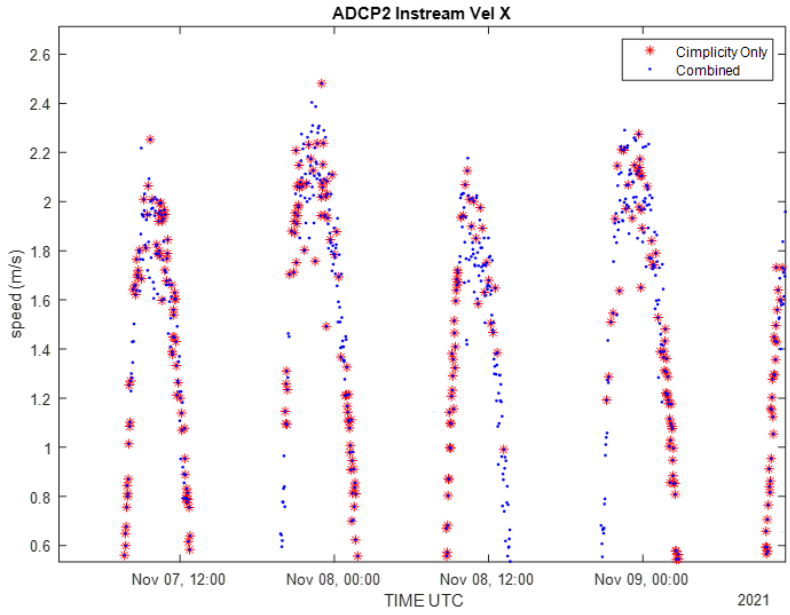

Figure 4.11: Sample record of Bow ADCP X-velocity during the period with irregular power. The ADCP LB-DAS record (red star) and combined data set (blue dot), after the data gap fill process was completed, highlight how many data points were missing from the LB-DAS record in certain time windows. Data is in the original instrument deployment orientation(Figure 4.8) with positive velocities corresponding with ebb tides. Only ebb tides are shown as these events are the most important for this study (when the turbine could be grid synchronized).

4.2.7 ADCP Data QC

After the data gap fill process was completed, quality control tests were performed on the combined LB-DAS and FQ data sets. The ADCP QC tests were adapted from *The Manual For Real-Time Quality Control Of In-Situ Current Observations: A Guide To Quality Control And Quality Assurance Of Acoustic Doppler Current Profiler Observations* [56]. Quality control tests were applied to each depth bin of the data set at each unique time point. This means that a different number of points will be flagged for removal from the data set at each depth bin. If any test at a particular depth bin fails than the velocity values were assigned a NAN. A summary of the QC test results are presented in Table 4.6. ADCP bins 0,1,2,3,4,5 span the turbine blade height in the water column. Depth bin #4 and depth bin #20 are presented to illustrate how the results vary with depth. The variation in the

number of flagged points with depth is based upon the design of this QC process and meets the expected attenuation in acoustic back scatter quality with depth.

	Stern ADCP 1		**Bow ADCP 2**	
ADCP Depth Bin	% of points removed from data set	Results table in Appendix J	% of points removed from data set	Results table in Appendix J
#4	5.39%	(Figure J.1)	7.53%	(Figure J.3)
#20	10.14%	(Figure J.2)	9.29%	(Figure J.4)

Table 4.6: ADCP Data QC Results Summary

For a complete description of ADCP processing scripts and quality control tests refer to [57]. Some notable QC tests are described below.

- Test 6 identifies data points where the signal strength, from all 4 beams (channels), is outside an acceptable range. If any of the values are outside this range the test fails and the index is flagged. This test is performed at each depth bin at every time point. The acceptable range was determined based upon visual inspection of the data in various depth bins and defined as -10dBm to -80dBm.

- Test 7 identifies data points where the signal to noise ratio, from all 4 beams (channels) , is outside an acceptable range. If any of the values are outside this range the test fails and the index is flagged. This test is performed at each depth bin at every time point. The acceptable range was defined as 10dB to 90dB. The minimum value was determined based upon insight obtained from the device manufacturer and the maximum value was determined by visual inspection of the data set.

- Test 21 determines if successive time points in the time vector are within an acceptable range from the desired $\Delta t = 120s$. The range was defined as $\Delta t + / - 10s$. If the current time point falls within this range of the previous or successive time point than it passes. If the test fails the index is flagged and all data for all depth bins is replaced with a NaN at that time point. This tests identifies points associated with the "time jitter" introduced in the data gap fill process.

4.3 ADV Deployment Methods and Data Quality Control

4.3.1 ADV Operating Principles

A Nortek Vector ADV consists of a bottle, containing a battery pack, data storage and processor, along with a probe head with three angled receivers and 4 acoustic transducers. A temperature sensor is located within the probe head, while an IMU and pressure sensor are contained within the bottle. The transducer central to the probe head ensonifies a discrete sampling volume of water with high frequency sound pulses which are reflected off of particles in the sampling volume. These reflected sound waves can scatter in all directions but the reflected signals, in line with the three angled receivers, can be used to compute water velocity estimates. These velocity estimates are orthogonal (along beam) to each probe head, the Vector converts these estimates into either a compass based coordinate system or instrument coordinate system, utilizing the known geometry of the probe head. The Vector is a pulse coherent profiler which requires two successive sonar pings to compute a velocity estimate. The Vector measure the phase shift between successive sonar pulses which has been found to improved individual sample resolution when compared to acoustic Doppler profilers. Acoustic Doppler profilers measure the frequency shift associated with the Doppler affect from each individual sonar pulse. Pulse coherent profilers use the time between successive sound pulses, transmission frequency of the sound pulse, the speed of sound in water, and the phase shift measurement to estimate the along beam (receiver) water velocity (Equation 4.14). (More on pulse coherent profiler theory – [58])

$$V_{ADV-Beam} = \frac{\Delta\varphi C}{4 * \pi F_{Source} \Delta t} \tag{4.14}$$

Where:

$V_{ADV-Beam}$ = Along beam water velocity [m/s]

$\Delta\varphi$ = Phase difference between successive sound pulses measured by each receiver [unitless]

C = Speed of sound in water [m/s]

f_{Source} = Source Frequency [Hz]

Δt = time between 2 successive transmitted sonar pulses [s]

This measurement method introduces the possibility of velocity ambiguity or phase wrapping in the determination of the phase difference. If the phase difference is greater than 360 degrees between the successive sonar pulses velocity ambiguity is introduced. During the design of an ADV deployment prior knowledge of the maximum expected velocity is required to provide bounds for the maximum number of phases that may need to be unwrapped. If a velocity measurement falls outside this nominal velocity range than the phase cannot be unwrapped and a velocity ambiguity is introduced. (More on velocity ambiguity [59])

4.3.2 ADV Deployment Specifications

Two Nortek ADV's were integrated into the UNH MODAQ system with deployment parameters, configured in the manufacturer software, Vector (detailed deployment parameters in Appendix H Table H.2). After the deployment configuration is verified, the deployment must be in initialized using the start data collection command in order to output the data from the instrument and stream into MODAQ. Next, the power to the ADV should be removed so that once it has been deployed, and repowered, the unit will enter its previous deployment/data-output setting. The Vectors deployed during this measurement campaign were deployed with the bottle above the water level, which is an important note regarding the pressure data, without the internal IMU recording and without data stored locally on the instrument.

4.3.3 ADV Deployment Orientation & Location

ADV's were deployed utilizing the instrument coordinate axis, XYZ, which reports velocity estimates in each direction relative to deployment orientation. The positive x direction is aligned from the center of the probe head outward along the probe that has black shrink tape. In order to align the x-axis of the instrument to the along platform direction, as accurately as possible, the bow and stern ADV's had to be deployed in opposite orientations. The positive z axis coincides with water moving toward the ADV probe head, or upwelling in our instrument orientation, with the probe facing downward in the water, following the right hand rule (Figure 4.12). The distance from the center of the bow ADV to the turbine axis was 7.16 m, or the ratio of distance to turbine diameter $x/D \approx 2.2$. The distance from the center of the stern ADV to the turbine axis was 5.65 m, or $x/D \approx 1.8$. Both ADV's were located $\approx 20in$ from the platform centerline in the Port direction. Final data tables contain velocity estimates that have been converted to the NOAA standard with positive velocities corresponding with flood tide direction.

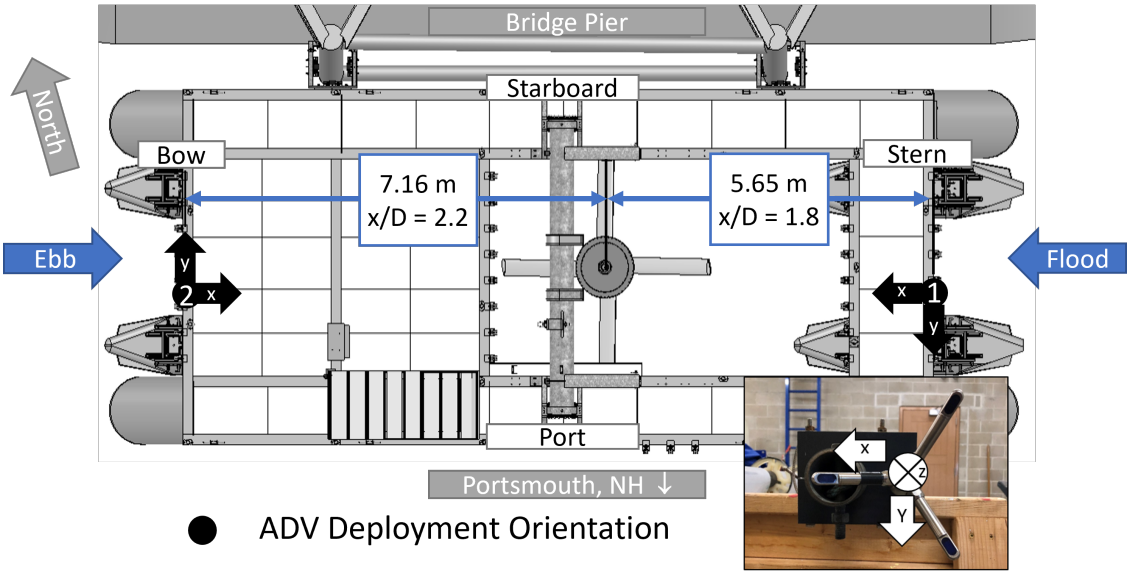

Figure 4.12: Top view of platform indicating deployed orientation of ADV instruments and location with respect to the turbine centerline. [Photo insert] ADV instrument coordinate axis. Note the final ADV data sets have been converted to coincide with the NOAA standard of (+) flood and (-) ebb.

To convert both final ADV data sets, that have been adjusted to coincide with the NOAA standard, from the instrument coordinate system x and y velocity estimates to a North and East coordinate system it is assumed the platform is parallel to the bridge pier it is moored too which has a 105.05° heading relative to true north.

$$V_{North} = V_{X-ADV} * \sin\theta_P - V_{Y-ADV} * \cos\theta_P \tag{4.15}$$

$$V_{East} = -V_{X-ADV} * \cos\theta_P - V_{Y-ADV} * \sin\theta_P \tag{4.16}$$

$$\theta_{NE} = 90° - \left(\arctan\frac{V_{North}}{V_{East}}\right)^{\circ} \tag{4.17}$$

Where:

V_{X-ADV}	= ADV velocity estimate in along platform direction (+ in flood direction)
V_{Y-ADV}	= ADV velocity estimate in cross platform direction (+ in Portsmouth shore line direction)
$Heading_{pier}$	= 105.05°
θ_P	= $Heading_{pier}$ - 90° [converter to radians]
V_{North}	= Converted ADV velocity estimate to true North heading
V_{East}	= Converted ADV velocity estimate to East heading relative to true North
θ_{NE}	= Resolved velocity direction with North = 0 °

4.3.4 ADV Data Guide

ADV's were deployed from the bow and stern of the TDP beginning on November 4, 2021 and ending on December 15th, 2021. From 11/4 to 11/9 both ADV's were deployed at a water depth of ≈2 meters to collect data during a spring tide event for a future axial flow hydrokinetic turbine project with a hub height at that depth. On November 9th 2021

at approximately 10am EST both ADV's were moved upward in the water column to a deployment depth of ≈1.30 meters to coincide with the center of the deployed cross-flow turbine swept area at approx. 1.34 meters. The deployment depth of the ADV is associated with the approximate location of the ADV measurement volume in relation to sea surface elevation. Table 4.7 presents a summary of ADV deployment specifications during the fall 2021 measurement campaign.

Location on TDP	Stern	Bow
Reference #	1	2
Manufacturer	Nortek	
Model	Vector ADV	
Probe S/N	VEC 5563	VEC 5455
Bottle S/N	40511-15-126	40511-15-127
Distance to turbine centerline [m]	5.65	7.16
Power Source	MODAQ 12 VDC PSU	
Deployment Depth = 2 meters Deployment Dates	11/04/21 to 11/09/21	
Deployment Depth = 1.30 meters Deployment Dates	11/10/21 to 12/15/21	
Distance between each ADV and the TDP centerline	20 [in] in Port Direction	
Sampling Rate (Output) [Hz]	16	
Nominal Velocity Range [m/s]	+/− 4	
Sampling Interval	Continuous	
Baud Rate	9600	

Table 4.7: ADV Deployment Summary

The ADV deployment from 11/4/21 to 12/15/21 can be subdivided into four data sets.

1. From 11/4/21 to 11/9/21 the ADV's were deployed at 2 meter water depth. The measurements are still within the swept area of the cross-flow turbine deployed during this study, which spans from roughly 0.5-2.2 meters in water depth from top to bottom of the blade. The turbine was operating well during this time frame but load cells were not yet installed and the Voltsys data was not yet integrated into MODAQ. Time drift on the Voltsys internal clock was monitored during this time and linear correction applied to the time vector. The shark meter was operating during this time as well

with a reliable time reference from the NTP Time Server. As such, both Voltsys and shark meter data sets would be valid for analysis during this time.

2. From 11/9/21 10am EST to 11/24/21 the system was mostly operating as intended with the turbine synchronizing to the grid but does include some days/times when an inverter error caused the turbine to be braked and in the water. This affects the measurement of the downstream ADV, depending on the tide and the running condition of the turbine. The downstream ADV could be measuring the wake of an operating turbine or the wake of a turbine that is fixed (braked) in the water. This is the primary data set of interest for analyzing grid synchronous power performance parameters associated with this deployment.

3. From 11/25/21 to 12/8/21 the system was not operating, due to the inverter error (subsection 4.4.2), resulting in the turbine being braked and in the water except for a brief period on 12/3/21 while trying to troubleshoot the error. This is an interesting data set where the form drag on the braked turbine could be analyzed in conjunction with the thrust load cell measurements.

4. On 12/9/21 the turbine was pitched out of the moon pool but the ADV deployment continued, allowing additional data collection on the raw tidal resource around the platform without a device interfering with the flow. On 12/15/21 the ADV's were retrieved marking the end of this data set.

4.3.5 ADV Data QC

Quality control tests performed on the ADV data sets were adapted from *The Manual for real-time quality control of in-situ current observations: a guide to quality control and quality assurance of acoustic doppler current profiler observations* [56]. This guide is specifically written for current profilers but many of the tests are relevant and applicable to an ADV. A qualitative representation of the ADV QC process is presented in Figure 4.13 and Fig-

ure 4.14 with quantitative description of individual test results in Appendix J Figure J.5 and Figure J.6.

The complete ADV QC test result tables in Appendix J include the QC test description, the limits associated with the test and test performance results. The number of points flagged by a test represent the number of points that did not pass each test individually followed by the increase in total number of points flagged after each successive test. The percentage in total points flagged, after each successive test, provides insight on how many points have been flagged and removed from each record. The QC tests resulted in nearly 4% of the ADV1 and over 7% of the ADV2 data points being flagged and removed from the data set prior to further analysis (Table 4.8).

Stern ADCP 1		**Bow ADCP 2**	
% of points removed from data set	Results table in Appendix J	% of points removed from data set	Results table in Appendix J
3.97%	(Figure J.5)	7.37%	(Figure J.6)

Table 4.8: ADV Data QC Results Summary

For a complete description of ADV processing scripts and quality control tests refer to [60]. Some notable QC tests are described below.

- Test 6 identifies data points where the signal strength is outside an acceptable range. The signal strength, recorded by the ADV, is in the units of counts. To convert between counts and dB a conversion estimate is presented in Nortek technical note No. 003 of 0.4-0.45dB/count [61]. A conversion factor of 0.4dB/count was used in this data set. A noise floor estimate for signal strength was completed in air on 4/19/2022. This was based on the procedure outlined in the Nortek Manual ([59] p.80-81). The results for minimum signal strength was determined to be 20.4 dB for ADV1 and 18 dB for ADV2.

- Test 7 identifies data points where the beam correlation is outside an acceptable range. The beam correlation recorded by the Nortek Vector is in units of percentage (%). A

minimum correlation value of 64% was selected based upon inspection/ trial and error as recommended in the Nortek Manual ([59] p.71).

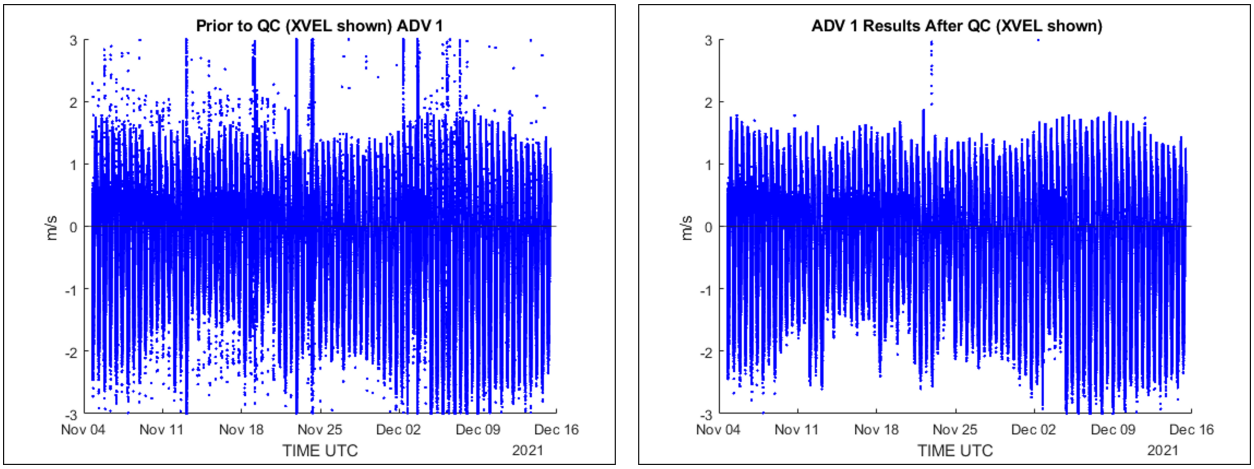

Figure 4.13: ADV1 - X velocity data for raw [Left] and post QC [Right] over entire record. Note the deployed orientation of ADV1 coincides with the NOAA convention (+) flood and (-) ebb.

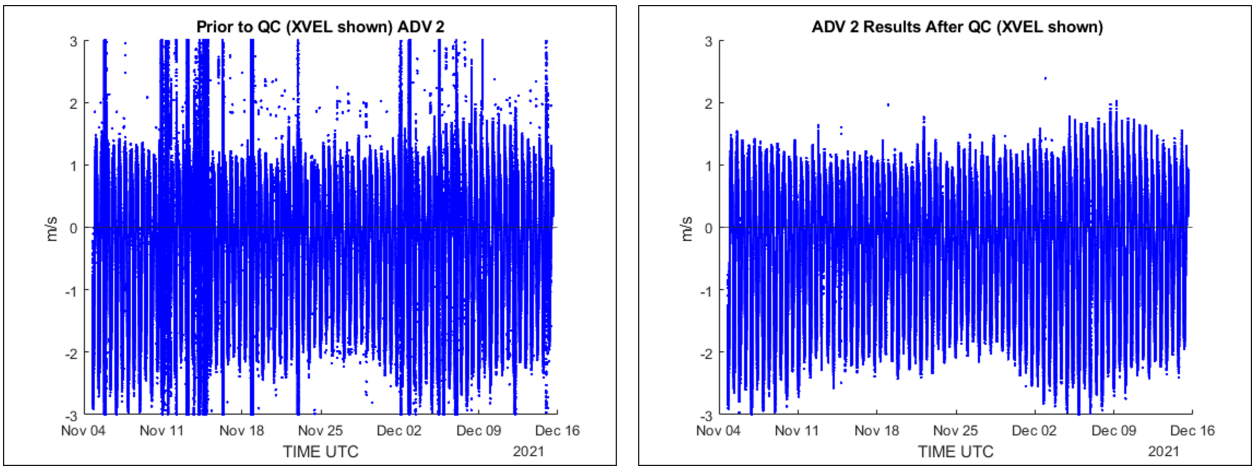

Figure 4.14: ADV2 – X velocity data for raw [Left] and post QC [Right] over entire record. Note the direction has been changed to correspond with NOAA convention (+) flood and (-) ebb.

4.4 Power Monitoring Methods and Data Quality Control

4.4.1 Deployment Specifications

The cross-flow turbine is connected to a direct drive generator with 25 kW capacity which outputs variable voltage AC power. The variable voltage AC power output from the generator is connected to a rectifier. The rectifier "rectifies" the sinusoidal 3-phase AC signal into a DC signal with diodes (that regulate the polarity of the AC signal) and capacitors that smooth between peaks in the AC signal. The rectifier installed on the Living Bridge TDP is a Voltsys Renewable Energy Model VS80A/DL800 which is rated at 25kW. This device was originally designed for small scale wind turbine control and was selected by New Energy for use with this TEC installation. The rectifier can transmit the DC power/signal it creates either to the 11 Ohm 25 kW load bank during off grid mode operation or to the grid-tied Solis Inverter for grid synchronized operation. The rectifier contains an internal data logger that monitors and records a variety of metrics associated with the electrical power produced by the turbine. A custom Arduino shield, supplied by Voltsys, was installed in the rectifier which allowed the data, from the internal logger, to be integrated into the MODAQ system. The data connection from the rectifier is RS485 and the communication protocol is Modbus. A data converter from RS485 to RS232 was installed prior to the connection to the RS232 serial port located on the cRIO controller.

The extent of the variables recorded are summarized in Appendix I Table I.1 and are useful for troubleshooting the system. The primary variables of interest, recorded by the rectifier, for this study are turbine frequency (variable 8) and inverter power (variable 31). The variable number corresponds with the column in the final Voltsys data table. Turbine frequency or more accurately generation frequency (f_G) is the frequency of the AC signal produced by the generator and can be converted to shaft speed (RPM) using Equation 4.18. This was the only means to measure shaft speed during this measurement campaign. The inverter power variable is a measurement of the DC power that is output from the rectifier

and supplied to the inverter during grid synchronous operation.

$$RPM_{shaft} = \frac{f_G 60}{\frac{\#ofpoles}{2}} \tag{4.18}$$

Where:

RPM_{shaft}	= Rotational rate of the generator drive shaft (i.e. the cross flow turbine) [revolutions per minute]
f_G	= Generation frequency [Hz]
60	= multiplier for output to be in revolutions per minute [RPM]
$\#ofpoles$	= The # of individual permanent magnetic poles on the generator field (summation of North and South poles)
2	= It takes one pole pair to create one complete electrical pulse (f_G) so the # of poles needs to be divided by 2

The rectifier internal data logger is intended to monitor important operating parameters and provide information for system troubleshooting. The maximum update rate for the rectifier data logger is 10Hz but not all parameters actually update at this rate.

An alternate means of monitoring power production was pursued to provide more reliable electrical power production estimates during grid synchronous operation. On October 15, 2020 a Electro Industries/GaugeTech model Shark 100 power meter was installed to collect revenue grade power generation data. The Shark 100 meter was installed in the breaker panel which connects the TDP to the Memorial Bride 480VAC bus Figure 4.15. This instrument measures electric current with current transformers and root mean square (RMS) voltage directly between each phase. The primary variable of interest from the Shark 100 meter for this study is apparent power 3-phase (variable 27) which should be analogous to the inverter power recorded by the rectifier. The remaining variables recorded by the Shark meter are summarized in Appendix I Table I.2 and provide additional opportunity for analysis.

The data from the Shark meter was integrated into LB-DAS which assigns a GPS syn-

chronized time stamp to the data as described previously in subsection 4.2.6. The Shark meter samples the voltage and current at a rate of 400 samples/electrical cycle (=400*60 Hz = 24,000Hz) and reports average values at 1Hz with select parameters being reported at 6 Hz (Watts, VAR, and VA). The 100 meter generic specifications sheet states, "the meter shall have an accuracy of +/- 0.1% or better for voltage and current, and 0.2% for power and energy function", for a power factor range of +/- 0.5 to 1 [62]. The power conversion equipment on the TDP does not include active power factor correction and as a result the power factor is very low when the system is running in comparison to commercial power generating equipment. Electro Industries/GaugeTech was contacted to access the expected accuracy of the instrument while operating outside this power factor range and reported an expected accuracy within 1%.

Figure 4.15: The Shark meter installed in the Memorial Bridge Motor Control Center (MCC) 480VAC breaker panel that feeds the TDP

4.4.2 Voltsys Data Guide

From 10/12/21 to 11/09/2021 20:00 UTC the rectifier was not connected to the MODAQ system and the data was stored in the internal data logger. This data was subject to time drift associated with the battery-powered clock installed within the rectifier. A linear time drift was estimated in the same method as described previously in subsection 4.2.6. The time drift correction was applied to the data during this time frame before combining with the record that was recorded to MODAQ. Rectifier data was recorded at 1 Hz until 11/18/21 15:27:38 UTC, after which the data rate was increased to 5Hz. After 11/24/21 the turbine

was only able to operate in grid connected mode during short periods while troubleshooting the system. This resulted in the turbine being braked (not rotating) in the water for the majority of the time between 11/25/21 and 12/9/21. On 12/9/21 the turbine was rotated out of the water marking the end of the relevant Voltsys data set.

The system's inability to stay in grid connected mode after 11/24/21 is believed to have been caused by a bad voltage sensor/connection within the inverter. This caused an error message to be sent to the rectifier which resulted in the system disconnecting from the grid and the generator electric brake being engaged. Figure 4.16 presents the 480VAC line to neutral voltage data collected by the Shark meter [Left] and inverter [Right], logged by the Voltsys. The Shark meter and inverter sensors are monitoring the same potential difference but at different points in the circuit so the values should correlate to one another. Additionally, it is not known which inverter circuits Ph1, Ph2, and Ph3, correlate with the Shark meter circuits A, B and C, but this is not critical for this analysis. All six line to neutral voltage readings should be near 277 VAC which is L-N neutral voltage expected from a 480 VAC-line to line three phase Wye connected circuit.

In Figure 4.16 it can be seen that the Voltsys inverter Ph1 reading began to trend toward a higher value sometime after 10/27/21 and remained at a higher value after 11/5/21. These higher readings resulted in the inverter registering an error (error code OV-G-V01) correlating to the grid voltage being too high. On 11/16/21 an attempt was made to troubleshoot this error. The system was shut down, the turbine was rotated out of the water and the 480VAC supply to the platform was electrically isolated. A high resistance joint was a potential cause of the error so all of the accessible 480VAC terminals on the platform, within the TIP, were inspected and re-terminated. After re-powering the system the error persisted, and it was suspected that either the 480VAC connections within the inverter, that are not readily accessible, or internal voltage monitor had gone bad. In either case the inverter was no longer serviceable on the platform. A replacement inverter was installed on June 21, 2022 at the UNH Pier, with help from NEI. It should be noted that this was the original inverter,

which had been swapped out while troubleshooting the "ILeak-PRO04 error" as described previously in subsection 2.3.1.

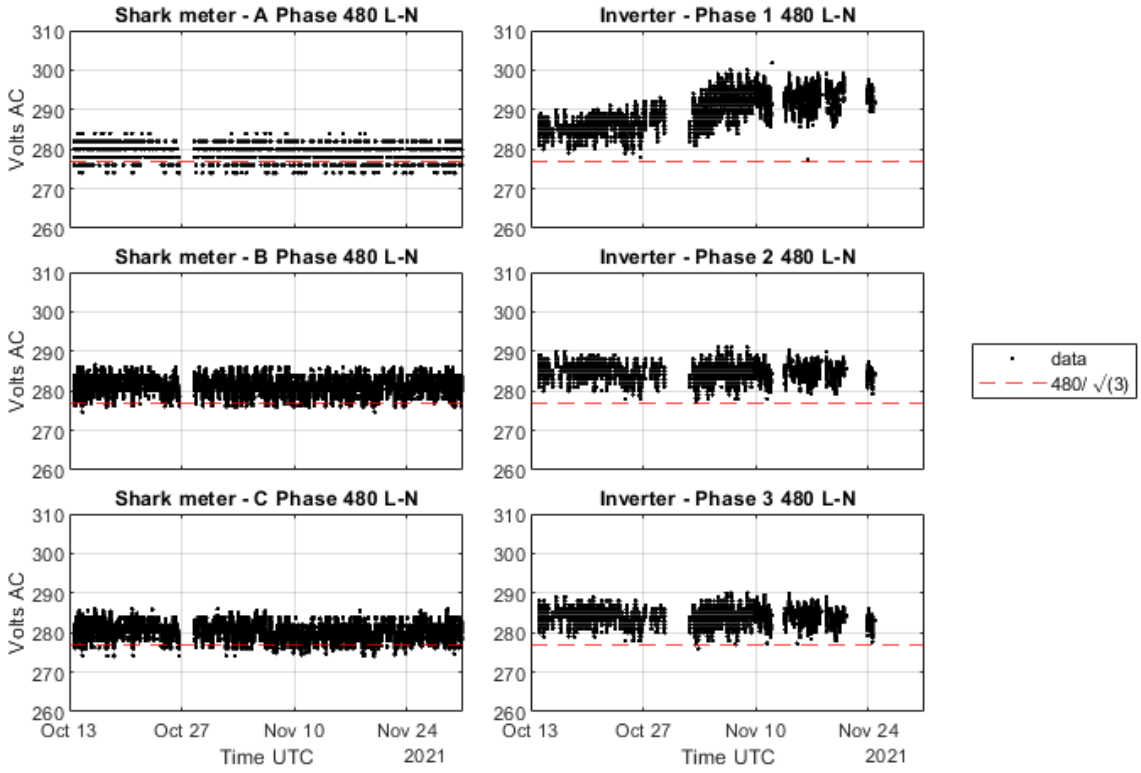

Figure 4.16: [Left column] Shark meter line to neutral data for each phase of the grid synchronous 480 VAC circuit. [Right column] Inverter line to neutral data for each phase of the grid synchronous 480 VAC circuit. All six plots should track the 277VAC value (red dashed line). Note: The inverter Phase 1 value trends upward in early November 2021, causing the OV-G-V01 inverter errors. When this error was registered by the inverter the signal was transmitted to the rectifier which caused the system to stop operating.

4.4.3 Shark 100 Meter Data Guide

The Shark 100 meter was successfully logging data to the LB-DAS from 10/12/21 to 11/30/21. During this time, the LB-DAS was set up to read the Shark 100 meter Modbus registers at 1Hz. On 11/30/21 Shark 100 meter data recording to the LB-DAS stopped due to a suspected network communication issue.

User imposed threshold values were established in the LB-DAS with the intent of only

recording Shark 100 meter data when the system was exporting power in grid synchronous mode. The thresholds were implemented to reduce the amount of data stored in the overall record, because during normal operating conditions the system would not be expected to operate in grid synchronous mode for long periods of time. The thresholds were modified during the Fall 2021 measurement campaign to try and include as much operational data as possible. Note: This method should not be used in future measurement campaigns, instead continuous sampling should be allowed to occur over the measurement campaign.

1. From 10/12/21 to 10/29/21 the LB-DAS project was set to record when the real power output exceeded 100 Watts. It was found that this setting did not record data for some grid synchronous operating periods.

2. After 10/29/21 the LB-DAS project was set to record when power factor readings were less than 0.40. Power factors below 0.40 were typical for this turbine in grid-synchronous operation due to the lack of rectification, as explained previously in subsection 4.4.1.

The use of these thresholds caused unexpected problems in the data which needed to be addressed in post-processing. The thresholds introduced missing time points during synchronous operation where the threshold conditions were not met, which caused data to stop being logged to the LB-DAS. These missing time points are illustrated in Figure 4.17 over a selected ebb tide while the turbine was operating in grid synchronous mode. The top plot presents the time difference Δt between successive time points in the original Shark 100 meter time vector and the bottom plot presents the power factor data, which was used as the threshold parameter after 10/29/21. The Δt spikes in Figure 4.17 indicate that the power factor briefly exceeded 0.4 and subsequently data was not recorded. These spikes indicate a discontinuity had been introduced in the time vector of the Shark 100 meter data set. The brief number of spikes in the majority of this time window are discontinuities that would limit spectral analysis of the Shark 100 meter data during synchronous operation and is the

motivation for filling in the gaps in the time vector.

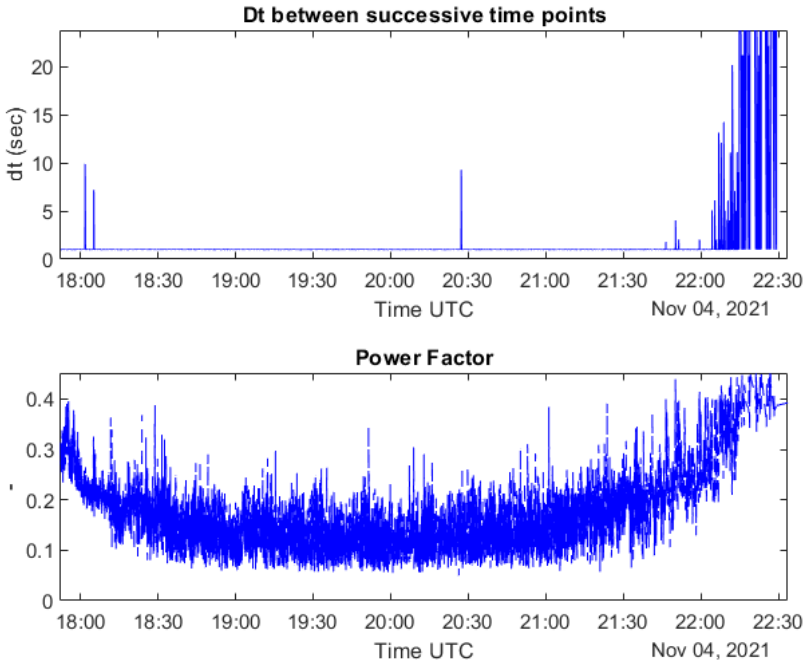

Figure 4.17: A selected time window is shown when the system is operating in grid synchronous mode and transmitting power. The top plot shows the Δt between successive time points in the original Shark 100 meter time vector and the bottom plot shows the power factor data. The brief spikes in the top plot indicate missing points in the time vector.

The missing time points identified above create discontinuities in the time vector which does not allow spectral analysis to be performed on the data set. Missing time points need to be identified and created in order to establish continuity in the time vector to allow for frequency analysis. This approach is different than that taken to fill in missing time points in the ADCP data set (subsection 4.2.6) but the goal is the same.

Missing time point indices were identified and recorded by flagging indices when the Δt between successive time points was greater than 1.2 sec. The Δt values, greater than 1.2 sec, at these missing time point indices provide insight to the number of time points that should be present with knowledge of the sample rate of 1 sec. New time points were then created within these windows in time. This resulted in a time vector where the maximum Δt between time points was 2 sec.

This time vector was then analyzed for Δt values greater than 1.9 sec where a new time point was inserted at the midpoint of the successive points. The resulting time vector had a the maximum Δt of 1.9s Figure 4.18. The data values at the missing time points can be generated by interpolation or otherwise during short missing time windows while the turbine was operating in grid connected mode.

The final column in the processed Shark 100 meter data set indicates the source for the time point either a 1 for a time point from the original data set or a 3 for an artificially generated time point from the method outlined above. Large time windows of missing data are not viable candidates for generating replacement data values and should be avoided in analysis. The final data set does not include any artificially generated data values at the missing time points. All data columns at missing time points are assigned as NAN.

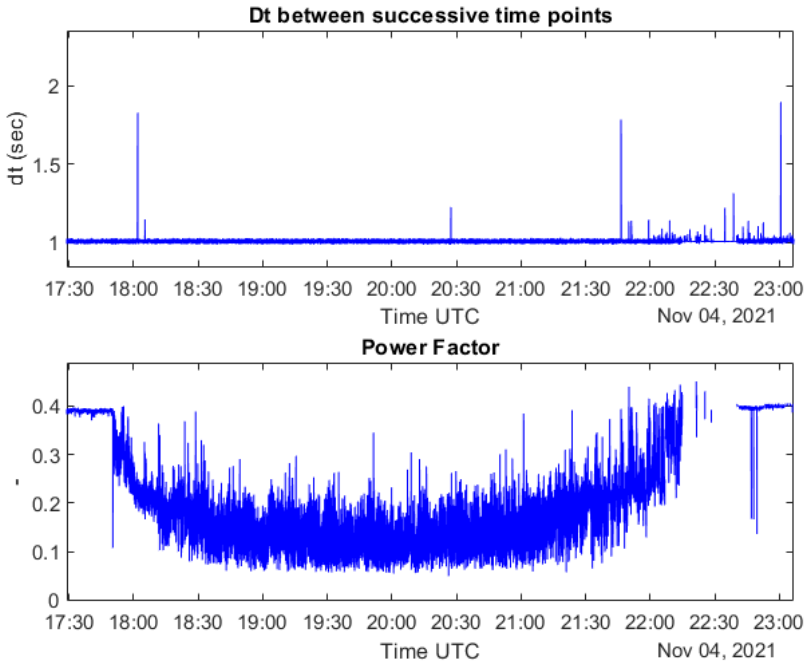

Figure 4.18: The same selected time window as Figure 4.17 is shown after the missing time point algorithm was applied to the data. The top plot shows the Δt between successive time points in the new time vector are all less than 1.9s from one another. The bottom plot shows the power factor data over the new time vector where data gaps are much easier to identify. The brief spikes that occurred while the system was operating can now be filled in with information from the points around them prior to analysis.

Another issue identified within the Shark 100 meter data set appears to be related to a buffer error either in the instrument itself or in the LB-DAS. An example of this issue is presented in Figure 4.19 where successive time points in the Shark 100 meter data set are assigned identical values. Note that the data in this figure is raw data, which had not yet been processed for missing time points as described above.

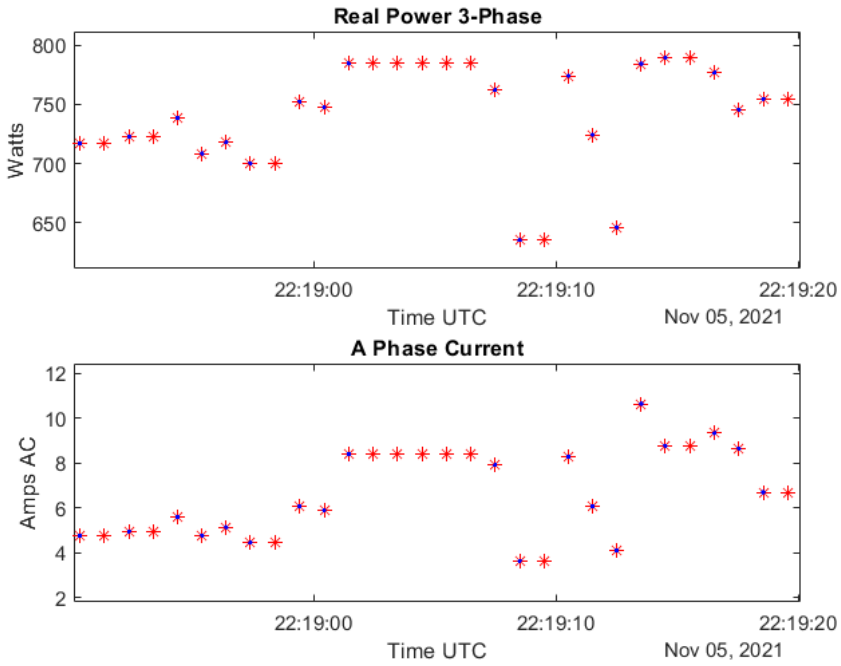

Figure 4.19: An example of Shark meter data illustrating two separate variables with repeated values over the same time window indicating the buffer error. The red dots are the unfiltered data points and the blue dots indicate the points selected after the quality control tests were applied which selected the first time point and data value when a buffer error is identified. Subsequent repeated values during a buffer error event were assigned as NAN.

4.4.4 Shark Meter Data QC

Quality control tests performed on the Shark 100 meter data set after the missing time points were added. The results are summarized in Figure 4.20. The large number of points flagged for many of the tests performed can be explained because they associated with artificially generated time points. At these artificially created time points a NAN was placed in the variable column which would result in a failed test during the QC process. The increase in

total points flagged column, in Figure 4.20, is indicative of the number of new data points flagged after each successive QC test. QC test 23, value repeat, identifies the points associated with the suspected buffer issue outlined above and illustrated in Figure 4.19. Flagged points from the QC process were replaced with a NAN in the final data set. Additional information regarding Shark 100 meter data processing can be found in [63].

Shark Meter	Test Description	Lower Limit	Upper Limit	# of points flagged	Increase in Total points Flagged	% of Total Points Flagged After each test
Test1	**VAR Hrs Negative**| (var-hrs)	0		0	0	0
Test2	**VAR Hrs Net**| (var-hrs)	0		0	0	0
Test3	**VAR Hrs Positve**| (var-hrs)		0	0	0	0
Test4	AB L-L Voltage| (Volts AC)	470		2141886	2141886	51.98333532
Test5	A Phase L-N Voltage| (Volts AC)	270		2141886	0	51.98333532
Test6	BC L-L Voltage| (Volts AC)	470		2141886	0	51.98333532
Test7	B Phase L-N Voltage| (Volts AC)	270		2141886	0	51.98333532
Test8	CA L-L Voltage| (Volts AC)	470		2141886	0	51.98333532
Test9	C Phase L-N Voltage| (Volts AC)	270		2141886	0	51.98333532
Test10	**kilo-Watt Hrs Delivered**| (kWatt Hrs)	0		0	0	51.98333532
Test11	**kilo-Watt Hrs Net**| (kWatt Hrs)	0		0	0	51.98333532
Test12	**kilo-Watt Hrs Recieved**| (kWatt Hrs)	0		0	0	51.98333532
Test13	**kilo-Watt Hrs Total**| (kWatt Hrs)	0		0	0	51.98333532
Test14	A Phase Current| (Amps AC)	0.2		2141898	17	51.98374791
Test15	B Phase Current| (Amps AC)	0.2		2141889	0	51.98374791
Test16	C Phase Current| (Amps AC)	0.2		2141894	5	51.98386926
Test17	Power Factor| (-)	-1	1	2141885	2	51.9839178
Test18	Grid Frequency| (0.01 Hz)	50		2141881	0	51.9839178
Test19	Reactive Power 3-Phase| (vars)	-20000		2141878	0	51.9839178
Test20	Apparent Power 3-Phase| (V-A)	400	1000000	2141902	0	51.9839178
Test21	Real Power 3-Phase| (Watts)	100		2141902	0	51.9839178
Test22	Time Repeat			1	1	51.98394207
Test23	Value Repeat			173803	173795	56.20192742

Figure 4.20: Shark 100 meter data quality control results indicating the tests performed, the number of points flagged from each test and the total number of points flagged. A total of 56% of the data was flagged and removed from the missing time point corrected data set. The large number of points flagged are indicative of the number of time points inserted in the data set by the missing time point process, which did not have associated data values. Note: ** (Test Description)** indicates that QC test was not performed.

4.4.5 Voltsys Data QC

The Voltsys data set was carefully reviewed for accuracy of variable names and units. No additional QC tests were performed to remove erroneous data points from the data set. Additional information regarding Voltsys data processing can be found in [64].

4.5 IMU Instrument Deployment Methods and Data Guide

4.5.1 IMU Instrument Description

A 9-axis YOST LABS 3 Space Sensor Watertight USB/RS232 standard model Inertial Measurement Unit (IMU) was deployed on the TDP from 11/11/21 to 12/15/21. This instrument utilizes three internal sensors an accelerometer, a gyroscope and a magnetometer (compass), each with readings with respect to 3 orthogonal coordinate axis, to determine the orientation of the instrument. The accelerometer measures the acceleration of the instrument in three coordinate directions and reports data in units of g. One g is defined as the acceleration due to gravity which all objects experience while at rest on the surface of the earth ($9.8 m/s^2$). The gyroscope measures angular velocity in radians/sec about each axis (roll about the x-axis (port to starboard), pitch about the y-axis (bow to stern), and yaw about the z-axis). The magnetometer measures magnetic field strength along each axis in units of Gauss. A typical range of magnetic field strength on the surface of the earth is between 0.25 and 0.65 Gauss [65]. The summary of variables collected by the IMU are in Appendix I Table I.3.

The IMU was deployed to quantify platform motion associated with wind/wave action in the hopes these signals could be removed from thrust load and ADV data sets. Collecting platform motion also provides an interesting data set to study how the platform performs during a variety of loading scenarios including turbine operation, turbine braked in the water and turbine pitched out of the water.

4.5.2 IMU Deployment Specifications

The IMU deployment specifications are summarized in Table 4.9. The component sensor data type selected for this deployment was corrected sensor data which is raw sensor data that has had bias and calibration matrix parameters applied ([66] p. 35). The reference mode was set to Single Auto which calculates gravity and north each time the unit is powered on. The default orientation filter, the Kalman filter, was selected.

Manufacturer	YOST LABS
Sensor	3 Space Sensor Watertight USB/RS232
Model	TSS-USB-WT-S standard model
Serial Number	1800063C
Gyroscope Range [$deg°/sec$]	+/- 2000
Accelerometer Range [g]	+/- 2
Magnetometer Range [Gauss]	+/- 1.3
Axis Direction	X: Right, Y: Forward, Z: Up (Right-Handed)
Filter Mode	Kalman
Reference Mode	Single Auto
Estimating Parameter	Oversampling
Calibration Mode	Scale Bias
Data Rate [Hz]	32
Baud Rate	115200

Table 4.9: IMU deployment Specifications

Prior to deployment the calibration process, available in the manufacturer software *3-Space Sensor Suite*, was completed with the sensor on a steel plate to partially simulate the magnetic field interference the sensor would experience when mounted to the steel support I-beam on the TDP (Figure 4.21). First, the sensor was confirmed to be in the default left handed Cartesian coordinate system which aligns with the orientations requested during the calibration process. Second, the sensor was tared and the auto calibration for the gyros was completed. Third, the run gradient decent calibration wizard was completed on top of the steel plate. Finally, the coordinate system was changed to the right hand Cartesian coordinate system shown in Figure 4.22. Once the sensor was installed on the platform the unit was tared to set the orientation in space. The IMU was installed on the TDP nearest to the center of the platform as possible with dimensions in Figure 4.22.

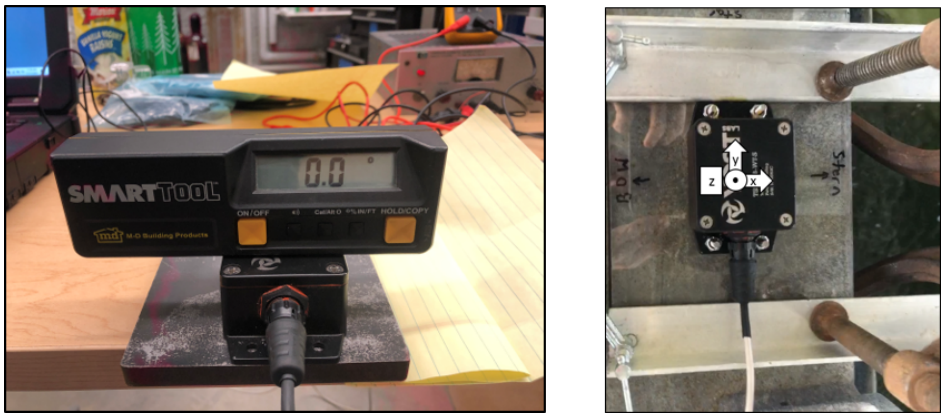

Figure 4.21: [Left] IMU calibrated on top of a steel plate to simulate magnetic interference from the structural I-beam it was deployed on. [Right] IMU deployed on the TDP located on the structural I-beam on the Bow side of the moon pool aligned with the centerline of the turbine (Figure 4.22).

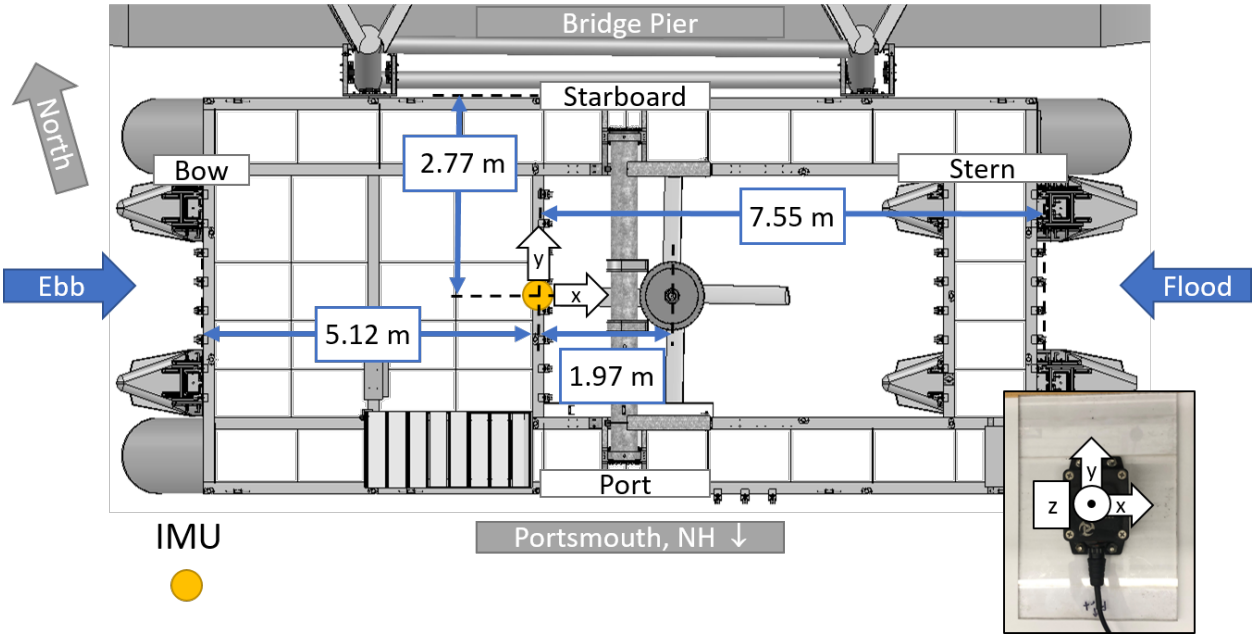

Figure 4.22: Top view of platform indicating deployed orientation of the IMU and location on the platform. The horizontal dimensions indicate the distance from the center of the IMU body to the centerline of the ADV instrument deployment pipes and the turbine energy extraction plane. The vertical dimension indicates the location of the IMU w.r.t to the outside edge of the I-beam on the stern side of the platform. [Photo insert] IMU instrument coordinate axis as deployed.

4.5.3 IMU Data Guide

The instrument deployment from 11/11/21 to 12/15/21 can be separated into three distinct data sets.

1. From 11/11/21 to 11/24/21 the system was mostly operating as intended with the turbine synchronizing to the grid but does include some days/times when an inverter error caused the turbine to be braked and in the water. This is the primary data set of interest for analyzing grid synchronous power performance parameters associated with this deployment.

2. From 11/25/21 to 12/8/21 the system was not operating, due to the inverter error, resulting in the turbine being braked and in the water except for a brief period on 12/3/21 while trying to troubleshoot the error.

3. On 12/9/21 the turbine was pitched out of the moon pool but the IMU deployment continued to collect more data on platform motion without the turbine deployed. On 12/15/21 the IMU deployment ended when MODAQ was removed from the platform.

Note: The single auto reference vector calculates gravity and north each time the unit is powered on and uses this as a reference for all data points going forward. This may introduced a step change in the magnetometer data when the IMU was powered off during troubleshooting efforts associated with the inverter error on 11/16/21 (subsection 4.4.2).

4.5.4 IMU Data QC

The IMU data set was carefully reviewed for accuracy of variable names and units. No additional QC tests were performed to remove erroneous data points from the data set. Additional information regarding IMU data processing can be found in [67].

4.6 Tower Weather Station (TWS) Instrument Deployment Methods and Data Guide

4.6.1 TWS Deployment Specifications

An Airmar WeatherStation Model 200WX has been installed on top of the Portsmouth tower of the Memorial Bridge at least since July 2017. The sensor is approximate height of 62.5m from M.L.W. level derived from the National Geodetic Vertical Datum of 1929 (NGVD-29) ([68] Drawing B1). Data from this sensor was recorded every 5 minutes and was connected to the LB-DAS for data streaming and storage. This sensor was originally calibrated by Airmar on December 23, 2015 with addition specifications given in Table 4.10. The summary of variables collected by the weather station are summarized in Appendix I Table I.4.

Manufacturer	AIRMAR Technology Corporation
Sensor	Weather Station
Model	200WX
Serial Number	3466863
Calibration Date	12/23/2015
Sample Rate [s]	300

Table 4.10: Tower WS Instrument Specifications

4.6.2 TWS Data Guide

The instrument has been continuously deployed since at least July of 2017. During the Fall 2021 measurement campaign data was collected from 10/12/2021 to 11/30/2021. On 11/30/2021 an error occurred with the connection to the weather station and the shark meter that prevented any further data collection from either instrument. The weather station reports wind direction relative to the orientation of the device and without the use of an internal compass. It is possible some damage has occurred overtime resulting in the loss of GPS location and compass orientation data strings sent from the instrument. At the time of the writing of this thesis it was unclear the orientation of the weather station, rendering the

wind directional data meaningless, until the sensor orientation can be verified with respect to a known heading angle. It is a challenge to access this sensor due to its location on top of the bridge tower.

4.6.3 TWS Data QC

The tower weather station data set was carefully reviewed for accuracy of variable names and units. No additional QC tests were performed to remove erroneous data points from the data set. Additional information regarding Tower Weather Station data processing can be found in [69].

CHAPTER 5

Results and Discussion

An overview of the results from the Fall 2021 grid-synchronous performance and load measurement campaign are given in Figure 5.1 to highlight the four distinct data sets obtained. The specifications of the turbine under test are given as a 4-blade, clockwise rotating, New Energy vertical axis cross flow turbine with diameter ($D = 3.2m$), blade length ($= 1.7m$), blade chord ($= 10in$), NACA profile ($= 0021$), and blade preset pitch angle, ($\beta = +4°$). The following results were selected to highlight the capabilities of this test site to complete TEC performance testing.

5.1 Overview of Measurements

Figure 5.1 presents an overview of the ≈65 days of the data collection reported in this thesis. The IEC TS 62600-200 refers to this as a Test Log. A complete Test Log is available in Appendix K. The columns are individual days during the deployment with rows corresponding to each instruments availability. The top row indicates the operating status of the turbine, (blue) if it is operating freely to synchronize with the grid, or (P) for partial day of operation or (-) for no operation. The four main data sets are framed within the timeline indicating the number of days where the various instruments were operating together. Note the main data set of more than 29 days of turbine performance (electrical power) and ADCP (tidal resource) spans 44 calendar days between 10/12/21 and 11/24/21 which coincide with data set objective 1. Objective 1 was a continuous data set of electrical power vs tidal current resource over a lunar month. This was not completely satisfied, as there were interruptions

in turbine operation over the 44 days. Objectives 2 and 3 were to investigate how large flow structures in the estuary affect thrust loading and power performance respectively. The data collected to meet these objectives was obtained from 11/10-11/24/21 with over 7 days of usable data collected. An important note is the Voltsys rectifier data stream rate was increased from 1Hz to 5Hz at 11/18/21 15:27:38 UTC.

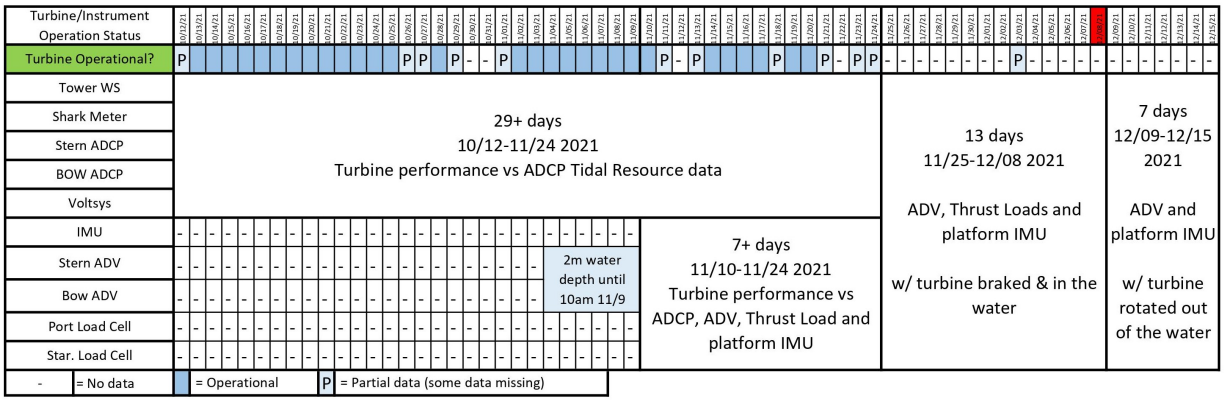

Figure 5.1: Test Log (simplified) - UNH TDP Fall 2021 (65day) Grid Synchronous Power Performance and Load Measurement Campaign

After 11/24/21 the system was no longer able to reliably synchronize to the grid likely due to inverter failure (subsection 4.4.2). From 11/25-12/8/21 the turbine remained deployed in the water with the electric brake engaged, keeping the rotor from spinning. This time frame provides an interesting data set with drag measurements on the stalled turbine vs ADV inflow data and platform motion. The final data set from 12/9-12/15/21 includes ADV and platform motion data with the turbine rotated out of the water.

The data collection for concurrent grid-synchronous power, thrust force and tidal resource measurements occurred during an intermediate range of tidal current velocities (slower than the fastest velocities measured during the experiments), as can be seen in Figure 5.2 showing bow ADCP measurements during ebb tidal flows to indicate the range of data available for analysis in this section. The data collection for concurrent grid-synchronous power, thrust force and tidal resource measurements occurred between 11/10-11/24/21, between the green and red vertical line in Figure 5.2. The range of missing Bow ADCP data between 10/15-

10/21 was previously discussed in subsection 4.2.5.

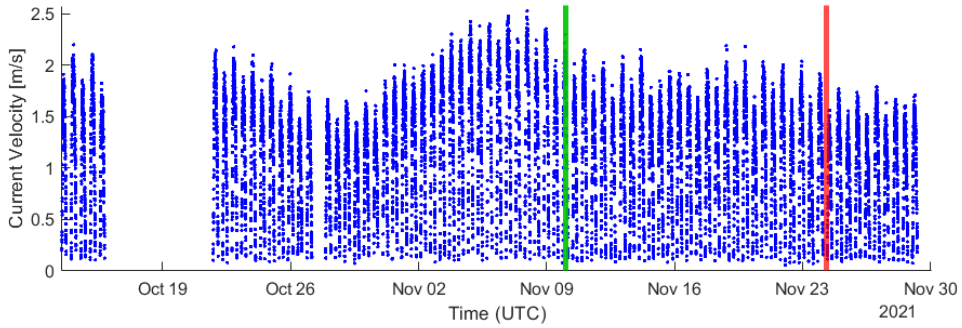

Figure 5.2: Tidal current resource | Bow ADCP Ebb tide data only | 10/13/21 and 11/30/21. The range of available grid synchronous power production, thrust force and tidal current resource data is indicated with vertical lines between 11/10/21 and 11/24/21

.

5.2 Tidal Current Resource

5.2.1 Bow ADCP and ADV Comparison

Figure 5.3 presents the tidal velocity data decomposed into horizontal velocity magnitude and direction from the Bow ADCP (blue) and ADV (red) instruments for ebb tides between 11/10/21 to 11/23/21. Both data sets were filtered to select velocities greater than 1m/s to coincide with turbine operational conditions. The bridge pier/platform heading $(--)$ is plotted as a reference. True North coincides with to 0° and East 90°. The ADCP is located in line with the rotor shaft and the ADV $\approx$ 20in to port with measurement volume aligned with the depth of the center of the turbine blades. The 16Hz ADV data was averaged over 60s intervals and the ADCP data is the weighted average of the 0.25m bins that span the depth range of the turbine blades, bins 0,1,2,3,4 & 5. The average velocity magnitude and direction of the data is shown in yellow for the ADCP(blue) and white for the ADV(red).

These results indicate relative agreement in mean velocity, 1.52m/s (ADCP) and 1.56m/s (ADV), with notable deviation in direction, 122.6° (ADCP) and 130.3°(ADV). The difference between ADCP and ADV average direction is likely in part due to the different sampling

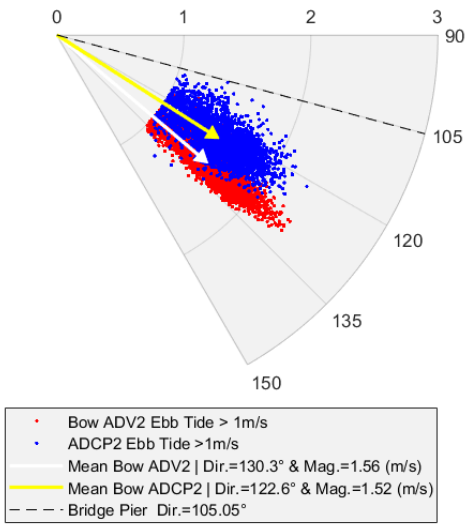

Figure 5.3: Tidal current resource measured at bow of TDP with ADCP and ADV, with average flow angles compared to pier alignment collected between 11/10/21 and 11/23/21. Bow ADCP & ADV ebb ride data only selected for velocities exceeding 1m/s. ADCP data is weighted average of 0.25m bin size spanning turbine blade depth in water column. North = 0° ‖ East = 90°. ADV **N** = 5818 ‖ ADCP **N** = 3069

volumes measured by each instrument. A more rigorous analysis would be to calculate the velocity direction from each ADCP beam radial velocity to see how much variation in direction there is between each of the 4 ADCP beams. The along beam velocity data, required for this analysis, is not recorded when the ADCP's are connected to the LB-DAS but are available in the raw FQ recorded to the instrument. Both instruments capture the misalignment between the average flow direction and the pier, which will cause a separated shear layer to develop. A separated shear layer will grow from the leading edge of the pier outward (perpendicular to the direction of the flow). This shear layer possibly could extend into the moon pool and affect turbine performance. Note that this shear layer was the reason for selecting a clockwise-rotating cross-flow turbine.

5.2.2 Bow and Stern ADCP Depth Profile

Figure 5.4 presents the inflow and wake profiles recorded with the platform-mounted ADCP'S. Figure 4.8 depicts the deployment orientation of the ADCP's, for an ebb tide the bow ADCP

measures inflow, and the stern ADCP measures the turbine wake, and/or flow separation from the bridge pier. For a flood tide, the stern ADCP measures inflow, and the bow ADCP measures the turbine wake. In Figure 5.4, the 1-hour time averaged ADCP horizontal velocity at each 0.25m depth bin during peak tidal current in an flood tide (+) and subsequent ebb tide (−) is shown. When first analyzing this plot it is best to imaging a vertical line between the center of both plots, separating ebb (left, -) and flood (right, +) events.

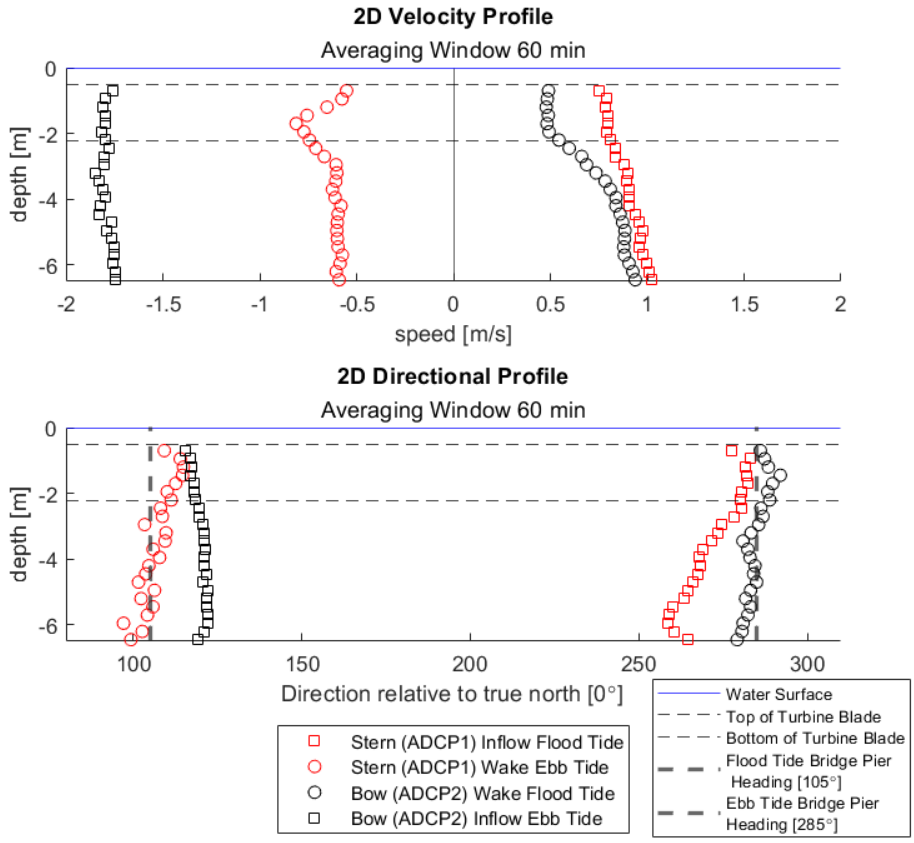

Figure 5.4: ADCP tidal current resource measurements on bow and stern of TDP. Velocity magnitude [Top] and direction [Bottom]. Plotted is the 60 min average of horizontal velocity magnitude, from the 2 minute ensemble averages for each depth bin during a peak flood tidal flow (10/14/21 21:57 to 22:57 UTC) and subsequent peak ebb tidal flow (10/15/21 02:57 to 03:57 UTC). The turbine was operating as expected, synchronized during the ebb tide and free spinning on the flood.

Figure 5.4 flood tide observations

The right side (flood) shows the inflow velocity profile, in red squares, from the stern ADCP1,

1.8 diameters (5.72 m) upstream of the turbine axis, and the wake profile, in black circles, from the bow ADCP2, 2.3 diameters (7.23 m) downstream of the turbine axis. Note, the turbine is rotating during the flood tide but not synchronized to the grid due to insufficient tidal current velocities. Viewing the right side of the top plot, the bow ACDP shows a velocity deficit, of nearly 0.5m/s, due to the turbine wake and wake spreading below the turbine down to about 4 m depth. Below this depth, flows measured by both ADCP's are approximately the same indicating the flow is consistent under the platform over the water column during flood tides. Viewing the right side of the bottom plot, with the same color and symbols as before, there is a tendency of the flow to align itself with the pier, vertical dashed line, over the length of the platform, red (inflow) and black (wake).

Figure 5.4 ebb tide observations

The left side of the top plot (ebb) shows the inflow velocity profile, in black squares, from the bow ADCP2, 2.3 diameters (7.23 m) upstream of the turbine, and the wake profile, in red circles, from the stern ADCP1, 1.8 diameters (5.72 m) downstream of the turbine. Note the turbine is rotating and synchronized to the grid during the ebb tide. The inflow profile (black square) and the downstream velocity profile (red circle) are significantly different over the entire water column. This is due to flow separation from the bridge pier introduced in Figure 5.3. The stern ADCP measures flow velocities inside a separated shear layer, with magnitudes much lower than what would be expected in the turbine wake due to energy extraction by the tidal turbine alone. Viewing the left side of the bottom plot, there is still a tendency of the flow to align itself with the pier over the length of the platform, black (inflow) and red (wake), even within the separated shear layer.

The ADCP's are located at either end of the platform and from this data, cannot discern how far this flow separation extends in the direction perpendicular from the bridge pier at the turbine energy extraction plane. If the separated shear layer reaches the turbine it will affect power production, thrust loading and turbine efficiency estimates which utilize these inflow velocity measurements.

5.3 Turbine Power

This section presents data collected during typical turbine operation through the ebb portion of the tidal signal:(1) the tidal velocity ramping up and the turbine synchronizing to the grid,(2) typical grid-connected operation, and (3) ramping down to a stop during slack tide (low tide). Power performance plots are presented including data filtered for grid synchronous operation, ebb tide data only, collected during the 29 days over a 44-day period between 10/12/21 and 11/24/21.

To preface the following plots in this section. The ADCP data presented is the horizontal velocity magnitude from the bow location and only during times when the turbine was synchronized to the grid. The values are the average of the 2min ensemble data from the 0.25m bins that encompass the turbine blade height. The electrical power and shaft speed data, collected from the Voltsys rectifier at 1Hz, was averaged over each 2min ensemble timeframe in which the ADCP was collecting data. The timeframe selected accounts for the spatial offset between the Bow ADCP and the turbine energy extraction plain (7.16m). For example, for a 1 m/s tidal current, the time window was adjusted by 7.16 seconds, for a 2 m/s tidal current, the time window was adjusted by 3.58 seconds, etc. which was applied as a time shift in the raw turbine data selected for averaging.

Note: that the IEC TS 62600-200 *Power Performance Assessment of Electricity Producing Tidal Energy Converters* does not prescribe how to account for the spatial and corresponding time offset between tidal current measurements, that is located at some distance from the tidal turbine, it only prescribes where the instrument should be placed (2-5 turbine diameters upstream of the turbine plane, and other criteria).

5.3.1 Ramp Up

Figure 5.5 presents ≈30 minutes of flow and turbine data for a typical "Ramp Up" sequence to grid synchronization during an ebb tide, on November 15, 2021. ADCP data at the bow

location is averaged over the turbine height using data from bins encompassing the turbine swept area in 2 minute ensemble averages (Fig 5.5a). ADCP data is only plotted after the turbine synchronized to the grid. Bow ADV data at turbine center depth is shown in 1 minute averages (Fig 5.5b). Raw 1Hz turbine shaft speed (black dot) and 2 minute moving average (blue square), are shown in (Fig 5.5c), Raw 1Hz turbine electrical power (black dot) and 2minute moving average (blue diamond), are shown in (Fig 5.5d). The moving average of shaft speed and electrical power data accounts for the advection of the flow from the ADCP to the turbine energy extraction plane as described in section 5.3. The data with blue symbols in plots a, c and d are synchronized in time, and shown in 2-minute averages after the turbine has synchronized to the grid.

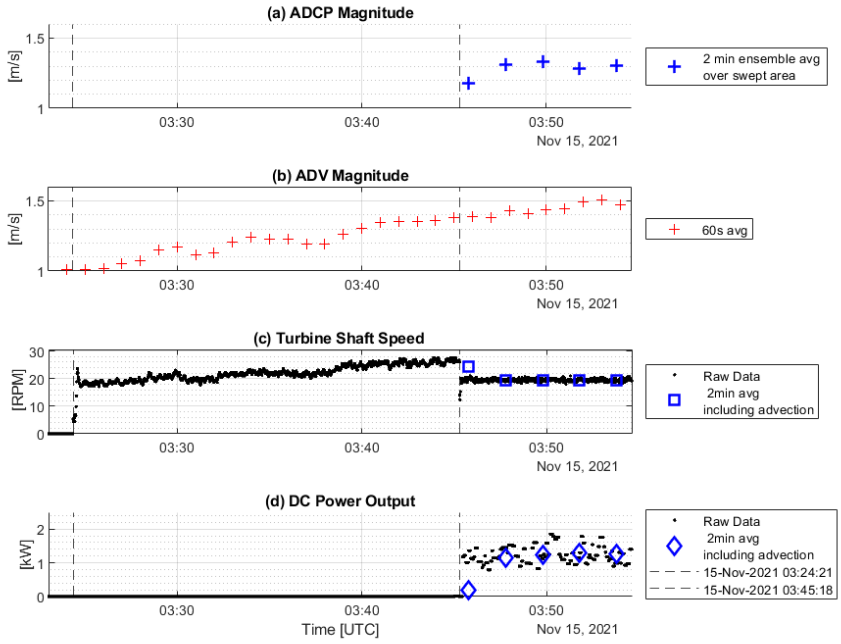

Figure 5.5: Turbine "Ramp Up" sequence to grid-synchronized operation. (a) Bow ADCP 2-D velocity magnitude averaged over bins covering turbine swept area (after grid sync only). (b) Bow ADV 2-D velocity magnitude at ≈centerline of turbine swept area, 16Hz data averaged over 60s. (c) Turbine shaft speed, raw 1Hz data (black dot) and 2min moving average (blue). (d) Rectifier DC power output, raw 1Hz data (black dot) and 2min moving average (blue). The data with blue symbols are synchronized in time with the turbine shaft speed and DC power output data selected to account for velocity advection of flow measured by the ADCP to the turbine energy extraction plane.

It can be seen that the turbine "cuts in", i.e., begins to rotate, when averaged ADV flow speed reaches ≈1m/s at 03:24, and that it synchronizes to the grid when average ADCP flow speed reaches ≈1.2m/s at 03:45 (Fig 5.5c). It is important to note there is a mandatory 5min wait period after the minimum DC voltage is supplied to the inverter prior to synchronization. It is observed that turbine shaft speed is significantly higher (27RPM), prior to synchronization (20RPM), which is caused by the turbine generator lacking an electrical load. Correspondingly, the rectifier DC power output is zero until the turbine synchronizes to the grid (Fig 5.5d).

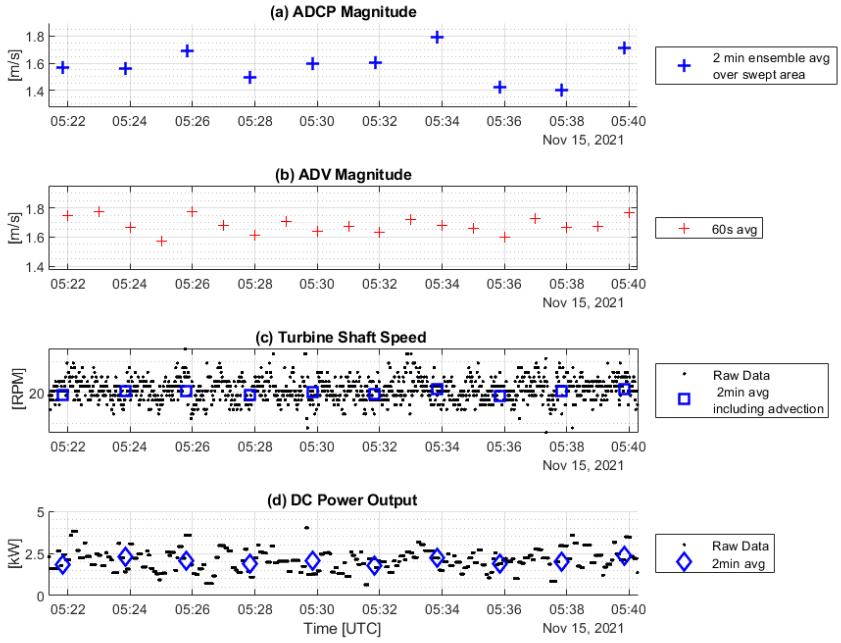

Figure 5.6: Turbine "steady" operation during an ebb tide on November 15, 2021 in grid-synchronous mode. (a) Bow ADCP 2-D velocity magnitude averaged over bins covering turbine swept area (after grid sync only). (b) Bow ADV 2-D velocity magnitude at ≈centerline of turbine swept area, 16Hz data averaged over 60s. (c) Turbine shaft speed, raw 1Hz data (black dot) and 2min moving average (blue). (d) Rectifier DC power output, raw 1Hz data (black dot) and 2min moving average (blue). The data with blue symbols are synchronized in time with the turbine shaft speed and DC power output data selected to account for velocity advection of flow measured by the ADCP to the turbine energy extraction plane.

5.3.2 Mid Ebb Tide

Figure 5.6 presents the turbine operating over a ≈25 minute window during the middle of the ebb tide on November 15, 2021. ADCP, ADV, turbine shaft speed and electrical power data is presented in the same manor as Fig 5.5. Figure 5.6 illustrates the signal variability in measured shaft speed and power output while synchronized to the grid compared to inflow tidal current resource. The shaft speed data primarily oscillates between 19-21RPM, shown here in Figure 5.6c. The DC power output signal is noticeably less variable than the shaft speed data, this is partially due to the capacitors used in the power rectification process. Between 05:32 and 05:34 an increase in flow, was measured by the ADCP and ADV, a corresponding increases in shaft speed and power output are observed.

5.3.3 Ramp Down

Figure 5.7 presents approximately 75 minutes of tidal resource and turbine data for a typical operating "Ramp Down" sequence at the end of the ebb tide on 11/15/21, the same ebb tide presented in Fig 5.5 & Fig 5.6. During ramp down the turbine is no longer capable of supplying the minimum voltage to the inverter which results in breaking grid synchronization followed by full rotor stop "cut out". ADCP, ADV, turbine shaft speed and electrical power data is presented in the same manor as Fig 5.5.

Figure 5.7 illustrates the grid synchronization "cuts out" at an average ADV and ADCP flow velocity less than 1 m/s at 7:49:45 in Fig 5.7(b). This is marked by the power output dropping to 0kW in Fig 5.7(d). Once the averaged ADV measurement reach ≈0.5 m/s at 08:23:33 the rotor stop rotating altogether. It is observed that turbine shaft speed is more variable after grid synchronization is broken and can freely respond to to changes in inflow velocity without the electrical load present.

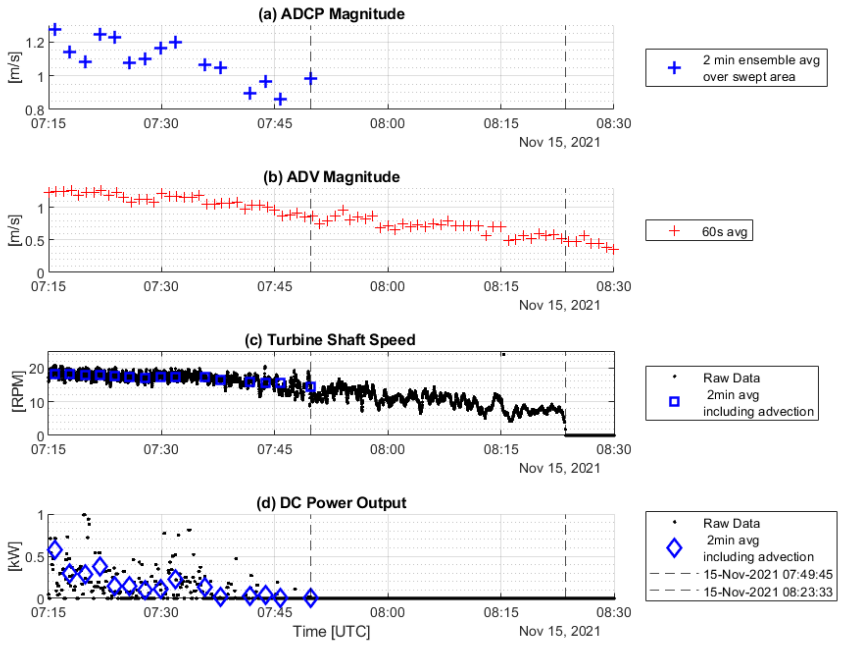

Figure 5.7: Turbine "Ramp Down" sequence of events including the turbine breaking synchronization and stopping rotation, prior to low tide. (a) Bow ADCP 2-D velocity magnitude averaged over bins covering turbine swept area (corresponding with grid sync only). (b) Bow ADV 2-D velocity magnitude at ≈centerline of turbine swept area, 16Hz data averaged over 60s. (c) Turbine shaft speed, raw 1Hz data (black dot) and 2min moving average (blue). (d) Rectifier DC power output, raw 1Hz data (black dot) and 2min moving average (blue). The data with blue symbols are synchronized in time with the turbine shaft speed and DC power output data selected to account for velocity advection of flow measured by the ADCP to the turbine energy extraction plane.

5.3.4 Power Curve (dimensional)

Figure 5.8 shows turbine power output vs tidal current velocity (blue) with 2-minute ensemble averages for grid-synchronized operation data only collected during 29 days over a 44-day period between 10/12/21 and 11/24/21. The ADCP data selected was the same as previously described in section 5.3. The moving average of shaft speed and electrical power data accounts for the advection of the flow from the ADCP to the turbine energy extraction plane as described in section 5.3. The black dashed curve presents the NECI power curve for the D =3.4m model which is the input model for the Voltsys rectifier connected to the D =3.2m model tested in this study. The red dashed curve is a least square fit applied to

the data set in blue. The black stars are the averaged power values (blue), averaged over 0.05m/s intervals. Velocity bins between bin (1.00-1.05) and bin (2.05-2.10) all included a minimum of 100 data points available to compute the average. The histogram presents the number of data points available in each velocity interval for averaging as a % of the total # of data points (blue). The green & yellow dashed curves are the constant C_p power curves for the $D = 3.4$m and $D = 3.2$m respectively, illustrating the expected cubic relationship between power and velocity.

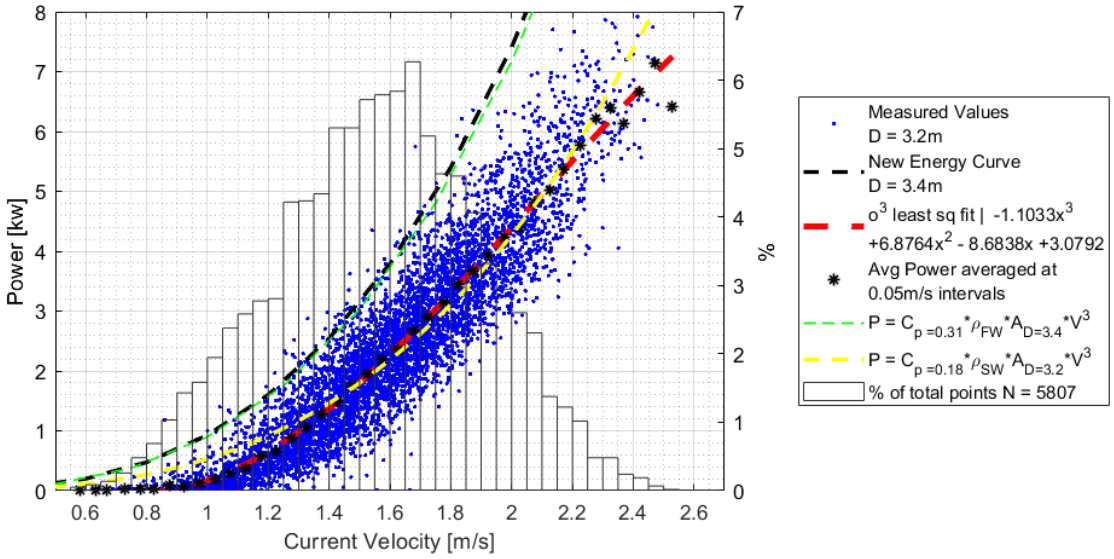

Figure 5.8: DC power output vs tidal current resource (blue). Ebb tide data while turbine was grid synchronized only, collected between 10/13/21 and 11/24/21 with $N_{points} = 5806$. Bow ADCP 2-D velocity magnitude averaged over bins covering turbine swept area. Turbine power and shaft speed, raw 1Hz data was averaged over 2 min time windows selected to account for velocity advection of flow measured by the ADCP to the turbine energy extraction plane. Black dashed curve represents the New Energy power curve for D =3.4m model. Red dashed curve is the o^3 least square fit applied to the data (blue) with polynomial coefficients$-1.1033, 6.8764, -8.6838, \&3.0792$. Black stars are averages of the data (blue) binned in 0.05 m/s velocity intervals and plotted at the average velocity within the bin. The number of data points available in each velocity interval for averaging is plotted as a % of total points in the histogram. Green & yellow dashed lines are the constant C_p power curves for the $D = 3.4$m and $D = 3.2$m respectively Equation 1.2. Note the turbine tested was D =3.2m diameter and is expected to have reduced performance.

The cut out speed,≈1m/s, from synchronization is lower than cut in of ≈1.2m/s. It is this period before cut out that power performance data below 1.2m/s is derived from. After

grid synchronization the power data appears to approximately follow a cubic relationship w.r.t. tidal current velocity. The average data slightly out performs the model estimate at speeds between 1.6-2.1m/s and under performs, more noticeably, outside this region. This can partially be explained by the non uniform device performance expected at different tip speed ratios shown in Figure 5.10. Note that there is some scatter in the average data (black star) at higher tidal current speeds because there are less data points that are averaged over. This will have an impact on the results that can be concluded at higher velocities above 2.1m/s where less than 100 data points were available to average. The maximum average power (black stars) was 7.15 kW at 2.47 m/s. The maximum 2-min ensemble average of power (blue dots) observed was 8.2 kW at 2.2 m/s. Tidal current velocity and power fluctuated over shorter time scales, and the highest instantaneous power measured during the deployment period was 18 kW.

5.3.5 Power Coefficient vs Velocity

Figure 5.9 presents non-dimensional power coefficient C_p vs tidal current velocity (blue) with 2-minute ensemble averages for grid-synchronized operation collected during 29 days over a 44-day period between 10/12/21 and 11/24/21. As with the ADCP data reported above, each time window used to select power data for averaging was adjusted slightly to account for the advection of the flow from the ADCP instrument location to the turbine energy extraction plane. The dashed black line indicates the derived C_p from the New Energy power curve for the D =3.4m model. The red stars are average C_p values in 0.05m/s velocity bins. The histogram presents the number of data points available in each velocity interval for averaging as a % of the total # of data points (blue).

Figure 5.9 provides a useful comparison between the constant C_p, used for the controller power curve and the C_p derived from the measurements over this range of velocities. Maximum average C_p, which can be comparable to "water to wire" rotor efficiency, was 0.204 at 1.66m/s with efficiencies greater than 0.2 in the range of 1.57-1.90m/s. The maximum

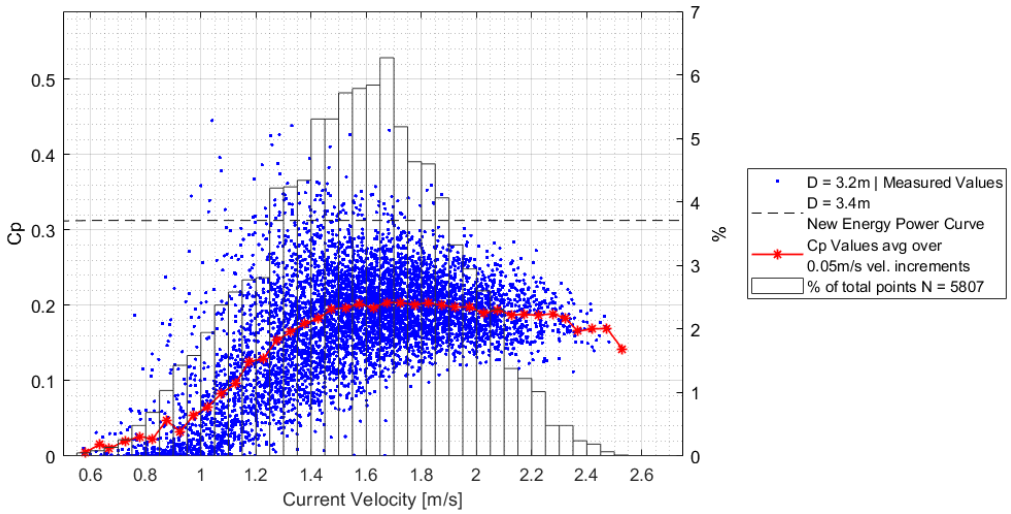

Figure 5.9: Power coefficient C_p vs tidal current resource (blue). Ebb tide data while turbine was grid synchronized only, collected between 10/13/21 and 11/24/21 with $N_{points} = 5807$. Bow ADCP 2-D velocity magnitude averaged over bins covering turbine swept area. Turbine power and shaft speed, raw 1Hz data was averaged over 2 min time windows selected to account for velocity advection of flow measured by the ADCP to the turbine energy extraction plane. The dashed line represents the C_p values determined from the D =3.4m NECI power curve. The blue data indicates the C_p values determined from the measured electrical power data using Equation 1.3. The red stars are the C_p values (blue) averaged over 0.05m/s velocity intervals. The number of data points available in each velocity interval for averaging is plotted as a % of total points in the histogram. Note the turbine tested was D =3.2m diameter and is expected to have reduced performance.

2-min ensemble average of C_p (blue dots) observed was 0.445 at 1.05 m/s. Note the average C_p remains greater than 0.18 for velocities $> 1.4m/s$ and $< 2.3m/s$ which account for over 70% of the data points presented here.

5.3.6 Power Curve (non-dimensional)

Figure 5.10 presents the data shown in Figure 5.8 in dimensionless form, non-dimensional power, or *power coefficient* C_p vs non dimensional rate of rotation, or *tip speed ratio* λ (blue) with 2-minute ensemble averages for grid-synchronized operation collected during 29 days over a 44-day period between 10/12/21 and 11/24/21. As with the ADCP data reported above, each time window used to select power data for averaging was adjusted slightly to account for the advection of the flow from the ADCP instrument location to the turbine

energy extraction plane. C_p values averaged over 0.05λ intervals are plotted (red star). The histogram presents the number of data points available in each TSR interval for averaging as a % of the total # of data points (blue).

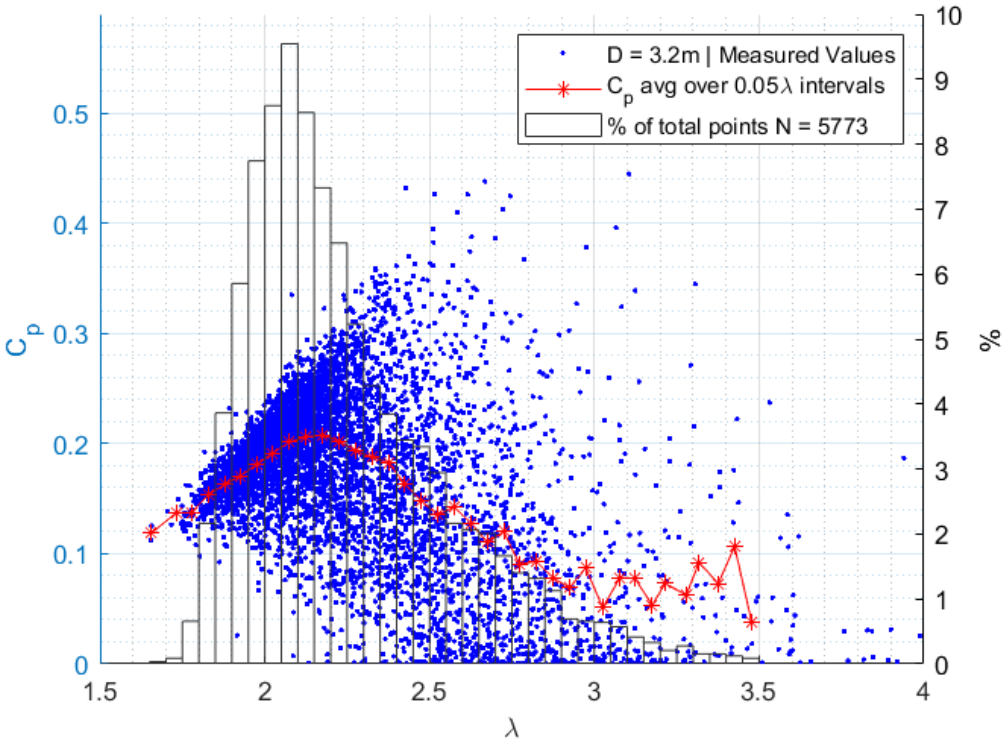

Figure 5.10: Power coefficient C_p vs Tip speed ratio λ (blue). Ebb tide data while turbine was grid synchronized only, collected between 10/13/21 and 11/24/21 with $N_{points} = 5773$. Bow ADCP 2-D velocity magnitude averaged over bins covering turbine swept area. Turbine power data (electrical power and shaft speed), raw 1Hz data was averaged over 2 min time windows selected to account for velocity advection of flow measured by the ADCP to the turbine energy extraction plane. The red stars are the C_p values (blue) averaged over 0.05λ intervals. The number of data points available in each TSR interval for averaging is plotted as a % of total points in the histogram.

Average C_p maximized at C_p =0.208 and λ =2.17 coinciding with a shaft speed of 21 RPM. The average C_p remains greater than 0.18 for $\lambda > 1.95$ and $\lambda < 2.4$ which account for over 60% of the data points presented here. Additionally, the TSR bins between 1.85 and 2.7 contained over 100 data points in each average and account for nearly 90% of the data reported here. This is a typical shape of a C_p vs λ curve indicating the relationship between

power coefficient and *tip speed ratio*. This shows importance of accurate tidal current resource characterization prior to turbine design/selection in order to maximize rotor efficiency. The maximum average C_p does not occur in the most frequent operating tip speed ratio band of 2.05-2.10λ, representing a slight reduction in overall TEC efficiency.

5.4 Turbine Thrust Force

Turbine thrust force measurements are important to determine the loading requirements when designing the turbine support structure. Here the thrust force developed by the turbine rotor parallel to the platform (bow to stern) is measured indirectly via moment arms on the turbine pitching mechanism and two load cells, as described in section 4.1. Cross-flow turbines also develop a smaller lateral force, however, this force is not measured with the present setup. The thrust force of a turbine typically increases monotonically with its rate of rotation, and the thrust force of a rotating turbine rotor is typically much larger than that of a stopped rotor.

5.4.1 Thrust Force Ramp Up

Figure 5.11 shows an ebb tide flow ramping up. The turbine begins to rotate before 18:30, (Figure 5.11b), when the tidal current reaches 1 m/s (Figure 5.11a). A correspond steep ramp can be observed in the thrust force measurement (Figure 5.11d). Figure 5.11e shows the corresponding thrust coefficient C_t, i.e., non-dimensional thrust calculated from the ADCP (a) and thrust force (d) data sets using Equation 1.4. Figure 5.11c & (d) show a strong relationship between thrust force and power output after synchronization, for example a coinciding "dip" in both time series is observed after 18:45. It can be seen that the turbine shaft speed drops slightly after synchronization around 18:36, since there is now a load on the generator. Additionally, the rate of change of thrust force (d) is observed to increase after synchronization around 18:36, corresponding with the increase in fluid velocity but also a reduction in shaft speed.

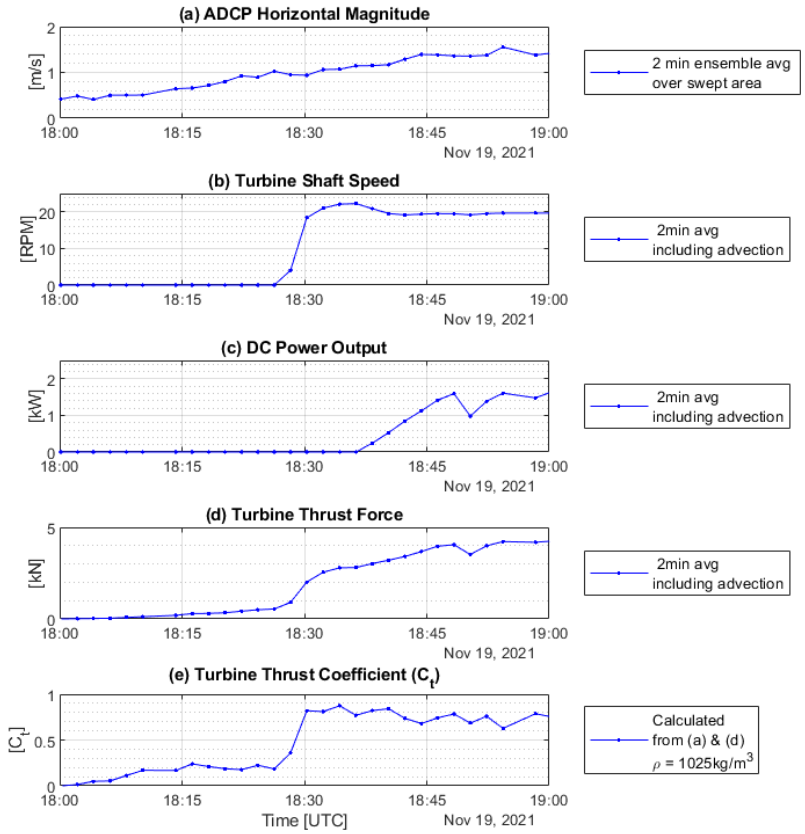

Figure 5.11: Turbine thrust force, example of a "Ramp Up" event with turbine rotor cut in, i.e. starts rotating, and subsequent jump in thrust force. (a) Bow ADCP 2-D velocity magnitude averaged over bins covering turbine swept area (ebb tide only). (b) Turbine shaft speed, raw 1Hz data averaged over 2min, accounting for advection. (c) Rectifier DC power Output, raw 1Hz data averaged over 2min, accounting for advection. (d) Turbine thrust force raw 100Hz data averaged over 2min, accounting for advection. (e) Thrust coefficient C_t calculated from ADCP and averaged thrust data.

5.4.2 Thrust Force - Operating vs Stopped Turbine

Figure 5.12 shows two subsequent ebb portions of the tidal cycle, first, with the turbine operating grid-synchronized, second, with the turbine failing to properly grid-synchronize, coinciding with the rotor being braked. The thrust forces and thrust coefficients for the second cycle are much lower than for the first. Turbine rotation and the attempt to synchronize can be briefly observed for the second cycle as thrust force and thrust coefficient briefly increase, and then drop back to lower, non-rotating values.

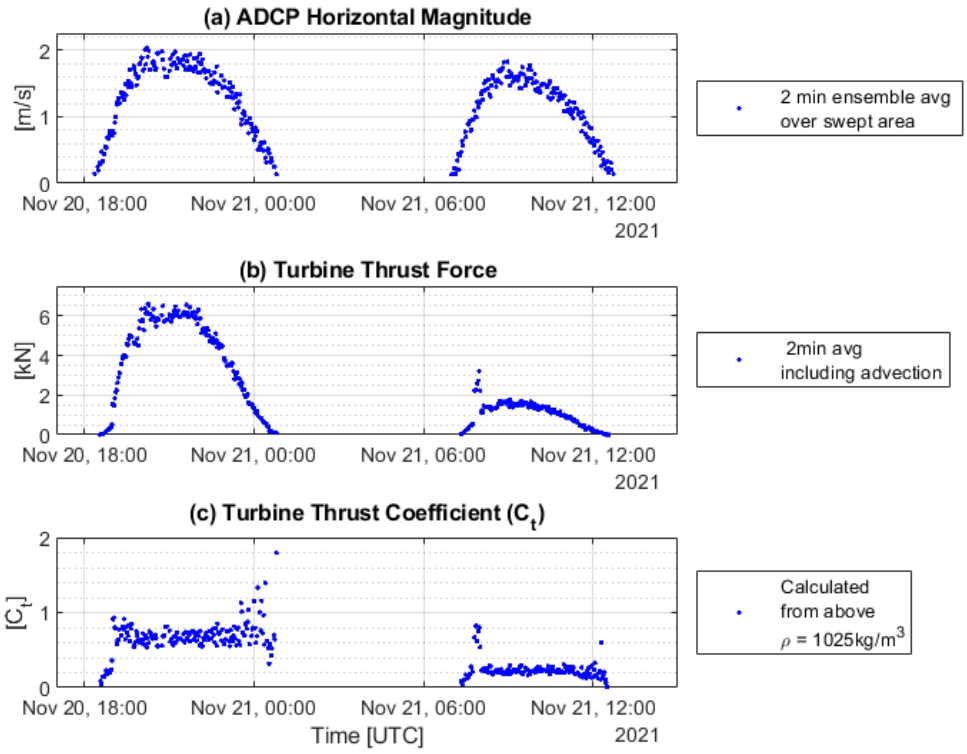

Figure 5.12: Two subsequent ebb tides when the turbine is synchronized to the grid [Left] and braked [Right] (due to inverter malfunction). A jump in thrust coefficient is observed followed by a decrease meaning the brake was engaged due to the fault. (a) Bow ADCP 2-D velocity magnitude averaged over bins covering turbine swept area (ebb tide only). (b) Turbine thrust force. (c) Thrust coefficient C_t calculated from avg. ADCP and thrust data.

5.4.3 Thrust Force vs Velocity (dimensional)

Figure 5.13 presents turbine thrust force vs tidal current velocity (blue) with 2-minute ensemble averages for grid-synchronized operation data only collected between 11/10/21 and 11/24/21. The ADCP data selected was the same as previously described in section 5.3. The 2min moving average of thrust data accounts for the advection of the flow from the ADCP to the turbine energy extraction plane as described in section 5.3. The red dashed curve is a least square fit applied to the data set in blue. The black stars are the averaged thrust values (blue), averaged over 0.05m/s intervals. The histogram presents the number of data points available in each velocity interval for averaging as a % of the total # of data points (blue). The yellow dashed curves is the constant $C_t = 0.65$ thrust curve for the $D = 3.2$m.

Figure 5.13 indicates the deviation between theoretical and experimentally determined thrust force as a function of inflow velocity. A maximum 2min average thrust force of 8.1kN was recorded, during an ebb tide while the turbine was grid synchronized. The maximum force coincided with an averaged inflow velocity of 2.3m/s, power output of 5.2kW and turbine shaft speed of 25 RPM on 11/10/2021 at 12:40:56am UTC. An average thrust force of 4.5kN was computed from the average values in the velocity bins (1.25-1.30) to (1.70-1.75), all containing a minimum of 100 data points for averaging which account for nearly 64% of the data reported here.

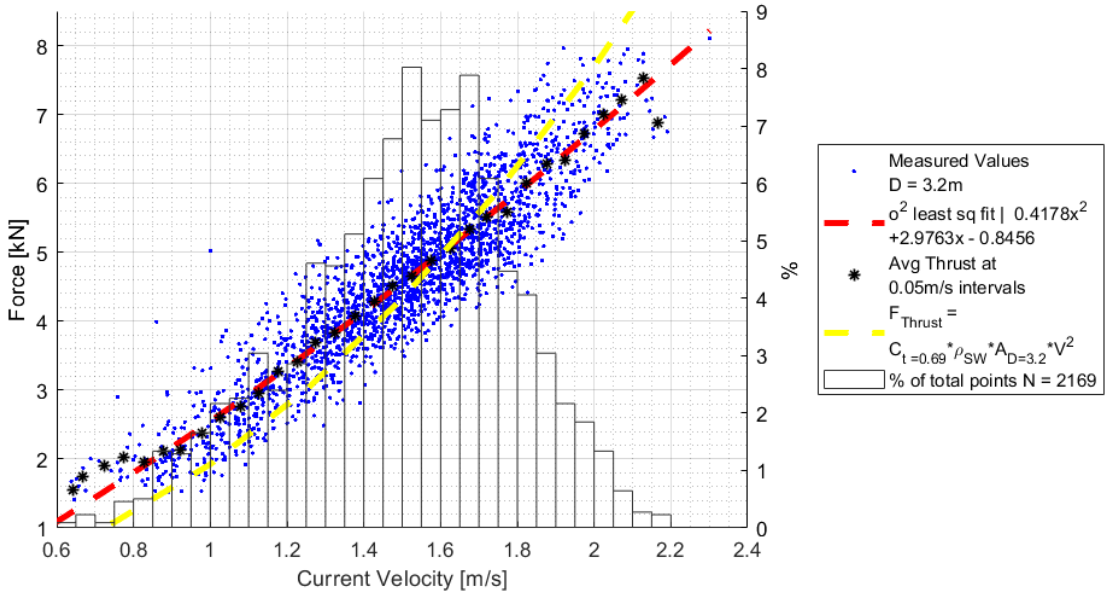

Figure 5.13: Thrust force vs tidal current resource (blue). Ebb tide data while turbine was grid synchronized only, collected between 11/10/21 and 11/24/21 with $N_{points} = 2169$. Bow ADCP 2-D velocity magnitude averaged over bins covering turbine swept area. Turbine thrust force, raw 100Hz data was averaged over 2 min time windows selected to account for velocity advection of flow measured by the ADCP to the turbine energy extraction plane. Red dashed curve is the o^2 least square fit applied to the data (blue) with polynomial coefficients in decending order $(0.4178, 2.9763, \& -0.8456)$. Black stars are averages of the data (blue) binned in 0.05 m/s velocity intervals and plotted at the average velocity within the bin. The number of data points available in each velocity interval for averaging is plotted as a % of total points in the histogram. Yellow dashed lines is a constant $C_t = 0.69$ thrust curve for the $D = 3.2$m turbine.

5.4.4 Thrust Force vs Velocity (Grid Synchronized & Stopped Turbine)

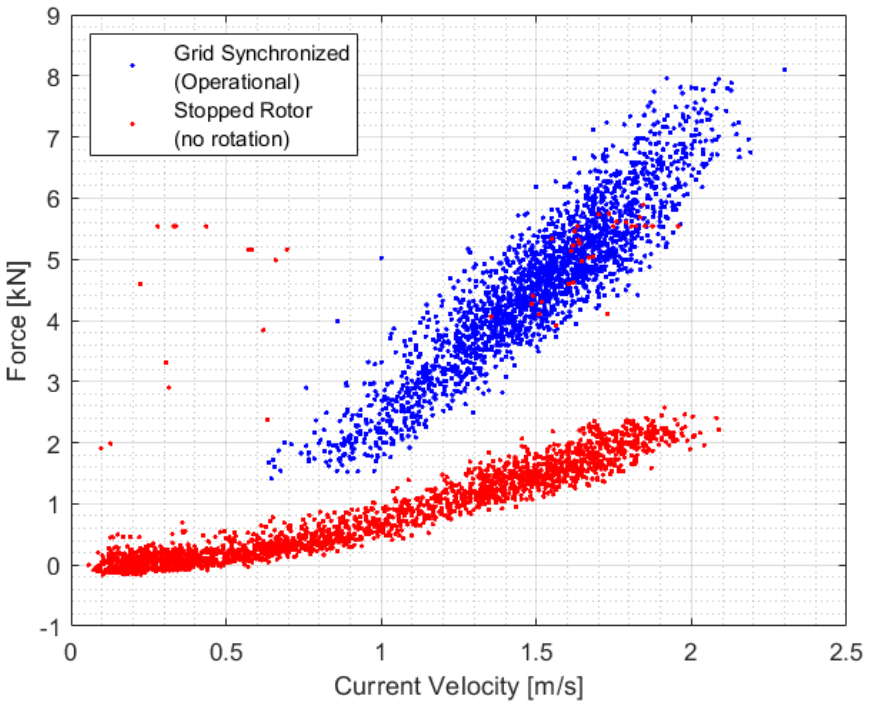

Figure 5.14: Thrust Force vs tidal current resource data collected between 11/10/21 and 11/24/21 during ebb tides only ‖ (blue) ebb tide data while turbine was grid synchronized only, N_{points} = 2169. ‖ (red) ebb tide data while turbine was not rotating (i.e. before rotation that preceeded synchronization and when the rotor was braked throughout an ebb tide), N_{points} = 2197. Bow ADCP 2-D velocity magnitude averaged over bins covering turbine swept area. Turbine thrust data, raw 100Hz data was averaged over 2 min time windows selected to account for velocity advection of flow measured by the ADCP to the turbine energy extraction plane.

Figure 5.14 presents the same turbine thrust force vs tidal current velocity (blue) in Figure 5.13 collected between 11/10/21 and 11/24/21 during ebb tides only. This data only includes points during times when the turbine was operating and grid synchronized. This figure does not include data for turbine rotation before synchronization (free-wheeling).

Figure 5.15 presents non-dimensional thrust force, or *thrust coefficient*, C_t, vs tidal current resource (blue) with 2-minute ensemble averages for grid-synchronized operation data only, collected between 11/10/21 and 11/24/21. The ADCP data selected was the same as previously described in section 5.3. The 2min moving average of the 100Hz thrust data

accounts for the advection of the flow from the ADCP to the turbine energy extraction plane as described in section 5.3. The red stars are the averaged thrust coefficient values (blue), averaged over 0.05m/s intervals. The histogram presents the number of data points available in each velocity interval for averaging as a % of the total # of data points (blue).

5.4.5 Thrust Coefficient C_t vs Velocity

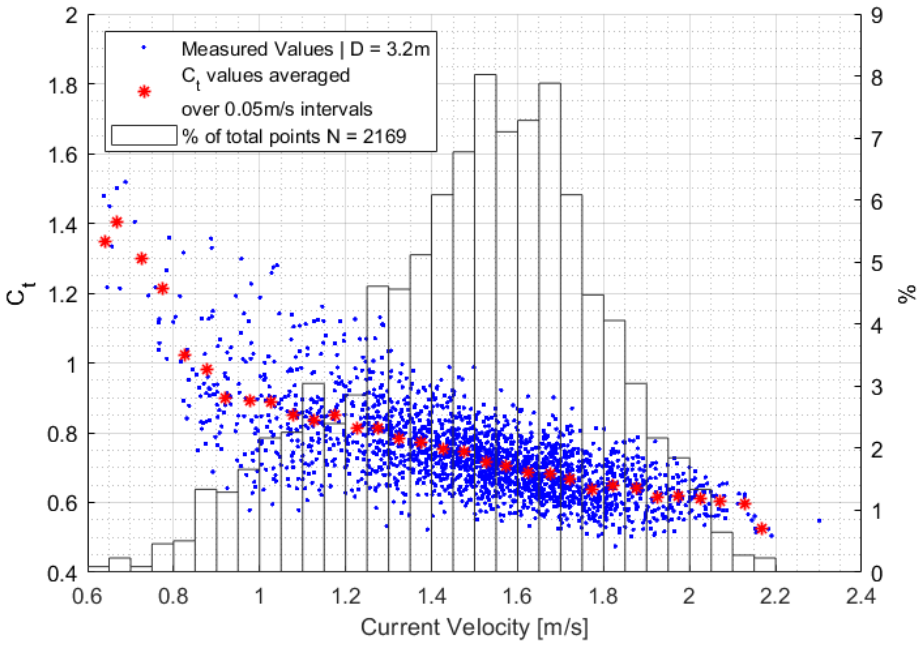

Figure 5.15: Thrust coefficient C_t vs tidal current resource || Ebb tide data while turbine was grid synchronized only, collected between 11/10/21 and 11/24/21 with $N_{points} = 2169$. Bow ADCP 2-D velocity magnitude averaged over bins covering turbine swept area. Turbine thrust data, raw 100Hz data was averaged over 2 min time windows selected to account for velocity advection of flow measured by the ADCP to the turbine energy extraction plane. Red stars indicate the average C_t calculated over 0.05 velocity intervals. The number of data points available in each velocity interval for averaging is plotted as a % of total points in the histogram.

Figure 5.15 illustrates a monotonically decreasing relationship between C_t and tidal current velocity. As turbine shaft speed increases there is an expected tendency for the turbine to behave more and more "solid" with a corresponding increase in C_t. The reduction in C_t, as a function of inflow velocity, in Figure 5.15 is due to the limited variation of 2min average

shaft angular velocity (3.2 to 3.4 rad/s) compared to more significant variations in inflow velocity (1.4 to 1.9 m/s) presented in Figure 5.16. This limited variations in shaft speed does not significantly affect the relative blockage the turbine presents to the flow. In turn the increase in rotor thrust force is primarily driven by the changes in inflow velocity, not shaft speed. This lack of shaft speed increase effectively lowers the relative blockage, C_t at higher flow rates.

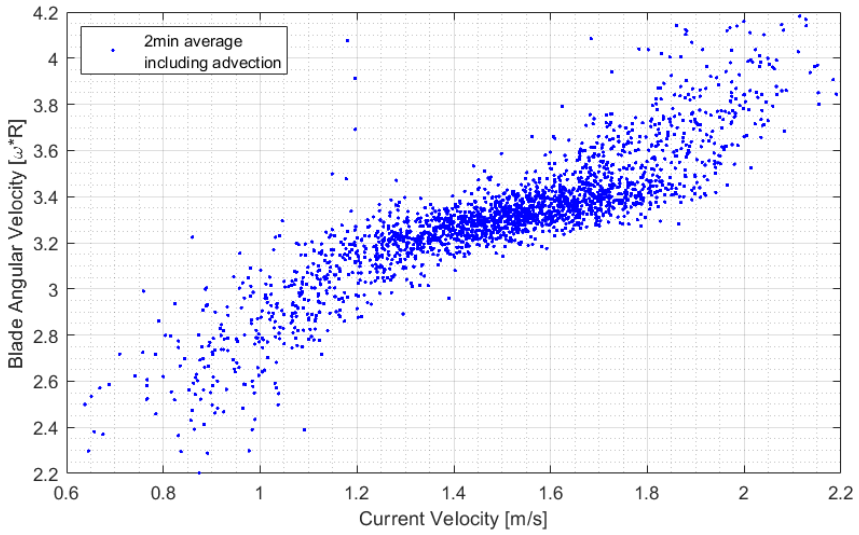

Figure 5.16: Turbine blade angular velocity $\omega * r$ vs tidal current resource || Ebb tide data while turbine was grid synchronized only, collected between 11/10/21 and 11/24/21 with $N_{points} = 2169$. Bow ADCP 2-D velocity magnitude averaged over bins covering turbine swept area. Turbine shaft speed data (used to calculated angular velocity), raw 1Hz data was averaged over 2 min time windows selected to account for velocity advection of flow measured by the ADCP to the turbine energy extraction plane.

5.4.6 Thrust Force vs Velocity (non-dimensional)

Figure 5.17 presents the data shown in Figure 5.13 in dimensionless form, non-dimensional thrust, or *thrust coefficient*, C_t, vs non dimensional rate of rotation, or *tip speed ratio*, λ, with 2-minute ensemble averages for grid-synchronized operation collected between 11/10/21 and 11/24/21. The ADCP data selected was the same as previously described in section 5.3. The 2min moving average of the 100Hz thrust data accounts for the advection of the flow from

the ADCP to the turbine energy extraction plane as described in section 5.3. The red stars are the averaged thrust values (blue), averaged over 0.05λ intervals. The number of data points available in each TSR interval for averaging is plotted as a % of total points in the histogram. The window has been zoomed slightly to highlight the trend over the majority of data points collected.

Figure 5.17 illustrates the expected monotonic relationship between C_t and λ. A mean C_t of 0.69 was computed from the average values from TSR bins (1.90-1.95) to (2.25-2.30) accounting for nearly 60% of the data reported here. These bins each contain over 100 data points available for averaging.

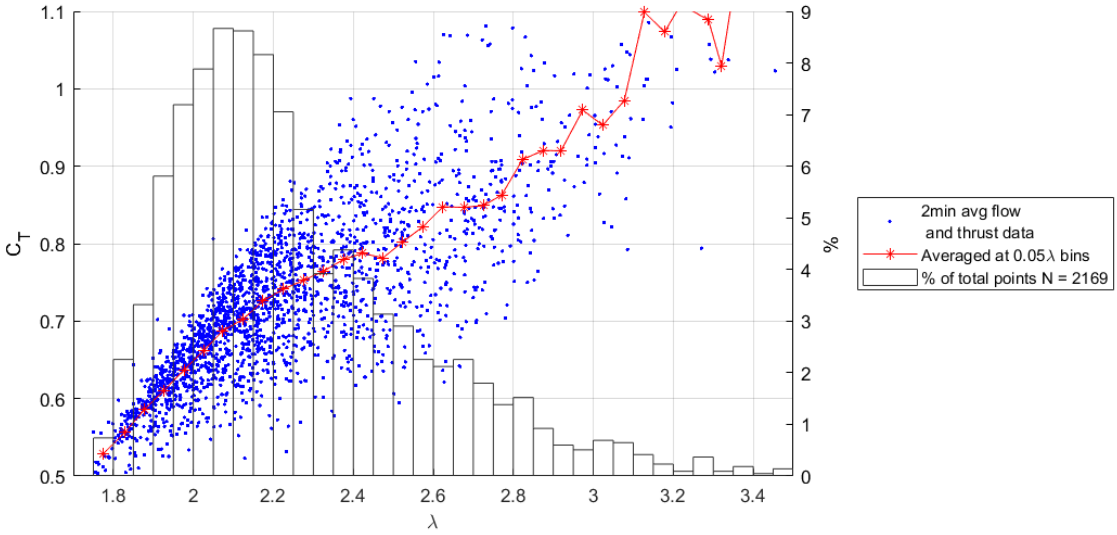

Figure 5.17: Thrust coefficient C_t vs tip speed ratio λ || Ebb tide data while turbine was grid synchronized only, collected between 11/10/21 and 11/24/21 with $N_{points} = 2169$. Bow ADCP 2-D velocity magnitude averaged over bins covering turbine swept area. Turbine thrust data, raw 100Hz data was averaged over 2 min time windows selected to account for velocity advection of flow measured by the ADCP to the turbine energy extraction plane. Red stars indicate the average C_t calculated over 0.05λ intervals.

5.5 Spectral Analysis of Time Series Data

This section presents frequency analysis performed on the time series data collected during this measurement campaign. Careful review and correction of missing time points in the

Shark meter data set were described in subsection 4.4.3 to prepare the data set for spectral analysis. This section seeks to provide insight on the large scale eddies that present "tidal gusts" to the turbine during operation as introduced by *Chancey 2019* [7]. Dominant flow structures were identified with integral time scales on the order of 10 to 100 seconds with the average length scale of 38.5m during ebb tides. Flow structures of these scales interacting with the turbine are sufficient to affect the power produced by the device.

Figure 5.18 presents the spectrum of the time series from six instruments measured during a 3-hour window while the turbine was operating synchronized to the grid on November 20, 2021. From top to bottom: Bow ADV data sampled at 16Hz, turbine shaft speed sampled at 5Hz, Shark meter apparent power sampled at 1Hz, thrust load data at 100Hz, & accelerometer data at 32Hz for$x$(along platform) direction (see Figure 4.21 for orientation on platform). For each time series, the spectrum was smoothed using a pre-whiten post color method with 50 degrees of freedom. The pre-whiten post color method was selected to limit the spectral "leakage" of low frequency energy into higher frequency bands. The number of ensembles is the number of times a time series is subdivided, the spectrum computed and then averaged. The number of ensembles selected was three to divide the record into equal 1 hour intervals. The spectrum was further smoothed by averaging the ensemble averaged results over 5 frequency bands. Each time series is plotted to the Nyquist frequency, f_N=1/2Δ, where Δ is the sample rate, except for the thrust force data for which higher frequencies are not shown for clarity. The vertical lines indicate the fundamental frequency of known cyclic motions imposed on the system by the rotating turbine generator system.

The turbine average shaft speed was computed over this time interval and found to be 2.85sec/rev (21 RPM) corresponding with a frequency of $f_{RPM} = 0.35075Hz$ (red vertical dashed line). The fundamental blade passage frequency (blue) is the number of blade $N = 4$ multiplied by the shaft speed f_{RPM}, $(4 * f_{RPM} = 1.403Hz)$. The AC voltage waveform produced by the generator (or any motor) will cause a mechanical vibration at that frequency. The average generation frequency over this time period was computed as $7.015Hz$ (black).

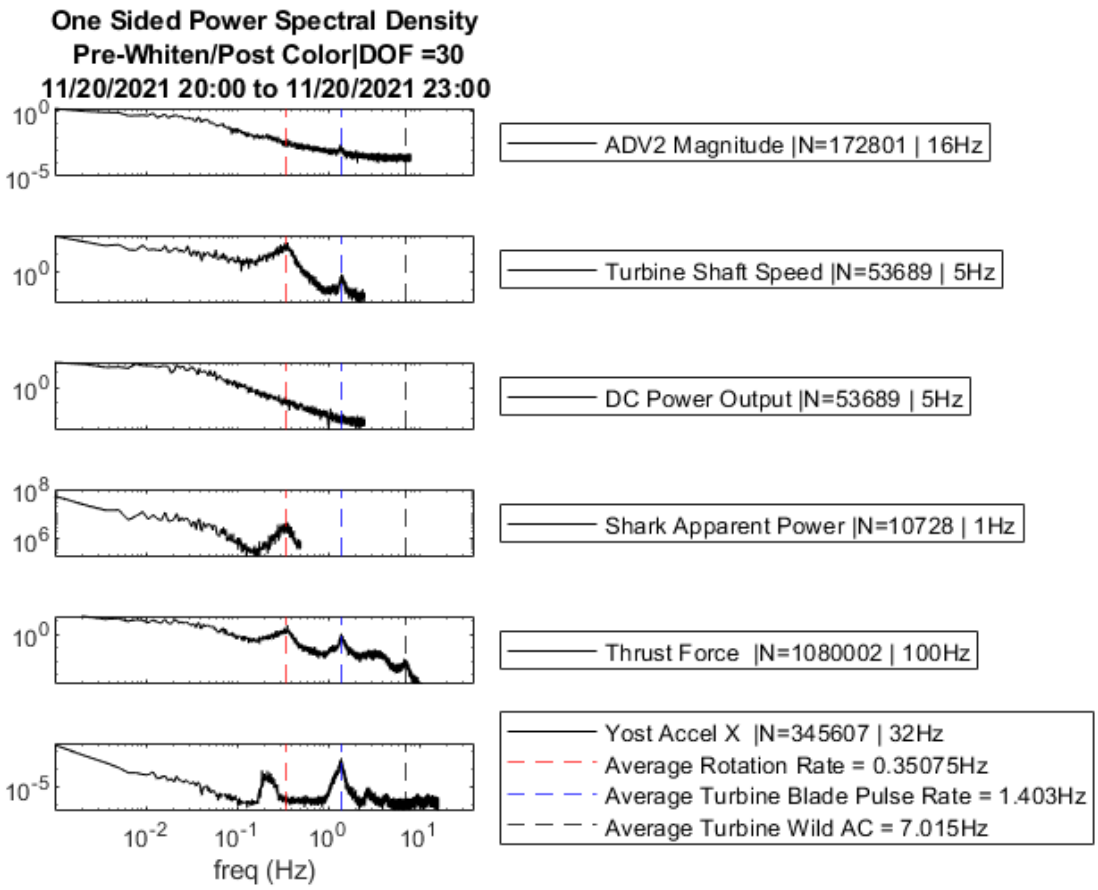

Figure 5.18: Power spectrum of select time series during a 3 hour window of an ebb tide while the turbine was grid synchronized on 11/20/2021. 16Hz Bow ADV horizontal velocity magnitude (QC'd data with NaN's replaced with linear interpolation). 5Hz Voltsys turbine shaft speed, converted to rotations/second from rpm. 5Hz Voltsys DC power output from rectifier supplied to the inverter. 1Hz Shark meter apparent power reading (QC'd data with NaN's replaced with linear interpolation). 100Hz, corrected thrust force measurement. 32Hz, platform IMU x acceleration data (along platform direction). The average turbine rotation rate (red), blade passage frequency (rotation rate/4) (blue) and generator wild AC frequency (black) are plotted as vertical lines to indicate important forcing frequencies on the structure.

The dominant energy in the ADV data is in the low frequency bands less than $10^{-1}Hz$. Additionally, an artifact, likely associated with platform motion, at the blade passage frequency is present. The IMU data could be used to removed this signal from the ADV velocity measurements. The turbine shaft speed data, has a strong peak present at its average speed and blade passage frequency as expected. The apparent power data also shows a dependence on the turbine shaft speed, but is not sampled fast enough to resolve if the blade passage

frequency is present in the signal. The thrust load data shows peaks at all three driving frequencies, and the higher frequencies, greater than 10^1 and less than f_N, are not shown in this window for clarity. The x acceleration data (along platform) indicates a peak at the blade passage frequency. Another spike in the IMU spectrum occurs at a slightly slower frequency than average blade passage, it is expected that this could be related to turbine rotation or flow structures, but this was not investigated further here.

On 11/18/21 at 15:27 UTC the Voltsys data logging frequency was increased from 1 Hz to 5 Hz, so there was comparatively little data recorded while the Voltsys data logger was sampling at 5Hz and the turbine was operating (Figure 5.18 Voltsys measurement of turbine shaft speed and DC power). The presence of the spectral peak, in the turbine shaft speed data, at the blade passage frequency coincides with anticipated results. This peak is near the the Nyquist frequency, so aliased energy may be present, but is likely a real feature in the signal. This provides confidence in the spectral analysis performed on the 1Hz shaft speed data in Figure 5.19. The turbine rotation rate signal is present in the Shark meter apparent power data but notably lacking in the DC power output. This is likely because the Shark meter samples at 400 samples/electrical cycle (=400*60Hz = 24,000Hz) and then reports an average of those values. This captures higher frequency signals than the Voltsys rectifier can.

Figure 5.19 presents the spectrum of 5 continuous time series measured during a 3 day period from 11/15 to 11/18, 2021. During this window the turbine experienced all normal operating conditions (i.e. there were no inverter faults and the electric brake was never engaged). These conditions include grid synchronization during the ebb tide and free spinning during the flood tide, with periods of no rotation between associated with low tidal current velocities. The plots are identified from top to bottom as: bow ADV2 data at 16Hz, Voltsys rectifier turbine shaft speed followed by DC output power at 1Hz, Shark meter apparent power at 1Hz, and thrust force at 100Hz. Note: The Bow ADV data set includes inflow data (during the ebb tide) and turbine wake data (during the flood tide).

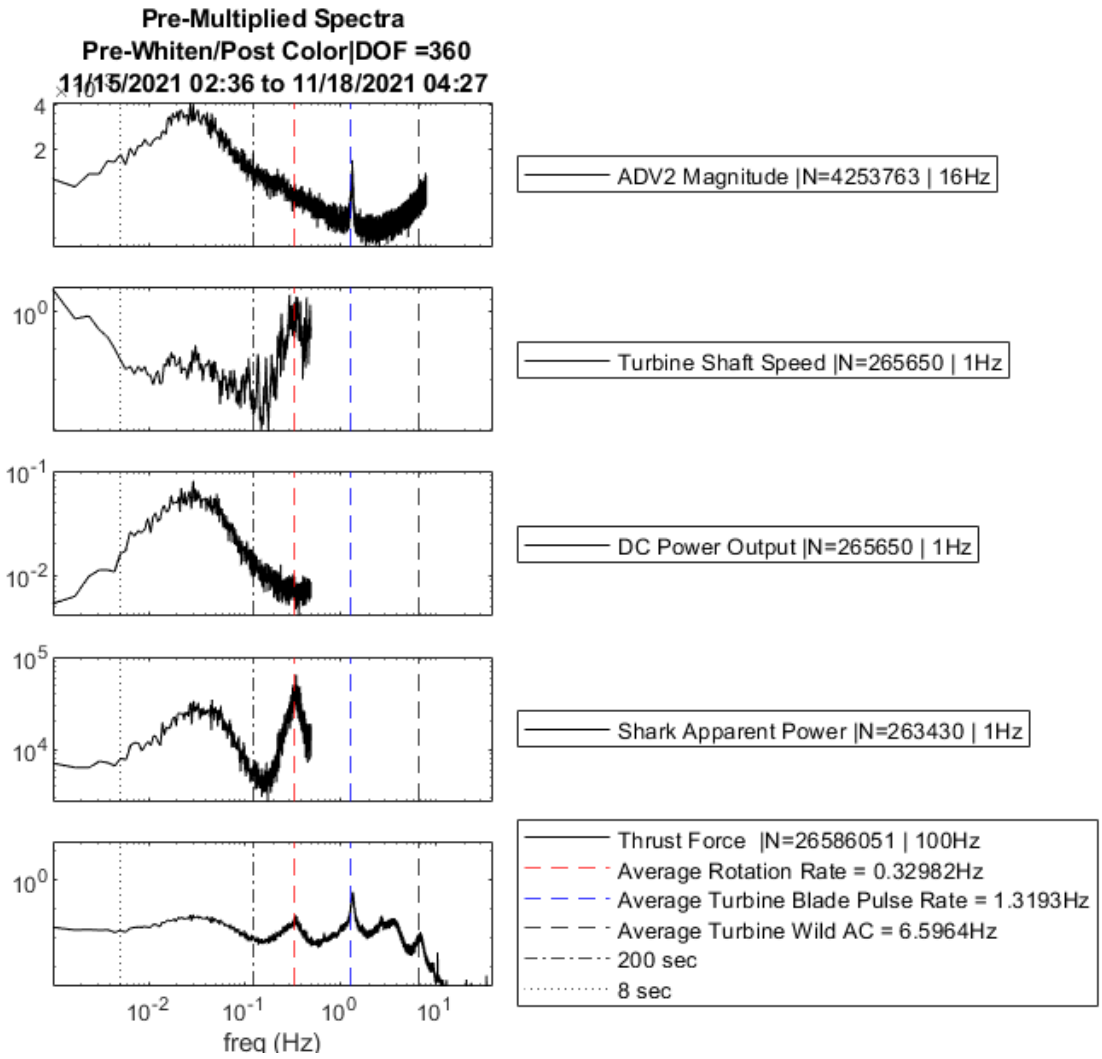

Figure 5.19: Power spectrum of select continuous time series during a 3 day window between 11/15/21 and 1/18/21. 16Hz Bow ADV horizontal velocity magnitude (QC'd data with NaN's replaced with linear interpolation). 1Hz Voltsys turbine shaft speed, converted to rotations/second from rpm. 1Hz Voltsys DC power output from rectifier supplied to the inverter. 1Hz Shark meter apparent power reading (QC'd data with NaN's replaced with linear interpolation). 100Hz, corrected thrust force measurement. The average turbine rotation rate (red), blade passage frequency (rotation rate/4) (blue) and generator wild AC frequency (black) are plotted as vertical lines to indicate important forcing frequencies on the structure. Note: The bow ADV data set includes inflow data (during the ebb tide) and turbine wake data (during the flood tide).

Chancey 2019 presented that the pre-multiplied spectra can be used to investigate the large scale flow structures present at the UNH turbine deployment platform ([7] 2.2.5.1). Additionally, for each time series, the spectrum was smoothed using a pre-whiten post color

method with 360 degrees of freedom. The pre-whiten post color method was selected to limit the spectral "leakage" of low frequency energy into higher frequency bands. The number of ensembles is the number of times a time series is subdivided, the spectrum computed and then averaged. The number of ensembles selected was six because it coincided with the number of ebb/flood tidal cycles during this time window. The spectrum was further smoothed by averaging the ensemble averaged results over 30 frequency bands. Each time series is plotted to the Nyquist frequency, except for the thrust force data for clarity. The vertical lines indicate the fundamental frequency of known cyclic motions imposed on the system by the rotating turbine generator system. The vertical lines indicating average turbine shaft speed (red), blade passage frequency (blue) and generation frequency (black) were recalculated to include all the grid synchronous operating data during this window. Additionally vertical lines framing the tidal gust range from $8 - 200s$ time scales are plotted.

Figure 5.19 illustrates the improved low frequency resolution that comes with a longer time series. The resolution of the spectrum is $\Delta f = f_s/N$ where f_s is the sample rate and N is the record length. The ADV data indicates energy peaks in the expected range associated with integral time scales of the turbulence. Similar peaks are present in the DC power output, Shark apparent power and thrust load data but notably lacking in the shaft speed data. The thrust load data again indicates peaks at the average turbine rotation rate, blade passage and generation frequencies.

The lack of a significant signal expression in the shaft speed data, over the tidal gust range, has some interesting suggestions. Note: The shaft speed is calculated based on the measurement of the AC signal from the generator with Equation 4.18 which may have an impact on the fidelity of this measurement, the following conclusion is based on the data collected and assuming it accuracy. The turbine shaft speed responds to local changes in velocity on short times scales as the flow speeds up and slows down as opposed to taking tens of seconds to react to variations in incoming flow. This would be aligned with what is expected from a system that has little rotational inertia (mass) like this cross flow turbine.

CHAPTER 6

Summary and Conclusions

6.1 Summary of Project

This thesis introduced the need for open water testing of marine cross flow turbines to support numerical model development. Improvements were made to the existing UNH Living Bridge tidal energy converter system which allowed for the first grid synchronous tidal turbine testing at this site. A new data acquisition system was designed and constructed based on the NREL modular ocean data acquisition (MODAQ) system in collaboration with the NREL marine energy research team. Two ADV's, two thrust load cells, platform IMU and Voltsys rectifier data were integrated to collect time synchronous power performance and load measurements. This upgrade to data acquisition capabilities helps move the UNH TDP closer in line with the IEC TC-114 testing guidelines.

In the fall of 2021 a measurement campaign on the UNH tidal energy converter, operating in grid synchronous mode, was completed between October 12 and December 15. During this period, more than 29 days of turbine operation were recorded, delivering 767kWh of renewable tidal energy to the NH grid. Following the data collection period, quality control (QC) code was developed to process the ADCP and ADV data, utilizing tests outlined in the Integrated Ocean Observing System (IOOS) real time manual. A custom algorithm was successfully designed to salvage the thrust load data and the shark meter time vector was restored to allow for spectral analysis. To our knowledge, this represents the first publicly accessible data set containing power performance and thrust load data for a grid connected cross-flow turbine in a tidal flow environment. This data set was published in the Marine

Hydrokinetic Data Repository (MHKDR Project Link: UNH Field Measurement Campaign), and is available for researchers, e.g., for numerical model validation.

6.2 Summary of Results

This work highlights the UNH tidal deployment platform's testing capabilities to adequately measure electrical power and turbine thrust force to characterize device performance. This provides confidence in the temporal accuracy of the instrumentation package which is useful for prospective turbine developers looking to characterize their device. Under the Atlantic Marine Energy Center (AMEC) grant from the Department of Energy, UNH will further develop the Tidal Energy Test Site at Memorial Bridge to be able to perform accredited testing of tidal energy converters under IEC TC-114 marine energy conversion systems standards. The UNH TDP and its capabilities will play a key role in that. Further, the UNH TDP will be listed as a tidal test site under the DOE initiative TEAMER (Testing & Expertise for Marine Energy). The tidal current/bridge pier shear layer was observed.

The interaction of the tidal current/bridge pier shear layer was observed in the stern ADCP data under ebb flow, but was not further quantified under this project. However, the presence of this shear layer did not prevent typical device characterization curves from being produced for the cross flow turbine tested here. For tidal currents ramping up, the minimum flow rate for the onset of turbine rotation was observed near 1 m/s with 60s averaged ADV data. Averaged ADCP flow values greater than 1.2 m/s were typically required for grid synchronization. For tidal currents ramping down, flow velocities falling below 1 m/s coincided with a loss of synchronization followed by a stop in turbine rotation at $\approx 0.5 m/s$. A maximum average C_p of 0.208 was observed corresponding with a tip speed ratio, $\lambda = 2.17$ TSR and shaft speed of 21rpm. The maximum 2min averaged thrust force was measured as 8.1kN corresponding with a 2.3m/s inflow velocity, 5.2kW power output and 25rpm shaft speed. The maximum 2min averaged power observed was 8.2 kW at 2.2 m/s. Thrust coefficient values monotonically increased with tip speed ratio as expected with typical values

$C_t = 0.55 - 0.85$.

Concurrent turbine thrust, shaft speed and tidal resource was collected for the first time which will provide important data to verify existing TDP and VGP structural models. Spectral analysis of ADV, power output, turbine shaft speed and thrust loading highlight the important forcing frequencies on the operating system. These frequencies need to be accounted for to avoid natural frequency resonant response in structural components and negative instrumentation performance. Spectral analysis also highlighted the impact of the tidal gusts, identified by *Chancey 2019*, on turbine electrical power output and thrust loading.

6.3 Recommendations for Future Work

To align the UNH TDP with the IEC TC114-202 guidelines, tidal current resource should be measured using a current profiler, collecting data over the turbine projected area, with a 1Hz sampling rate. This will require the integration of the Nortek Signature ADCP's, already procured, to be integrated into the UNH MODAQ system. If power quality testing is designated for this site, additional power sensors will be required for on grid or off grid operating modes. Ideally, the AC voltage and current would be measured before the signal enters the rectifier and is converted to DC. This will require a minimum of 3 voltage sensors and 1 current sensor with sample rates exceeding 100Hz, an additional cRIO card will be required. To improve network data transmission rate capabilities, UNH should work with North East Integration (NEI) to upgrade platform/bridge networking devices to Gigabit Ethernet (GBE). If future studies wish to operate in grid synchronous mode and utilize the Shark power meter some improvements need to be verified. The buffer issue presented in this thesis needs to be resolved and the sample rate of the data stream improved to 6Hz. The tower weather station has not been serviced or calibrated in some time, it is recommended it is removed and sent out for calibration, along with the replacement of the NMEA 0183 to USB converter. The McCartney underwater multiplexer umbilical cord, with 120VAC power and network cables, was recently found to be defective, likely with insulation damage

near the cable gland connection to the topside panel. It is recommended that the power and network cables be separated to prevent the failure of the MOXA network extender that has now occurred twice. This would only be required if continued use of the LB-DAS system was intended for collecting concurrent Bow and Stern ADCP, CTD, and platform weather station data sets. It is recommended that any new instrument integration be configured with the UNH MODAQ system. If future unattended operation of the UNH TEC is planned, it is recommended that an automatic CO2 based fire suppression system be integrated into the power electronic shelters various control cabinets. To improve the use of the data collected in this thesis, to better characterize turbine rotor performance, the generator efficiencies should be quantified. This would create a generator performance curve which would allow turbine mechanical power estimates to be derived from the electrical power measurements collected. Additionally, the IMU data collected during this measurement campaign, could produce interesting studies on platform motion under various operating conditions, turbine braked, rotating and pitched out of the water.

LIST OF REFERENCES

[1] United States Environmental Protection Agency, "Inventory of U.S. Greenhouse Gas Emissions and Sinks." `https://www.epa.gov/ghgemissions/inventory-us-greenhouse-gas-emissions-and-sinks` Apr. 14, 2022 [Online].

[2] U.S. Energy Information Administration, "Sources of U.S. Electricity Generation, 2021." `https://www.eia.gov/energyexplained/electricity/` Jul. 15, 2022 [Online].

[3] L. Kilcher, M. Fogarty, and M. Lawson, "Marine energy in the united states: An overview of opportunities," Tech. Rep. NREL/TP-5700-78773, National Renewable Energy Laboratory, Golden, CO, USA, 2021 [Online].

[4] P. Bachant, *Physical and Numerical Modeling of Cross-Flow Turbines*. PhD thesis, University of New Hampshire, Durham, NH USA, 2016.

[5] P. Bachant, "Experimental investigation of helical cross-flow axis hydrokinetic turbines, including effects of waves and turbulence," Master's thesis, University of New Hampshire, Durham, NH USA, 2011.

[6] I. Gagnon, "A hydrokinetic turbine deployment system for use at bridges with the memorial bridge as a case study," Master's thesis, University of New Hampshire, 2018.

[7] K. Chancey, "Assessment of the localized flow and tidal energy conversion system at an estuarine bridge," Master's thesis, University of New Hampshire, 2019.

[8] J. Ulliac, *Living Bridge 25 kW Envirogen Installation Drawings*. New Energy Corporation Inc., #473, 3553 - 31st NW Calgary, Alberta T2L 2K7, 2019.

[9] Arias, P.A., N. Bellouin, E. Coppola, R.G. Jones, G. Krinner, J. Marotzke, V. Naik, M.D. Palmer, G.-K. Plattner, J. Rogelj, M. Rojas, J. Sillmann, T. Storelvmo, P.W. Thorne, B. Trewin, K. Achuta Rao, B. Adhikary, R.P. Allan, K. Armour, G. Bala, R. Barimalala, S. Berger, J.G. Canadell, C. Cassou, A. Cherchi, W. Collins, W.D. Collins, S.L. Connors, S. Corti, F. Cruz, F.J. Dentener, C. Dereczynski, A. Di Luca, A. Diongue Niang, F.J. Doblas-Reyes, A. Dosio, H. Douville, F. Engelbrecht, V. Eyring, E. Fischer, P. Forster, B. Fox-Kemper, J.S. Fuglestvedt, J.C. Fyfe, N.P. Gillett, L. Goldfarb, I. Gorodetskaya, J.M. Gutierrez, R. Hamdi, E. Hawkins, H.T. Hewitt, P. Hope, A.S. Islam, C. Jones, D.S. Kaufman, R.E. Kopp, Y. Kosaka, J. Kossin, S. Krakovska, J.-Y. Lee, J. Li, T. Mauritsen, T.K. Maycock, M. Meinshausen, S.-K. Min, P.M.S. Monteiro, T. Ngo-Duc, F. Otto, I. Pinto, A. Pirani, K. Raghavan, R. Ranasinghe, A.C. Ruane, L. Ruiz, J.-B. Sallée, B.H. Samset, S. Sathyendranath, S.I. Seneviratne, A.A. Sörensson, S. Szopa,

I. Takayabu, A.-M. Tréguier, B. van den Hurk, R. Vautard, K. von Schuckmann, S. Zaehle, X. Zhang, and K. Zickfeld, "2021: Technical Summary. *In Climate Change 2021: The Physical Science Basis. Contribution of Working Group I to the Sixth Assessment Report of the Intergovernmental Panel on Climate Change*," pp. 33–144, Cambridge, United Kingdom and New York, NY, USA: Cambridge University Press, 2021 [Online] doi: 10.1017/9781009157896.002.

[10] J. R. Petit, J. Jouzel, N. I. Raynaud, D. andBarkov, J. Barnola, I. Basile, M. Bender, J. Chappellaz, M. Davisk, G. Delaygue, M. Delmotte, V. M. Kotlyakov, M. Legrand, V. Y. Lipenkov, C. Lorius, L. Pe pin, C. Ritz, E. Saltzmank, and M. Stievenard, "Climate and atmospheric history of the past 420,000 years from the vostok ice core, antarctica," *Nature*, vol. 399, pp. 429–436, Jun 1999.

[11] F. Parrenin, J. Jouzel, C. Waelbroeck, C. Ritz, and J.-M. Barnola, "Dating the vostok ice core by an inverse method," *Journal Of Geophysical Research*, vol. 106, pp. 31,837–851, Dec 2001.

[12] NOAA Earth System Research Laboratories Global Monitoring Laboratory, "Monthly average mauna loa CO2." `https://gml.noaa.gov/ccgg/trends/`Nov 2022 [Online].

[13] E. d. l. Vega, T. B. Chalk, P. A. Wilson, R. Priya Bysani, and G. L. Foster, "Atmospheric co2 during the mid-piacenzian warm period and the m2 glaciation," *Scientific Reports*, vol. 10, Jul 2020 [Online]. doi: https://doi.org/10.1038/s41598-020-67154-8.

[14] Department Of Energy: Office of Energy Efficiency Renewable Energy: Water Power Technologies Office, "History of hydropower." `https://www.energy.gov/eere/water/history-hydropower` Accessed Nov. 14, 2022 [Online].

[15] K. A. Haas, H. M. Fritz, S. P. French, B. T. Smith, and V. Neary, "Assessment of energy production potential from tidal streams in the united states," Jun 2011 [Online]. `https://www.osti.gov/biblio/1219367` doi: 10.2172/1219367.

[16] National Renewable Energy Laboratory, "Turning the tide for renewables in alaska." `https://www.nrel.gov/news/features/2021/turning-the-tide-for-renewables-in-alaska.html`, Oct. 26, 2021 [Online].

[17] R. H. Stewart, "Coastal processes and tides," in *Introduction to Physical Oceanography*, ch. 17, 17.4, pp. 300–310, sept.'08 ed., 2008.

[18] D. T. Pugh, *Tides, Surges and Mean Sea-Level*. New York, NY USA: John Wiley Sons, june'96 ed., 1987.

[19] A. T. Doodson, "The harmonics of the tide-generating potential," *Proceedings of the Royal Society of London A*, vol. 100, pp. 305–329, Dec. 01, 1921 [Online] `http://dx.doi.org/10.1098/rspa.1921.0088`.

[20] Pacific Northwest National Laboratory, "Tidal energy." [Accessed] Nov. 14, 2022 [Online] `https://www.pnnl.gov/explainer-articles/tidal-energy#:~:text=People%20in%20Europe%20first%20used,turn%20waterwheels%20to%20mill%20grain`.

[21] T. Hooper and M. Austen, "Tidal barrages in the uk: Ecological and social impacts, potential mitigation, and tools to support barrage planning," *Renewable and Sustainable Energy Reviews*, vol. 23, pp. 289–298, 2013 [Online] https://www.sciencedirect.com/science/article/pii/S1364032113001500.

[22] A. Copping and e. Hemery, L.G., *OES-Environmental 2020 State of the Science Report: Environmental Effects of Marine Renewable Energy Development Around the World.* Report for Ocean Energy Systems (OES), 2020 DOI: 10.2172/1632878.

[23] J. McEnte, "Hydrokinetic baseload microgrids," in *2021 International Conference on Ocean Energy*, 2021 [Online].

[24] Village of Igiugig, "Welcome to igiugig," 2022 [Online] https://www.igiugig.com/.

[25] Ocean Renewable Power Company, "Rivgen power system." 2021 [Online] https://orpc.co/rivgen-power-system-integrated-microgrid-solutions/.

[26] J. Hardisty, "Power intermittency, redundancy and tidal phasing around the United Kingdom," *The Geographical Journal*, vol. 174, pp. 76–84, Mar 2008.

[27] A. Eastman, "Scaling green hydrogen for a global market," Sep 2022 [Online] https://kleinmanenergy.upenn.edu/podcast/scaling-green-hydrogen-for-a-global-market/.

[28] T. A. Adcock, S. Draper, R. H. Willden, and C. R. Vogel, "The fluid mechanics of tidal stream energy conversion," *Annual Review of Fluid Mechanics*, vol. 53, no. 1, pp. 287–310, 2021 [Online] https://doi.org/10.1146/annurev-fluid-010719-060207.

[29] J. H. Stickland, "The Darrieus turbine: A performance prediction model using multiple streamtubes," Tech. Rep. SAND75-0431, Sandia Laboratories, Albuquerque, New Mexico USA, 1975.

[30] M. Barone and J. Murray, "The development of CACTUS, a wind and marine turbine performance simulation code," Jan 2011 doi: 10.2514/6.2011-147.

[31] M. Wosnik, P. Bachant, V. S. Neary, and A. W. Murphy, "Evaluation of design analysis code, CACTUS, for predicting crossflow hydrokinetic turbine performance," Tech. Rep. SAND2016-9787, Sandia Laboratories, Albuquerque, New Mexico USA, Sept. 2016 [Online] https://www.osti.gov/biblio/1431494 doi:10.2172/1431494.

[32] National Renewable Energy Laboratory, "Cross flow turbine," Feb. 10 2022 [Online] https://openei.org/wiki/PRIMRE/Databases/Projects_Database/Technologies/Cross_Flow_Turbine.

[33] H. Ross, M. Hall, D. R. Herber, J. Jonkman, A. K. Sundarrajan, T. T. Tran, A. Wright, D. Zalkind, and N. Johnson, "Development of a control co-design modeling tool for marine hydrokinetic turbines: Preprint," Jul 2022 [Online] https://www.osti.gov/biblio/1876869.

[34] DNV, *Tidal Bladed Tidal Turbine Design Software*. Utrechtseweg 310 6812 AR Arnhem, the Netherlands, 2015 [Online] https://www.dnv.com/services/industry-standard-tidal-turbine-software-modelling-tool-tidalbladed-3799.

[35] J. Colby, "The path to commercialization for the marine energy sector," UNH Center for Coastal and Ocean Mapping/Joint Hydrographic Center, Center for Ocean Engineering, Seminar Series, 2022.

[36] International Energy Agency: Ocean Energy Systems, "Annual report: An overview of ocean energy activities in 2021," Tech. Rep. 21, Mar. 2022 [Online] https://www.ocean-energy-systems.org/publications/oes-annual-reports/document/oes-annual-report-2021/.

[37] B. Sellar and D. Sutherland, "Tidal energy site characterisation at the fall of warness, EMEC, UK," Tech. Rep. V4.0, University of Edinburgh, Dec. 2016.

[38] E. Bell, M. Wosnik, and L. Hamilton, "NSF award search: Award # 1430260 - PFI:BIC: The living bridge: The future of smart, user-centered transportation infrastructure," 2022 [Online] https://www.nsf.gov/awardsearch/showAward?AWD_ID=1430260.

[39] US Department of Energy, "Technology readiness assessment guide," Tech. Rep. DOE G 413.3-4A, 2011.

[40] E. Robinson, *17D04 – UNH Living Bridge Electrical Commissioning Procedure*. New Energy Corporation Inc., #473, 3553 - 31st NW Calgary, Alberta T2L 2K7, 2018.

[41] A. Taber, "I-leak error for ginlong solis inverters," 2022 [Online] https://ginlongsolis.freshdesk.com/support/solutions/articles/36000100020-i-leak-pro-error-explained#:~:text=An%20I%20leak%20is%20a,inverter%20circuit%20(%20Parasitic%20Capacitance%20).

[42] BDI, "University of new hampshire monitoring of the memorial bridge in portsmouth, nh," Tech. Rep. 151104-NH, 2016.

[43] C. Fuller, *Living Bridge Data Acquisition System User's Manual*. North East Integration, North Hampton, NH USA, 2017.

[44] MacArtney Underwater Technology, *UNH - NEXUS MK-C - OT Manual - REV A*. Gl. Guldagervej 48, DK-6710 Esbjerg V, Denmark, 2016.

[45] E. Nelson, *Modular Oceanographic Instrumentation System (MOIS) User Guide*. National Renewable Energy Laboratory, Golden, CO, 2015.

[46] NREL, "Open water testing support," 2022 [Online] https://www.nrel.gov/water/open-water-testing.html.

[47] M. Rowell, M. Wosnik, J. Barnes, and J. King, "Experimental evaluation of a mixer-ejector marine hydrokinetic turbine at two open water tidal energy test sites in nh and ma," *Mar Technol Soc J*, vol. 47, no. 4, pp. pp 67–79, 2013 [Online]. doi: http://dx.doi.org/10.4031/MTSJ.47.4.15.

[48] Voltsys, *Wind Turbine Controller With Dump Load V3.0*. Coomanore North, Bantry, Co. Cork. Republic of Ireland.

[49] M. Wosnik, "University of new hampshire center for ocean renewable energy CORE infrastructure enhancements," 2009 [Online] https://www.osti.gov/biblio/1635378 doi: 10.2172/1635378.

[50] MasterClock, *NTP100-GPS Time Server Data Sheet*. St. Charles, MO USA.

[51] Avonmore Electrical, "Vacuum pressure impregnation VPI," 2022 [Online] https://www.avonmore-electrical.com/workshop/our-equipment-processes/vpi/.

[52] P. O'Byrne, "UNH CORE: Living Bridge TDP Operation Manual." unpublished, 2021.

[53] A. Taber, "PV-ISO-PRO 01/02 Alarm," 2022 [Online] https://ginlongsolis.freshdesk.com/support/solutions/articles/36000010527-pv-iso-pro-01-02-alarm.

[54] P. O'Byrne, "UNH TDP Fall 2021 Load Cell READ ME." unpublished, 2022.

[55] R. L. Gordon, "Acoustic Doppler current profiler principles of operation a practical primer," Tech. Rep. Second Edition for Broadband ADCP's, RDI, San Diego, CA, USA, 1996.

[56] Integrated Ocean Observing System (U.S.), *Manual for real-time quality control of in-situ current observations : a guide to quality control and quality assurance of acoustic Doppler current profiler observations*. Silver Spring, MD, USA, 2015 [Online] http://doi.org/10.7289/V5WM1BMZ.

[57] P. O'Byrne, "UNH TDP Fall 2021 ADCP READ ME." unpublished, 2022.

[58] P. Rusello, "A practical primer for pulse coherent instruments," Tech. Rep. TN-027, NortekUSA, Boston MA, USA, 2009.

[59] Nortek, *The Comprehensive Manual for Velocimeters: Vector, Vectrino, Vectrino Profiler*. Rud, Norway, 2022.

[60] P. O'Byrne, "UNH TDP Fall 2021 ADV READ ME." unpublished, 2022.

[61] A. Lohrmann, "Monitoring sediment concentration with acoustic backscattering instruments," Tech. Rep. TN-003, Nortek AS, Rud, Norway, 2001.

[62] E. Industries/GaugeTech, "Generic specification for multifunction power and energy meter shark 100 meter," Tech. Rep. E141723 V.1.07, Westbury, NY USA, 2021.

[63] P. O'Byrne, "UNH TDP Fall 2021 Shark Meter READ ME." unpublished, 2022.

[64] P. O'Byrne, "UNH TDP Fall 2021 Voltsys READ ME." unpublished.

[65] NOAA, "Geomagnetism frequently asked questions," 2022 [Online] https://www.ngdc.noaa.gov/geomag/faqgeom.shtml.

[66] Yost Labs, *3-Space Sensor Miniature Attitude Heading Reference System with Pedestrian Tracking User's Manual*. Portsmouth, Ohio, USA, 2017.

[67] P. O'Byrne, "UNH TDP Fall 2021 IMU READ ME." unpublished, 2022.

[68] A. W. C. . H. Corporation, *State of New Hampshire Department of Transportation Construction Plans NH Project No. 13678F, A000 (911)*. 2839 Paces Ferry Road SE Suite 1200 Atlanta, Georgia 30339, 2014.

[69] P. O'Byrne, "UNH TDP Fall 2021 Tower WS READ ME." unpublished, 2022.

APPENDIX A

Existing MHK Test Facilities & Data Set Summary Tables

Tidal Energy Test Sites	Operator	Location	Site Type	Operational?	Grid Connected?	Test Site	Max Current (m/s)	Max Power (kW)	Max Device Size
Perpetuus Tidal Energy Centre (PTEC)	PTEC in collaboration with EMEC	Isle of Wight, UK	Coastal	'25	Yes	Full Scale	2.9	30,000	NA
Fundy Ocean Research Center for Energy (FORCE)	FORCE	Minas Passage, Nova Scotia, CA	Constricted Channel	Yes	Yes	Full Scale	> 5	22,000	NA
Fall of Warness	EMEC	Orkney, UK	Constricted Channel	Yes	Yes	Full Scale	4	4,000	NA
Paimpol-Bréhat Site	Seeneoh / EDF	Brittany, FR	Open Water	Yes	Yes	Full Scale	3.1	2,500	NA
Cobscook Bay Tidal Energy Project	ORPC	Cobscook Bay ME, USA	Tidal Strait	exp. '22	Yes	Full Scale	3	750	NA
Bordeaux Site	Seeneoh	Gironde Estuary, FR	Tidal River	Yes	Yes	Scale	3.5	100	10m x 6m
Igiugig Hydrokinetic Project	Igiugig Village & ORPC	Kvichak River AK, USA	River	Yes	Yes	Remote	NA	25	NA
AMEC Tidal Energy Test Site (formerly Living Bridge)	University of New Hampshire / AMEC	Piscataqua River NH, USA	Tidal River	Yes	Yes	Scale	> 3	25	3 m dia
Canadian Hydrokinetic Turbine Test Centre	University of Manitoba	Winnipeg River Manitoba, CA	River	Yes	Yes	Scale	2.5	NA	NA
Soderfors Project	Uppsala University	River Dal, SE	River	NA	Yes	Scale	2	NA	NA
Roosevelt Island Tidal Energy (RITE) Project	Verdant Power	New York NY, USA	Tidal River	No	Yes	Scale	2.7	170	NA
Smart Bay	Marine Institute of Ireland	Galway Bay, IE	Enclosed Bay	Yes	No	Scale	NA	NA	NA
Tanana River Test Site (TRTS)	Pacific Marine Energy Center (PMEC)	Tanana River AK, USA	River	Yes	No	Scale	>2.5	NA	NA
Bourne Tidal Test Site (BTTS)	Marine Renewable Energy Collaborative	Bourne, MA, USA	Tidal River	Yes	No	Scale	> 2	NA	3 m dia
Tidal Thames Test Site	Port of London	RIver Thames, England, UK	Tidal River	2021	No	Scale	> 0.75	NA	NA
Shapinsay Sound	EMEC	Scotland, UK	Enclosed Bay	Yes	No	Scale	1.5	NA	NA
R/V Russell Davis Light	Univeristy of Washington	Pudget Sound WA, USA	Vessel	Down for Service	No	Scale	2.5	NA	1.8m x 3m
Strangford Lough	Minesto	Strangford Lough, NIR	Tidal Strait	NA	NA	Scale	0.8	NA	NA

Key NA = Not Available / Not Applicable exp = expired

Available Tidal Energy Converter Related Data Sets	Device Type	Test Site	Test Owner	MHK # / Web Link	Rated Power (kw)	Rated Speed (m/s)	Swept Area (m^2)	# of Devices	Grid Connected?	Resource/Inflow Data	Wake Data - Operating	Wake Data - Stalled	Thrust Data - Operating	Thrust Data - Stalled	Electrical Power Data	Turbine Shaft Speed	Shaft Torque	Modeling Data Available
Cross-Flow Turbine UNH Vertical Axis Turbine Operational Dataset	Straight Blade Cross Flow	AMEC - Tidal Energy Test Site	University of New Hampshire	394	25	3	5.44	1	✓	✓	✓	✓	✓	✓	✓	✓	×	×	✓
Gen5 KHPS Performance Period A	Axial Flow	RITE	Verdant Power	383	35	2.2	20	3	✓	✓	?	?	?	?	✓	?	?	?	Nov 26'
Gen5 KHPS Performance Period B	Axial Flow	RITE	Verdant Power	389	35	2.2	20	3	✓	✓	?	?	?	?	✓	?	?	?	Dec 26'
ORPC RivGen 2.0 at Igiugig, AK Operational Data 2019 and 2020	Helical Cross Flow	Igiugig Hydrokinetic Project	ORPC	411	40	3.5	9	2	×	✓	?	?	?	?	✓	?	?	×	May 27'
RivGen Controller Performance Raw Data, Igiugig, AK	Helical Cross Flow	Igiugig Hydrokinetic Project	ORPC	3914	40	3.5	9	2	×	✓	?	×	×	×	✓	✓	×	×	✓
Physical and Numerical Modeling for 1:6 Scale Reference Model 2	Straight Blade Cross Flow	UNH Tow Tank	University of New Hampshire	143	?	?	0.87	1	×	✓	✓	✓	✓	✓	✓	✓	✓	✓	✓
Coordinated Control of Tidal Cross-flow Turbines	Cross Flow	Laboratory	University of Washington	167	?	?	0.01	2	×	✓	×	×	✓	×	✓	✓	×	×	✓
Experimental determination of power and thrust coefficients	Shrouded Axial Flow	University of Manitoba Flume	CHTTC	Shahsa	?	1.1	0.03	1	×	?	?	?	✓	?	✓	✓	✓	?	✓
ADV data from the UNH-AMEC Tidal Energy Test Site during a Perigean Spring Tide	Straight Blade Cross Flow	AMEC - Tidal Energy Test Site	University of New Hampshire	444	25	3	5.44	1	✓	✓	✓	×	×	×	×	×	×	×	Sep 23'
ReDAPT - Field-Measurements aligned to the implementation of a tidal energy converter's power performance	Axial Flow	The Fall of Warness	University of Edinburgh	ReDAPT - 2014	?	?	?	?	✓	✓	✓	?	×	×	×	×	×	×	✓
RivGen Wake Data	Helical Cross Flow	Igiugig Hydrokinetic Project	University of Washington	n Wake	40	3.5	9	2	×	?	✓	×	×	×	×	×	×	×	✓
Memorial Bridge Tidal Current Survey 2013-14	NA	AMEC - Tidal Energy Test Site	University of New Hampshire	Griffith	×	×	×	×	×	✓	×	×	×	×	×	×	×	×	✓
TideGen LCOE workbook	Helical Cross Flow	Model	ORPC	4100	40	3	15.7	4	?	×	×	×	×	×	×	×	×	✓	✓
Advanced TideGen OpenFOAM CFD	Helical Cross Flow	Model	ORPC	275	40	3	15.7	4	?	×	×	×	×	×	×	×	×	✓	✓
Advanced TidGen Power System - ProteusDS Version 2.43.5 Files	Helical Cross Flow	Model	ORPC	276	40	3	15.7	4	?	×	×	×	×	×	×	×	×	✓	Jun 23'
ORPC RivGen Hydrokinetic Turbine Wake Characterization	Helical Cross Flow	Igiugig Hydrokinetic Project	University of Washington	248	40	3.5	9	2	×	✓	✓	✓	×	×	×	×	×	×	✓
Hydrokinetic Canal Measurements: Inflow Velocity, Wake Flow Velocity, and Turbulence	Cross Flow	Roza Canal Yakima WA, USA	Instream Energy & Sandia National Laboratory	53	25	3	4.5	1	?	✓	✓	?	×	×	×	×	×	×	✓	✓
PerAWaT - Test Schedule and Test System Design of 1:10th Scale Tidal Turbines (WG4 WP5 D2)	Axial Flow	Strangford Lough	University of Edinburgh	& Finla	×	×	1.3	2	×	×	×	×	×	×	×	×	×	×	✓	✓

APPENDIX B

UNH MODAQ Spec Sheet

UNH Mobile DAQ Spec Sheet | Version 1 | 12/01/2021

Enclosure

- Steel treated with ANSI 61 Polyester Powder Coating
- 22” W x 28” L x 10” D Interior Dimension

Power Distribution/Cooling

- 10 A Breakers for Line and Neutral 120VAC Power
- Q. 1 - MA15D1SI – Surge Suppressor
- Q. 1 - 24VDC 120W Power Supply
- Q. 1 - 5VDC 15W Power Supply
- Q. 1 - 12VDC 50W Power Supply
- Q. 1 - 9VDC 20W AC/DC Converter
- Q. 2 -24 Volt Radial Cooling Fans
- DIN Rail space for addition PSU’s and terminal blocks

Ethernet

- Stride SE2-SW5U Unmanned 5 port ethernet switch

Remote Monitoring/Programming

- Beelink Mini PC 4 Core 8th Intel Core i5-8259U 3.8Ghz 16GB RAM 512GB
- Q. 2 - RMS-100 remote monitoring boards with two auxiliary relay boards totaling:

⇒ Q. 6 - Volt Meters (+/- 100VDC)

⇒ Q. 14 - relays switching up to 240v - 5 amps AC/DC

NI Compact Rio – 9066 (8 slots total)

- 9467, 9871, 9870, 9237, 9219, 6 open, 7 open, 8 open
- LaCie 500GB Solid State External Hard Drive for data

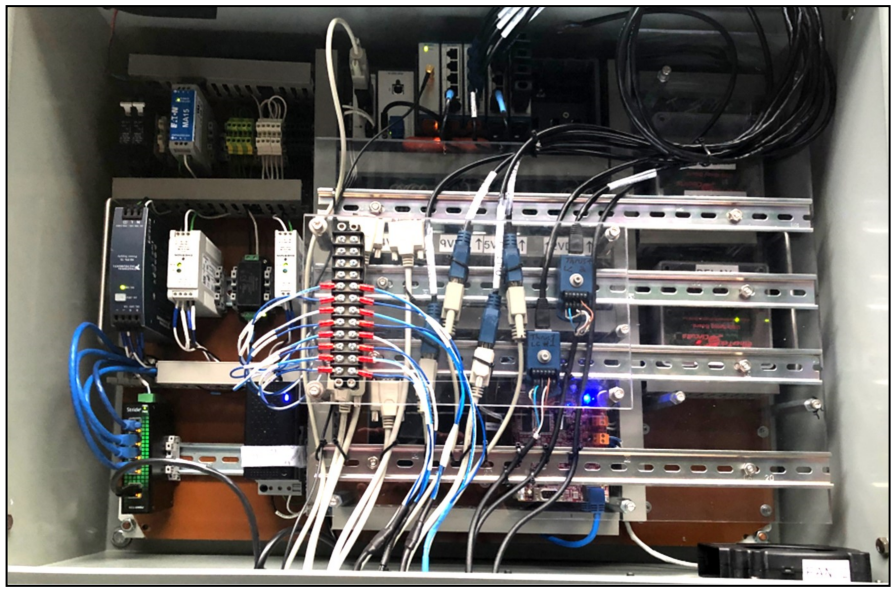

Instruments interface with the enclosure through a Roxtec EZENTRY 32/32 cable gland providing up to 32 ports for cables. Programmable instruments have separate barrel style power connector, wired to a relay on the RMS-100 platform. Serial (db9) cables carry data to interface with instruments to simplify connection to field laptop for deployment configuration using instrument software. Load Cell power and signal are transmitted through M16, series 425, miniature connectors.

The current UNH MODAQ build is configured to interface with:

- Q. 1 - AC Power Input Cable
- Q. 1 - Ethernet Input Cable
- Q. 1 - GPS Antenna - for 9467 C Series Module
- Q. 1 - Voltsys Rectifier MODBUS 485 Interface Cable
- Q. 4 - Sensix Tank Level Monitors
- Q. 3 - Nortek Vector ADV’s (each connected to separate power relay)
- Q. 1 - YOST Watertight IMU (connected to separate power relay)
- Q.2 - 100kN - LCM Thrust Load Cells

APPENDIX C

UNH MODAQ Power and Data Connection Drawings

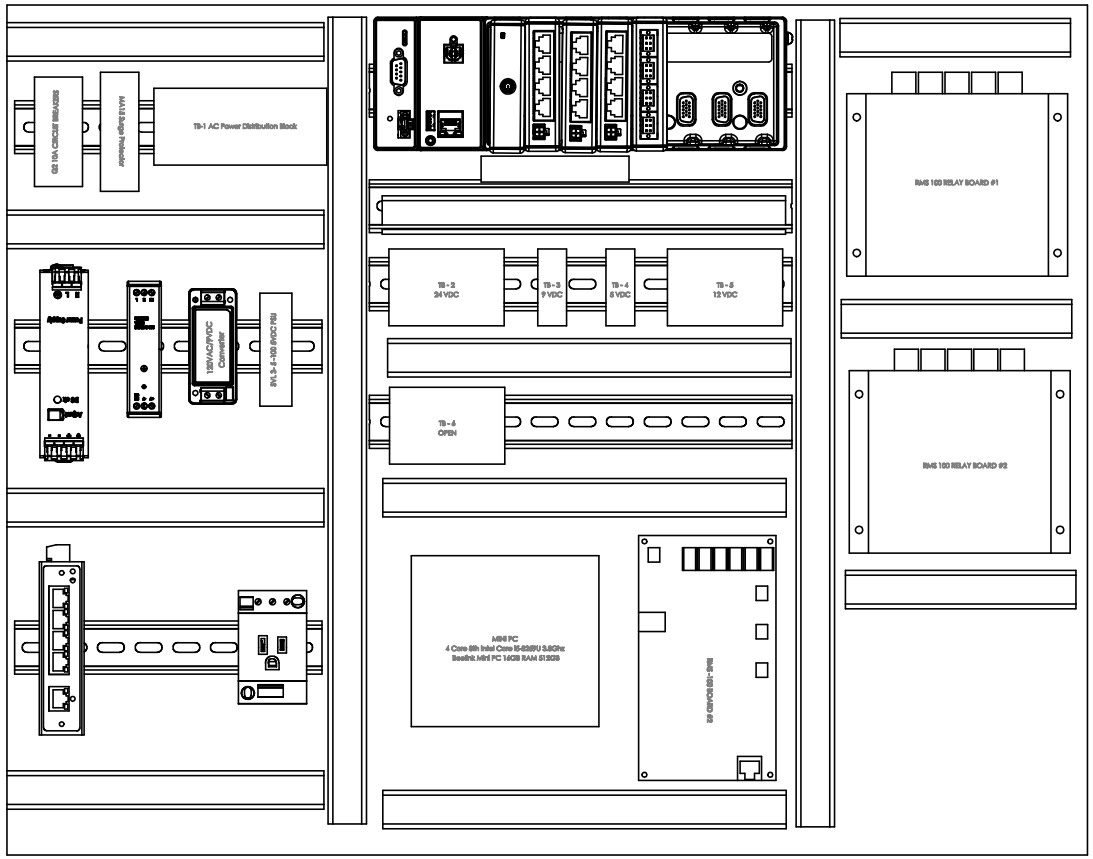

		UNLESS OTHERWISE SPECIFIED:		NAME	DATE
		DIMENSIONS ARE IN INCHES TOLERANCES: FRACTIONAL ANGULAR: MACH BEND TWO PLACE DECIMAL THREE PLACE DECIMAL	DRAWN	POB	12/06/21
			CHECKED		
			ENG APPR.		
			MFG APPR.		
		INTERPRET GEOMETRIC TOLERANCING PER:	Q.A.		
		MATERIAL	COMMENTS:		
NEXT ASSY	USED ON	FINISH			
APPLICATION		DO NOT SCALE DRAWING			

TITLE:

UNH MOBILE DAQ

SIZE	DWG. NO.	REV
A	POB-2021-14	
SCALE: 1:12	WEIGHT:	SHEET 1 OF 1

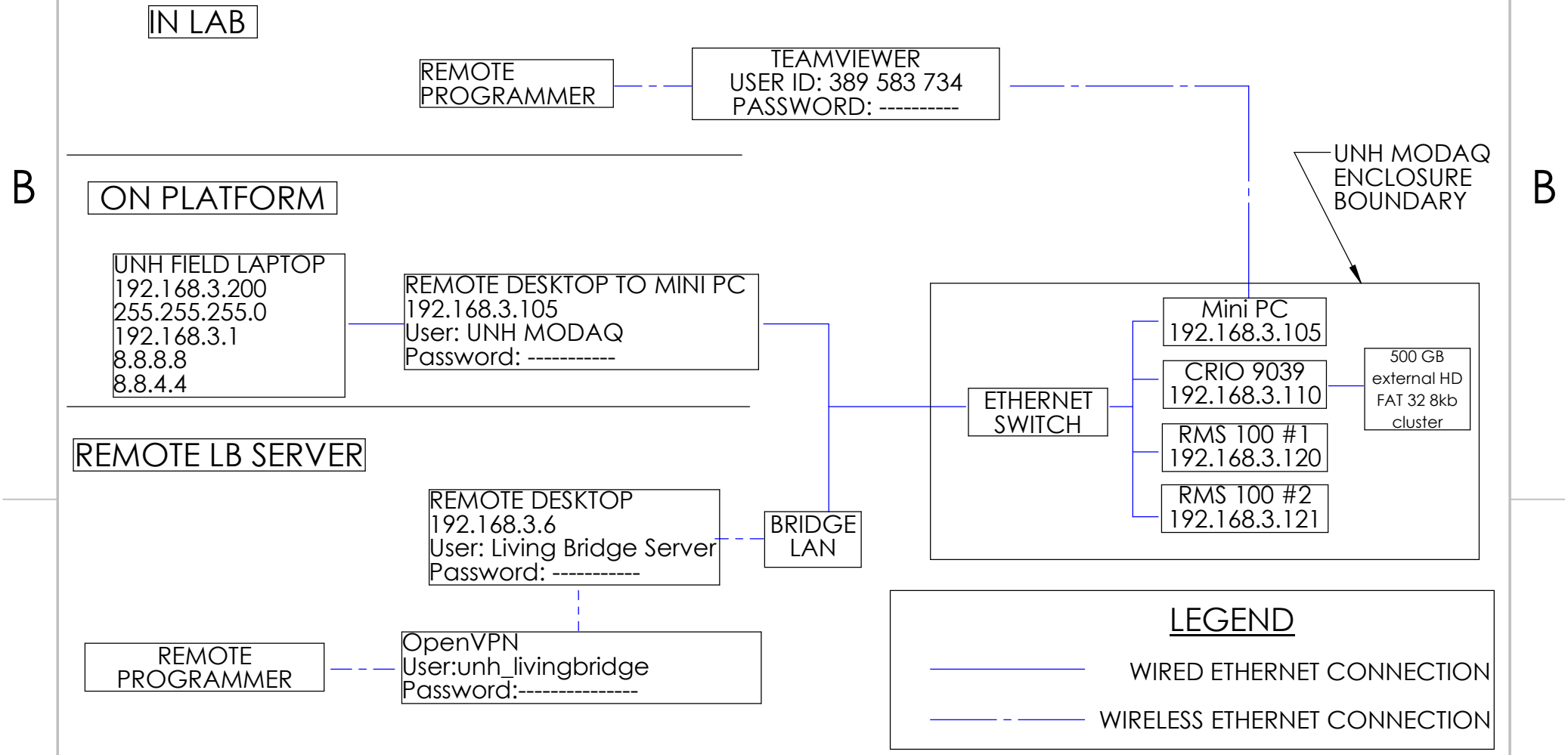

		UNLESS OTHERWISE SPECIFIED:		NAME	DATE
		DIMENSIONS ARE IN INCHES TOLERANCES: FRACTIONAL ANGULAR: MACH BEND TWO PLACE DECIMAL THREE PLACE DECIMAL	DRAWN	POB	08/2/22
			CHECKED		
			ENG APPR.		
			MFG APPR.		
		INTERPRET GEOMETRIC TOLERANCING PER:	Q.A.		
		MATERIAL	COMMENTS:		
NEXT ASSY	USED ON	FINISH			
APPLICATION		DO NOT SCALE DRAWING			

TITLE:

ETHERNET PLAN

SIZE	DWG. NO.	REV
A	POB.2021.5	2

SCALE: 1:1 | WEIGHT: | SHEET 1 OF 1

LOAD SOURCE	MAX A AC	ESTIMATED A AC
NI 24 VDC PSU | MODEL PS-15	3.0 A	1.9 A
MW 12 VDC PSU | MDR-40-MODEL 12	1.1 A	0.67 A
CUI INC 9VDC | PSK-20D-9	0.5 A	0.03 A
SOLA 5VDC PSU | SVL 3-5-100	0.5 A	0.5 A
MINI PC	0.5 A	0.5 A
SOURCE 120VAC	10 A	3.6 A

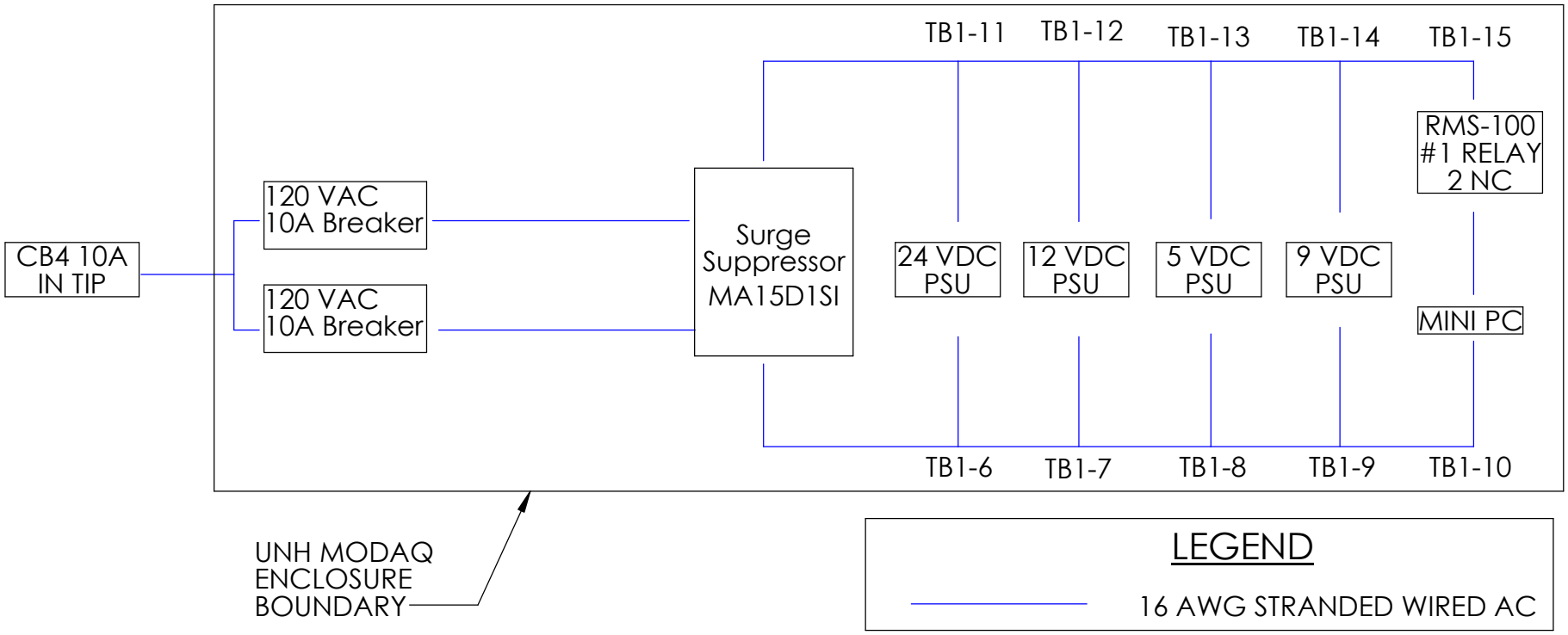

		UNLESS OTHERWISE SPECIFIED:		NAME	DATE
		DIMENSIONS ARE IN INCHES TOLERANCES: FRACTIONAL ± ANGULAR: MACH ± BEND ± TWO PLACE DECIMAL ± THREE PLACE DECIMAL ±	DRAWN	POB	12/03/21
			CHECKED		
			ENG APPR.		
			MFG APPR.		
		INTERPRET GEOMETRIC TOLERANCING PER:	Q.A.		
		MATERIAL	COMMENTS:		
NEXT ASSY	USED ON	FINISH			
APPLICATION		DO NOT SCALE DRAWING			

TITLE:

AC Power Plan

SIZE	DWG. NO.	REV
A	POB.2021.1	
SCALE: 1:1	WEIGHT:	SHEET 1 OF 1

24 VDC PSU	120 W
STRIDE SE2-SW5U ETHERNET SWITCH	3.4 W
RMS-100 BOARD #1	5.7 W
CRIO 9066 CONTROLLER	25 W
MODAQ ENCLOSURE FANS 1&2	28.8 W
RMS-100 BOARD #2	5.7 W
SPARE POWER	51.4 W

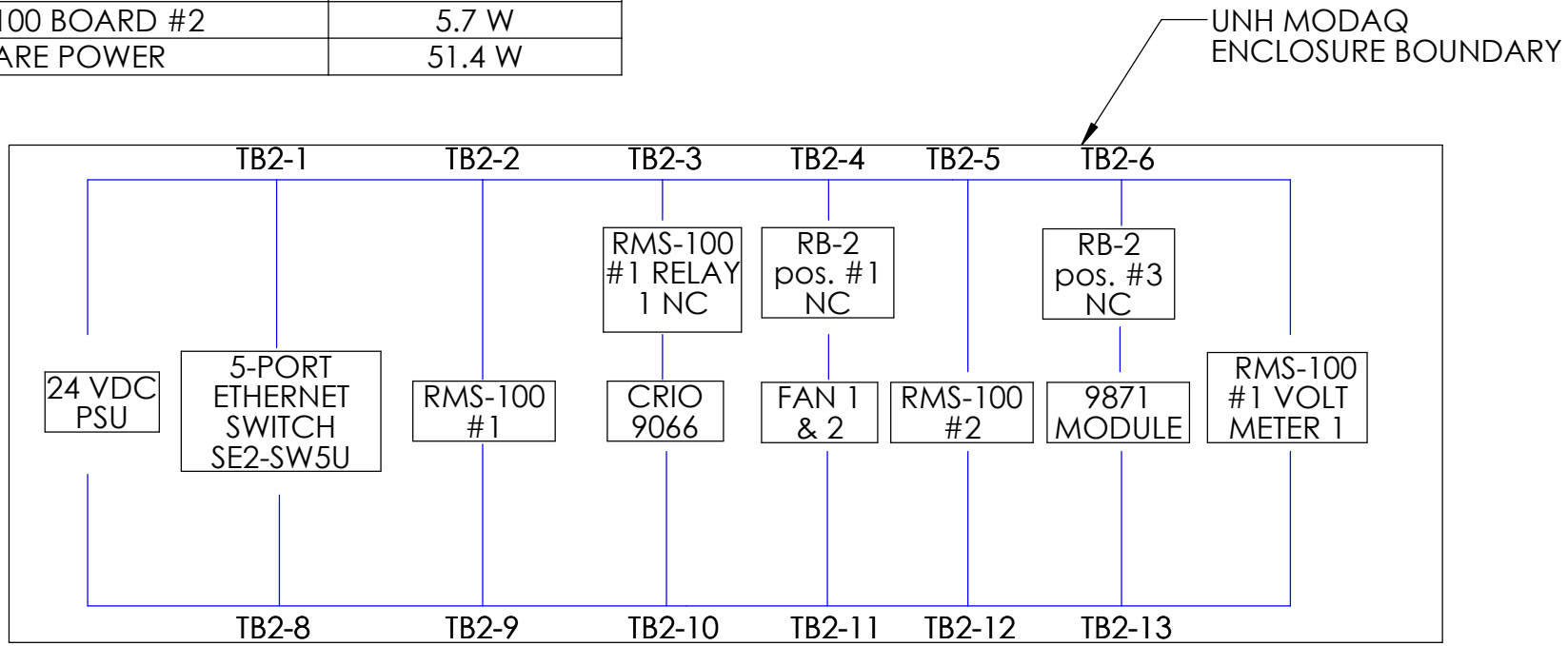

LEGEND

20 AWG STRANDED WIRE DC
SOLID BLUE (+) | BLUE/WHITE (-)

		UNLESS OTHERWISE SPECIFIED:		NAME	DATE
		DIMENSIONS ARE IN INCHES TOLERANCES: FRACTIONAL ± ANGULAR: MACH ± BEND ± TWO PLACE DECIMAL ± THREE PLACE DECIMAL ±	DRAWN	POB	12/03/21
			CHECKED		
			ENG APPR.		
			MFG APPR.		
		INTERPRET GEOMETRIC TOLERANCING PER:	Q.A.		
		MATERIAL	COMMENTS:		
NEXT ASSY	USED ON	FINISH			
APPLICATION		DO NOT SCALE DRAWING			

TITLE:

24 VDC PLAN

SIZE	DWG. NO.	REV
A	POB.2021.2	
SCALE: 1:1	WEIGHT:	SHEET 1 OF 1

12 VDC PSU	40 W
NORTEK VECTOR #1	1.5 W
NORTEK VECTOR #2	1.5 W
9870 MODULE	2.0 W
NORTEK VECTOR #3	1.5 W
SPARE	33.5 W

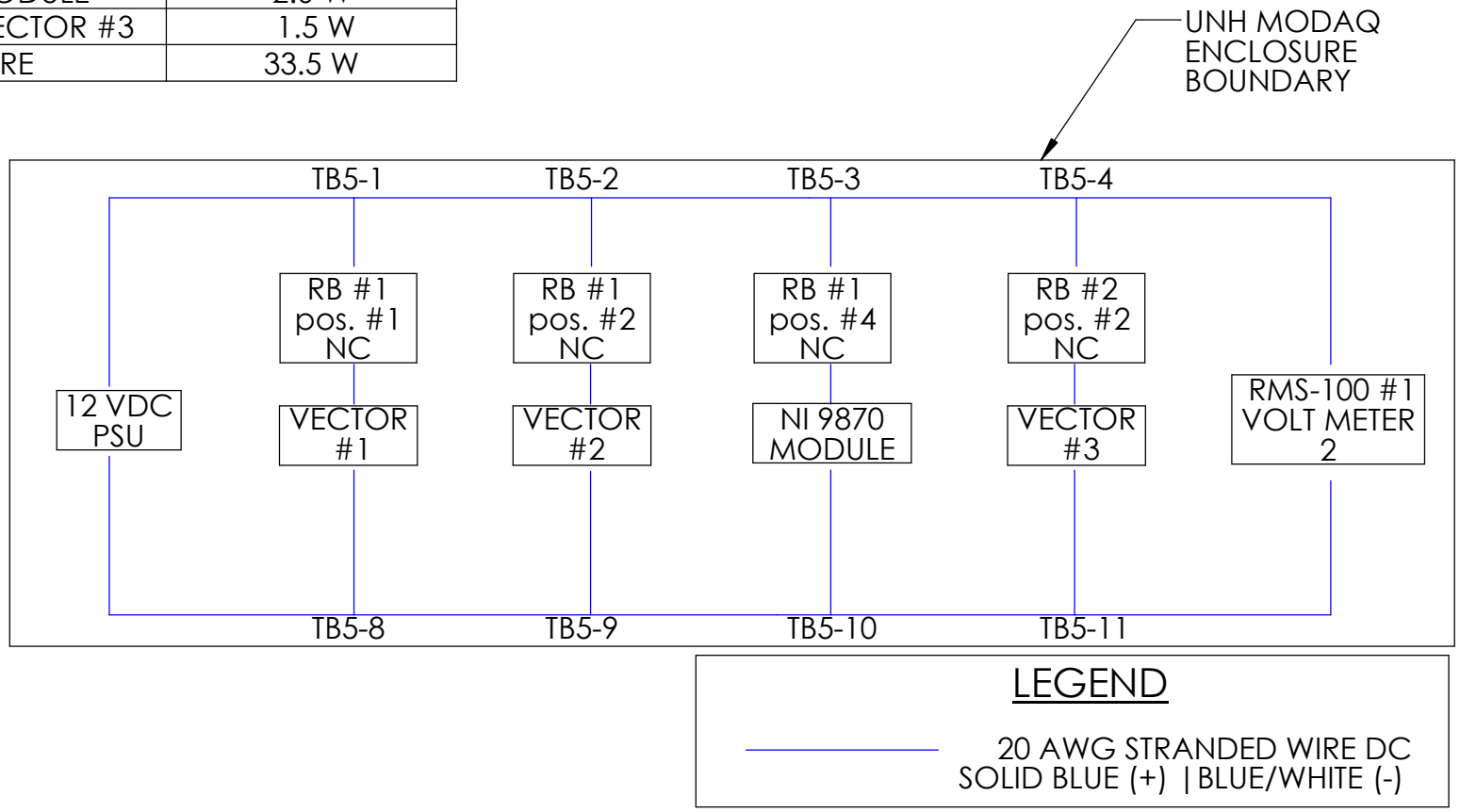

LEGEND

20 AWG STRANDED WIRE DC
SOLID BLUE (+) | BLUE/WHITE (-)

		UNLESS OTHERWISE SPECIFIED:		NAME	DATE
		DIMENSIONS ARE IN INCHES TOLERANCES: FRACTIONAL ± ANGULAR: MACH ± BEND ± TWO PLACE DECIMAL ± THREE PLACE DECIMAL ±	DRAWN	POB	12/03/21
			CHECKED		
			ENG APPR.		
			MFG APPR.		
		INTERPRET GEOMETRIC TOLERANCING PER:	Q.A.		
		MATERIAL	COMMENTS:		
NEXT ASSY	USED ON	FINISH			
APPLICATION		DO NOT SCALE DRAWING			

TITLE:

12 VDC PLAN

SIZE	DWG. NO.	REV
A	POB.2021.3	
SCALE: 1:1	WEIGHT:	SHEET 1 OF 1

9 VDC PSU	20 W
9237 MODULE	740 mW
THRUST LC #1	101.25 mW
THRUST LC #2	101.25 mW
SPARE	19 W

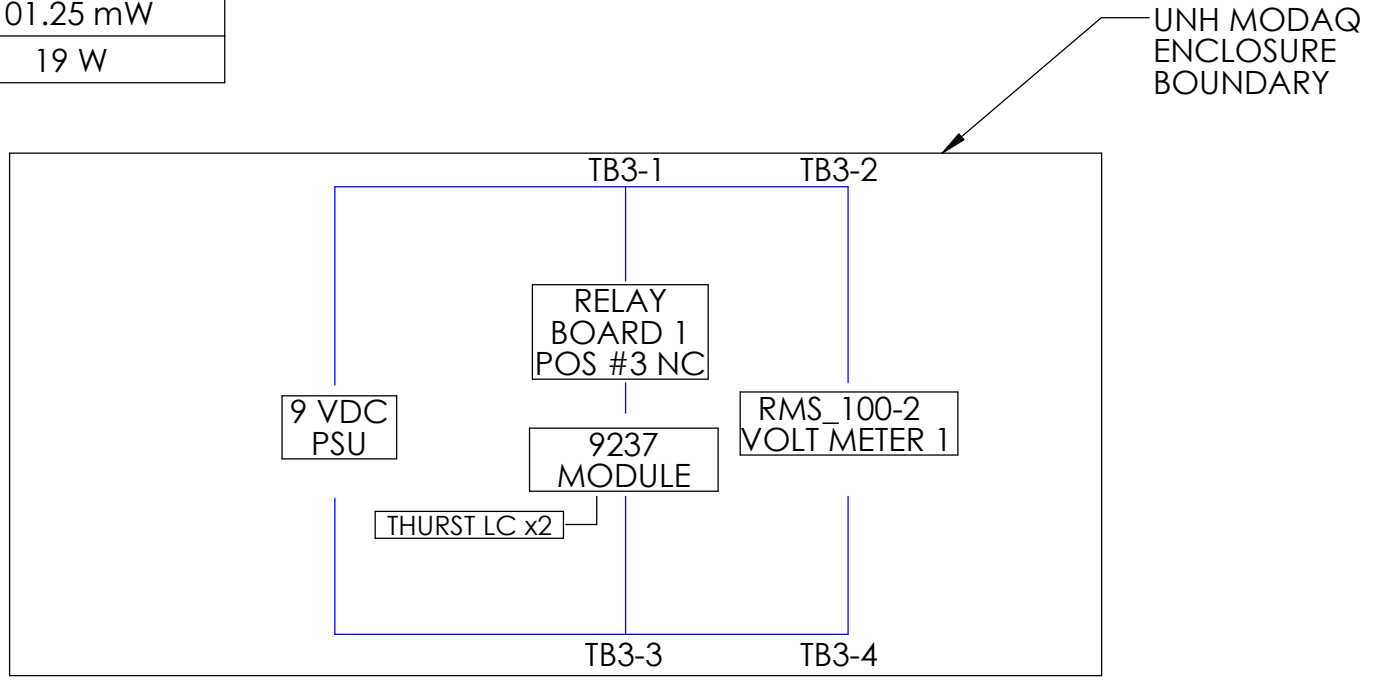

LEGEND

20 AWG STRANDED WIRE DC
SOLID BLUE (+) | BLUE/WHITE (-)

		UNLESS OTHERWISE SPECIFIED:		NAME	DATE
		DIMENSIONS ARE IN INCHES TOLERANCES: FRACTIONAL ± ANGULAR: MACH ± BEND ± TWO PLACE DECIMAL ± THREE PLACE DECIMAL ±	DRAWN	POB	12/03/21
			CHECKED		
			ENG APPR.		
			MFG APPR.		
		INTERPRET GEOMETRIC TOLERANCING PER:	Q.A.		
		MATERIAL	COMMENTS:		
NEXT ASSY	USED ON	FINISH			
APPLICATION		DO NOT SCALE DRAWING			

TITLE:

9 VDC PLAN

SIZE	DWG. NO.	REV
A	POB.2021.13	

SCALE: 1:1 | WEIGHT: | SHEET 1 OF 1

5 VDC PSU	15 W
IMU	15 W
SPARE	0 W

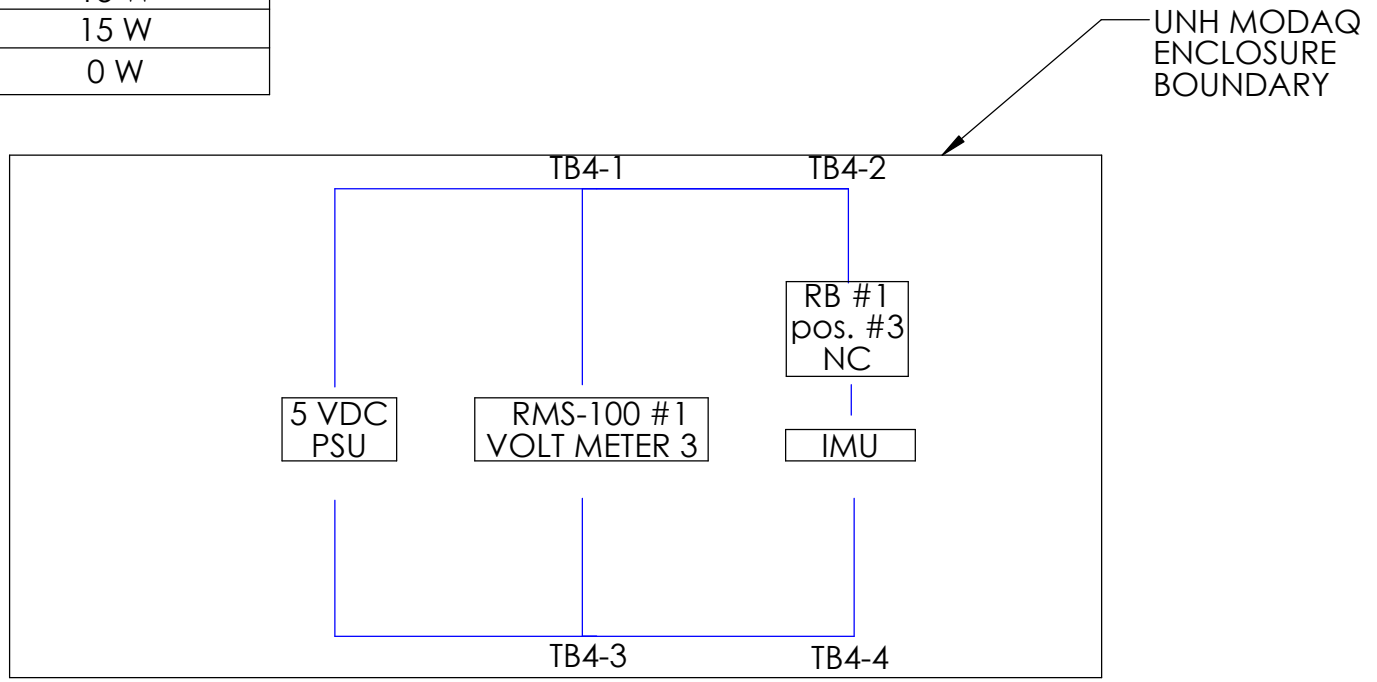

LEGEND

20 AWG STRANDED WIRE DC
SOLID BLUE (+) | BLUE/WHITE (-)

		UNLESS OTHERWISE SPECIFIED:		NAME	DATE
		DIMENSIONS ARE IN INCHES TOLERANCES: FRACTIONAL ± ANGULAR: MACH ± BEND ± TWO PLACE DECIMAL ± THREE PLACE DECIMAL ±	DRAWN	POB	12/03/21
			CHECKED		
			ENG APPR.		
			MFG APPR.		
		INTERPRET GEOMETRIC TOLERANCING PER:	Q.A.		
		MATERIAL	COMMENTS:		
NEXT ASSY	USED ON	FINISH			
APPLICATION		DO NOT SCALE DRAWING			

TITLE:

5 VDC PLAN

SIZE	DWG. NO.	REV
A	POB.2021.4	

SCALE: 1:1 | WEIGHT: | SHEET 1 OF 1

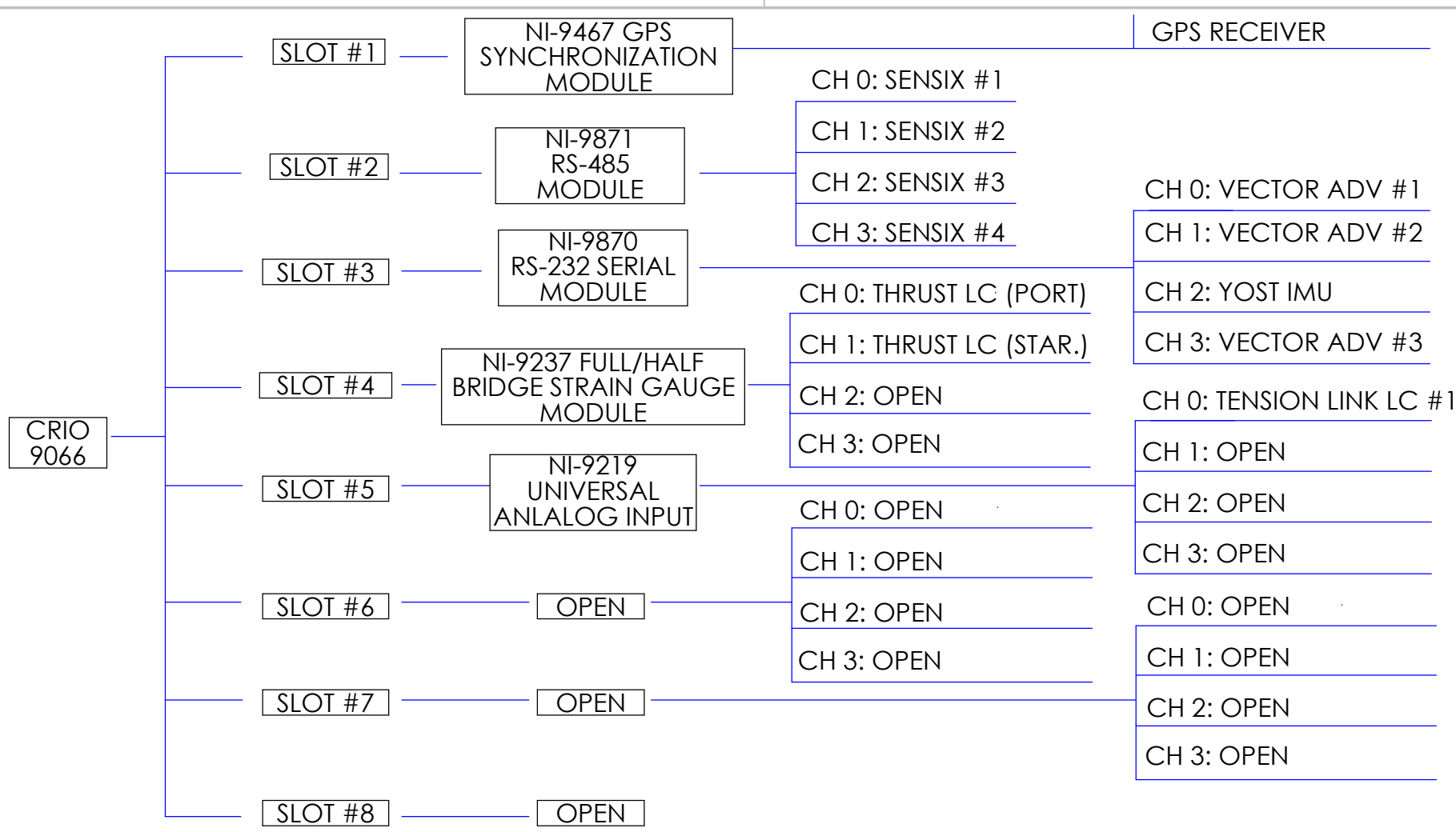

		UNLESS OTHERWISE SPECIFIED:		NAME	DATE
		DIMENSIONS ARE IN INCHES TOLERANCES: FRACTIONAL ± ANGULAR: MACH ± BEND ± TWO PLACE DECIMAL ± THREE PLACE DECIMAL ±	DRAWN	POB	12/03/21
			CHECKED		
			ENG APPR.		
			MFG APPR.		
		INTERPRET GEOMETRIC TOLERANCING PER:	Q.A.		
		MATERIAL	COMMENTS:		
NEXT ASSY	USED ON	FINISH			
APPLICATION		DO NOT SCALE DRAWING			

TITLE:

CRIO SLOT ALLOCATIONS

SIZE	DWG. NO.	REV
A	POB.2021.6	

SCALE: 1:1 | WEIGHT: | SHEET 1 OF 1

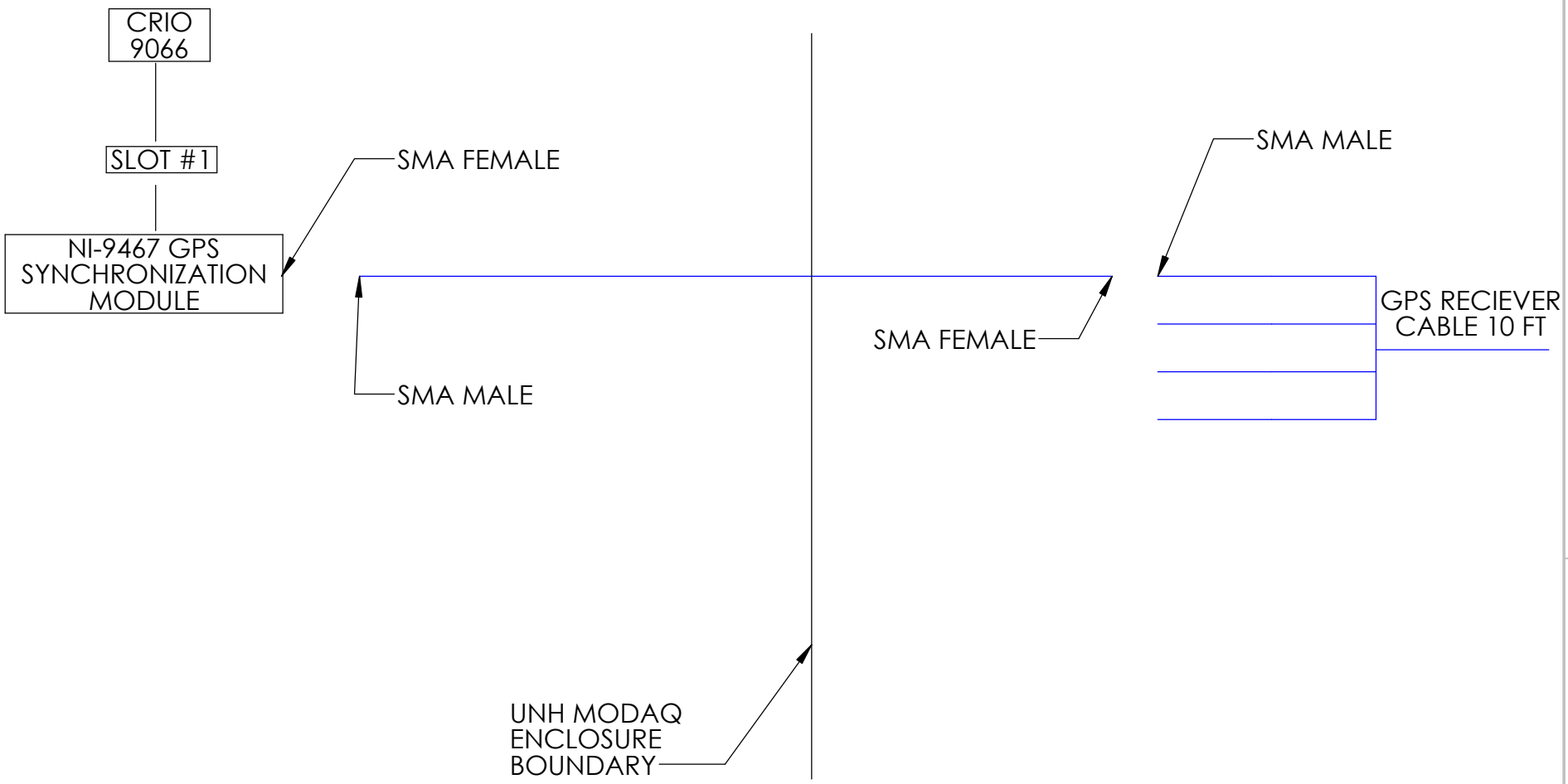

		UNLESS OTHERWISE SPECIFIED:		NAME	DATE
		DIMENSIONS ARE IN INCHES TOLERANCES: FRACTIONAL ANGULAR: MACH BEND TWO PLACE DECIMAL THREE PLACE DECIMAL	DRAWN	POB	12/06/21
			CHECKED		
			ENG APPR.		
			MFG APPR.		
		INTERPRET GEOMETRIC TOLERANCING PER:	Q.A.		
		MATERIAL	COMMENTS:		
NEXT ASSY	USED ON	FINISH			
APPLICATION		DO NOT SCALE DRAWING			

TITLE:

NI-9467 DATA CONNECTION

SIZE	DWG. NO.	REV
A	POB.2021.7	
SCALE: 1:1	WEIGHT:	SHEET 1 OF 1

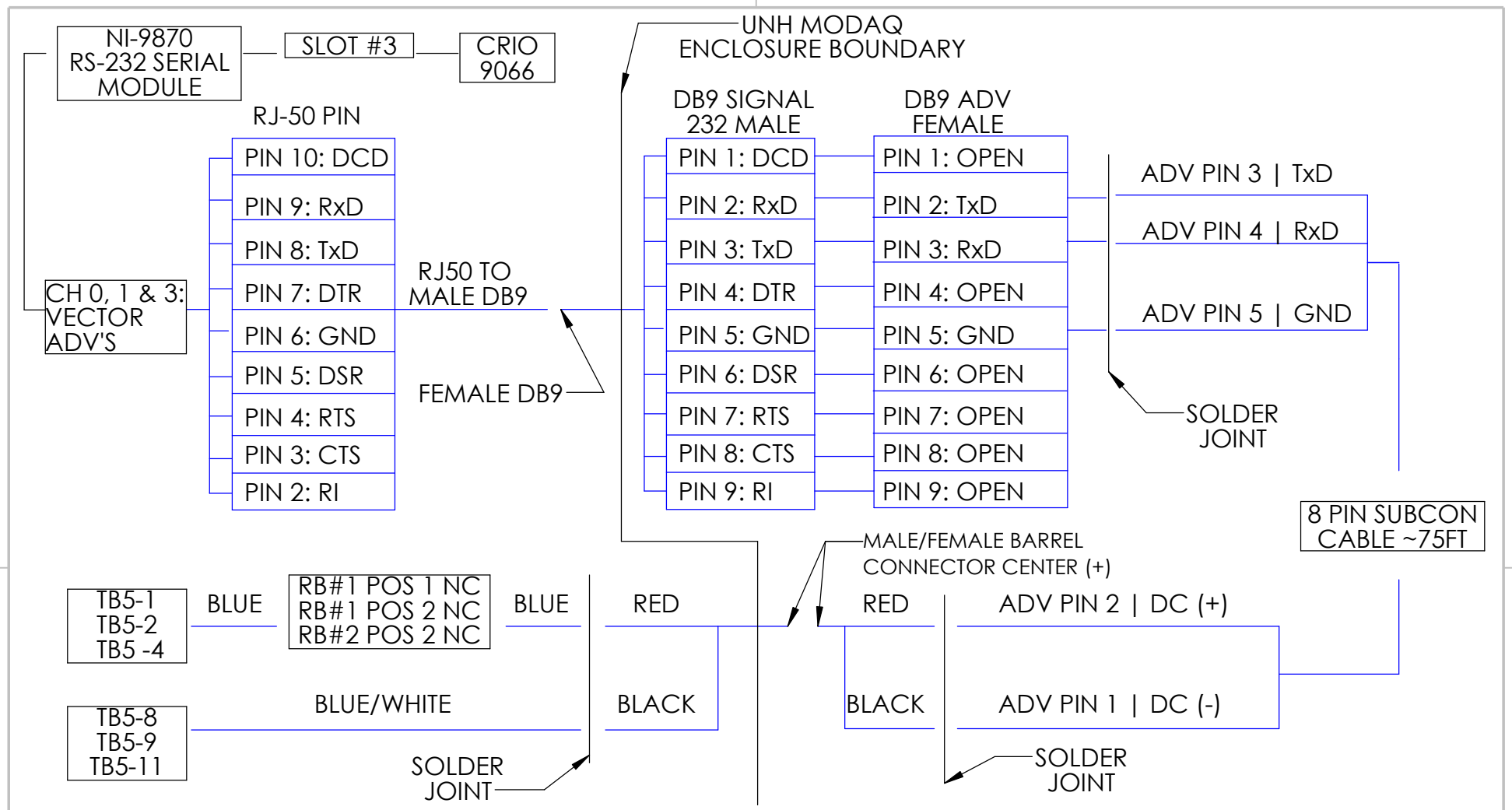

		UNLESS OTHERWISE SPECIFIED:		NAME	DATE
		DIMENSIONS ARE IN INCHES TOLERANCES: FRACTIONAL ± ANGULAR: MACH ± BEND ± TWO PLACE DECIMAL ± THREE PLACE DECIMAL ±	DRAWN	POB	12/03/21
			CHECKED		
			ENG APPR.		
			MFG APPR.		
		INTERPRET GEOMETRIC TOLERANCING PER:	Q.A.		
		MATERIAL	COMMENTS:		
NEXT ASSY	USED ON	FINISH			
APPLICATION		DO NOT SCALE DRAWING			

TITLE:

ADV DATA CONNECTION

SIZE	DWG. NO.	REV
A	POB.2021.10	

SCALE: 1:1	WEIGHT:	SHEET 1 OF 1

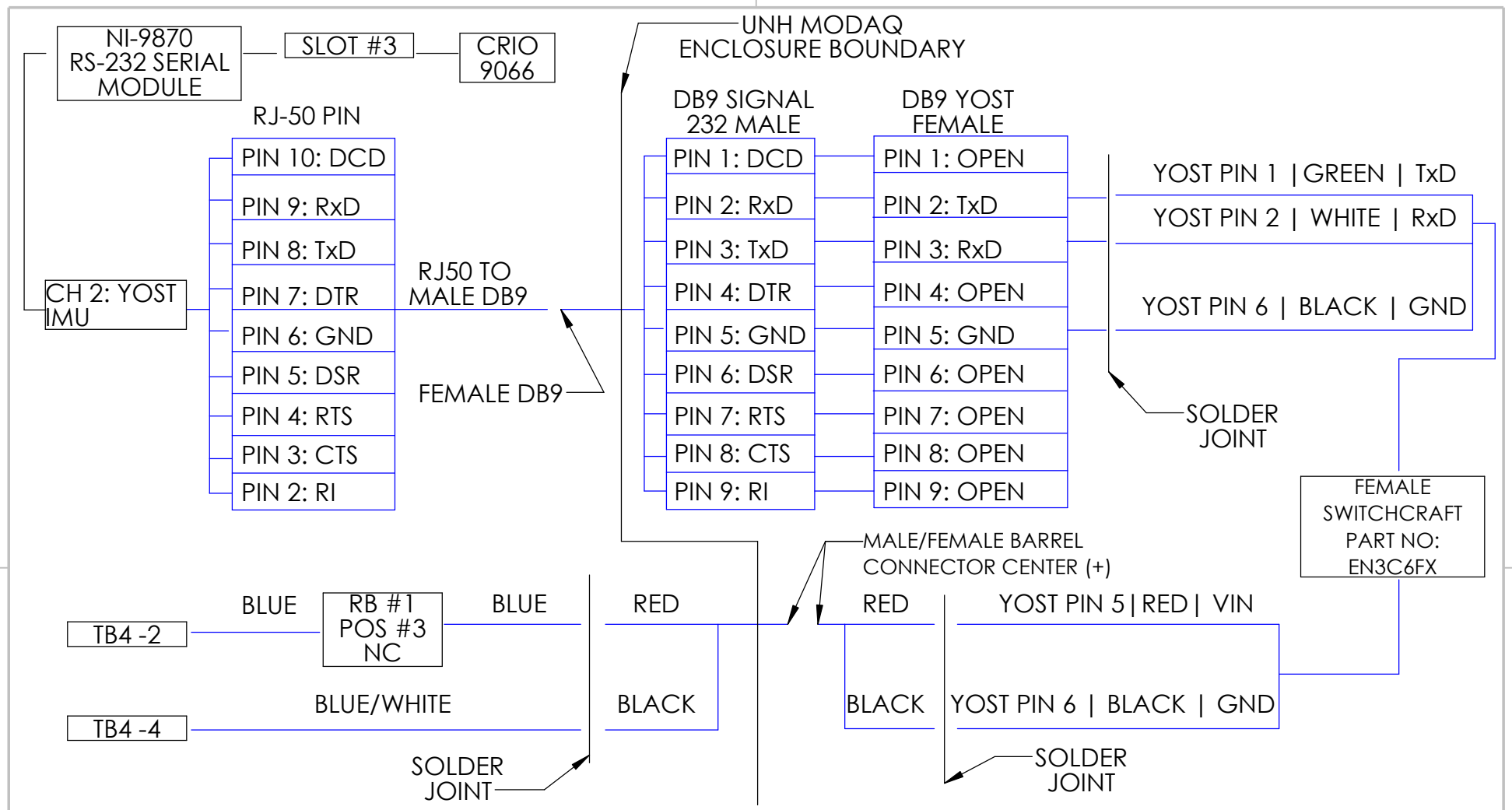

		UNLESS OTHERWISE SPECIFIED:		NAME	DATE
		DIMENSIONS ARE IN INCHES TOLERANCES: FRACTIONAL ± ANGULAR: MACH ± BEND ± TWO PLACE DECIMAL ± THREE PLACE DECIMAL ±	DRAWN	POB	12/03/21
			CHECKED		
			ENG APPR.		
			MFG APPR.		
		INTERPRET GEOMETRIC TOLERANCING PER:	Q.A.		
		MATERIAL	COMMENTS:		
NEXT ASSY	USED ON	FINISH			
APPLICATION		DO NOT SCALE DRAWING			

TITLE:

IMU DATA CONNECTION

SIZE	DWG. NO.	REV
A	POB.2021.12	
SCALE: 1:1	WEIGHT:	SHEET 1 OF 1

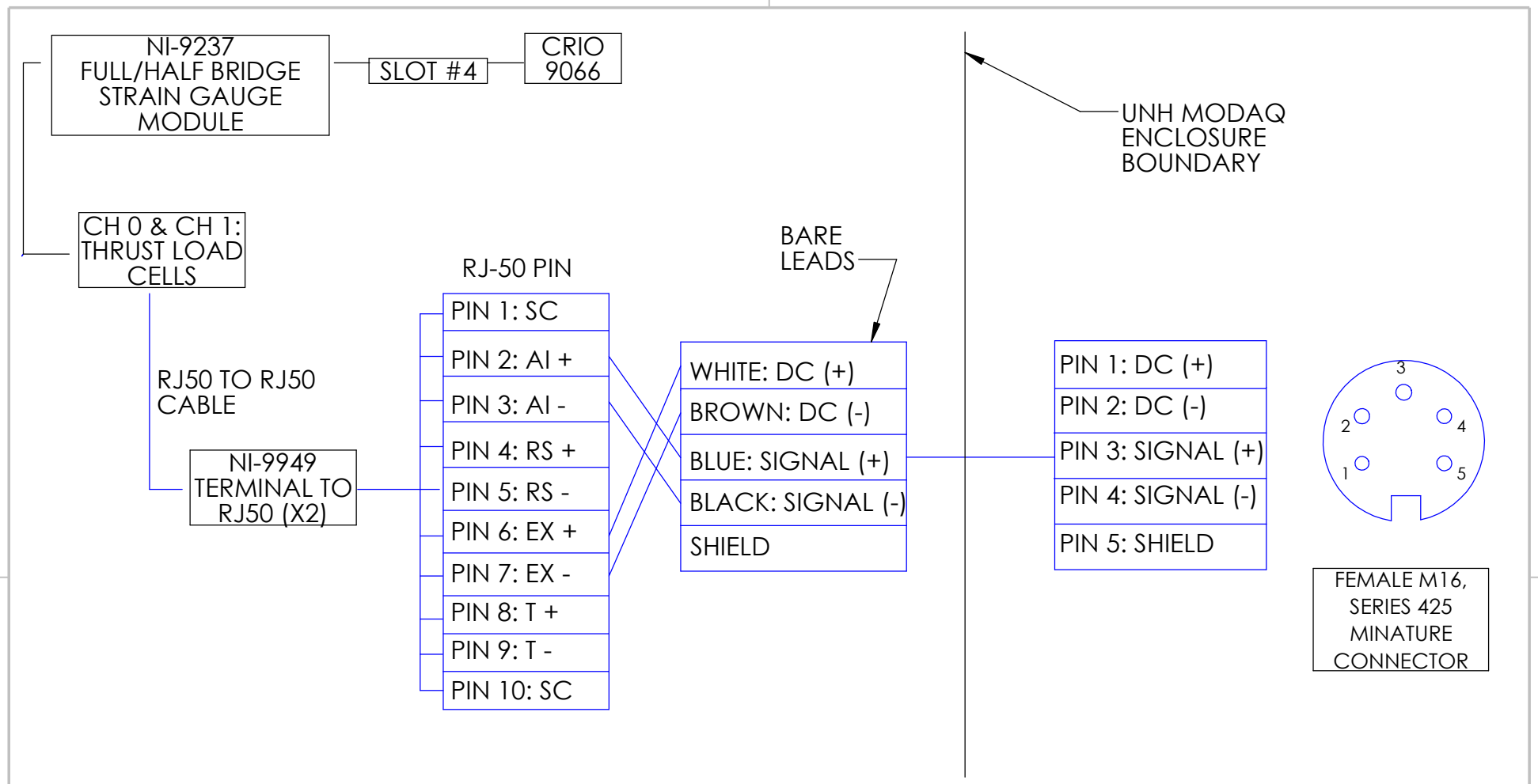

		UNLESS OTHERWISE SPECIFIED:		NAME	DATE
		DIMENSIONS ARE IN INCHES TOLERANCES: FRACTIONAL ± ANGULAR: MACH ± BEND ± TWO PLACE DECIMAL ± THREE PLACE DECIMAL ±	DRAWN	POB	12/03/21
			CHECKED		
			ENG APPR.		
			MFG APPR.		
		INTERPRET GEOMETRIC TOLERANCING PER:	Q.A.		
		MATERIAL	COMMENTS:		
NEXT ASSY	USED ON	FINISH			
APPLICATION		DO NOT SCALE DRAWING			

TITLE:

THRUST LC DATA CONNECTION

SIZE	DWG. NO.	REV
A	POB.2021.9	

SCALE: 1:1 | WEIGHT: | SHEET 1 OF 1

NI-9219 UNIVERSAL ANLALOG INPUT — SLOT #5 — CRIO 9066

CH 0: Tension Link LC #1		
	PIN 1: OPEN	PIN 4: + SIGNAL
	PIN 2: OPEN	PIN 5: - SIGNAL
	PIN 3: OPEN	PIN 6: OPEN

+24VDC

-24VDC

CH 1: OPEN	PIN 1: OPEN	PIN 4: OPEN
	PIN 2: OPEN	PIN 5: OPEN
	PIN 3: OPEN	PIN 6: OPEN

CH 2: OPEN	PIN 1: OPEN	PIN 4: OPEN
	PIN 2: OPEN	PIN 5: OPEN
	PIN 3: OPEN	PIN 6: OPEN

CH 3: OPEN	PIN 1: OPEN	PIN 4: OPEN
	PIN 2: OPEN	PIN 5: OPEN
	PIN 3: OPEN	PIN 6: OPEN

PIN 1: + POWER
PIN 2: - POWER
PIN 3: - SIGNAL
PIN 4:+ SIGNAL

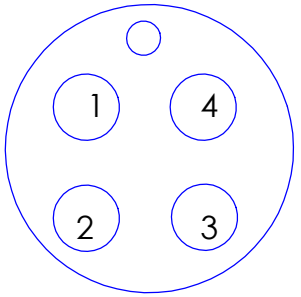

FEMALE M16, SERIES 425 MINATURE CONNECTOR

UNH MODAQ ENCLOSURE

NEXT ASSY	USED ON	
APPLICATION		DO NOT SCALE DRAWING

UNLESS OTHERWISE SPECIFIED:

DIMENSIONS ARE IN INCHES
TOLERANCES:
FRACTIONAL ±
ANGULAR: MACH ± BEND ±
TWO PLACE DECIMAL ±
THREE PLACE DECIMAL ±

INTERPRET GEOMETRIC TOLERANCING PER:

MATERIAL

FINISH

	NAME	DATE
DRAWN	POB	12/03/21
CHECKED		
ENG APPR.		
MFG APPR.		
Q.A.		

COMMENTS:

TITLE:

TENSION LINK LC DATA CONNECTION

SIZE	DWG. NO.	REV
A	POB.2021.8	

SCALE: 1:1 | WEIGHT: | SHEET 1 OF 1

APPENDIX D

UNH MODAQ Roxtec Gland Allocations

1	3	5	7	9	11	13	15	17	19	21	23	25	27	29	31
2	4	6	8	10	12	14	16	18	20	22	24	26	28	30	32

Position	Cable Assignment	Position	Cable Assignment	Position	Cable Assignment	Position	Cable Assignment
1	AC Input	9	ADV #1 Power	17	Thrust LC #1 (Port)	25	Open
2	Ethernet Jack	10	ADV #1 Data	18	Thrust LC #2 (Star)	26	Open
3	GS Signal	11	ADV #2 Power	19	Tension Link LC #1	27	Open
4	Voltsys Rectifier	12	ADV #2 Data	20	Open	28	Open
5	Sensix #1	13	YOST IMU Power	21	Open	29	Open
6	Sensix #2	14	YOST IMU Data	22	Open	30	Open
7	Sensix #3	15	ADV #3 Power	23	Open	31	Open
8	Sensix #4	16	ADV #3 Data	24	Open	32	Open

**As Viewed from the outside of the enclosure

APPENDIX E

UNH MODAQ Component List

Sub assembly	Item description	Supplier	Part No	Justification
Component	GDSTIME Brushless Radial Blower Fan High Speed 24V DC Centrifugal Fan 120mm x120mm x 32mm	Amazon		Cooling Fan
Component	Side Hinge and Slotted Latch 30"L x 24"W x 12"D	McMaster	7619K142	MODAQ Enclosure
Component	Electrical-Insulating Garolite XX Sheet, Brown 36"L x 24"W x 1/4"T	McMaster	8525K204	Insulated Back Plate Material
Component	Roxtec EZENTRY 32/32 Cable Gland	Excel Automation Inc.		Waterproof gland for MODAQ enclosure
Component	WIRE DUCT SOLID 2PC RIVET 6.56'	Digi-Key	3240191	Cable management
Component	Additional RMS-100 Relay Boards	Ethertek Circuits		
Component	T-H MARINE–Cable Boot w/Ring 4-1/2" hole	West Marine	415085	gland for smaller connection box
Component	RMS-100 Remote Monitoring System	Ethertek Circuits	RMS-100	Additional RMS-100 board to control secondary relay board
Component	4 Core 8th Intel Core i5-8259U 3.8Ghz Beelink Mini PC 16GB RAM 512GB	Amazon		Mini PC to run labivew locally inside Enclosure
Component	Cell Modem/ Ethernet router			
Component	RMS-100 Remote Monitoring Board	Ethertek Circuits		
Component	USB Relay Board	Ethertek Circuits		
cRIO Controller	LaCie Rugged SSD 500GB Solid State Drive	Amazon		Local Data Storage for MODAQ
cRIO Controller	NI cRIO- 9066 (CompactRIO Controller)	NI		Controller to match the NREL MODAQ software platform
cRIO Controller	NI-9237: 4 ch, +/- 25mV/V, 50kS/s/ch, 24-Bit	NI		4-ch RJ50 Input Simultaneous Bridge Module
cRIO Controller	NI-9467: GPS Module	NI		
cRIO Controller	NI-9219: Universal Analog	NI		
cRIO Controller	NI-9870: Serial Connection w/ 10P10C to DE9 Cables	NI		
cRIO Controller	NI-9915: DIN Rail Mounting Kit 8-slot chassis	NI		
cRIO Controller	Standard Service Plan	NI		
Data Connection	Connector DB9 RS232 D-SUB Male Serial Adapter 9-pin Port Adapter to Terminal Connector Signal Module with case	Amazon		Terminate the IMU Cable to connect to female DB9 connector passing through gland
Data Connection	Digi-Serial Cable-DB-9 (f)-Bare Wire-4 Ft	Amazon		Pass through DB9 Cable for IMU - connect to NI9949 and 5VDC Power Supply
Data Connection	Thrust Load Cell Extension Cables Series 425 5 pin 2m	binder-usa	79-6114-20-05	
Data Connection	RJ-50 connection crimping tool	Amazon		To make custom length RJ-50 connections for C-Series Module Interface Cables
Data Connection	RJ-50 connection heads pk of 10	Amazon		New Ends for RJ-50 custom Cables
Data Connection	Cable Strain Relief Boots pk of 100	Amazon		Verify proper size for exitsting cables
Data Connection	Diagnostic Breakout Board with Switches and RJ50 (10P10C) Connectors	Winford	BTS10P10CSJ-R-FT	RJ50 cable connection verification and in line troubleshooting tool
Data Connection	NI 9942 4-Position Connector Kit	NI	194611-01 (Connector)	Power Supply cable for NI 9237 module
Data Connection	6FT DB9 SERIAL STRAIGHT M/F	Digi-Key	2768-M05-101-ND	D-sub 9 serial extension cables
Data Connection	USB TYPE A TO TYPE C CABLE 6"	Digi-Key	1528-4472-ND	Longer Cable for LACIE External Hard drive
Data Connection	Female cable connector, shielded	binder-usa	79-6114-20-05	Tension Link SSM Load Cell Cable Connection
Data Connection	Cable plug connector, shielded	binder-usa	79-6113-20-05	Tension Link SSM Load Cell Cable Connection

Sub assembly	Item description	Supplier	Part No	Justification
Data Connection	DTECH USB to RS485 Adapter RS422 Serial Port Cable with CP2102 Chip Terminal Board LED Lights Ferrite Core for Windows 10 8 7 XP Mac (5 Feet)	Amazon		Voltsys arduino interface to connect with MODAQ
Data Connection	DTECH RS232 to RS485/RS422 Serial Communication Data Converter	Amazon		Voltsys arduino interface to connect with MODAQ
Data Connection	DFRobot Accessories RS232 Shield	Mouser	426-DFR0258	RS232 adruino shield to try and connect Rectifer data output into MODAQ
Data Connection	Cable Assembly Coaxial SMA to SMA RG-174 60.0" (1.5m) 5.0'	Digi-Key	2217-Q-2V034000306 0I-ND	Connection Cable for GPS Antenna to 9467 module
Data Connection	Voltsys RS 485 MODBud Arduino Shield	Voltsys	CUSTOMC1	To inteface the Rectifer data with MODAQ
Data Connection	USBGear 2ft. Black Right to Straight A to B 28/28AWG Cable USB 2.0 RoHS	amazon		RMS 100 to RMS100 Relay Board cable
Data Connection	USBGear 1ft. Black Right to Straight A to B 28/28AWG Cable USB 2.0 RoHS	amazon		RMS 100 to RMS100 Relay Board cable
Data Connection	MCDLS-F locking sleeve BLACK	MacArtney	1308480	For Thrust Load Cell Cables
Data Connection	NI-9949: RJ-50 to Screw Terminal	NI		
Hardware	Dull 316 Stainless Steel, 4" Center-to-Center Width, 5/16" Grip Diameter	McMaster	18645A23	Threaded-Hole Round Pull Handle
Hardware	Electrical-Insulating Hard Fiber Washer No 10 Screw Size, 0.203" ID, 0.438" OD pk of 100	McMaster	96100A130	Din Rail Mounting Hardware insulators
Hardware	External Hex Head Drilling Screws for Metal Corrosion-Resistant Steel, No 10 Size, 1" L - pk of 100	McMaster	91324A510	Din Rail Self Tapping Mounting Hardware
Hardware	Threaded-Hole Round Pull Handle Dull 303 Stainless Steel, 6" Center-to-Center Width, 1/4"Grip Diameter	McMaster	1726A3	
Hardware	Electrical-Insulating Female Threaded Standoff Glazed Grade L5 Ceramic, Round, 1/4" OD, 1" Long	McMaster	94335A119	
Hardware	Zinc-Plated Alloy Steel Socket Head Screw 6-32 Thread Size, 5/8" Long pk 50	McMaster	90128A150	
Hardware	Zinc-Plated Alloy Steel Socket Head Screw 6-32 Thread Size, 3/8" Long pk 50	McMaster	90128A146	
Hardware	Zinc-Plated Steel SAE Washer for Number 6 Screw Size, 0.156" ID, 0.375" OD pk 100	McMaster	90126A509	
Hardware	Zinc-Plated Steel Split Lock Washer for Number 6 Screw Size, 0.148" ID, 0.25" OD pk 100	McMaster	91102A730	
Hardware	Zinc-Plated 12L14 Steel Female Threaded Hex Standoff 1/2" Hex, 5" Long, 1/4"-20 Thread	McMaster	92230A054	
Hardware	Unthreaded-Hole Round Pull Handle Polished 304 Stainless Steel, Straight, 20-1/4" C-to-C Width	McMaster	1871A21	Handles to be able to move the MODAQ enclosure
Hardware	Sealing Hex Head Screw 18-8 Stainless Steel 3/8"-16 Thread Size, 3/4" Long	McMaster	92205A622	Sealing mounting hardware for handles
Hardware	Sealing Hex Head Screw 18-8 Stainless Steel 1/4"-20 Thread Size, 3/4" Long	McMaster	92205A540	Sealing mounting hardware for fans
Hardware	Nylon 6/6 Female Threaded Round Standoff 1/4" OD, 1" Length, 6-32 Thread Size	McMaster	96110A024	RMS-100 Mount
Hardware	Nylon 6/6 Female Threaded Round Standoff 1/4" OD, 2" Length, 6-32 Thread Size	McMaster	96110A048	RMS-100 Mount
Hardware	Nylon Threaded Rod 6-32 Thread Size, 2 Feet Long	McMaster	98831A320	RMS-100 Mount
Hardware	Clear Impact-Resistant Polycarbonate 24" x 24" x 3/8" Sheet	McMaster	8574K56	2nd level for MODAQ build
Hardware	Single Clip Mounting Adapter for DIN 3 Rail	McMaster	8961K28	din rail adapter clips
Hardware	Super-Corrosion-Resistant 316 Stainless Steel Socket Head Screw M4 x 0.7 mm Thread, 30 mm Long pk 25	McMaster	92290A180	
Hardware	DIN RAIL 35MMX7.5MM SLOTTED 1M	Digi-Key	277-2064-ND	Din Rail for second level
Hardware	Super-Corrosion-Resistant 316 SS Socket Head Screw- 1/4"-20 Thread Size, 1" Long pk 10	McMaster	92185A542	

Sub assembly	Item description	Supplier	Part No	Justification
Hardware	DIN RAIL MOUNTED AC OUTLET INTER	Digi-Key	277-0804152-ND	For Mini PC AC Input
Hardware	Super-Corrosion-Rst 316 SS Sckt Head Screw M3 X 0.5 mm Thread, 10 mm Long, Packs of 50	McMaster	92290A115	metric m3-0.5 3/8" long Q.2 for mini pc mount
Hardware	Moisture-Resistant Cushioning Washer for 5/16" Screw Size, 0.317" ID, 0.562" OD pk 25	McMaster	93650A155	Vibration resistant washer for panel mount in enclosure
Hardware	Female Threaded Hex Standoff 18-8 SS, 1/2" Hex, 1-7/8" Long, 1/4"-20 Thread, undefined: undefined	McMaster	91115A952	
Hardware	Super-Corrosion-Rst 316 SS Sckt Head Screw 1/4"-20 Thread Size, 3/4" Long, Packs of 10	McMaster	92185A540	
Network	Ethernet Switch	Automation Direct	SE2-SW5U	5 port ethernet switch for inside of Enclosure
Network	Ethernet Switch Panel Mounting Bracket	Automation Direct	SE2-PM1	5 port ethernet switch mounting bracket
Network	NETWORK CABLE TESTER	Digi-Key	TL1119-ND	To test RJ-45 cables
Network	CABLE MOD 8P8C PLUG TO PLUG 3'	Digi-Key	TL1200-ND	For internal ethernet connections to CRIO and RMS 100's
Network	Modular Cable Plug to Plug 8p8c (RJ45, Ethernet) 2.00' (609.6mm) Unshielded	Digi-Key	1847-1061-ND	Network cable for mini pc to network switch in modaq
Network	Modular Cable Jack to Plug 8p8c (RJ45, Ethernet) 5.00' (1.52m) Shielded	Digi-Key	1847-BM-1BJPK005F-ND	Network Interface Cable Network switch to External newtwork lead
Network	Modular Cable Plug to Plug 8p8c (RJ45, Ethernet) 20.00' (6.10m) Shielded	Digi-Key	MP-6ARJ45SNNB-020-ND	Platform Network Switch to MODAQ interface
Network	USB 3.0 TO ETHERNET ADAPTER	Digi-key	TL824-ND	
Power Distribution	Surge Protection Filter - 120VAC 15A	Digi-Key	MA15D1SI	Protect MODAQ system components
Power Distribution	Cicuit Breaker 10A 120VAC	Digi-Key	9926251010	Protect MODAQ system components
Power Distribution	CONN TERM BLK FEED THRU 12-26AWG - Black	Digi-Key	3045088	UNH MODAQ Power Distribution
Power Distribution	CONN TERM BLK FEED THRU 12-26AWG - White	Digi-Key	3045075	UNH MODAQ Power Distribution
Power Distribution	CONN TERM BLK FEED THRU 12-26AWG - Blue	Digi-Key	3044089	UNH MODAQ Power Distribution
Power Distribution	CONN TERM BLK GROUND 12-26AWG - Yellow/Green	Digi-Key	3044092	UNH MODAQ Power Distribution
Power Distribution	CONN TERM BLK FEED THRU 12-26AWG - Gray	Digi-Key	3044076	UNH MODAQ Power Distribution
Power Distribution	CONN TERM BLK END BRCKT RAIL GRY	Digi-Key	3022276	UNH MODAQ Power Distribution
Power Distribution	15W 5V DIN PS 85-264VAC	Digi-Key	SVL35100	5VDC IMU Power Supply
Power Distribution	HOOK-UP STRND 16AWG 300V BLK 50'	Digi-Key	1569-16-1-0500-001-1-TS	120VAC 10A Live Wire
Power Distribution	HOOK-UP STRND 16AWG 300V WHT 50'	Digi-Key	1569-16-1-0500-002-1-TS	120VAC 10A Nuetral Wire
Power Distribution	HOOK-UP STRND 16AWG 300V GRN 50'	Digi-Key	1569-16-1-0500-007-1-TS	120VAC 10A Ground Wire
Power Distribution	HOOK-UP STRND 20AWG 300V BLU 50'	Digi-Key	1569-20-1-0500-005-1-TS	DC High Voltage
Power Distribution	HOOKUP STRND 20AWG BL/WH QTY 50ft	Digi-Key	31663250	DC Neutral Voltage
Power Distribution	JUMPER TERM BLK 4POS FLAT PIN	Digi-Key	3030187	Terminal Block Jumpers
Power Distribution	WIRE DUCT SOLID 2PC RIVET 6.56'	Digi-Key	3240193	Cable management
Power Distribution	WIRE DUCT SOLID 2PC RIVET 6.56'	Digi-Key	3240191	Cable management

Sub assembly	Item description	Supplier	Part No	Justification
Power Distribution	CBL TWIST LOCK 5.5X2.5MM PLUG	Digi-Key	10-02937	Instrument Power Quick disconnects
Power Distribution	CBL TWIST LOCK 5.5X2.5MM JACK	Digi-Key	10-02938	Instrument Power Quick disconnects
Power Distribution	BMP21 Plus Series PermaSleeve Heat-Shrink Tubing Black on White 16-22AWG	Bradyid	B-342	Wire Labelmaker cartridge
Power Distribution	BMP21-PLUS Portable Label Printer	Bradyid	BMP21-PLUS	Label Printer
Power Distribution	CONN TERM BLK END BRCKT RAIL GRY	Digi-Key	3022276	UNH MODAQ Power Distribution
Power Distribution	CBL TWIST LOCK 5.5X2.5MM PLUG	Digi-Key	10-02937	Instrument Power Quick disconnects
Power Distribution	CBL TWIST LOCK 5.5X2.5MM JACK	Digi-Key	10-02938	Instrument Power Quick disconnects
Power Distribution	120W 24V DIN PS 85-264VAC	Digi-Key	2106-SVL5-24-100-ND	24 VDC Power Supply to Have in the Lab
Power Distribution	CONN TERM BLK FEED THRU 12-26AWG - Blue	Digi-Key	3044089	UNH MODAQ Power Distribution
Power Distribution	CONN TERM BLK FEED THRU 12-26AWG - Gray	Digi-Key	3044076	UNH MODAQ Power Distribution
Power Distribution	HOOK-UP STRND 20AWG 300V BLU 50'	Digi-Key	1569-20-1-0500-005-1-TS	DC High Voltage
Power Distribution	HOOKUP STRND 20AWG BL/WH QTY 50ft	Digi-Key	31663250	DC Neutral Voltage
Power Distribution	50W 12V DIN PS 85-264VAC	Digi-Key	2106-SVL412100-ND	Upgraded 12 VDC PSU for MODAQ
Power Distribution	AC/DC CONVERTER 9VDC 20W	Digi-Key	102-PSK-20D-9-DIN-ND	120VAC to 9VDC converter to power NI 9237
Power Distribution	Heat Shrink EPS300-1/2-6"-BLACK-10-10 PC PKS	Digi-Key	3M161190-ND	Tension Link SSM Load Cell Cable Connection
Power Distribution	CORD IEC320-C14 - 320-C13 6.56'	Digi-Key	486-3778-ND	AC Power Cable Female -
Power Distribution	PWCD-515PC13-10A-10F-BLK	Digi-Key	2830-PWCD-515PC13-10A-10F-BLK-ND	AC Power Cable Male
Power Distribution	BMP21 Plus Series PermaSleeve Heat-Shrink Tubing Black on White 16-22AWG	Bradyid	B-342	Wire Labelmaker cartridge
Power Distribution	WRISTBAND ELASTIC W/6'CORD 4MM	Digi-Key	16-1087-ND	Self Grounding to prevent static discharge
Power Distribution	PC-MF4-PT CSERIES Microfit Power Cable female to Pigtail	NI (provided by NREL)	198159-01	For 9237 external power supply input
Power Distribution	Ring Terminals Nylon Insulated, for 22-18 GA and NO. 6 Screw, undefined: undefined, Packs of 50	McMaster	7113K451	
Power Distribution	NI PS-15: 24V Power Supply	NI		

APPENDIX F

Upgrades & Maintenance of Existing DAQ's

F.1 LB-DAS/BDI DAQ Maintenance

- Fall 2019 - LB Server Hard drive failure thankfully Seagate could recover the drive
- 12/12/19 cloned drive replaced in LB-Server and went back up and running
  - Hard drives used in LB-Server were used and sourced from Chase OE department
  - NEI maintains a backup of the Cimplicity Project code in their cloud storage
- 3/19/2021 - Replacement of two Fiber to Network Converters in Memorial Bridge control room to fix OPEN VPN connectivity issue
- March 2021 - First signs of something wrong with platform weather station – high air temp readings greater than 100F recorded
- July 14, 2021 - MacArtney Multiplexer removed from platform
- 8/6/2021 - A new Core was installed in the BDI Cabinet
- 10/12/21 - VGP strain gauges were tested by BDI personnel and deemed not functional & need to be replaced
- 9/8/2021 - MUX installed back on platform and a replacement MOXA VDSL network extender was installed in the MacArtney Topside Panel

F.2 MacArtney Mux Repairs (July/August 2021)

After communication was lost between the instruments in main Cimplicity DAQ and the MacArtney multiplexer, the AC power was verified at the terminals of the umbilical. When this was confirmed the MUX was removed from the platform on 7/14/2021 and brought back to Chase Ocean Engineering Lab. After the unit was disassembled it was determined the internal AC to DC Power Supply unit had failed as the power packs internal fan was not functioning nor was there any voltage on the output terminals. The VOX Power NEVO+600S

power supply was replaced and as a precaution the (Q. 2) 24VDC outputs and (Q. 1) 48VDC output units were also replaced (Figure F.1).

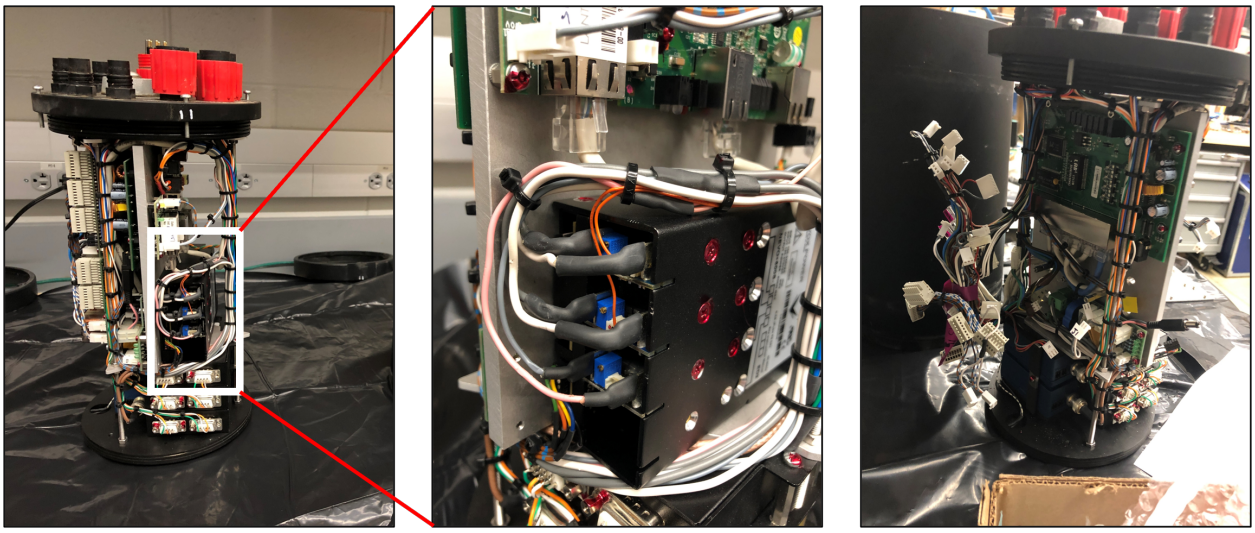

Figure F.1: Photos indicating the location of the power supplied that was replaced within the MUX

Additionally, around the same time, the MOXA IEX-402-VDSL2 unit failed which provides the network connection to the Lantronix board inside the multiplexer. This component is located inside the MacArtney topside box mounted between the inverter and TIP (Figure 2.4). The unit was extensively evaluated by NEI who concluded the unit needed to be replaced. A new MOXA IEX-402-VDSL2 was procured, and a bench test was performed using the New_Hampshire_Mux.exe interface software provide by MacArtney. To complete the bench test follow along with the MacArtney manual [44] along with the following details:

Multiplexer Communication Port Settings	
Baud Rate	19200
Parity	None
# bits	8
stop bits	1

1. CPR software needed to be installed on the field laptop to generate a virtual com port via an IP address.

2. The Lantronix was already set up to be on the Living Bridge Server and was assigned a new IP address, not the 10.0.70.1 as stated in the MacArtney Manual. The new IP address is 192.168.3.2 on the bridge subnet which corresponds to the MacArtney Mux nomenclature in the NEI Living Bride Manual.

3. There was no configuration file required for the IEX-402-VDSL except to ensure all the switches are in the off position.

Multiplexer Network Cable Connection			
Inside MUX		End Terminal on Cable	IEX-402-VDSL2
Tip	Green Wire	Green Wire to T/R +	DSL -1
Ring	Orange Wire	White Wire to T/R -	DSL - 2

APPENDIX G

Resistor Bank Rebuild - IR Test Results

Incoming Insulation Resistance (IR) Test Results			
Date: 8/31/2021 Test Voltage: 500 VDC			
Circuit Tested	IR Results (M-Ohms)	Circuit Tested	IR Results (M-Ohms)
Full Circuit	0.40	HV Terminal to 1 Jumper	>55
HV terminal to Res. #9	1.28	Resistor 1-4	1.8
LV terminal to #9 Jumper	0.61	Resistor 5-9	4.18
9-10 Jumper to 18	1.3	Resistor 10-14	3.63
18-19 Jumper to LV terminal	1.05	Resistor 15 – 18	2.25
22 to LV Jumper	177	Resistor 19-20	3.3

Table G.1: 8/31/2021 Incoming Insulation Resistance (IR) Test Results

Individual Resistors IR Test Results 500VDC									
Results in Mega-Ohms 8/31/2021									
#	IR	#	IR	#	IR	#	IR	#	IR
1	4.35	6	16.8	11	25.2	16	23.6	21	2.18
2	15.13	7	24.1	12	25.6	17	7.92	22	9.35
3	7	8	14.8	13	16.6	18	9.36		
4	26.1	9	34	14	12.5	19	5		
5	135	10	48.8	15	10	20	14.95		

Table G.2: 8/31/2021 Individual Resistors IR Test Results 500VDC

Resistor 10 Results IR Test Results		
8/31/2021	9/1/2021	9/1/2021
500 VDC	1000 VDC	1000 VDC
48.8 M-Ohms	11 G-Ohms (hot)	600 M-Ohms (room temp)

Table G.3: 8/31/2021 to 9/1/2021 Resistor 10 Results IR Test Results

Individual Resistors IR Test Results 1000VDC									
Results in Mega-Ohms 9/15/2021 3:22pm humid air high bay door open									
#	IR	#	IR	#	IR	#	IR	#	IR
1	352	6	>11k	11	360	16	453	21	61.2
2	35.7	7	141.2	12	3k	17	60	22	-
3	50	8	160	13	1.2 G	18	29.5		
4	255	9	360	14	-	19	38.5		
5	-	10	1.5k	15	300	20	476		

Table G.4: 9/15/2021 Individual Resistors IR Test Results 1000VDC

Individual Resistors IR Test Results 1000VDC									
Results in Mega-Ohms 9/16/2021 8am									
#	IR	#	IR	#	IR	#	IR	#	IR
1	>11k	6	>11k	11	>11k	16	>11k	21	>11k
2	10.6k	7	>11k	12	>11k	17	2.8k	22	-
3	>11k	8	>11k	13	>11k	18	>11k		
4	>11k	9	>11k	14	-	19	>11k		
5	-	10	>11k	15	>11k	20	>11k		

Table G.5: 9/16/2021 Individual Resistors IR Test Results 1000VDC

Individual Resistors IR Test Results 1000VDC									
Results in Mega-Ohms 9/23/2021 8am 30s values									
#	IR	#	IR	#	IR	#	IR	#	IR
1	1.18k	6	1.28k	11	1.22k	16	1.13k	21	1.04k
2	1.23k	7	1.28k	12	1.20k	17	1.12k	22	1.01k
3	1.25k	8	1.26k	13	1.17k	18	1.09k		
4	1.36k	9	1.26k	14	1.15k	19	1.08k		
5	1.27k	10	1.25k	15	1.14k	20	1.05k		
Winding Resistance							11.3 Ohms		

Table G.6: 9/23/2021 Individual Resistors IR Test Results 1000VDC

9/23/2021 Individual Resistors IR Test Results 1000VDC									
Results in Mega-Ohms 10/01/2021 8am 30s values									
#	IR	#	IR	#	IR	#	IR	#	IR
1	6.3k	6	7.6k	11	7.9k	16	6.6k	21	6.0k
2	6.6k	7	7.8k	12	7.4k	17	6.5k	22	6.0k
3	7.0k	8	7.8k	13	7.3k	18	6.3k		
4	7.5k	9	8.0k	14	7.0k	19	6.2k		
5	7.6k	10	7.8k	15	6.7k	20	6.1k		
Strip Heater Studs 100VDC IR							>110 Mega-Ohms		
Winding Resistance							11.53 Ohms		

Table G.7: 10/01/2021 Individual Resistors IR Test Results 1000VDC

APPENDIX H

Instrument Deployment Specification Tables

Location	Stern	Bow
Reference #	1	2
Power Source	Multiplexer 24 VDC PSU	
Power	Low	
Coordinate System	XYZ	
Transducer Orientation	4 Beam Convex	
Transducer Beam Angle [°]	22	
Deployment Orientation	Downward Facing	
Serial Output	Enabled	
Baud Rate	9600	
Communication Protocol	RS232 Serial	
Velocity Accuracy [mm/s]	0.25 % +/- 2.0	
Temperature [° C]	+/- 0.4 from -5 to 45	

Table H.1: ADCP Deployment Specifications

Standard Tab	
Sampling Rate (Output) [Hz]	16
Nominal Velocity Range [m/s]	+/- 4
Sampling Interval	Continuous Sampling
Coordinate System	XYZ
IMU	No
Speed of Sound	measured
salinity (ppt)	35
Geography	Open Ocean
Advanced Tab	
Sampling Volume (mm)	14.9
Transmit Length (mm)	4.0
Power Level	High
Horizontal velocity range [m/s] (calculated in software)	5.25
Vertical velocity range [m/s] (calculated in software)	1.50
Additional Information	
Velocity Accuracy	±0.5% of measured value ±1 mm/s
Operating Frequency [MHz]	6
Analog Outputs	Not Enabled

Table H.2: ADV Deployment Settings

APPENDIX I

Instrument Data Set Column Headers and Units

Voltsys Output Variables		
No.	Variable Name/Unit	Units/Resolution
1	UTC yyyy	yyyy
2	UTC MM	MM
3	UTC dd	dd
4	UTC HH	HH
5	UTC mm	mm
6	UTC ss	ss.sssssssss
7	Anemo Frequency	0.1 m/s
8	Turbine Freq.	0.1 Hz
9	Turbine Voltage V-AC L-L	0.1 V
10	Controller Voltage V-DC	0.1 V
11	DC Load Turbine Level	0-255
12	DumpLoad Power 1sec	0.1 kW
13	DumpLoad Power 10sec	0.1 kW
14	DumpLoad Power 100sec	0.1 kW
15	Turbine Voltage Ph.1 V-AC L-N	0.1 V
16	Turbine Voltage Ph.2 V-AC L-N	0.1 V
17	Turbine Voltage Ph.3 V-AC L-N	0.1 V
18	Inverter Ph1 V-AC L-N	0.1 V
19	Inverter Ph2 V-AC L-N	0.1 V
20	Inverter Ph3 V-AC L-N	0.1 V
21	Inverter Address	1-255
22	Inverter State	0-255
23	Inverter Input V-DC	0.1 V
24	Inverter Input A-DC	0.01 A

25	Inverter V-AC L-L	0.1 V
26	Inverter A-AC L-L	0.01 A
27	Inverter Grid Freq.	0.01 Hz
28	Inverter Power Level	0.10%
29	Inverter I Leak	0.1 mA
30	Controller Temp.	0.1 C
31	Inverter Power	kW
32	Inverter Power Meter	Whr
33	Status Code 1	-
34	Status Code 2	-
35	Status Code 3	-
36	Rectifier Cont Hour	U8
37	Recifier Min. and Sec.	U16
38	Anemo Peak 2	0.1 Hz
39	Peak Turbine Freq.	0.1 Hz
40	Controller Ram	-
41	Dumpload V-DC Avg.	0.1 V-DC
42	Controller Pulse Meter	Whr
43	AuxRelay	-
44	RS485 Stage	-
45	RS485 com/sec	Com/sec
46	DumpLoad V-DC High Setting	V-DC
47	DumpLoad V-DC Low Setting	V-DC
48	Capacitor V-DC	V-DC
49	Contactor Voltage	0.1V
50	Solis Energy Today	1 kWh

51	Solis Energy Yesterday	1 kWh
52	Solis Energy this Month	1 kWh
53	Solis Energy Last Month	1 kWh
54	Solis Energy this Year	1 kWh
55	Cntrl. Txt char 1	char dbl
56	Cntrl. Txt char 2	char dbl
57	Cntrl. Txt char 3	char dbl
58	Cntrl. Txt char 4	char dbl
59	Cntrl. Txt char 5	char dbl
60	Cntrl. Txt char 6	char dbl
61	Cntrl. Txt char 7	char dbl
62	Cntrl. Txt char 8	char dbl
63	Cntrl. Txt char 9	char dbl
64	Cntrl. Txt char 10	char dbl
65	Cntrl. Txt char 11	char dbl
66	Cntrl. Txt char 12	char dbl
67	Cntrl. Txt char 13	char dbl
68	Cntrl. Txt char 14	char dbl
69	Cntrl. Txt char 15	char dbl
70	Cntrl. Txt char 16	char dbl
71	Cntrl. Txt char 17	char dbl
72	Cntrl. Txt char 18	char dbl
73	Cntrl. Txt char 19	char dbl
74	Cntrl. Txt char 20	char dbl

Table I.1: Voltsys data variables and units

Shark Meter Output Variables		
No.	Variable Name/Unit	Units/Resolution
1	YYYY	Time UTC
2	MM	Time UTC
3	dd	Time UTC
4	HH	Time UTC
5	mm	Time UTC
6	ss.sssssss	Time UTC
7	Sequence Number	#
8	VAR Hrs Negative	var-hrs
9	VAR Hrs Net	var-hrs
10	VAR Hrs Positve	var-hrs
11	AB L-L Voltage	Volts AC
12	A Phase L-N Voltage	Volts AC
13	BC L-L Voltage	Volts AC
14	B Phase L-N Voltage	Volts AC
15	CA L-L Voltage	Volts AC
16	C Phase L-N Voltage	Volts AC
17	kilo-Watt Hrs Delivered	kWatt Hrs
18	kilo-Watt Hrs Net	kWatt Hrs
19	kilo-Watt Hrs Recieved	kWatt Hrs
20	kilo-Watt Hrs Total	kWatt Hrs
21	A Phase Current	Amps AC
22	B Phase Current	Amps AC
23	C Phase Current	Amps AC
24	Power Factor	-

25	Grid Frequency	0.01 Hz
26	Reactive Power 3-Phase	vars
27	Apparent Power 3-Phase	V-A
28	Real Power 3-Phase	Watts
29	Time Source	1=Real — 3=Artificial

Table I.2: Shark 100 meter data variables and units

Yost IMU Output Variables		
No.	Variable Name/Unit	Units/Resolution
1	YYYY	Time UTC
2	MM	Time UTC
3	dd	Time UTC
4	HH	Time UTC
5	mm	Time UTC
6	ss.sssssss	Time UTC
7	String Length Checksum	Characters
8	Corrected Gyro X	Radians/sec
9	Corrected Gyro Y	Radians/sec
10	Corrected Gyro Z	Radians/sec
11	Corrected Accel X	g
12	Corrected Accel Y	g
13	Corrected Accel Z	g
14	Mag Vector X	Gauss
15	Mag Vector Y	Gauss
16	Mag Vector Z	Gauss

Table I.3: Yost IMU data variables and units

Tower Weather Station Output Variables		
No.	Variable Name/Unit	Units/Resolution
1	YYYY	Time UTC
2	MM	Time UTC
3	dd	Time UTC
4	HH	Time UTC
5	mm	Time UTC
6	ss.sssssss	Time UTC
7	Sequence Number	#
8	Absolute Humidity- Empty	
9	Air Temp (C)	0.1 deg C
10	Air Temp (F)	F
11	Barometric Pressure	0.001 bar
12	Dew Point (C)	0.1 deg C
13	Dew Point (F)	F
14	Relative Humidity	0.10%
15	Water Temp - Empty	C
16	Wind Direction Magnetic	0.1 deg
17	Wind Speed (m/s)	0.1 m/s
18	Wind Chill	0.1 deg C
19	Pitch - Empty	
20	Roll - Empty	
21	Script Running	
22	Magnetic Deviation - Empty	0.1 degree
23	Magnetic Sensor Heading - Empty	0.1 deg
24	Heat Index	0.1 deg

25	Magnetic Variation	0.1 deg
26	Wind Direction Relative	0.1 deg
27	Wind Speed (knots)	0.1 knots

Table I.4: Tower Weather Station data variables and units

APPENDIX J

Instrument Data Quality Control Test Results

ADCP_1_Bin_4	Test Description	Lower Limit	Upper Limit	# of points flagged	Increase in Total points Flagged	% of Total Points Flagged After each test
Test1	Battery Voltage (0.1 V)	12	24	0	0	0.00
Test3a	Heading (1 deg)	29	38	46	46	0.10
Test3b	Pitch (1 deg)	-2	2	7	1	0.11
Test3c	Roll (1 deg)	-2	2	6	0	0.11
Test6	Signal Strength (0.25 dBm)	-10	-80	702	701	1.68
Test7	Sig to Noise Ratio (0.25 dB)	10	90	701	0	1.68
Test9	Good Pings (#)	58	60	182	166	2.06
Test10	Current Magnitude (m/s)	0	3.5	0	0	2.06
Test12a	INS XVEL MAX (mm/s)	0	3000	0	0	2.06
Test12b	INS YVEL MAX (mm/s)	0	2000	0	0	2.06
Test13	INS ZVEL MAX (mm/s)	0	1000	0	0	2.06
Test15a	Ins X Vel Rate of Change (mm/s)		500	545	514	3.21
Test15b	Ins Y Vel Rate of Change (mm/s)		500	90	81	3.39
Test16a	Ins X Vel Spike (mm/s)	-500	500	113	27	3.46
Test16b	Ins Y Vel Spike (mm/s)	-500	500	2	0	3.46
Test17	Repeat Value in successive points ()			453	436	4.44
Test20	Vertical 2-D Velocity Gradient()	0	300	264	242	4.98
Test21	Time Vector dt outside 120 +/- 10s()	110	130	344	184	5.39

Figure J.1: ADCP 1 Bin# 4 (approx. center of turbine swept area) quality control results table indicating the tests performed, the number of points flagged from each test and the total number of points flagged. A total of 5.39% of the data was flagged and removed at this depth bin.

ADCP_1_Bin_20	Test Description	Lower Limit	Upper Limit	# of points flagged	Increase in Total points Flagged	% of Total Points Flagged After each test
Test1	Battery Voltage (0.1 V)	12	24	0	0	0.00
Test3a	Heading (1 deg)	29	38	46	46	0.10
Test3b	Pitch (1 deg)	-2	2	7	1	0.11
Test3c	Roll (1 deg)	-2	2	6	0	0.11
Test6	Signal Strength (0.25 dBm)	-10	-80	690	689	1.66
Test7	Sig to Noise Ratio (0.25 dB)	10	90	673	0	1.66
Test9	Good Pings (#)	58	60	1839	1717	5.52
Test10	Current Magnitude (m/s)	0	3.5	0	0	5.52
Test12a	INS XVEL MAX (mm/s)	0	3000	0	0	5.52
Test12b	INS YVEL MAX (mm/s)	0	2000	0	0	5.52
Test13	INS ZVEL MAX (mm/s)	0	1000	0	0	5.52
Test15a	Ins X Vel Rate of Change (mm/s)		500	1402	1117	8.03
Test15b	Ins Y Vel Rate of Change (mm/s)		500	303	243	8.58
Test16a	Ins X Vel Spike (mm/s)	-500	500	419	87	8.77
Test16b	Ins Y Vel Spike (mm/s)	-500	500	14	3	8.78
Test17	Repeat Value in successive points ()			435	389	9.66
Test20	Vertical 2-D Velocity Gradient()	0	300	177	54	9.78
Test21	Time Vector dt outside 120 +/- 10s()	110	130	344	162	10.14

Figure J.2: ADCP 1 Bin# 20 (approx. 5m below water level) quality control results table indicating the tests performed, the number of points flagged from each test and the total number of points flagged. A total of 10.14% of the data was flagged and removed at this depth bin.

ADCP_2_Bin_4	Test Description	Lower Limit	Upper Limit	# of points flagged	Increase in Total points Flagged	% of Total Points Flagged After each test
Test1	Battery Voltage (0.1 V)	12	24	0	0	0.00
Test3a	Heading (1 deg)	135	150	6	6	0.01
Test3b	Pitch (1 deg)	-2	2	4	0	0.01
Test3c	Roll (1 deg)	-2	2	4	0	0.01
Test6	Signal Strength (0.25 dBm)	-10	-80	2481	2480	5.79
Test7	Sig to Noise Ratio (0.25 dB)	10	90	518	0	5.79
Test9	Good Pings (#)	58	60	19	17	5.83
Test10	Current Magnitude (m/s)	0	3.5	0	0	5.83
Test12a	INS XVEL MAX (mm/s)	0	3000	0	0	5.83
Test12b	INS YVEL MAX (mm/s)	0	2000	0	0	5.83
Test13	INS ZVEL MAX (mm/s)	0	1000	0	0	5.83
Test15a	Ins X Vel Rate of Change (mm/s)		500	152	141	6.16
Test15b	Ins Y Vel Rate of Change (mm/s)		500	88	83	6.35
Test16a	Ins X Vel Spike (mm/s)	-500	500	19	5	6.36
Test16b	Ins Y Vel Spike (mm/s)	-500	500	9	2	6.37
Test17	Repeat Value in successive points ()			361	336	7.15
Test20	Vertical 2-D Velocity Gradient()	0	300	45	44	7.25
Test21	Time Vector dt outside 120 +/- 10s()	110	130	241	122	7.53

Figure J.3: ADCP 2 Bin# 4 (approx. center of turbine swept area) quality control results table indicating the tests performed, the number of points flagged from each test and the total number of points flagged. A total of 7.53% of the data was flagged and removed at this depth bin.

ADCP_2_Bin_20	Test Description	Lower Limit	Upper Limit	# of points flagged	Increase in Total points Flagged	% of Total Points Flagged After each test
Test1	Battery Voltage (0.1 V)	12	24	0	0	0.00
Test3a	Heading (1 deg)	135	150	6	6	0.01
Test3b	Pitch (1 deg)	-2	2	4	0	0.01
Test3c	Roll (1 deg)	-2	2	4	0	0.01
Test6	Signal Strength (0.25 dBm)	-10	-80	3094	3093	7.22
Test7	Sig to Noise Ratio (0.25 dB)	10	90	3061	0	7.22
Test9	Good Pings (#)	58	60	22	17	7.26
Test10	Current Magnitude (m/s)	0	3.5	0	0	7.26
Test12a	INS XVEL MAX (mm/s)	0	3000	0	0	7.26
Test12b	INS YVEL MAX (mm/s)	0	2000	0	0	7.26
Test13	INS ZVEL MAX (mm/s)	0	1000	0	0	7.26
Test15a	Ins X Vel Rate of Change (mm/s)		500	201	176	7.67
Test15b	Ins Y Vel Rate of Change (mm/s)		500	254	211	8.16
Test16a	Ins X Vel Spike (mm/s)	-500	500	26	7	8.17
Test16b	Ins Y Vel Spike (mm/s)	-500	500	42	12	8.20
Test17	Repeat Value in successive points ()			352	327	8.96
Test20	Vertical 2-D Velocity Gradient()	0	300	24	21	9.01
Test21	Time Vector dt outside 120 +/- 10s()	110	130	241	122	9.29

Figure J.4: ADCP 2 Bin# 20 (approx. 5m below water level) quality control results table indicating the tests performed, the number of points flagged from each test and the total number of points flagged. A total of 9.29% of the data was flagged and removed at this depth bin.

	Test Description	Lower Limit	Upper Limit	# of points flagged	Increase in Total ...	% of Total Points Flagged After each test
Test6	Signal Strength (db)	20.4000	100	0	0	0
Test7	Correlation (%)	64	100	2198829	2198829	3.9528
Test10	Current Magnitude (m/s)	0	5.2500	10506	886	3.9544
Test12a	INS XVEL MAX (m/s)	-4	4	29882	2556	3.9589
Test12b	INS YVEL MAX (m/s)	-4	4	2115	7	3.9590
Test13	INS ZVEL MAX (m/s)	-1.5000	1.5000	40	0	3.9590
Test15a	Ins X Vel Rate of Change (m/s)	NaN	1.2000	124390	9313	3.9757
Test15b	Ins Y Vel Rate of Change (m/s)	NaN	1.2000	48649	274	3.9762
Test16a	Ins X Vel Spike (m/s)	NaN	1.2000	70290	628	3.9773
Test16b	Ins Y Vel Spike (m/s)	NaN	1.2000	30372	226	3.9777
Test21	Standard Deviation Filter x=4.5std | y=11std | z=12std	NaN	NaN	2213768	1049	3.9796
ADV1 QC Results						

Figure J.5: ADV1 quality control results table indicating the tests performed, the number of points flagged from each test and the total number of points flagged.

	Test Description	Lower Limit	Upper Limit	# of points flagged	Increase in Total points Flagged	% of Total Points Flagged After each test
Test6	Signal Strength (db)	18	100	21	21	3.7625e-05
Test7	Correlation (%)	64	100	4097682	4097661	7.3417
Test10	Current Magnitude (m/s)	0	5.2500	89506	146	7.3419
Test12a	INS XVEL MAX (m/s)	-4	4	40846	387	7.3426
Test12b	INS YVEL MAX (m/s)	-4	4	143487	1001	7.3444
Test13	INS ZVEL MAX (m/s)	-1.5000	1.5000	566	4	7.3444
Test15a	Ins X Vel Rate of Change (m/s)	NaN	1.2000	658439	15047	7.3714
Test15b	Ins Y Vel Rate of Change (m/s)	NaN	1.2000	694308	79	7.3715
Test16a	Ins X Vel Spike (m/s)	NaN	1.2000	260695	349	7.3721
Test16b	Ins Y Vel Spike (m/s)	NaN	1.2000	369260	1287	7.3744
Test21	Standard Deviation Filter x=3std | y=4.5std | z=9std	NaN	NaN	4118236	2254	7.3785
ADV2 QC Results						

Figure J.6: ADV2 quality control results table indicating the tests performed, the number of points flagged from each test and the total number of points flagged.

APPENDIX K

Measurement Campaign Test Log

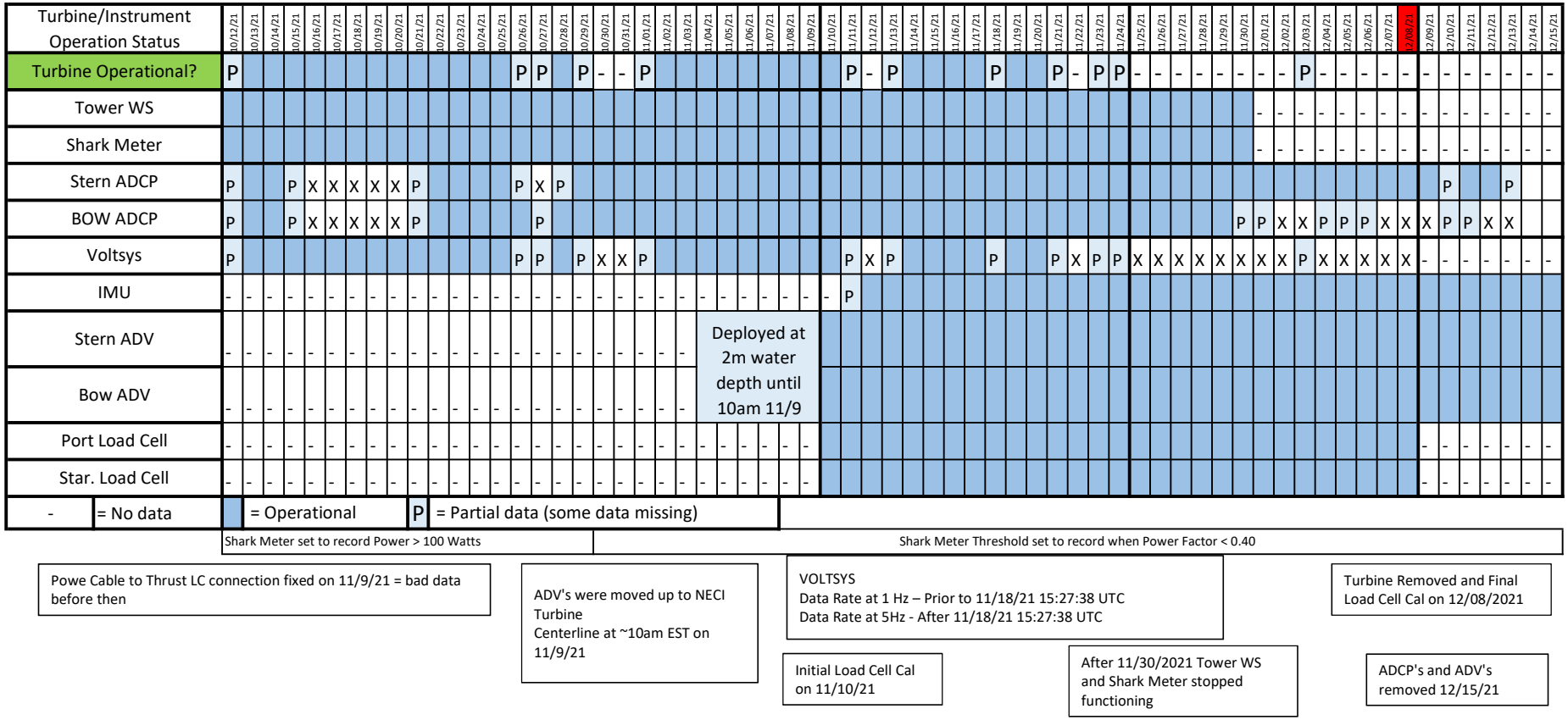
Turbine/Instrument Operation Status
Turbine Operational?
Tower WS
Shark Meter
Stern ADCP
BOW ADCP
Voltsys
IMU
Stern ADV
Bow ADV
Port Load Cell
Star. Load Cell
Deployed at 2m water depth until 10am 11/9
- = No data
= Operational
P = Partial data (some data missing)
Shark Meter set to record Power > 100 Watts
Shark Meter Threshold set to record when Power Factor < 0.40
Powe Cable to Thrust LC connection fixed on 11/9/21 = bad data before then
ADV's were moved up to NECI Turbine
Centerline at ~10am EST on 11/9/21
VOLTSYS
Data Rate at 1 Hz – Prior to 11/18/21 15:27:38 UTC
Data Rate at 5Hz - After 11/18/21 15:27:38 UTC
Initial Load Cell Cal on 11/10/21
After 11/30/2021 Tower WS and Shark Meter stopped functioning
Turbine Removed and Final Load Cell Cal on 12/08/2021
ADCP's and ADV's removed 12/15/21